# General Disclaimer

## One or more of the Following Statements may affect this Document

- This document has been reproduced from the best copy furnished by the organizational source. It is being released in the interest of making available as much information as possible.

- This document may contain data, which exceeds the sheet parameters. It was furnished in this condition by the organizational source and is the best copy available.

- This document may contain tone-on-tone or color graphs, charts and/or pictures, which have been reproduced in black and white.

- This document is paginated as submitted by the original source.

- Portions of this document are not fully legible due to the historical nature of some of the material. However, it is the best reproduction available from the original submission.

# NASA

## Technical Memorandum 85095

# CIRCINUS X-1: A LABORATORY FOR STUDYING THE ACCRETION PHENOMENON IN COMPACT BINARY X-RAY SOURCES

Julia Lee Robinson-Saba

August 1983

APPROVAL SHEET

Title of Thesis: Circinus X-1: A Laboratory for Studying the Accretion

Pheromenon in Compact Binary X-Ray Sources

Name of Candidate: Julia Lee Robinson Saba

Doctor of Philosophy, 1983

Thesis and Abstract Approved: _____

Elihu A. Boldt

Adjunct Professor

Department of Physics and Astronomy

Date Approved: _____14 June 1983_____

CURRICULUM VITAE


Name:  Julia Lee Robinson Saba.


Permanent address:  4209 Oglethorpe Street, Apt. 203
                    Hyattsville, Maryland  20781.


Degree and date to be conferred:  Doctor of Philosophy, August 1983.


Date of birth:  ███████████████


Place of birth:  █████████████


Secondary education:  Regina High School, Hyattsville, Maryland, June 1966.


| Collegiate institutions attended | Dates | Degree | Date of Degree |
|---|---|---|---|
| University of Maryland | 1966-1971 | B.S. | June 1971 |
| University of Maryland | 1974-1983 | M.S. | May 1979 |
| University of Maryland | 1974-1983 | Ph.D. | August 1983 |


Major:  Physics.

Professional positions held:

Summer, Fall 1970:   Intern at Laboratory for High Energy Astrophysics, Code
   661, NASA/Goddard Space Flight Center, Greenbelt, MD  20771.
   Calibration of balloon experiment; library research, resulting in
   in-house technical report on X-ray production and polarization.
   Supervised by Dr. F.B. McDonald and Dr. E.A. Boldt.

June 1971 - Aug. 1974:   University of Maryland faculty research assistant
   for X-Ray Group at NASA/Goddard Space Flight Center.  Electronics
   technician, lab assistant, and data analyst, in detector development
   program, under supervision of Dr. P.J. Serlemitsos.

Sept. 1974 - Dec. 1975:   University of Maryland Physics graduate research
   assistant with NASA/Goddard X-Ray Group.  Calibration and testing of
   X-ray proportional counters and observational planning program for the
   OSO-8 satellite, under supervision of Dr. P.J. Serlemitsos and Dr. F.B.
   McDonald.

Jan. - May 1976:   Graduate teaching assistant at Physics Department,
   University of Maryland, for modern physics course for physics majors.

Sept. 1976 - Aug. 1983:   University of Maryland Physics graduate research
   assistant, with NASA/Goddard X-ray Group, studying X-ray satellite
   observations of cosmic binary X-ray sources.  Work supervised by Dr.
   F.B. McDonald, Dr. E.A. Boldt, and Dr. J.H  Swank.

Professional publications:

"A New Measurement of the Hercules X-1 X-ray Pulse Profile", S.S. Holt,
E.A. Boldt, R.E. Rothschild, J.L.R. Saba, and P.J. Serlemitsos, Ap. J.
(Letters), 190, L109-111, 1974.

"Spectral Variability of Cygnus X-3", P.J. Serlemitsos, E.A. Boldt, R.E.
Rothschild, and J.L.R. Saba, Ap. J. (Letters), 201, L9-13, 1975.

"A 4.8 hour Periodicity in the Spectra of Cygnus X-3", R.H. Becker, J.L.
Robinson-Saba, E.A. Boldt, S.S. Holt, S.H. Pravdo, P.J. Serlemitsos,
and J.H. Swank, Ap. J. (Letters), 224, L113-117, 1978.

"Brief X-Ray Transient", L.J. Kaluzienski, J.L. Robinson-Saba, E.A. Boldt,
S.S. Holt, J.H. Swank, P.J. Serlemitsos, and R.E. Rothschild, I.A.U.
Circ. No. 3174, 1978.

"X-Ray Spectra of X Persei", R.H. Becker, E.A. Boldt, S.S. Holt, S.H.
Pravdo, J.L. Robinson-Saba, P.J. Serlemitsos, and J.H. Swank, Ap. J.
(Letters), 227, L21-24, 1979.

Conference presentations:

"Detailed Spectra of Three Compact Binary X-Ray Sources", J.L.R. Saba, E.A.
Boldt, S.S. Holt, R.E. Rothschild, and P.J. Serlemitsos, Bull. Am.
Phys. Soc., 19, 530, 1974.

"X-Ray Observations of Circinus X-1 Over a Complete 16.6 Day Period", J.R.
Saba, E.A. Boldt, S.S. Holt, P.J. Serlemitsos, and J.H. Swank, Bull.
Am. Astron. Soc., 9, 297, 1977.

"A 4.8 Hour Periodicity in the Spectra of Cygnus X-3", J.L. Robinson-Saba,
R.H. Becker, E.A. Boldt, S.S. Holt, S.H. Pravdo, P.J. Serlemitsos, and
J.H. Swank, Bull. Am. Phys. Soc., 23, 528, 1978.

"A Search for Spectral Variations with Binary Phase in a High State of
Cygnus X-3", J.L. Robinson-Saba, R.H. Becker, S.H. Pravdo, E.A. Boldt,
S.S. Holt, P.J. Serlemitsos, and J.H. Swank, Bull. Am. Astron. Soc.,
10, 420, 1978.

"X-Ray Spectra of Strong Galactic Sources", P.J. Serlemitsos, J.H. Swank,
and J.R. Saba, Tenth Texas Symposium on Relativistic Astrophysics,
Baltimore, 1980.

"Spectral Clues to the Nature of Circinus X-1", J.L. Robinson-Saba, J.H.
Swank, P.J. Serlemitsos, and E.A. Boldt, Bull. Am. Phys. Soc., 27, 545,
1982.

CIRCINUS X-1:  A LABORATORY FOR STUDYING THE

ACCRETION PHENOMENON IN COMPACT BINARY X-RAY SOURCES

by

Julia Lee Robinson-Saba

Dissertation submitted to the Faculty of the Graduate School

of the University of Maryland in partial fulfillment

of the requirements for the degree of

Doctor of Philosophy

1983

# ABSTRACT

Title of Dissertation:  Circinus X-1:  A Laboratory for Studying the
Accretion Phenomenon in Compact Binary
X-Ray Sources

Julia Lee Robinson Saba, Doctor of Philosophy, 1983

Dissertation directed by:  Doctor Elihu Boldt

The observations of the binary X-ray source Circinus X-1 discussed in
this thesis provide samples of a range of spectral and temporal behavior
whose variety is thought to reflect a broad continuum of accretion
conditions in an eccentric binary system.  The data support an
identification of three or more X-ray spectral components, probably
associated with distinct emission regions:

(1) A luminous optically thick component, associated with the cyclic
outburst, has a spectrum which is to good approximation a blackbody of
$kT \sim 0.8 - 1.0$ keV, with an apparent radius of $\sim 40$ kilometers for an
assumed spherical emitter at a distance of 10 kiloparsecs.  This component
sometimes exhibits large amplitude fluctuations, including quasiperiodic
oscillations on a timescale of seconds, corresponding to individual square
shots of luminosity $> 10^{37}$ erg.  The luminosity, size, and variability of
this component suggest an origin in the inner region of an optically thick
accretion disk around a compact object of mass $\gtrsim$ three solar masses.  If
the compact objects in Circinus and other black hole candidates such as

Cygnus X-1 and GX339-4, which exhibit a component with similar characteristics, are neutron stars, they form a separate class whose properties are not predicted by any current model of accretion onto neutron stars.

(2) A low level residual component, steady on a timescale of days, comes from a region larger than the binary system if the source is not continuously fed. The spectrum is optically thin, with little absorption and strong iron line emission. The latter suggests the presence of thermal gas, though a nonthermal contribution to the flux is also likely, from inverse Compton scattering of quiescent infrared flux by nonthermal electrons associated with the extended quiescent radio source.

(3) A post-outburst X-ray flare component, possibly related to the radio and infrared flares, shows a flat, absorbed spectrum. Variability on a timescale of minutes restricts the emission region to $<< 10^{13}$ cm, smaller than the radio flare region. A likely origin of the X-ray flares is inverse Compton scattering of infrared flux by a low energy extension of the nonthermal electrons producing the radio flares. Comparable luminosity in gamma-ray flares seems probable.

# FOREWORD

"The problem of darkness does not exist for a man gazing at the stars. No doubt the darkness is there, fundamental, pervasive, and unconquerable, except at the pinpoints where the stars twinkle; but the problem is not why there is such darkness [with apologies to Olber], but what is the light that breaks through it so remarkably; and granting this light, why we have eyes to see it and hearts to be gladdened by it."

--George Santayana, Obiter Scripta

This thesis is dedicated

with love, respect, and gratitude

to my mother, my first teacher,

Jean Dumont Robinson,

to my father, my first intellectual companion,

Herbert Eugene Robinson,

and to my husband,

Jack Leonard Saba,

partner in the quest

for knowledge and understanding.

# ACKNOWLEDGMENTS

taught by Dr. Elihu Boldt. Time and again, in the classroom or at the lunch table, he has renewed that spark with his particular view of the interplay between physics and astrophysics. Frequently his perspective on a given problem has caused me to rethink and understand more fully the fundamental physics involved. For the past year and a half, since his appointment as adjunct professor to the University of Maryland Physics Department, Elihu has assumed the official role of thesis advisor and helped me draw this chapter of my education to a close. I gratefully acknowledge his interest and support over the years and his recent concentrated efforts on my behalf.

In the months before and several years after I received my bachelor's degree at Maryland, I was privileged to work with Dr. Peter Serlemitsos in the X-ray lab at Goddard. Under his guidance, I participated in an epoch of detector development which produced prototypes of the high quality, reliable satellite instruments whose data are analyzed in this thesis. It was largely due to Peter's influence that I returned to school and pursued a Ph.D. After my coursework and exams, he supervised my initial analyses of OSO-8 data, getting me started on research in earnest. His continuing encouragement has given me confidence to proceed in good times and bad.

Over the past three years, Dr. Jean Swank of the X-Ray Group has worked closely with me to help me shape a thesis and bring it to a meaningful conclusion. Her broad-based, multi-dimensional support has been so extensive, that the only way I could begin to acknowledge it properly was by finishing.

For background material for portions of this thesis, I have relied heavily on a number of references, listed by topic at the back. My general astrophysical knowledge is based largely on courses taught by Dr. David

accessible through the efforts of a host of dedicated, talented software personnel. Mr. Louis Perrazoli and Mr. Philip Yu were largely responsible for the initial OSO-8 analysis software. Dr. Allan Stovtlemyer directed the formation of the HEAO A2 data base. I have had personal assistance in obtaining or processing data from Ms. Deborah Derrick, Ms. Mary Ann Esfandiari, Ms. Jenny Jacques, Ms. Nancy Laubenthal, Ms. Denise Lengel-Frey, Mr. Fernando Lopez, Ms. Marilyn Newhouse, Ms. Betty Pynn, and Ms. Kim Tolbert.

Throughout my stay at Goddard, I have received outstanding secretarial support, particularly from Ms. Barbara Pratt, Ms. Barbara Shavatt, and Ms. Sandra Shrader. I am overwhelmed by the zeal with which Sandy has carried out the arduous task of typing multiple versions of this manuscript. She has translated my midnight scrawl, shaped cumbersome tables, and incorporated innumerable changes with equanimity and consummate skill, working extra hours and weekends to let me meet deadlines which seemed impossible. Far beyond the call of duty, her assistance in getting me through demonstrates a warm personal interest and concern.

Messrs. Frank Shaffer, Adam Thompson, and Harry Trexel have given skilled, efficient drafting support for the figures in this thesis, and for presentation and publication artwork over the years. I have been continually gratified by the excellence of the final representations of my initial drawings. I am especially indebted to Mr. Harry Trexel for his expert interfacing with contractors for many complex thesis figures. His prior advice on what was effective and possible was invaluable. Always he came through in meeting tight deadlines, even if it meant correcting or redoing the figures himself in the midst of other heavy commitments.

I would like to acknowledge here those not noted above who have had a

major influence on my graduate career:

My interactions with the Physics Department and the Graduate School were greatly facilitated by the late Mrs. Mary Dobbins Mason, who served as advocate and confidante for the graduate students, along with her more official duties in Graduate Records. She rejoiced in our triumphs, consoled us in our trials, and found ways to help us survive. Over the years Mary evolved from something of a mother figure to me to a very special friend.

Enroute to her own Physics Ph.D. at the University, Dr. Deborah Van Vechten gave generously of her time and energy as a student advisor, providing counsel, sympathy, and friendship.

In a pre-qualifying exam tutorial, Dr. J. Robert Dorfman of the Physics Department helped me gain experience in doing physics on my feet. Beginning with our joint tenure on the Physics Community Committee, he has also served as my model for combining scientific excellence with human values.

At a critical point in my graduate studies, when my thesis topic had not yet taken shape, my work with Dr. Robert Becker helped me decide to continue in graduate school, and spurred my progress in independent research. While the thesis does not explicitly include our investigations of Cygnus X-3, it has benefitted from the data analysis techniques and approaches I learned as Bob's colleague.

A very close circle of friends has given helpful advice and long-term support to keep me going: Dr. Judith Karpen, Ms. Barbara Lambird, Dr. Antoinette Galvin, and Dr. Chhanda Samanta. My sister, Ms. Susan King, has made significant contributions to maintaining my sense of balance and human perspective. Throughout the lengthy gestation of this thesis, I have

drawn considerable strength from the unwavering faith and encouragement of my family.

The whole-hearted support of Jack Leonard Saba has been crucial in carrying me through. He has tolerated my outrageous schedule, and offered stability, reassurance, and hot meals through the darkest hours. In the final push, he has taken time from his own research to supply xeroxing services and to edit the penultimate version of the thesis in its entirety. His intervention is responsible for many substantial improvements in clarity of word and thought. For more than a dozen years, through all of our shared adventures in learning, his presence at my side has made all things possible.

## TABLE OF CONTENTS

# LIST OF TABLES

# LIST OF FIGURES

# I. INTRODUCTION

## A.  The Role of Pattern-Seeking in Astrophysics

The roots of astronomy go back to the earliest humans, who sought from patterns in the changing of the seasons and the phases of the moon, and the motions of the planets and the stars, some predictability, in the universe about them.  Developing astronomy was bound up with astrology and mythology and religion -- other human attempts to come to terms with the universe. Eclipses and comets were viewed with superstition and terror, which threatened to undermine the beginnings of understanding.  Yet, even as the heavens were worshipped or feared, the rhythms of the moon and regularities in the motion of the stars and planets were becoming tools -- for astrological predictions, yes, alas, but also to forecast times for planting and harvesting, as aids in navigation, in the establishment of a calendar.

Astrophysics, the investigation of astronomical phenomena in terms of physical laws, probably began with Newton's leap of insight that a falling apple and a planetary body might be governed by the same force.  This leap required the firm foundation built on Brahe's painstaking celestial observations and Kepler's reduction of them to empirical laws of planetary motion, on Galileo's development of an astronomical telescope and application of the scientific method to sky-gazing.  Since that time, progress in astrophysics has generally resulted from a similar synthesis of

physical theory with meticulous observation and laboratory experiment, supported by the development of some new technology, which opened a new window for viewing the universe. Laboratory spectroscopy and investigation of the basic laws of radiation, for example, allowed stellar spectral sequencing, wherein a pattern was perceived and partially understood in terms of the developing atomic physics, an essential step in recognizing the role of nuclear burning in the evolution of stars.

In a physics laboratory, much of what we learn is the result of scattering experiments: we probe the internal structure of matter by bombarding it with particles and light, varying the materials, angles, incident energies and then studying the products to identify and characterize the important parameters of the problem. Similarly, astrophysical information is obtained by accumulating observations of radiation given off, reflected by, and transmitted through astronomical objects. A major difference is the lack of opportunity to manipulate conditions in the cosmic laboratory. Instead, an astronomer observes phenomena in all their complexity and seeks out underlying patterns. Rather than constructing a simplified version in the laboratory, the astronomer usually proceeds by identifying classes of objects which can be treated somewhat as ensembles of systems, making cross-comparisons of similarities and differences to map out the allowed portions of parameter space. The trick is to guess the interesting parameters and find a representation of the data which is not merely a scatter plot. Natural restrictions on the parameters (those not a result of selection effects imposed by the method of observation) generally represent physical constraints on the systems, often an important clue to their nature. Thus, the Hertzsprung-Russell (H-R) diagram, essentially a plot of luminosity

versus temperature (or, equivalently, spectral class or color) for a set of stars, is fundamentally related to the way stars evolve.

In an H-R diagram, roughly 99% of all stars lie along a narrow band called the main sequence, stretching diagonally across the plot from hot (blue) bright massive stars to cool (red) faint low mass stars. Stars spend most of their lives as main sequence dwarfs, converting hydrogen to helium as their source of luminosity. When a significant fraction of a star's hydrogen has been converted, structural changes cause the star to expand, brighten, and move off the main sequence into the red giant region. The more massive stars burn fuel more quickly and thus evolve more rapidly, remaining on the main sequence for only a few million years, while a star like the sun remains there a thousand times as long. Eventually, when all the nuclear fuel has been consumed, the star may gravitationally collapse down to a compact object or the energy release may lead to ejection and dispersal of mass and leave at most a remnant to collapse. Whether the resulting object becomes a roughly earth-sized white dwarf held up by electron degeneracy pressure, a neutron star of order 10 km radius held up by neutron degeneracy, or an ever collapsing black hole with a Schwarzchild radius of about 3 km per residual solar mass -- so dense that even light cannot escape its surface -- depends on how much mass it had initially, how much it lost during episodes of instability or through wind outflow, and the details of the collapse.

## B.  Variability in Astrophysics

For many centuries the only challenges to belief in the constancy of the stars, a dogma handed down by Aristotle, came from observations of comets (attributed at first to atmospheric effects) and occasional "guest

stars", or supernovae (originally believed to be new stars, but actually stars in a final explosive stage of evolution). At the end of the sixteenth centry, the German astronomer David Fabricius, a colleague of Kepler, noted that the third magnitude star Omicron Ceti faded and then disappeared. He took it for a nova, a weaker version of Tycho Brahe's star, which had erupted in a blaze of glory some two dozen years earlier, temporarily rivaling Venus in brightness. By mid-seventeenth century, Mira Ceti ("the wondrous one in the Whale") was known to have an eleven-month variability cycle. Two centuries later, nearly two dozen assorted naked-eye variables were recorded. The General Catalogue of Variable Stars (Kukarkin et al. 1970) now lists some 25,000 entries--periodic (eclipsing, pulsating, rotating) and nonperiodic (mostly eruptive variables). There are likely to be many more variable stars found with closer examination. Still, probably at most a few percent of stars show major variations on timescales short compared to a human lifespan.

It is believed that all stars pass through fairly short-lived periods of variability -- during their very early stages, near the end of their nuclear burning lives, and in one or more episodes of instability in between, when a particular thermonuclear energy supply is depleted, causing changes in internal structure and composition, and thus in luminosity and radius, making the star unstable against pulsations or eruptions.

Variability studies have been important astrophysical tools, both for revealing the nature of the varying objects, and for tangential applications. The Period-Luminosity correlation for classical Cepheids, reported by Henrietta Leavitt (1912), showed that the pulsations were not due to orbital motion and also provided a measuring stick for the cosmic distance scale. This empirical relation was developed and used some years

before the pulsation mechanism was understood. In 1917, Sir Arthur Eddington (1917,1918) derived the wave equation describing the pulsations, and showed that the underlying reason for the period-luminosity law was the proportionality of the period to the inverse-square-root of the density.

For most of the pulsating variables, the period, amplitude, and shape of the lightcurve (i.e., the plot of intensity versus time) are correlated with position in the H-R diagram, that is, with mass, luminosity, and age. Thus a distant pulsating star can sometimes be identified by its light curve, when its spectrum is too faint to measure, and its distance is otherwise unknown.

Soon after radio "pulsars" were discovered in the late 60's (Hewish et al. 1968; Pilkington et al. 1968) by a new type of radio telescope built to study fast changes in the solar wind, the characteristics of the extremely stable periodic signals helped pin down the nature of the objects. Though the naming appears irrevocable, pulsations were ruled out when slow increases in period were observed, since the period of pulsations should decrease with time. For the subsecond periods observed, orbital motion of two compact objects could not have held against gravitational radiation. That left rotation as the source of the clock, with the gradual decrease in period most readily explained as a loss of rotational energy. The periods implied anything less compact than a neutron star would have a surface velocity greater than the escape value and hence be torn apart by rotation. Thus the pulsars came to be recognized as rapidly rotating neutron stars.

In turn, the observed wavelength dependence of the pulse arrival times can be used to study the interstellar medium through which the pulsar beam propagates. The delayed frequencies are greater than the plasma frequency

(proportional to the square root of the electron number density) of the dispersing medium, and thus put an upper limit on the number density of the medium. Further, the time delay is proportional to the integrated number density along the line of sight, which gives an estimate of the distance to the pulsar if the average interstellar number density $<n>$ is known. (Or, if the distance is otherwise known, an improved value of $<n>$ in that direction is obtained.)

## C.  Compact Objects

At the beginning of the century, a massive observational effort with large telescopes, spectrometers, and photography allowed astronomers to come to an understanding of stars in terms of classical thermodynamics and radiation laws:  stars were large, hot, ionized bodies of gas held together by gravity. Soon a few small, dense "white dwarfs" were found, which would not fit into this picture. By classical standards, their high densities ($\gtrsim 10^5$ gm cm$^{-3}$) should have made them more luminous than was observed.

Following the development of quantum mechanics and quantum statistics in the 1920's, Fowler (1926) proposed that quantum physics be applied to the high density regimes of white dwarfs. Within a few years, the fundamental properties of white dwarfs had been worked out (principally by Milne, Stoner, Chandrasekhar and Landau) from the core idea that they were supported by a degenerate electron gas, too cold to radiate photons despite the high internal energy. What was not accepted for a number of years (largely due to the influence of Eddington [see, e.g. Wali 1982]) was the concept of a critical mass for the white dwarf against gravitational collapse. This effect, generally called the "Chandrasekhar mass limit"

(although it was described independently at about the same time by Landau (1932) and Chandrasekhar (1931)), is due to a relativistic "softening" of the equation of state (i.e., a decrease in the dependence of the pressure on the density in the relativistic regime).

Soon after the discovery of the neutron, Landau (1932) discussed the possible existence of a star built from degenerate neutron gas, orders of magnitude denser than a white dwarf. Baade and Zwicky (1934) suggested ("with all reserve") that "supernovae represent transitions from ordinary stars into neutron stars", and Gamow (1936) described the configuration of such a star. Carrying out detailed computations of equilibrium configurations of neutron stars, Oppenheimer and Volkoff (1939) showed that there is a limiting mass above which there is no stable solution to the general relativistic equations; then Oppenheimer and Snyder (1939) presented a fully relativistic theory of the gravitational collapse of a star above that mass. But, in the astronomical community, neutron stars and the even more exotic ever-collapsing objects (later to be called "black holes") were largely ignored for many years as curiosities without experimental verifiability.

In the 1950's the seminal work of Burbidge, Burbidge, Fowler, and Hoyle (1957) led to the expectation that massive stars ($\sim 50$ $M_0$) should evolve to a state in which a dynamic implosion would occur, leaving a degenerate iron core. Cameron (1959), reviving the 20-year-old idea of Baade and Zwicky, suggested that this core would collapse to a neutron star through inverse beta decay, blowing off the outer envelope of the star. Still, it was generally believed that neutron stars (and black holes), lacking an internal source of energy, would be virtually undetectable.

## D. X-Ray Binaries

The discovery of bright discrete cosmic X-ray sources in the early 60's came as a complete surprise, although they might conceivably have been anticipated as the logical consequence of collapsed objects in binary systems accreting material from their companions. The radio pulsars, visible confirmation of the existence of neutron stars, had not yet been found. Moreover, the evidence that many of the X-ray sources were in binary systems at first seemed to argue against their being neutron stars because early calculations indicated that supernova explosions would almost certainly disrupt the binary systems in which they occurred. As observations of radio pulsars and X-ray objects accumulated, theoretical progress in astrophysics accelerated. Once it was found that binary systems would remain intact after supernova explosions for a fair range of initial conditions, a binary X-ray system began to appear as a natural stage in the evolution of a normal binary (see, e.g., Kraft 1975, and references therein). Most of the X-ray bright objects in our galaxy are now believed to be such systems: close binaries in which one member is a very compact object--a neutron star or, perhaps, a black hole--accreting material from its companion and releasing of order ten percent of the rest mass energy at X-ray wavelengths in its deep gravitational potential well. With this level of efficiency, a mass transfer rate of $10^{-10}$ solar masses per year is enough to produce an X-ray luminosity of about $10^{36}$ ergs $s^{-1}$. If the infalling material carries too much angular momentum to fall directly onto the compact object, as in overflow of the companion through the inner Lagrangian point, it forms an accretion disk in which the angular momentum must be dissipated before the material can flow in further. The flow of material from a stellar wind, on the other hand, tends to be

spherically symmetric and essentially prompt, though a wind which is slow enough compared to the binary orbit velocity may form a marginal disk (§ III. A2b). If the inner part of an accretion disk becomes unstable and puffs up, as it may when the mass transfer rate is high, the flow near the compact object may again become approximately spherical.

In fact, these X-ray bright objects are relatively rare, with $\sim 10^2$ known in a galaxy with $\sim 5 \times 10^{10}$ binary star systems. Most stars become white dwarfs in a process considerably quieter than a supernova explosion. As discussed in § III.A, the white dwarf systems probably do not become strong X-ray sources (though after accreting sufficient material, the white dwarf may at length be transformed into a neutron star). Of those binaries in which a supernova explosion does occur, leaving a residual neutron star (or black hole) and an intact system, not all will have sufficient mass accret , rates: the stellar separation may be too great for significant interception of the companion's outflow, the companion may not be sufficiently massive or at the correct stage of evolution to have a strong outflowing wind or to overflow its (generalized) Roche lobe (i.e., its gravitational equipotential surface). Further, the compact object may be rotating too fast too accrete efficiently, or the companion may be rotating so fast that material leaves the stellar surface with sufficient velocity to escape the system, so that little can be captured. Even a system which meets all of the necessary criteria will have a transitory existence as an X-ray source. Eventually the companion, having given up sufficient mass, will become stable against wind outflow, shrink back inside its Roche lobe, or itself move on to a more compact state of existence.

## E.   Variability of X-Ray Binaries

As a class, close binary systems containing compact objects may constitute the most variable objects in the sky. They show at least two types of variations, sometimes at many wavelengths:  the periodic changes which in fact help identify them and the characteristics of which provided the first insight into their nature, and aperiodic changes, which are harder to interpret, but which likely reflect the basic physical conditions of accretion disks and the accretion process.

Periodic variations are thought to arise from three natural clocks in the system:

1) Rotation of the compact object (fractions of a second to hours). It is assumed in most cases that a strong magnetic field channels the accretion flow onto one or more spots which rotate in and out of view.  In cases where the pulse is very sharp, it is thought that the X-rays produced at the spot are beamed, with the beam crossing the line of sight as the compact object rotates.

2) Orbital motion (hours to days for close binaries).  The orbital motion of the two stars changes the line of sight configuration in a systematic way.  The exact form of the resulting modulation (its depth, duration and shape) depends on the angle of inclination of the orbit, the relative size and separation of the objects, their nature and that of the accretion disk, and the ambient material in the system.  As discussed briefly below and at greater length in Chapter III, if the orbit has a substantial eccentricity, the real as well as the apparent configuration changes, so that the physical conditions also vary in a systematic way, leading to changes in accretion and emission.

3) Precession of the accretion disk (some weeks). The accretion disk, in general tilted and twisted, can periodically shadow the X-ray source.

Aperiodic variations on a variety of timescales are even more common, perhaps nearly universal, in X-ray binaries. Long term variations (months to years), frequently involving a change of spectral state, are thought to reflect changes in the accretion rate (possibly from changes in the companion) and perhaps formation or evolution of an accretion disk. Flares and bursts lasting some seconds to tens of seconds may be related to inhomogeneities in the accretion flow, transient events in the outer part of an accretion disk, or instabilities in the accretion process. In some cases they are thought to be thermonuclear flashes on the surface of a neutron star. Some sources show highly erratic variations on a timescale of seconds or less, sometimes with flares as short as milliseconds. There has been partial success in a mathematical description of this activity in terms of shot noise (a superposition of random narrow pulses of similar intensity and duration), but the underlying physics is not understood. Several mechanisms have been suggested as responsible -- such as hydrodynamical instabilities, transient magnetic structure, rotating hot spots in the inner part of the accretion disk -- but it is not clear which if any should apply.

Realistic modeling of the aperiodic variability requires further confrontation of theory with observations. An ideal observational goal would be an accumulation of data from many sources in their various spectral, intensity, and activity states. However, a more accessible goal is a detailed study of the different states of a single highly variable system. Details of spectral shape as a function of luminosity may reveal

the structure of the emission region, the size a.d mass of the compact object, parameters of a magnetosphere if one is present. Comparison with less variable, partially understood sources with matching characteristics may help shed light on both if it can be established to what extent the differences are fundamental, or whether they arise from a basically similar mechanism with different constraints (stellar mass, mass loss rate, orbital eccentricity, for example).

## F.   Circinus X-1, Eccentric Binary:   A "Scattering Experiment"

The source Circinus X-1 seems a particularly appropriate candidate for study: its behavior is especially various, and it might therefore reveal sufficient clues to allow us to interpret its nature. It exhibits large amplitude, irregular changes on virtually all timescales, with spectral similarities to a variety of sources. Its short-term chaotic fluctuations are reminiscent of the black-hole candidates Cygnus X-1 and GX339-4; to date no known neutron stars have shown such fluctuations on timescales much less than a second. It shows quasi-periodic behavior (possibly related to transient events in the outer part of an accretion disk) on timescales from fractions of a second to seconds, but no known true pulsations. It flares on timescales from seconds to hours, possibly a result of inhomogeneities in accretion flow. Its irregular modulation on timescales of months to years resembles the long-term transients. During periods of low flux the source is virtually undetectable. At its brightest, its flux is 20% that of Scorpius X-1, the brightest galactic X-ray source. Because its distance is believed to be 8-10 kiloparsecs, such a flux implies a very large luminosity indeed--several times the "Eddington limit" for a one solar mass object at which radiation pressure inhibits further accretion--unless a

special geometry is invoked. At such times it is perhaps the most luminous
X-ray object in the galaxy, accreting at a supercritical rate unless it is
rather massive ($\gtrsim 3$ $M_O$) compared to the standard neutron star model.

When not in its low state, Circinus shows a 16.6 day presumably binary
period with a short duty-cycle asymmetric peak, likely indicating a highly
eccentric orbit, perhaps with an eccentricity of 0.7 or more. Sharp
turn-ons of the flux could indicate the presence of a magnetic field which
holds off the accretion until a sufficiently high pressure is reached.
Abrupt declines in the flux on timescales of minutes or less suggest
catastrophic triggering of an instability in the accretion. (For a more
detailed discussion of the source behavior and general background
information available in the literature, see Chapter II.)

In an eccentric orbit, the compact object samples a large continuum of
physical environments in a systematic way: as the stellar separation
changes, so does the relative velocity and ambient particle density. and
even more drastically the accretion rate, the resulting luminosity, and the
ionization state of the local material. Further, as the stars approach and
recede, the gravitational potentials change, with a resulting change in the
contribution to accretion from outflow through the first Lagrangian
point. Last, the binary lightcurve appears to be evolving on a timescale
of years; this has been taken as evidence that the system may be precessing
fairly rapidly, as much as $-10^{o}$ per year (see § IIC). If this is so, we
are presented with a changing vantage point, which should allow us to
determine the extent to which the observed variations are intrinsic rather
than a matter of varying optical depth along the line of sight.

In a sense the Circinus system approaches a laboratory scattering
experiment for studying the accretion phenomenon. It provides systematic

changes in accretion conditions modulated by a variable input from the companion, with episodes of critical accretion. It probably has an accretion disk which varies with time because of changes in the wind parameters, changes in the overflow, or both. It produces a range of spectral and variability states with similarities to a variety of different kinds of sources. If its own code can be unlocked, it might serve as a Rosetta stone to help decode observations of several types of sources.

## G.   Contributions of this Thesis to an Understanding of Circinus

The observations of Circinus reported in this thesis provide a sampling of a variety of interesting behavior from the source. In efforts to understand the Circinus system, several groups of workers have proposed models which attempt to account for previously reported data, and which make certain testable predictions. The Goddard detectors on the OSO-8, HEAO-1, and HEAO-2 (Einstein Observatory) satellites provide some of the spectral and temporal detail needed to check the implications of the models.

Coe, Engel, and Quenby (1976) suggested that the large outbursts of soft flux from Circinus are due to periodic removal (as might occur in an eccentric binary system) of a dense screening gas to expose a relatively stable source with a power law spectrum.

Murdin et al. (1980) elaborated on this idea with a detailed eccentric binary model which proposed to explain all of the available radio, infrared, optical, and X-ray information. In particular, they modeled the envelope of the observed periodic lightcurves in terms of photoelectric absorption by the dense (cold) wind of an early type companion for an X-ray source of nearly constant intrinsic luminosity (as from steady disk

accretion). They account for the evolution of the lightcurves over a decade of satellite observations as an effect of a changing line-of-sight orbit orientation as the orbit precesses rapidly.

Noting that the hydrogen column densities for Circinus during periods of low flux were low compared to that predicted by this model, Chiappetti and Bell-Burnell (1981, 1982) instead proposed a fast wind accretion model to provide intrinsic modulation in a less eccentric orbit, reducing the required optical depths.

Fransson and Fabian (1979) suggested that the companion of Circinus is an early-type supergiant with a wind strongly affected by the luminous X-ray source. In their picture, the resulting complex structure of the stellar wind could be responsible for the abrupt X-ray transition and the residual X-ray flux, as well as the infrared and radio flaring which begin as the X-rays subside.

While each of these pictures describes some aspects of the Circinus system, the analyses presented in this thesis show that the reality is more complex, probably involving a combination of wind accretion, disk accretion, and ionization and absorption effects (see Figures 7-3 to 7-11). In particular, the simple photoelectric absorption model requires drastic revision. Also, a recent decrease of 2-3 magnitudes in the optical flux from the system gives strong evidence that the companion is not an early-type supergiant as suggested in some of the models. Instead the bulk of the optical flux probably comes from the outer part of a variable accretion disk which shows large long-term changes (Nicolson, Feast, and Glass 1980).

A moderate outburst covered by OSO-8 (see Figure 5-3) showed a multi-component spectrum with complex spectral/temporal evolution: a

relatively steady optically thin component with a strong iron line emission feature which persisted after the transition to low flux, a softer optically thick component associated with the outburst, and a brief hard flare after the transition. The outburst spectrum at low energies was not a simple extrapolation of the harder flux (see Figures 5-3 and 6-2) and thus not a simple uncovering of a constant source.

The steady component, consistent with a power law of photon index ~ 2 or thin thermal bremsstrahlung emission at kT ~ 8 keV, varied by less than a factor of 2 over several days and probably originated in an extended region. The optically thick highly variable component, well fit by a blackbody of kT ~ 0.8 keV, probably came from a region closer to the compact object. The large-scale variations in this component were not entirely an effect of absorption (see Figure 7-6). At peak flux, the source showed flickering on a timescale of seconds (see Figure 6-3), ascribable to changes in temperature of a nearly constant-sized blackbody, with an equivalent radius of ~ 40 km for a spherical emitter at a distance of 10 kpc, an interesting size which will be discussed below.

HEAO-1 coverage of the first part of a larger outburst some 20 cycles later (see Figure 5-5) indicated a somewhat hotter blackbody (kT ~ 0.95 keV) of about the same size (see Figure 6-4). Quasi-oscillations in intensity (see Figure 5-6) with amplitudes of a factor of 2 or more on timescales of a few seconds, and rise times as short as 160 msecs, could be attributed to large changes in absorption (see Figures 6-4 and 6-6). The quasi-periods of these oscillations are somewhat longer than those reported by NRL (Sadeh et al. 1979) for observations very close in time, from the A1 experiment on the same satellite. The difference might be due to a change with time or intensity of the source behavior.

Additional HEAO-1 observations during times of low source intensity showed that the "steady" component of the source is not constant over many cycles, and provided another sample of a brief hard flare and significant line emission, whose parameters are closely related to emission region conditions.

HEAO-2 observations of Circinus with combined data from the Solid State Spectrometer (SSS) and Monitor Proportional Counter (MPC) added to the sample of spectral states during low flux (Figures 6-8, 6-11), and also provided a rather different-looking example of a two-component spectrum during an episode of hard flaring on a timescale of seconds (see Figures 5-11, 5-12, 6-9, 6-10).

As intriguing as these glimpses of Circinus offered by the Goddard detectors are, it is not clear how the information gathered from them fits together. We have snapshots of a continuum of behavior, with moderate spectral and temporal coverage of the source twice a year when its region of the sky became accessible to the available satellite. Frequently the observational mode was not optimal for the phenomena observed: Scanning data gave low duty-cycle coverage when the source was varying on a timescale less than or comparable to the scan cycle; high resolution spectra were accumulated on time scales long compared to that of spectral changes, so that details of the changes were washed out; high resolution temporal coverage of fast fluctuations did not preserve the spectral information needed to delineate the multi-component spectra frequently exhibited by Circinus; pointed observations monitored the interesting regime of fluctuations at low intensities without sufficient sensitivity for more than suggestive results. Clarification of the complex nature of Circinus requires high resolution, broad band spectral and temporal

coverage with good sensitivity to low flux levels. The source should be monitored routinely, with special effort given to following it during times of exceptionally interesting activity (as flagged by the alarm system of an "all sky monitor") and mapping the properties of the quasi-oscillatory behavior with time and intensity. At the same time, efforts should be made on the theoretical front to understand possible sources of the quasi-periodic fluctuations observed (along with those of GX339-4 and Cygnus X-1, the clearest example of short-period oscillations from sources other than white dwarfs, that do not show true pulsations). Further studies of the complex ionization conditions expected in the system are needed to locate the variety of emission regions observed. The prospective gain in understanding of accretion in X-ray binaries is large.

The complex spectra shown by Circinus in this thesis study, with an optically thick component (approximately a blackbody) associated with the periodic outbursts and a relatively steady optically thin component, are evocative of a class of low-mass, high luminosity X-ray sources near the galactic center, though the specific spectral parameters and the details of their change with intensity differ. For several observations, the effective radius of the optically thick component of Circinus appears to be ~40 km (for an assumed blackbody spherical emitter at 10 kpc). This size is large compared to the typical neutron star radius (~ 10 km), but small for the inner edge of an accretion disk around a neutron star with a typical magnetic field strength (~ $10^{12}$ Gauss). It is comparable to the innermost stable orbit around a nonrotating black hole of about four solar masses. Because the emissivity is not known, this estimated size does not place a strong constraint on the mass of a possible Schwarzchild black hole in the system, but with the observed peak luminosities, the number is

suggestive.

The three black hole candidates Cygnus X-1, GX339-4, and Circinus X-1, all show a general trend of softening with overall intensity increase, though the details of their spectral shape and evolution, especially during flare events, have important differences. As discussed here briefly and at greater length later in the thesis, the presence of an accretion disk in the Circinus system seems likely, as in Cygnus X-1. However, the two disks are likely to be quite different. The two-component spectrum of Cygnus X-1 is thought to reflect a two-temperature disk. The lack of correlated variation in the two components of the Circinus spectrum argues against a close analogy. The range of mass flows intrinsic to an eccentric orbit, possibly shared by GX339-4 (which shows long-term modulation and a complex spectrum similar to that of Circinus) but absent in Cygnus, may be responsible for the bulk of the differences. Spectral changes during fast variability are likely related to instabilities in the accretion flow, a strong function of the amounts of material involved and the consequent ionization state. Thus, observations of such changes can be used to constrain conditions in the disk.

While it is not presently possible to rule out a model of Circinus based on a neutron star with an atypically weak magnetic field moderating the inner portion of an accretion disk, it may be more straightforward to appeal to a black hole as the condensed object. Whatever the object in the Circinus system, it is at least a constant in the problem and can be constrained by accumulated observations. If it is truly an object with a weak magnetic field and a mass large compared with the standard neutron star model upper limit, its existence has important implications for the neutron star equation of state and for the question of detecting stellar

mass black holes. If it is not massive and its distance determination holds up, then either it has an interesting geometry or it provides crucial information about objects accreting at extreme limits. If it is a black hole and consequently without a magnetic field, the abrupt turnons may teach us something important about accretion disk evolution and instabilities.

The observations of Circinus X-1 reported in this thesis do not combine into a single simple picture of the system. Instead they demonstrate a richness of behavior whose prospective clues to the nature of the accretion process warrant long-term broadband coverage, from radio to gamma-ray frequencies, and high resolution spectral and temporal examination by the next generation X-ray satellites. Many of the X-ray requirements noted have been incorporated into design considerations for the X-ray Timing Explorer. This thesis will help provide a framework for further investigations of the interesting phenomena of accretion it has identified.

## II.  BACKGROUND FOR CIRCINUS X-1

### A.  X-Ray Observations

#### 1.  Early Confusion

Circinus X-1 (4U1516-56) is a highly variable source located in a region of the galactic plane ($\ell = 322°.1$, $b = 0°.0$, Bradt, Doxsey, and Jernigan 1979) that is both crowded and changeable.  Variability of neighboring sources, including transients, and the erratic behavior of Circinus itself, including long-term low-intensity states similar to those of Cen X-3, have compounded the standard problem of source confusion; this was particularly true in the early observations with instruments with broad fields of view, when only "snapshots" of the region were available from rockets and balloons.  It appears quite possible that Norma X-2, discovered by an NRL rocket survey in 1965 (Friedman, Byram and Chubb 1967) is actually the same object as Circinus X-1.  Harries et al. (1971) observed a source they identified as Nor X-2 whose error box was consistent with the NRL and MIT (Lewin, Clark and Smith 1968) positions for Nor X-2 and which also intersected the early error region of Cir X-1 (Margon et al. 1971), and concluded that the two sources were probably the same.  It is also likely that some observations of flux attributed to a combination of Nor X-2 and Lupus X-1 (also discovered in the 1965 NRL survey) were really observations of Circinus.  Unfolding the two sources was frequently difficult and required prior knowledge of the source positions (see, e.g., Harries et al. 1971; MacGregor, Seward, and Turiel 1970; Cooke and Pounds 1971).  For one such instance, MacGregor, Seward and Turiel (1970) remarked that an alternative interpretation of their data was that Nor X-2 was much stronger than Lup X-1, with its galactic longitude a couple of degrees too high. The amended position falls close to that of Cir X-1.  Baity, Ulmer, and

Peterson (1975) pointed out that "the original locations and error boxes of Lup X-1 and Nor X-2 (Friedman, Byram and Chubb 1967) and those used by early observers (e.g. Lewin, Clark, and Smith 1968) and found in catalogs (Seward 1970) do not correspond to any source in the 3rd Uhuru (3U) Catalogs; they were unable to detect flux from either position with the OSO-7 satellite. Thus, if the positions were correct, both sources are strongly variable or perhaps transient. Certainly the region is not without transients (Matilsky et al. 1972; Matilsky, Gursky and Tananbaum 1973). On the other hand, the lack of correspondence in position may be due to the lack of uniqueness in unravelling the positions of variable sources in a complex region of the sky, from single scans with instruments with broad fields of view.

A remaining obstacle to equating Cir X-1 and Nor X-2 involves their respective spectra. Most measurements of Nor X-2 in the range of 2-20 keV give a very hard spectrum, consistent with a thermal fit of $kT \sim 11$ keV (see compilation of spectra in Harries et al. 1971). While Circinus shows large spectral variations (discussed below), at moderate or high intensity, its reported spectra are soft at low energies (Margon et al. 1971; Jones et al. 1974; Davison and Tuohy 1975; Buff et al. 1977; Saba et al. 1977; Dower 1978). For a source strength comparable to the strongest observed for Nor X-2 (when the Norma data fit the 11 keV thermal discussed by Harries et al. (1971)), Margon et al. (1971) fit their spectral data for Circinus with a 3 keV thermal spectrum. Thus the sources may be irreconcilably different. If the sources are distinct, Nor X-2 may recur, and would then have to be accounted for in future observations of Cir X-1. If they are identical the baseline for the long-term behavior of Circinus could be extended backwards in time, perhaps furnishing further clues. The spectral/temporal behavior

of Circinus would then take on additional complexity. There does not appear to be a simple way to resolve the issue at present.

## 2. Discovery

The earliest unambiguous detection of Circinus X-1 was made from an Aerobee rocket flight on 14 June 1969 by Margon et al. (1971). The observers established a fairly accurate position ($\ell = 321^\circ.4 \pm 0^\circ.9$, , b $= -0^\circ.5 \pm 2^\circ$) in the constellation Circinus ("a pair of compasses"), and named the source Circinus XR-1. Their data showed a soft spectrum, consistent with thermal bremsstrahlung at a temperature of $3.7 \times 10^7$ K (kT ~ 3 keV) or a blackbody of temperature $1.1 \times 10^7$ K (kT ~ 1 keV). Both spectral models required absorption corresponding to a hydrogen column density of more than $10^{22}$ atoms $cm^{-2}$ in the line of sight, compatible with 21 cm emission measurements in the same direction (McGee, Milton, and Wolfe 1966); this indicated a source distance of at least several kiloparsecs if the absorption was interstellar and not intrinsic to the source. (The more recent 21 cm absorption measurements of Goss and Mebold (1977), discussed below, imply a conservative lower limit to the distance of ~ 8 kpc.) Thus the 1-10 keV source intensity of $2.85 \pm 0.17$ photons $cm^{-2}$ $s^{-1}$, or $(1.52 \pm 0.09) \times 10^{-8}$ erg $cm^{-2}$ $s^{-1}$, implied a luminosity of ~ $10^{38}$ erg $s^{-1}$, of order the Eddington limit for a 1 $M_0$ star. The observers found evidence for pulsing at a period of $685 \pm 30$ msec, providing 10% of the source intensity in their 10-second scan. While a regular subsecond periodicity has not turned out to be a stable aspect of the source's behavior, other observers have reported possible pulse trains with periods from fractions of a second to several seconds, lasting tens of seconds (Forman et al. 1973, Jones et al. 1974, Torr 1977, Sadeh et al. 1979). Such rapid quasi-periodic

fluctuations have also been associated with Cygnus X-1 (Oda et al. 1971, Schreier et al. 1971, Boldt et al. 1975) and may be a characteristic feature of accretion onto black holes (Shakura and Sunyaev 1973; Pringle and Rees 1972; Rees 1973). Boldt et al. (1975) have shown that the quasi-periodicities of Cygnus X-1 may be another manifestation of shot-noise behavior.

### 3. Short-Term Behavior

Several bursts lasting less than 10 msecs were seen from Circinus in a 1976 rocket observation, with the strongest burst showing a factor of 16 increase over the average rate and structure at the 1 msec level (Toor 1977). [Similar bursts reported from SAS-3 data (Dower, Bradt, and Canizares 1977) are now believed to be spurious (Dower, Bradt, and Morgan 1982), and bursting from Cir X-1 on timescales of 10 msec or less has not yet been confirmed.] The source behavior was erratic with each 10 second scan of the source showing qualitatively different behavior. During one scan a pulsed component at 0.47 Hz provided 15% of the total flux. The flux varied by an order of magnitude during the observation, with an average intensity of ~ 470 Uhuru counts, comparable to the flux level seen by Margon et al. (1971). Rapid irregular intensity variations were present, with the spectral indices correlated with intensity in the sense that the hardest spectra corresponded to the highest count rate. Such spectral hardening with intensity has also been observed from Cir X-1 in SAS-3 data for flares of 3-20 seconds duration, though other such flares showed softening or little or no spectral change (Dower 1978). Goddard observations analyzed in this thesis covered three episodes of extended flaring on the timescale of seconds, two of which showed spectral hardening

and one which showed softening with intensity, as well as two hard bursts of several minutes duration. Details of the spectral changes during these times will be discussed in Chapter VI. An active phase with continual 1-10 sec flaring has been observed for Cygnus X-1, where both hard and soft flares were seen, with a mean flare spectrum the same as the non-flare (low-state) spectrum (Canizares and Oda 1977). A high resolution autocorrelation analysis of the data showed evidence for a 20 ms characteristic time scale. Evidence for a similar 20 ms component for Circinus was found in SAS-3 data during an episode of particularly erratic variability (Dower, Bradt, and Morgan 1982).

While the second and subsecond fluctuations of Cir X-1 and Cyg X-1 show qualitative similarities from analysis of Uhuru data, Weisskopf and Sutherland (1980) show that there are possibly significant differences. The short-term behavior of Cyg X-1 seems fairly well characterized by a shot-noise model, where random shots of time constant $\tau$ and Poisson occurrence rate $\lambda$ are superposed on a steady non-fluctuating background identifiable with the soft spectral component which dominates the high state. In contrast, while Cir X-1 was stronger and less contaminated by statistical problems, the estimates of shot noise parameters were much more variable than for Cyg X-1, indicating that a shot-noise description of Cir X-1 with "steady" parameters may be invalid. Dower (1978) also found that a simple shot noise picture did not apply to the SAS-3 data from Cir X-1. In addition to distinctly different time constants at different times, he found a large variation in the shot parameters for different size bins, with a third moment that was typically negative and close to zero. His work as well as results presented in Chapter VI show that a linear falloff in the autocorrelation function is sometimes a more appropriate description

than an exponential decay.

During an active state of Circinus in August 1977, Sadeh et al. (1979) found non-random burst events in HEAO A-1 data. They suggested that, as opposed to a shot-noise picture of completely independent events, there might be a characteristic delay following a burst before another could occur. Overlapping HEAO A-2 observations, discussed in Chapter VI, showed quasi-oscillations with a period of 4-5 seconds, about a factor of 2 longer than the A-1 timescale, possibly indicating a drift in the timescale with time or a change with intensity.

In addition to intermittent and transitory pulsed behavior, Circinus exhibits chaotic variations on virtually all timescales, a behavior also associated with Cygnus X-1. Intensity variations of a factor of 20 or more on the timescale of seconds were observed from 2-6 keV Uhuru data (Giacconi et al. 1974)from Circinus, with lower amplitude irregular variability on timescales down to 100 msec [involving changes in intensity of up to a factor of 3 in 0.1 sec (Forman, Jones and Tananbaum 1976b)]. In a 1973 rocket observation when Cir X-1 was at ~ half its maximum Uhuru intensity, Spada et al. (1974) found irregular variations of ~ 20% for times of 1 to several seconds, but no subsecond flaring activity, regular or aperiodic. Copernicus data in the 2.5-7.5 keV band showed slow changes over the time scale of a few days, as well as fluctuations over minutes and hours (Davison and Tuohy 1975).

The Copernicus data corroborated the earlier conclusion of Jones et al. (1974) from Uhuru data that the increases in source intensity were generally accompanied by a softening in the spectrum, but could not be used to check their suggestion that the spectrum shows more absorption at times of low average intensity. [Later work shows low intensity spectra with

measured absorption not much more than that due to intervening interstellar material (Saba et al. 1977; Dower 1978; Chiappetti and Bell-Burnell 1981,1982; this thesis).] Extrapolation of three Copernicus spectra out to 20 keV yielded a flux of ~ 0.001 photons $cm^{-2}$ $s^{-1}$ $keV^{-3}$, consistent with the range of values given by Baity, Ulmer, and Peterson (1975) from UCSD OSO-7 scintillator counter observations, strengthening their conclusion that the long-term intensity fluctuations were due to low energy variability. Davison and Tuohy noted that highly variable low-energy flux could be explained either by changes in circumstellar absorption or by soft X-ray flaring. Goddard OSO-8 data with sufficient spectral resolution to resolve a complex outburst spectrum (Saba et al. 1977; this thesis) endorse the latter explanation. The regular outbursts appear to be associated with the onset of a flaring component, though absorption effects are present and can be quite large and variable. SAS-3 observations of Circinus in January 1976 showed a 2-day flare event resembling a fast transient, with a smaller preceding flare reminiscent of precursor flares seen in Cen X-4 and other long-lived transients (Buff et al. 1977). Again, the data showed clear spectral softening with intensity, with a very soft spectrum at maximum, and significant fluctuations on timescales of seconds or less. Observations presented in this thesis help clarify the character of the spectrum at peak intensity and provide further spectral clues to the nature of the short-term fluctuations.

To round out the picture of this "supervariable" source (so-classed by Forman et al. 1973), SAS-3 data have also shown an extended (~ 19 h) high steady state resembling that of certain galactic bulge sources (e.g., GX13+1), where the usual ~ half-second aperiodic component was absent (Dower 1978). This stable state occurred in close proximity to times of

extreme erratic variability, including factor of 2-4 intensity dips lasting 3-300 s and flares lasting 3-20s, which showed no marked spectral dependence on average.

### 4. Long-Term Behavior

The long-term modulation of intensity from Circinus is not well understood. Davison and Tuohy (1975) found the sum of observations consistent with a fairly regular interval of about 220 days between periods of high emission at low X-ray energies, but with an extended baseline, Wilson and Carpenter (1976) found that the intervals were irregular rather than strictly periodic. In light of the possible association of Circinus with the supernova remnant G321.9-0.3, Clark, Parkinson and Caswell (1975) proposed a model of a young, runaway, highly eccentric binary system, in which "OFF" states occurred due to a breakdown of the accretion process near apastron of a very long period orbit, while the "ON" states occurred near periastron. However, the existence of an extended low state of at least 300 days (Kaluzienski et al. 1976) was difficult to reconcile with orbital effects being solely responsible for the long term modulation. While there is good evidence that Circinus is in fact an eccentric binary system (see discussion below), the timescale associated with the binary period is considerably shorter, with the longer-term variations modulating the peak in a given cycle without a clear pattern. The episodes of "high" and "low" intensity states are somewhat reminiscent of those of Cygnus X-1 (discussed by Tananbaum et al. 1972). The latter, however, have a 2-10 keV band flux ratio of 4 or 5 rather than the factor of 20 or so for Circinus.

Buff et al. (1977) pointed out that SAS-3 observations of flare events from Cir X-1 and Aql X-1 would have been "indistinguishable from the

phenomenon of transient X-ray sources if the quiescent intensities of the flare sources were smaller by a factor of 10." These flaring sources seem to be "ON" more often than transient sources and their increases in intensity, amounting to a factor of about 20, are smaller than those of many transients. They suggest that "the differences between the class of highly variable sources like Aql X-1 and Cir X-1 and the class of transient X-ray sources may be only a quantitative one." This association of highly variable sources and transients was previously suggested by Forman, Jones, and Tananbaum (1976a), who showed that several transient X-ray sources were detected at a low intensity years before or after their dramatic outbursts.

## 5. Binary Periodicity and Lightcurve

Despite reports of eclipse-like behavior of the Cir X-1 (Tuohy and Davison 1973; Jones et al. 1974), at first no binary period consistent with all observations could be found (Canizares, Li, Clark 1974; Baity et al. 1975; Davison and Tuohy 1973). The search was hampered by the long-term variations and by the lack of long-term coverage of the source before the launch of Ariel V in October 1974. With the All Sky Monitor (ASM) on Ariel-5, Kaluzienski et al. (1976) examined the behavior of Circinus from launch through April 1976 and found a 16.6 day modulation in the 3-6 keV flux. When not in its low-activity state, Circinus showed approximately regular outbursts of soft flux, the most periodic feature of which was the precipitous drop from high to low flux seen during the larger outbursts, in phase with the 16.6 day period. [The smaller outbursts ended up to half a day earlier than the time predicted by an ephemeris based on the larger bursts (Kaluzienski, private communication)].

The asymmetric binary lightcurve determined by Kaluzienski et al.

(1976) is not typical of the known occulting binaries Cen X-3, Her X-1, and Vela X-1. The ASM observations from 1974 to 1977 showed a short duty-cycle, with the bulk of the emission coming after phase 0.75 (where phase 0.0 is centered on the rapid transition from high to low intensity). The 3-6 keV band intensity often increased by more than an order of magnitude in less than a day, then gradually increased or remained high for up to 5 days before the abrupt (< 90 minutes) falloff. There was no sharp emergence from an eclipse after the turnoff, in contrast to the behavior observed by Uhuru in 1972 (Jones et al. 1974), in which an abrupt turn-on occurred 1.3 days after the turnoff and the intensity remained fairly high for 5 days after.

## 6. High-Energy X-Ray Measurements

At higher X-ray energies, the 16.6 day period of Circinus noted by Kaluzienski et al. (1976) may not always be present. Between Sept 1971 and May 1973, OSO-7 scintillation counter data showed no evidence for periodicity between 5 hr and 100 day, even in the lowest energy channel (7-11 keV), though the 7-57 keV flux varied irregularly by as much as a factor of 25 (Baity, Ulmer and Peterson 1975). The authors noted that other sources in the field of view or possible "aliasing" in the observing schedule might have masked such a period. They did find a steepening of the spectrum with increasing intensity, with the change being due primarily to a relatively greater increase in the 7-11 keV band, with the flux above 20 keV fairly steady. However, during HEAO-1 A4 coverage of Circinus during August 1977 and February 1978, Nolan (1982) found that the observed flux above 15 keV broadly correlated with concurrent All Sky Monitor outbursts seen in the 3-6 keV band.

Simultaneous observations of Circinus by the scintillation telescope
(ST) and rotation modulation collimator (RMC) on Ariel-5 revealed that the
outburst seen at 2.9-7.6 keV by the RMC (Wilson and Carpenter 1976) was not
visible above the 26 keV threshold of the ST (Coe, Engel and Quenby
1976). The joint spectra before, during, and after the outburst were
consistent with a power law source with varying amounts of absorption by
cold material. In this model, two orders of magnitude increase in the soft
flux during the outburst corresponded to a change in the low energy cutoff
from 12 to 3 keV, or a change in the column density from 2.5 x $10^{24}$
to ~ $10^{22}$ atoms $cm^{-2}$. From their own data and previous observations
(summarized by Baity, Ulmer, and Peterson 1975), Coe, Engel and Quenby
(1976) suggested that the large scale low energy outbursts of Circinus be
interpreted as corresponding to the periodic removal of a dense screening
gas to expose a relatively stable source with a power law spectrum, with an
eccentric binary system an obvious model for the source. While an
eccentric orbit provides a natural clock mechanism for the regular
outbursts of soft flux, this simple absorption picture is ruled out by
important observational facts: unabsorbed low intensity spectra, complex
spectra during outburst, and the broad correlation of flux above 15 keV
with the soft outbursts.

B. Other Waveband Measurements

   1. Variability at Other Wavelengths

   A search for a counterpart to Circinus at other wavelengths was
made possible by an improved Uhuru position and error box (Jones et al.
1974). No optical object brighter than 15th mag was found within the 2' x
1' error box (Jones et al. 1974), but a point radio source located ~ 16"

from the best Uhuru position, with a flux density of ~ 0.5 Jy at 408 MHz (75 cm), was suggested by Clark, Parkinson, and Caswell (1975), who planned a search for short-term correlated activity. From two flux measurements made 18 months apart at 408 MHz and 5000 MHz, the source was known to have a flat or variable spectrum different than most extragalactic sources or HII regions. The authors noted that the spectrum could be similar to that shown by the radio counterpart of Cygnus X-1. However, the ratio of radio to X-ray emission was at least an order of magnitude greater for the Circinus X-1 candidate than for Cygnus X-1.

The point radio source identification was corroborated when strong 6-cm flaring (from 0.3 to 4.1 Jy) was observed shortly after the X-ray peak (Haynes, Caswell, and Simons 1976). Subsequent radio observations established that the flares occurred regularly, with the onset occurring during or after the soft x-ray transition (Whelan et al. 1977), with an increasing time lag with decreasing frequency (Haynes et al. 1978). At 6 cm, the flares were characterized by an abrupt (~ 2 hr) increase, with a gradual decay over a time of 1-10 days. Longer wavelength observations showed a "washed out" version of this behavior. The flares frequently showed a double-peaked (Haynes et al. 1978) or sometimes triple-peaked structure (Thomas et al. 1978), with the time-frequency evolution of a given outburst consistent with the van der Laan (1966) model of an adiabatically expanding cloud of relativistic electrons emitting synchrotron radiation (Haynes et al. 1978). Basically, the maximum flare intensity was lower and occurred later at longer wavelengths. For the first peak where the determination was least ambiguous, the maximum flare intensity satisfied $S_{max}$ $(\nu) \propto \nu^{1.0\pm0.2}$, while the time lag $\Delta\tau$ from the X-ray transition to the peak satisfied $\Delta\tau \propto \nu^{-0.8\pm.1}$. Additionally, the

longer wavelength steep part of the flare spectrum had a flux density consistent with $S(\nu) \propto \nu^{5/2}$, expected for an optically thick synchrotron source with a power law energy spectrum; it was not consistent with a slope of 2.0 expected for an optically thick free-free emitting source (Haynes et al. 1978). Haynes et al. (1978) note that the radio flares they observed for Circinus X-1 are remarkably similar to the giant radio bursts of Cygnus X-3 seen in September 1972, which Gregory and Seaquist (1974) explained in terms of the van der Laan model. There is some evidence that the strength of the radio flares and X-ray outbursts are at least partially correlated, in the sense that strong radio flares are associated with strong X-ray outbursts, and no radio flares are detected when the X-ray activity is low (Kaluzienski and Holt 1978, 1979). As noted by Nicolson, Feast, and Glass (1980), this correlation of radio and X-ray activities may imply a physical connection between the radiation in these two regimes. However, there appears to be at least one counter-example: a strong 6-cm flare in March 1979 when the ASM showed no detectable flux (Kaluzienski, private communication).

An optical candidate for Circinus was suggested by Mayo et al. (1976) on the basis of positional coincidence to within 2" of the radio source position. The object was a faint (B ~ 22.5 mag) red star having a variable emission line spectrum with very strong Hα and weak HeI lines, and diffuse interstellar bands which suggest the object is distant and significantly reddened (Whelan et al. 1977; Mayo, Whelan, and Wickramasinge 1976). The star was found to be exceptionally bright in the infrared, with a K (2.2 μm) magnitude of 7.67 (Glass 1976). Subsequent infrared observations showed variations with the X-ray period, securing the identification (Glass 1977). The infrared light curve showed a flare shortly after the X-ray

decline, characterized by a sudden rise in a couple of hours followed by a slow exponential or near exponential decay with no change in color. The range of intensity in a given cycle was observed to be about 2 magnitudes, with the magnitude at a given phase varying from cycle to cycle (Glass 1978a). Optical observations in May 1977 showed an optical flare near the soft X-ray transition, with an amplitude in both the R-band and the Hα band $\geq$ 0.5 mag (Haynes et al. 1978).

The approximate equivalence of the peak low-energy X-ray flux and the known total flux in the optical, infrared, and radio regimes at maximum led Glass (1978) to suggest that the soft X-ray photons might be "somehow degraded into optical, infrared and radio radiation by a transient absorbing cloud" (such as that suggested by Coe, Engel, and Quenby (1976)) during the X-ray "OFF" state.) He noted difficulties, however, with the gradual X-ray increase, the abrupt transfer of power to longer wavelengths at the transition, and the subsequent exponential decay in such a model.

The early observations of the optical-infrared counterpart of Circinus X-1 were consistent with the primary being a highly-reddened early-type supergiant with a strong stellar wind and an infrared excess, or with a rather dusty symbiotic star (that is, a binary system whose composite spectrum shows a luminous cool component, a less luminous hot component, and, typically, high-excitation emission lines). Both possibilities were discussed at some length by Whelan et al. (1977).

The observed optical companions for a number of identified X-ray stars (e.g., Cyg X-1, SMC X-1, Cen X-3) are early-type supergiants, and such an interpretation was adopted by Haynes et al. (1980) and Murdin et al. (1980) for their model for the Circinus system, discussed below. However, this possibility no longer seems likely in light of the recent dramatic drop in

the infrared and optical continua discussed shortly.

A symbiotic star has been previously suggested as the optical candidate for 3U1728-24 (= GX 2+5?) by Glass and Feast (1973) and Davidsen, Malina, and Bowyer (1977). While Cir X-1 does not show the usual high-excitation lines of a symbiotic star, nor the high Hα/HeI ratio expected, symbiotic stars are known to show wide variety of excitation properties. On at least one occasion, the more typical symbiotic candidate for 3U1728-24 was observed to look very similar to the Circinus counterpart (Whelan et al. 1977). Long term variations of up to ~ 2 mag have been observed for the subset of symbiotic stars with large amounts of dust (Allen 1979). Further, Allen (1980) has shown spectral evidence that some symbiotic stars are systems with a late-type star feeding an accretion disk around a white dwarf or neutron star.

More recent infrared and optical results (Nicolson, Feast and Glass 1980) show that the 1978-1979 infrared and visual continua have dropped by $\gtrsim$ 2 magnitudes, compared to the 1976-77 values at similar phase, probably implying that the infrared and visual fluxes are physically related. The drop in intensity of Hα emission over the same period was much larger, the mean equivalent width dropping by a factor of 5-15. Despite these large changes in intensity, the infrared colors and the mean Hα width (~ 25A) showed little change. Variable structure in Hα, earlier suggested by the photographic work of Feast (quoted by Glass 1978a), was confirmed, with the line profiles "best interpreted as double-peaked with variations in the relative intensities of the two components." The mean radial velocity of the Hα profile was ~ 230 km s$^{-1}$, with an error of a few tens of km s$^{-1}$ (phase 0.0-0.2), considerably smaller than the 1976-77 photographic value of Feast (327 km s$^{-1}$, with about the

same accuracy, at phase 0.45).

The same authors report that radio observations at 6 cm showed low flux for most of 1978 (with the exception of two strong flares in February); activity resumed in 1979, with five strong (1-2 Jy) flares observed between January and May, while the infrared and optical flux remained low.

The authors note that the large correlated drops in the visual and infrared fluxes probably exclude a binary model in which the infrared flux comes from a cool giant while the visual flux comes from a hot companion. Further, the large change in flux rules out the possibility that the main part of the visual and infrared flux comes from a normal (but reddened) OB supergiant, unless geometric factors are involved. They believe the evidence supports instead a binary model in which a compact object is surrounded by a disk of matter being replenished by an optically faint companion. The infall of matter to the disk could vary greatly with time, providing for large changes in flux at approximately constant colors. The presence of a disk component, seen nearly edge on, could explain the wide double Hα lines, with the mean velocity of Hα expected to vary with the orbital period, consistent with the (admittedly rather incomplete) observations.

In the context of their model, the apparent decoupling of the radio/X-ray activity from the visual/infrared continuum levels implies that the fluxes arise in different regions. Perhaps, they suggest, the X-rays and radio flux originate close to the compact object, while the infrared and optical continua are produced further out, with the densities in different parts not necessarily varying together as the accretion rate changes. The Hα flux would be excited in the outer part of the disk by the

continuum, and would depend on both the density and the continuum flux, which itself depends on the density. A fall in density in the outer disk could thus lead to a drop in Hα intensity which is roughly the square of the drop in continuum intensity, as was observed.

## 2. Distance to Circinus X-1

The distance to Circinus X-1 enters in a number of crucial luminosity and size determinations. The maximum sustained X-ray luminosity puts a lower limit on the mass of the compact object via the Eddington limit, at which radiation pressure prevents further accretion. The absolute optical magnitude helps decide the nature of the optical companion. Various brightness temperatures and emission region sizes constrain production mechanisms. The transverse velocity of the proposed runaway system scales with the distance.

As noted above, the early observation of Circinus by Margon et al. (1971) showed a spectrum very absorbed at low energies, consistent with the column density ($1.4 \times 10^{22}$ atoms $cm^{-2}$) given by 21-cm emission measurements (McGee, Milton and Wolfe 1966), indicating a very distant source:  an assumed average interstellar hydrogen density of $\sim 1$ $cm^{-3}$ would imply a distance of $\sim 5$ kpc.  Comparing the surface brightness and angular diameter of the SNR G321.9-0.3 with those supernova remnants with well-determined distances, Clark, Parkinson, and Caswell (1975) inferred a distance of 5.5 kpc for Cir X-1, assuming association with the SNR. An estimate of the interstellar reddening of the optical companion of Cir X-1 (based on the observed strength of the λ6284 diffuse interstellar absorption line, as calibrated by Murdin 1972), in conjunction with the estimated $\lesssim 0.8$ mag/kpc reddening-distance relation in the direction of Circinus (Webster 1974),

gives a minimum distance to the star of 4 kpc.

These estimates are all consistent, but nonetheless very uncertain, with possible errors of a factor of 2. A more direct measure of the distance was achieved in a 21-cm absorption line measurement carried out by Goss and Mebold (1977) during Circinus X-1 radio outbursts in December 1976. Using a standard technique in pulsar absorption experiments, they obtained an HI absorption spectrum by subtracting a quiescent source line spectrum from a flare spectrum. They found six prominent HI absorption features including one extending to -90 km s$^{-1}$, the velocity associated with the tangential point of HI at 7.9 kpc, implying a conservative lower limit to the distance of 8 kpc. The lack of absorption from HI at velocities corresponding to distances > 16 kpc gave a firm but not very restrictive upper limit. For present purposes of computation, a distance of 10 kpc will be taken as "representative", following Whelan et al. (1977), except when a strict lower limit is needed. The physical association of Cir X-1 and the SNR is probably compatible with an 8 kpc lower limit because of the large scatter in the surface-brightness/diameter relationship.

3. Possible Association of Cir X-1 with Supernova Remnant G321.9-0.3

As noted briefly above, Clark, Parkinson, and Caswell (1975) suggested the possible association of Cir X-1 with the supernova remnant (SNR) G321.9-0.3 centered 23 arc min to the south of the point radio source. They speculated that Cir X-1 might be a runaway binary system ejected from the supernova, with the eccentricity and period of the orbit increased by the explosion. Comparing the surface brightness of the SNR with values measured for the few remnants of known age implied an age in

the range of $2 \times 10^4$ to $10^5$ yr. The authors concluded that Cir X-1 could be a relatively young system whose orbit was not yet circularized, in contrast to the older, better understood binary systems. If this association is confirmed, it will have been the first example discovered. The more recently noticed connection between the source SS433 and the supernova remnant W50 (Ryle et al. 1978) is now regarded as firm (see, e.g., Begelman et al. 1980).

Radio observations in May and October 1977 by the University of Sydney Fleurs synthesis telescope at 1.4 GHz showed a weak ($\sim 0.1$ Jy) extended region centered $\sim 1$ arc min south of the flaring point radio source (Haynes et al. 1978). The authors note that this extension may support the association of Cir X-1 with the SNR, and may well be the "fossil wake" created by previous flares as Cir X-1 moved north. Nicolson, Feast, and Glass (1980) note that the large and positive values determined at various phases for the mean Hα velocity indicate that the net velocity of the system is likely to be high ($\sim 200$-$300$ km s$^{-1}$), lending support to the hypothesis of a runaway system.

Despite their support of the Cir X-1/SNR association, Haynes et al. (1978) discount the idea of a runaway binary on the basis of energetics. Their basic argument, with somewhat more conservative numbers, follows.

The best distance estimate gives a lower limit of 8 kpc for Cir X-1 (Goss and Mebold 1977). Assuming this distance for the SNR, and the SNR diameter-age relationship formulated by Clark and Caswell (1976), then the age of the SNR is at most $\sim 10^5$ yrs. If the Cir X-1 system was ejected from the SNR $10^5$ years ago, its average transverse velocity was at least $\sim 500$ km s$^{-1}$. (This is comparable to the maximum velocity observed for pulsars (see, e.g. Manchester and Taylor 1977), a more typical value

being $\sim$ 100 km s$^{-1}$. It is also only one component of the velocity--the radial component was estimated by Nicolson, Feast, and Glass (1980) to be $\sim$ 200-300 km s$^{-1}$.) If the optical star identified with Cir X-1 is in fact a massive object of $\sim$ 20 M$_0$ (Whelan et al. 1977) the kinetic energy associated with the transverse motion is at least $\sim$ 10$^{50}$ ergs. (The corresponding value for Haynes et al. is $\sim$ 7 times as large.) Haynes et al. argued that the ejection energy implied was inconceivable, and suggested instead that the Cir X-1 binary system could have been created when the ($\sim$ M$_0$) compact object ejected from the SNR was captured by a supergiant star. [However two-body capture is itself not regarded as probable (see, e.g., Batten 1973).] In light of the recent IR/optical results of Nicolson, Feast, and Glass (1980), the optical companion may well be less massive than originally thought, reducing the energy requirement to an acceptable level. Or, if the distance assumed is too high or the age too low, the inferred velocity would be correspondingly too high compared to the true velocity. The lower limit to the distance seems rather firm, but the age determination is rather uncertain. If the expansion of the SNR takes place in an unusually dense region, and is consequently slower, the age could be underestimated. However, if we make the age of the SNR too large, we have difficulty arguing that Cir X-1 is too young for circularization of the orbit.

In several years' time, the predicted transverse angular rate of 0.01 to 0.1 arc sec per year should amount to a detectable proper motion, providing a check on the physical association of Cir X-1 and the SNR.

Recent work shows that some of the basic observational "facts" about Circinus X-1 are changing: the 16.6 day presumably binary light curve has been evolving, even within the brief era of X-ray satellites. The

characteristic 16.6 day modulation of the soft X-ray flux discovered by Kaluzienski et al. (1976) from ASM data (epoch 1975) is changing its shape and perhaps its period. The modulation has never been an exact clock. The light curves show considerable variation from cycle to cycle, particularly for the smaller outbursts. But for the larger outbursts, the general trend of the envelope was quite reproducible and the time of the transition to low flux quite predictable for several years. However, the COS-B light curve of Bignami et al. (1977; epoch Mar 1976) shows a rapid downward transition to ~ half-maximum intensity, followed by a quite gentle tail, and epoch 1977-1978 lightcurves show enhanced emission shortly after the "cutoff" (Dower 1978; see Figure 4 from Murdin et al. 1980). The 1979 ASM lightcurves show even further evolution, with flux low before the predicted transition, followed by an abrupt turn-on at transition -- essentially a mirror image of the early ASM "sawtooth" shape. We should recall that the early (epoch 1972), eclipse-like Uhuru light curve (Jones et al. 1974) also did not fit the characteristic "sawtooth" shape.

## C.   Eccentric Binary Model of Murdin et al.

Murdin et al. (1980) explain this progressive change in envelope in terms of a change in orientation of a highly eccentric orbit with a very large precession rate. Their model is an elaboration of the Coe, Engel, Quenby (1976) picture of a compact object immersed in the dense, cold stellar wind of its companion, shining out periodically each orbit.

Using data on the optical counterpart from Whelan et al. (1977), and a distance of 10 kpc (Goss and Mebold 1977), Murdin et al. estimated an absolute magnitude for the primary star $M_v \approx$ -6 to -7, and thus a mass $M_p \sim 20\ M_\odot$, implying an early type star, say an OB supergiant, with a

radius of $\sim 30\ R_0$ ($\sim 2 \times 10^{12}$ cm). With the standard interpretations that the 16.6 day period comes from the binary orbit and the secondary is a compact star with $M_c \sim 1\ M_0$, Kepler's third law gives a semi-major axis $a \sim 0.5$ a.u. Thus, at periastron when the separation of centers is $a(1-e)$ or $\sim 7.5\ 10^{12}\ (1-e)$ cm, the secondary star approaches close to the surface of the primary if the eccentricity is high. The early-type primary would be expected to lose mass via a stellar wind at a rate of $10^{-6}$ to $10^{-5}\ M_0$ $yr^{-1}$ (Lamers and Morton 1976; Hearn 1975). In this model, the shape of the soft X-ray light curve is due to the variation in the amount of material in the line of sight to the X-ray object, as it travels in an eccentric orbit through the stellar wind of its companion. The outflow from the primary is assumed to be spherically symmetric and of constant velocity ($\sim 10^3$ km/s), so that the stellar wind density follows an inverse square law.

The exact shape of the lightcurve depends on the values chosen for eccentricity, inclination angle, and orientation of the orbit with respect to the line of sight. The short duty cycle of the soft flux arises naturally for an orbit of high eccentricity with periastron pointing within a few degrees of Earth. Following Kepler's second law, the compact object in such a configuration will rapidly transit the primary, but spend a long time at apastron, with a high optical depth through the intervening stellar wind even though the density near the object is low. The downward transition occurs essentially at periastron where the compact object is closest to the primary star and the density is quite high. Between the two extremes, the soft X-ray intensity goes through a maximum as the column density along the line of sight goes through a minimum. By choosing an appropriate angle for the inclination of the orbit to the plane of the sky ($i \sim 75^0$), deep modulation of the soft X-ray light curve can be

achieved while eclipse of the hard X-ray flux is avoided. The shape and sense of the asymmetry of the light curve depend on the precise orientation of the orbit with respect to the line of sight. For example, if periastron is within a few degrees of the line of sight to the observer and the compact object transits the companion before reaching periastron, there will be a gradual buildup of emission to a peak which is cutoff sharply, while if periastron is reached before the transit, there will be a sharp turnon, followed by a gradual decay. With the major axis nearly perpendicular to the line of sight, the light curve will be closer to the eclipse shape seen by Uhuru, with an interval of a little more than a day between times of high flux.

The curves in Figure 3 of Murdin et al. show lightcurves for a progression of periastron angles, for the case $e = 0.7$, $i = 75^{\circ}$. (For an inclination angle of $90^{\circ}$, a periastron angle of zero ($\theta = 0$) corresponds to the major axis along the line of sight, with periastron closest to the observer.) The authors associate the Uhuru eclipse-like lightcurve (epoch May 1972) with $\theta \sim 60^{\circ}$-$90^{\circ}$; the Copernicus lightcurve of Davison and Tuohy (epoch April 1974) with $\theta \sim 30^{\circ}$; the early ASM sawtooth light curve (epoch 1975) with $\theta \sim 20^{\circ}$ (for which the sharpest transition is observed); the abrupt downward transition to half-maximum intensity followed by a gentle tail seen by COS-B (epoch Mar 1976) with $\theta \sim 10^{\circ}$. They compare the enhanced flux just after transition seen by SAS-3 (late 1977) and early 1978 ASM light curves to the double-peaked structure seen for $\theta \sim 0^{\circ}$. The precession implied by these associations amounts to -10$^{\circ}$/year, or an apsidal period of $\sim 40$ years (see Figure 5 from Murdin et al.). Murdin et al. argue that this enormous precession rate is consistent with the tidal interaction expected (Sterne 1939) for the close approach, highly eccentric

orbit implied by the shape of the light curve. Apparently, the model's prediction of a reversal in the sense of the sawtooth is borne out by the ASM light curves for 1979, extracted from the data for two cases where the source is strong and unconfused. A further extrapolation implies that the light curve should return to the eclipse-like state in the not too distant future (within ~ 10 years).

Within the framework of their detailed eccentric binary model, Haynes, Lerche, and Murdin (1980) and Murdin et al. (1980) account for the observed radio emission from Circinus X-1 in terms of shocks driven by radiation pressure due to supercritical accretion near periastron passage. They suggest that energetic electrons at the shock front produce synchrotron radiation at 1-15 GHz due to the magnetic field compressed in the infalling material, with successively lower frequencies becoming visible as the cloud of electrons expands adiabatically (Shklovsky 1960; van der Laan 1966). The multiply-peaked radio flares in this picture are due to successive formation of shocks which dissipate in the stellar wind after ~ $2 \times 10^4$ seconds.

Haynes et al. (1979) suggest that: 1) The nonthermal quiescent radio source could be produced by relativistic electrons which leak into an accretion disk around the compact object, giving rise to a steady radio output away from periastron. 2) Disk replenishment near periastron, at a rate of $5 \times 10^{-10}$ to $5 \times 10^{-8}$ $M_0$ per orbit, could produce "steady" X-ray radiation from matter dribbling down onto the surface of the compact star. 3) Variable optical emission might arise from the changing Roche lobe surface and from "degradation of shock-produced X-ray photons to the optical band by material overlying the expanding shock."

Despite its appeal, the wind-absorption model of Murdin et al. has a

number of major difficulties. It is not clear that it is consistent with
the recent infrared and optical results of Nicolson et al. which show a
large overall drop in the IR and optical flares, making an early-type
supergiant companion seem rather unlikely. Critical X-ray observational
discrepancies include the abruptness of the turnoff of large outbursts,
including a very rapid (~ 60 second) X-ray intensity transition observed by
SAS-3 during which the spectrum remained virtually the same (Dower 1978),
and minimal absorption observed by SAS-3 (Dower 1978), Ariel-5 (Chiappetti
and Bell-Burnell 1981,1982), and OSO-8 (present work) in residual flux
after transition.

In the following we will present results of precise measurements of
spectra and spectral evolution which clarify the need for a more thorough
consideration of the details of accretion processes and accretion disks in
understanding the Circinus system.

# III.  THEORETICAL BACKGROUND

## A.  Accretion Onto Compact Objects In Binary Systems

### 1.  Basic Considerations

For an ordinary isolated star, the luminosity resulting from accretion of matter is generally insignificant:

$$L_{acc} \sim \frac{GM_*}{R_*} \; \dot{m}_{acc} \sim 10^{33} \; (\frac{M_*}{M_0} \; \frac{R_0}{R_*} \; \frac{\dot{m}_{acc}}{10^{-8} \; M_0 \; yr^{-1}}) \; erg \; s^{-1}, \qquad 3\text{-}1$$

where $\dot{m}_{acc}$ is the matter accretion rate, and $M_*$, $M_0$, $R_*$, $R_0$ are the masses and radii of the star and the sun, respectively.  The gravitational potential at the surface of the sun, $GM_0/R_0$, is only $10^{-6} \; c^2$, yielding an energy release from infall much smaller than that available from nuclear reactions.  For accretion onto a white dwarf, the kinetic energy from infall is still $\sim 50$ times less than that from hydrogen burning ($\sim 6 \times 10^{18}$ erg $g^{-1}$).  However, for a neutron star or a black hole, with $GM_*/R_* \gtrsim 0.1$ $c^2$, infalling material releases $\gtrsim 10^{20}$ erg $g^{-1}$.  In close proximity to a companion which has a strong outflowing wind, or which sheds material because of the gravitational effect of its presence, such an object can sometimes intercept enough of the material to become a powerful X-ray source.  A mass transfer rate of $10^{18}$ g $s^{-1}$ ($\sim 10^{-8} \; M_0 \; yr^{-1}$) can produce a luminosity comparable to the "Eddington limit", $L_{Edd}$, at which the outward force of the radiation balances the inward force of gravity.  In that case the gravitational source term GM is effectively reduced by the factor $(1 - L/L_{Edd})$.

A simple estimate of this limit can be made by assuming that the cross-sectional area for stopping an infalling atom by radiation pressure is the Thomson scattering cross-section $\sigma_T$ of its electrons, while the effective gravitational mass per electron is $m \approx (\frac{A}{Z}) m_H$. (The infalling plasma is charge neutral; the electrons couple to the radiation field, the nuclei couple to the gravitational field, and the electrons couple to the nuclei by Coulomb attraction to the protons.) The net force then vanishes for a luminosity $L_{Edd}$ such that

$$\frac{GM_* m}{R_*^2} = \frac{\sigma_T L_{Edd}}{4\pi R_*^2 C} \; , \qquad\qquad 3\text{-}2$$

or

$$L_{Edd} = \frac{4\pi c \; G \; m M_*}{\sigma_T} \approx 1.26 \times 10^{38} \frac{M_*}{M_0} \; \text{erg s}^{-1} \qquad\qquad 3\text{-}3$$

for hydrogen accretion.

For scattering in the presence of a strong magnetic field, the cross-section is greatly suppressed for photons below the cyclotron frequency traveling along the magnetic field direction (Lodenquai et al. 1974); when luminosity emerges primarily in photon energies $\gtrsim m_e c^2$ (but not $\gg m_e c^2$ so that additional sources of opacity such as pair production are important), the appropriate relativistic cross-section is also less than the Thomson value. Otherwise, the above estimate is an upper bound since it ignores electron-photon interactions other than scattering. For a source emitting soft X-rays, unless the infalling ions are completely stripped, the relevant opacity may be due primarily to photoionization, for which $\sigma \gg \sigma_T$ (see Tarter and McKee 1973; Buff and McCray 1974; Hatchett,

Buff, and McCray 1976).

As pointed out by Basko and Sunyaev (1976), this limit assumes that the radiation produced by the infalling matter emerges in a direction to counter the accretion. This condition is always met for accretion with spherical symmetry, but could be violated for anisotropic flows. In the case of accretion onto a magnetic neutron star, for example, strong channeling of the accretion flow onto the poles with radiation escaping preferentially from the sides of the column might allow $L \sim 10 \, L_{Edd}$. Lightman, Rees, and Shapiro (1977) suggest an analogous situation might occur for accretion disks. Further, Lamb, Pethick, and Pines (1973) argue that, even for isotropic accretion with $\sigma_T$ the relevant cross-section, matter accreting above the Eddington limit will only be decelerated and not actually halted by radiation pressure unless the optical depth is sufficiently large. Last, the Eddington limit is a steady-state condition, and is not relevant for an unsteady or explosive situation. In particular, it does not exclude super-Eddington bursts of radiation produced by dumping of material.

If the kinetic energy from hydrogen atoms free falling onto the surface of a 1 $M_0$ neutron star ($R \sim 10^6$ cm) is converted entirely into photons, the maximum energy achievable is $\sim 100$ MeV, with an equivalent brightness temperture of $\sim 10^{12}$ K. If the accretion luminosity ($10^{36}$ - $10^{38}$ erg s$^{-1}$) from accretion of $10^{16}$ - $10^{18}$ g s$^{-1}$ onto the surface is completely thermalized, i.e., the radiation is distributed over the Planck function (see Eq. 3-54), the resulting effective temperature,

$$T_{eff} \sim [\frac{L}{4\pi R^2 \, \sigma_{S-B}}]^{1/4} ,$$

where $\sigma_{S-B}$ is the Stefan-Boltzmann constant, is $\sim 10^7$ K , corresponding to $kT_{eff} \sim 1$ keV, provided an appreciable fraction of the neutron star surface is involved in the radiation.

If the flow is halted some distance away from the surface by a shock, by the strong magnetic field of a neutron star, or perhaps in a disk, and incompletely thermalized, the resulting temperature is of order

$$T \sim \eta \, m_p \, \frac{G}{K} \, \frac{M_*}{R}, \qquad\qquad 3\text{-}5$$

where $\eta$ is an efficiency factor depending on how the gas is heated, and R is the distance from the center of the object at which the flow is stopped. For adiabatic heating in a strong shock, $\eta \sim 0.1$ (Landau and Lifshitz 1959). For processes such as viscous heating in a disk, $\eta$ can be as low as $10^{-5} - 10^{-6}$ (see, e.g., Pringle and Rees 1972, Shakura and Sunyaev 1973).

## 2. Mass Transfer

Substantial mass outflow from the close binary companion of a compact object does not automatically lead to a bright X-ray source. Material which has sufficient velocity to escape the companion star may also escape the compact star. The capture efficiency for accretion from a fast wind may be very low ($\lesssim 10^{-4}$, see discussion below.) If material infalling onto a black hole has insufficient angular momentum to form a disk (a criterion discussed below), approximately spherical infall may not produce much observable X-ray flux. If the mass transfer rate is very large compared to that capable of producing the Eddington luminosity, the source may be blanketed.

### a. Roche Lobe Overflow

Still, the existence of bright X-ray sources indicates that
conditions for optimum accretion do occur. It has been conventional to
discuss mass transfer in X-ray binary systems in terms of two idealized
modes: overflow of the mass-giving star beyond the critical gravitational
equipotential surface, with spillage through the gravitational saddle
point; and gravitational capture by the compact object of material from the
companion's outflowing wind. The standard discussion of the first case
assumes that the companion corotates with the system; the critical surface
is then called the critical Roche surface and the mode is called Roche lobe
overflow. Sometimes discussion of this mode is generalized to include
arbitrary rotation rate of the mass-giving star and a rotation spin axis
inclined with respect to the orbit revolution axis. In particular,
Davidson and Ostriker (1973) and Petterson (1978) have argued that the
"tidal limit" of a nonrotating star may be a more relevant approximation
for many X-ray binary systems than that of corotation. In the
nonsynchronous case, the potential at a fixed geometrical point in the
revolving system varies with time and one can define only an instantaneous
Roche surface. Still, the time-averaged surface allows one to proceed with
overflow calculations in analogy with the synchronous case, and for most
purposes the two cases will not be distinguished here.

For a circular orbit with the rotation axis of the primary parallel to
the orbital angular momentum, the generalized Roche potential has the form
(Kruszewski 1963, Avni and Bahcall 1975):

$$\psi = \frac{-Gm_1}{D}[\frac{1}{r_1} + \frac{1}{r_2} - q\ x + \frac{(1+q\ \Omega^2(x^2+y^2)}{2}]\ , \qquad\qquad 3\text{-}6$$

where D is the separation of the centers of mass of the two stars; $q = m_2/m_1$, $\Omega = \omega(\text{rotation})/\omega(\text{orbit})$ is the ratio of rotational to orbital frequencies; $r_1$ and $r_2$ are the distances (in units of D) from the stellar centers; x and y (in units of D) are Cartesian coordinates with the origin at the center of mass of the primary (optical star), with the z-axis parallel to the orbit angular momentum axis, and the x-axis pointing toward the secondary (X-ray source).

A mean value for the radius R of the critical surface can be obtained by setting the volume of the lobe equal to $\frac{4}{3}\pi R^3$. Solutions for three cases of interest are:

i) for Roche geometry ($\Omega = 1$) and $0.05 < q < 3$ (Kopal 1959, Paczynski 1971):

$$\frac{R_R}{D} \simeq 0.38 - 0.20 \log_{10} q; \qquad\qquad 3\text{-}7$$

ii) for tidal geometry ($\Omega = 0$) and $0.03 < q < 1.4$ (Avni 1977):

$$\frac{R_T}{D} \simeq 0.41 - 0.23 \log_{10} q; \qquad\qquad 3\text{-}8$$

iii) for fast rotation ($\Omega = 2$) (Avni 1977):

$$\frac{R_F}{D} \simeq 0.327 - 0.174 \log_{10} q + A (\log_{10} q)^2, \qquad\qquad 3\text{-}9$$

where A = -0.044 for $0.03 < q < 1$ and A = 0.022 for $1 < q < 8$.

For a given q, the critical radius is largest for the tidal case and smallest for the fast rotation case (where the high surface velocity makes

escape of material easier). When the equilibrium radius of the primary photosphere is $\gtrsim$ the mean radius of the generalized Roche surface, copious outflow is expected. In fact estimates of outflow as high as $10^{-3}$ $M_0$ $yr^{-1}$ for a massive primary (van den Heuvel 1975) would lead to densities sufficient to absorb any X-rays produced, or, if too much of the flow is intercepted, to a smothering of the X-ray source. If instead only the outer atmosphere of the primary is shed, as suggested by Savonije (1978,1979), conditions may be optimum for fueling of a bright X-ray source.

The outflowing material streaming through the gravitational saddle point has a trajectory which depends strongly on the rotation rate of the companion. The velocity $v_s$ of a point on the equator of the primary near the saddle point, with respect to the compact object, can be expressed as

$$v_s = \omega_{orbit} \, D \, [1 - \Omega \, (\frac{R_c}{D})]$$
3-10

where $R_c$ is the appropriate mean critical radius.

By comparing the specific kinetic energy of a fluid element at the saddle point, $\epsilon_k \approx \frac{1}{2} v_s^2$, with its specific potential energy relative to the compact object, $\epsilon_p \approx G \, M_x/(D-R_c)$, Petterson (1978) found that material could be accreted for all values of q for the case of synchronous rotation, while capture was harder for a more slowly rotating companion. For the limiting tidal case, he found matter tended to escape the system or fall back on the primary unless $q \gtrsim 0.75$. Thus, even if overflow occurs, in a system where the companion has a mass large compared to the compact object's and rotates slowly, much of the matter does not accrete onto the compact object. If the overflow rate is large, the reduced capture efficiency may still be sufficient to produce a bright X-ray source. In such a system, streams of outflowing matter may produce strong, variable

absorption effects, as a function of binary phase.

Roche-lobe overflow (or its nonsynchronous equivalent) occurs if the mass-giving star expands beyond the Roche lobe due to internal nuclear evolution, or if the Roche lobe shrinks due to shrinking of the orbit as mass is lost from the system. It is not clear to what extent the Roche lobe overflow picture carries over to the case of an eccentric orbit. Avni (1976) has discussed calculation of the generalized Roche potential for non-circular orbits in terms of the instantaneous separation of the two stellar components, but Pringle (1982) argues that the instantaneous Roche surface is never actually attained by the primary because the gravitational potentials change too rapidly for the star to respond. Still, he agrees that, for sufficiently close periastron passage, the compact object will likely pull off and capture matter from the companion. Haynes, Lerche, and Wright (1980) have performed numerical simulations of Roche lobe overflow in noncircular orbits. Examining the response of test particles on the surface of the companion to gravitational potentials which change with orbit phase, they found that a time-dependent tidal bulge reached the instantaneous Roche lobe for highly eccentric orbits ($e \gtrsim 0.6$) provided the mass ratio of the compact object to the primary was greater than about 0.1 and the periastron separation was less than about two primary stellar radii. For mass ratios $\gtrsim 0.2$, mass capture by the compact object appeared likely, though their procedure did not give a good estimate of the rate. While comparison of the equilibrium surface of the primary to the instantaneous critical surface in an eccentric orbit may not give a precise criterion for overflow and consequent accretion, it gives some estimate of the regime where overflow may give an important contribution to accretion.

## b. Wind Accretion

The other standard mass transfer problem considered for X-ray binaries is accretion onto the compact object from a spherically outflowing wind, a mode whose relevance was first pointed out by Davidson and Ostriker (1973). Roughly, matter is gravitationally captured within a cylinder of radius

$$R_a \sim 2\ GM_x/v_{rel}^2 \sim 2.7\ 10^{10}\ \frac{M_x}{M_o}\ (\frac{1000\ km\ s^{-1}}{v_{rel}})^2\ cm, \qquad 3\text{-}11$$

where $v_{rel}$ is the velocity of the wind relative to the compact object. Matter within the cylinder converges downstream from the object, forms a shock or accretion wake, and then falls approximately radially inward toward the compact object. The resulting mass accretion rate onto the compact object is

$$\dot{m}_x \approx \xi\ \pi\ R_a^2\ \rho_{wind}\ v_{rel}, \qquad 3\text{-}12$$

where $\rho_{wind}$ is the local wind density and $\xi$ is an efficiency factor $< 1$ which corrects for radiation pressure and a finite cooling time after passage through the tail shock. If the gas cools about as fast as it falls toward the compact object (see, e.q., Davidson and Ostriker (1973), or McCray (1977)), $\xi \sim 1$ except for luminosities near $L_{Edd}$, where the repulsive force of the radiation effectively reduces the gravity of the X-ray source and introduces a self-limiting effect. In this case, $\xi \sim (1 - L/L_{Edd})^2$ (Eddington 1926).

Substituting for the local wind density $\rho_{wind} \sim \dot{m}_* / (4\pi D^2 v_{wind})$ yields a mass accretion rate onto the X-ray object of

$$\dot{m}_X \simeq \xi \frac{G^2 M_X^2}{D^2 \, v_{rel}^3 \, v_{wind}} \, \dot{m}_*$$

$$\simeq 2 \times 10^{-4} \, \xi [(\frac{M_X}{M_o})^2 \, (\frac{10^{12} \text{ cm}}{D})^2 \, \frac{(1000 \text{ km s}^{-1})^4}{v_{rel}^3 \, v_{wind}}] \, \dot{m}_* . \qquad \text{3-13}$$

The resulting luminosity from wind accretion is then

$$L_w \sim \frac{GM_X}{R_X} \, \dot{m}_X$$

$$\sim 1.5 \; 10^{36} \, \xi \; (\frac{M_X}{M_o})^3 \; (\frac{10^6 \text{ cm}}{R_X}) \; (\frac{10^{12} \text{cm}}{D})^2$$

$$\cdot \; \frac{(1000 \text{ km s}^{-1})^4}{v_{rel}^3 \, v_{wind}} \; (\frac{\dot{M}_*}{10^{-6} M_o \text{ yr}^{-1}}) \text{ erg s}^{-1} . \qquad \text{3-14}$$

It appears difficult to produce the brightest X-ray luminosities observed from accretion of a fast wind onto a 1 $M_o$ compact object unless the mass loss rate is very high. However, in a close binary system, the compact object may intercept the wind before its velocity has reached a substantial fraction of its terminal velocity, $v_\infty \simeq 4 \; (GM_*/R_*)^{1/2}$ (see, e.g., Lamers, van den Heuvel, and Petterson 1976). Castor, Abbott, and Klein (1975) predict a velocity profile

$$V_W(r) = V_\infty \; (1 - R_*/r)^{1/2} \qquad \text{3-15}$$

for a wind accelerated by radiation pressure due to absorption and scattering of line radiation, while infrared measurements of OBA supergiants by Barlow and Cohen (1977) suggest a much more gradual acceleration, described by a velocity profile

$$V_W(r) = V_\infty \ (10^{-1.74 \ R_*/r}) \ (1 - R_*/r)^{0.21}, \qquad \text{3-16}$$

where r is measured from the center of the optical star. The two profiles yield $V_W \ (2R_*)/V_\infty = 0.71$ and 0.15, respectively. At $D \sim 2R_*$, the latter profile implies an accretion efficiency a factor of 500 times the former. Photoionization of the wind by the accreting X-ray source reduces the cross-section for acceleration by the primary radiation field, so the wind velocity local to the compact object may well be closer to the Barlow-Cohen value than to the theoretical prediction. Fransson and Fabian (1980) propose that collisions between the radiatively driven wind and the stagnant, hot, photoionized gas produce shocks, causing dense sheets of gas to trail the X-ray source. Friend and Castor (1982) find that including the effects of gravity and radiation pressure from the compact object, and the centrifugal force due to orbital motion on a radiation-driven stellar wind, destroys the spherical symmetry of the wind and makes mass loss and accretion strong functions of the size of the primary relative to the critical potential lobe.

The mass transfer in a given X-ray binary system may not fall neatly into one of the two standard descriptions. Various authors (e.g., Petterson 1978, Ziolkowski 1978) have suggested an accretion picture involving a mixture of a strong stellar wind and weak Roche-lobe overflow to explain observations of some systems. Wang (1981) and Friend and Castor

(1982) suggest that for some systems, the accretion mode might be intermediate between the two limits, with a slow, asymmetric "wind" directed preferentially toward the compact object.

## B. Accretion Disks

### 1. Accretion Disk Formation

For the typical case of accretion from Roche-lobe overflow and for certain circumstances of wind accretion discussed below, the accreting material may have too much angular momentum to fall directly onto the compact object. The standard test for disk formation requires that the radius $r_D$ at which the specific angular momentum $J_K = (G\,M_x r_D)^{1/2}$ of a Keplerian orbit around the compact object matches the specific angular momentum of infalling material, be larger than the radius $r_I$ of the innermost possible orbit around the compact object. For a nonmagnetic white dwarf or neutron star, this radius is the radius of the object; for a black hole, the radius is taken to be that of the innermost stable orbit, equal to $6\,G\,M_x/c^2$ ($= 3 \times$ the Schwarzschild radius) for a nonrotating black hole (Bardeen 1970); for a magnetic neutron star, the radius is taken to be the Alfven radius, $R_{Alf}$, where the magnetic field of the compact object begins to dominate the flow. To a first approximation, $R_{Alf}$ can be calculated by equating the energy density of the magnetic field, $B^2/8\pi$, with the kinetic energy density of the infalling matter, $\frac{1}{2}\rho\,v_{ff}^2$, where the freefall velocity $v_{ff} = (2\,GM_x/R_{Alf})^{1/2}$ and the mass density $\rho \sim \dot{m}_*/(4\pi R_{Alf}^2\,v_{ff})$. Assuming the magnetic field strength ($= B_0$ at the neutron star surface $R_x$) drops off roughly like a dipole, $B(R) \sim B_0\,(R_*/R)^3$ (not strictly true for nonspherical accretion), this yields a radius (see, e.g., Davidson and Ostriker 1973)

$$R_{Alf} \simeq \left( \frac{B_0^2 R_X^6}{4 \dot{m}_X GM_X/c} \right)^{2/7}$$

3-17

$$\simeq (2.4 \times 10^8 \text{ cm})$$

$$\cdot \left( \frac{B_0}{10^{12} \text{ gauss}} \right)^{4/7} \left( \frac{R_X}{10 \text{ km}} \right)^{12/7} \left( \frac{\dot{m}_X}{10^{17} \text{g s}^{-1}} \right)^{-2/7} \left( \frac{M_X}{M_0} \right)^{-1/7} .$$

The accretion disk is assumed to extend down to $R_I$, the radius of the innermost orbit. The outer edge of the disk, at least for the steady-state case, is expected to be considerably larger than $r_D$ -- the same viscous processes which allow some of the material to lose angular momentum and spiral slowly inwards onto the compact object requires other material to move outward, carrying away the excess angular momentum so that the total angular momentum is conserved. The outer edge, at least for a Roche-fed disk, is thought to be fairly near the Roche surface of the compact object, with the exact location determined by tidal interaction of the companion, which removes angular momentum from the disk, feeding it back into orbital motion (Papaloizou and Pringle 1977).

In the standard treatment of Roche lobe overflow, with the axis of the synchronously rotating primary parallel to the orbital angular momentum axis, the matter transferred through the inner Lagrangian point is expected to flow into the orbital plane because of symmetry. With the assumption of optically thick cooling, the vertical structure of the disk is neglected

and the problem is treated as 2-dimensional.

Lubow and Shu (1975) have given a semi-analytical description of the resulting disk formation around a degenerate object. Initially most of the matter follows an approximately ballistic path toward the object, then overshoots and flows around the object in a highly eccentric orbit. The orbiting material hits the incoming stream and forms a shock, which does not affect the upstream flow, but which changes the downstream flow into an approximately circular orbit with the same specific angular momentum with respect to the compact object as the initial stream. Lin and Pringle (1976) show that this ring of matter then spreads if viscosity is present; most of the matter is transported inwards while some of the matter transports most of the angular momentum outwards (Lynden-Bell and Pringle 1974). Near the outer edge, the disk is expected to be highly noncircular due to distortion by gravitational interaction with the primary and interaction with the incoming stream (Lin and Pringle 1976); closer to the compact object, motion in the disk is fairly well described by differential rotation in Keplerian orbits, with angular velocity $\omega(r) = (G\, M_x/r^3)^{1/2}$, corresponding to a Kepler velocity $\vec{V}_K = r\,\vec{\omega}(r)$, with a small radial velocity $\vec{V}_r$ superposed.

Accretion from a spherically outflowing stellar wind may also be moderated by an accretion disk whose size is very strongly dependent on the velocity of the wind relative to the compact object. Because of the orbital motion of the compact object, the axis of the accretion cylinder is tilted at an angle $\beta \approx \tan^{-1}(v_x/v_w)$ from the line joining the centers of the two stars, in the direction of the relative wind velocity, with $\vec{v}_x$ the velocity of the compact object. Shapiro and Lightman (1976) show that for a spherically symmetric wind of constant velocity the variation in speed

and density of the incident gas across the tilted cylinder face lead to a net angular momentum per unit mass of

$$J = \frac{1}{2} \ v_x \ D \ (R_a/D)^2, \qquad\qquad 3\text{-}18$$

where $R_a$ is the accretion radius given above and D is the separation distance of the stellar centers. The outer edge of the disk (before viscous spreading) forms at the radius $r_D$ where the angular momentum per unit mass above equals that of the corresponding Kepler orbit

$$J = (GM_x \ r_D)^{1/2}. \qquad\qquad 3\text{-}19$$

As before, the existence of the disk depends on the size of $r_D$ relative to the innermost orbit possible around the compact object.

Wang (1981) generalizes the above analysis to include an accelerated wind profile.

## 2. Accretion Disk Models

The equations needed to describe the flow through the disk are the hydrodynamic equations of a viscous fluid: mass continuity, 3-component momentum conservation (in the radial, azimuthal and vertical directions) and energy conservation (keeping track of the change in internal energy of a fluid element as it moves through the disk, subject to work done by pressure, heating generated by viscous forces, and energy loss by cooling). Auxiliary equations giving the equation of state of the gas and radiation, the cooling equation, and a definition of the viscous stress tensor must also be chosen. Typically, builders of standard disk models

simplify the set of equations by making a number of assumptions: The disk
is assumed axisymmetric about the compact object with effects of the binary
orbit and the gravitational influence of the mass-giving star neglected.
The disk is assumed thin, with the half-thickness h much less than the
local disk radius r, h/r << 1 [This requires the pressure to be much less
than the kinetic energy density since pressure thickens the disk; and
implies $v_z(\sim \frac{h}{r} v_r) << v_r$.]. Elements of the viscous stress tensor $t_{ij}$ are
taken to be $\lesssim$ the pressure, and hence much less than the kinetic energy
density, so that $v_r << v_k$ and $GM_x/r_c^2 << 1$), an assumption made for
simplicity which is valid except for $r \lesssim 3 r_M$ for disks around black
holes. For stationary disks, partial derivatives of the equations of
motion with respect to time are zero. Vertical integration of the
approximate hydrodynamic equations then allows separation of the radial and
vertical structure, reducing the 2-dimensional problem to two 1-dimensional
problems, though at the price of an intrinsic uncertainty in the vertical
structure.

The basic differences between the standard disk models lie in the
choice of the auxiliary equations. [Verbunt (1982) gives an excellent
summary and comparison of the choices made in the literature.] The usual
choices for the equation of state and the transport equation are the
ordinary equation of state for a mixture of radiation and an ideal gas, and
a radiative transport equation similar to that used for stellar atmospheres
with the addition of a non-zero radiation production per unit length, with
opacity coming chiefly from Compton scattering and free-free absorption.
One must also choose a viscosity law, for which no clear natural choice
exists, since the mass flows required ($\dot{m} \sim 10^{17}$ g s$^{-1}$) though the thin disk
(h < $10^{10}$ cm) imply a viscosity > $10^7$ g s$^{-1}$ cm$^{-1}$, orders of magnitude

larger than ordinary viscosity. In the first detailed treatment of a steady disk, Shakura and Sunyaev (1973) proposed a viscosity law $t_{r\phi} = \alpha P$, reducing the uncertainties in viscosity to a constant of proportionality $\alpha$, taken to be constant through the disk for simplicity. The viscosity enhancement is generally envisioned as coming from turbulence or the presence of small magnetic fields ($\sim 10^5$ gauss) in the accreted matter, though no straightforward calculation has been achieved.

This prototypical thin disk model predicts a large, concave disk, with h/r increasing with r almost out to the Roche surface. Gas pressure dominates at radii $\gtrsim 1000$ km, while radiation pressure dominates in the inner disk. For $r \gtrsim 5000$ km (the outer disk), $\sigma_{ff} \gg \sigma_T$, while at smaller radii $\sigma_T \gg \sigma_{ff}$. About half of the energy available from accretion is released in the disk quite close to the inner edge, in the approximate range 6 $R_g$ < R < 30 $R_g$, with $R_g = 2 GM_x/c^2$; the annulus giving the peak luminosity, $\propto$ emissivity $\cdot R^2$, occurs at $\sim 6.75$ $R_g$. The other half of the energy resides in the rotational velocity, and is released in a boundary layer at the inner edge of the disk if that interfaces with neutron star or white dwarf, but is "swallowed" if the central object is a black hole. Actually, as noted by Pringle (1981), the luminosity of the boundary layer is reduced by a factor $1 - (\Omega_x/\Omega_0)^2$, where $\Omega_x$ is the angular velocity of the compact object and $\Omega_0 = (GM/R_x^3)^{1/2}$. However, the reduction is quite small except for rotation near the breakup rate, so radiation from the boundary layer is generally quite important (see, e.g., Lynden-Bell and Pringle (1974), Pringle (1977), and Pringle and Savonije (1979).).

### 3. Time-Dependent Disks

Relaxing the assumed time-independence of the standard disk model

but retaining the remaining assumptions, Lightman (1974a,b) has studied variability and instabilities in the disk in terms of a nonlinear radial diffusion equation for the surface density. Such an equation describes the spreading of a density disturbance, such as the spreading of a ring to a disk or the evolution of the disk for a mass flow entering at the outer edge. For the Shakura-Sunyaev model, the diffusion time for such a density disturbance as quoted by McCray (1977) is

$$\tau_D \equiv \frac{r}{V_r} \simeq 4 \times 10^6 \ (R/10^{11} \ \mathrm{cm})^{5/4} \ (M_x/M_0)^{1/4} \ (\dot{m}_{18})^{-0.3} \ \alpha^{-4/5} \ \mathrm{sec} \ . \quad 3\text{-}20$$

This can be used to describe the diffusion of a perturbation or it can be evaluated in the middle of the disk, where it gives approximately the spiral-in time for the disk material.

The time-dependent equations allow analysis of the disk stability. Generally the outer regions of the disk where gas pressure dominates are considered to be stable, although there are recent reports of instabilities which can occur in the outer cool regions for certain forms of opacity (see, e.g., Abramowicz (1983) and references therein).

Most stability analyses have centered on the innermost part of the disk where radiation pressure is dominant, studying small perturbations of the stationary disk equations. (Verbunt (1982) has pointed out, however, that the equations are generally solved by neglecting terms that may be of the same magnitude as the small perturbations, particularly in the inner region.) Two modes of instability have received particular attention: the so-called viscous and thermal instabilities.

Lightman (1974) investigated the viscous instability, also called a "secular mode", which causes clumping of matter into rings, with a growth

time $\tau = (\lambda/r)^2 \tau_D$ for modes of wavelength $\lambda \gtrsim h$. This mode arises in the inner region where radiation dominates the pressure and electron scattering the opacity, implying the Rosseland mean opacity $\bar{\kappa} \sim$ constant. Equating the energy generation rate ($\propto hP$) with the radiative diffusion rate toward the surface, $R \propto T^4 (\bar{\Sigma\kappa})^{-1}$, with $\Sigma$ the surface density, gives $h \propto \Sigma^{-1}$ and, for hydrostatic equilibrium ($P \propto h\Sigma$), a pressure independent of the surface density. Then the stress, proportional to $hP$, is inversely proportional to the surface density. Low stress in local regions of high density and high stress in regions of low density means that matter will be moved preferentially to regions of high density (low stress), and the contrast will grow.

Lightman argues that the existence of this instability points to a necessary modification of the standard thin disk models, with the most likely revisions being reformulation of the models of viscosity and/or energy transport, or departure from thinness in the inner region. Making the viscous stress proportional to the gas pressure rather than the total pressure leads to a thin disk model similar to the standard ones but with an inner re?' n stable against viscous clumping, and with much higher densities. The instability could also be removed by assuming convection provides an effective means of energy transport, or that energy generation occurs near the disk surface, so that radiative diffusion would no longer be dominant.

Last, Lightman suggests that the viscous instability might imply that the inner disk is not thin, but instead puffs up, forming a cloud around the compact object of order tens to hundreds of times its size, with an effective radius given by the boundary radius of the inner region

$$R_B \propto (1.1 \times 10^8 \text{ cm}) \; \alpha^{2/21} \; M_X^{1/3} \; \left(\frac{\dot{m}_X}{10^{18} \text{ g s}^{-1}}\right)^{4/5}. \qquad \text{3-21}$$

The emission properties of the cloud would depend on the efficiency of the dissipative processes. If this is high, the cloud would emit X-rays as a hot thin plasma, with Comptonization likely to be important (Felten and Rees 1972, Illarinov and Sunyaev 1972). Time variations in intensity and spectrum would be expected on the hydrodynamic time scale of the cloud $\tau_H$ (~ $h/c_s$ ~ $r/V_K$, $\gtrsim$ tens to hundreds of msec for a black hole), unless the cloud is optically thick to Compton scattering. In that case, time scales less than the random walk time of a photon through the cloud,

$$\tau_R \sim \frac{N\lambda_{es}}{c} \sim \tau_{es} \left(\frac{h}{c}\right) \sim \alpha^{-1}\tau_H , \qquad \text{3-22}$$

are lost.

It is possible that the dependence of $\alpha$ on pressure is different than in the Skakura-Sunyaev model and the viscous instability does not occur (Lightman 1974), but in the inner region, when scattering gives the dominant contribution to the opacity, the thermal instability seems difficult to avoid. The time scale for this instability at a given disk radius is about that of the local Kepler period, unless the disk has become spatially thick.

Shakura and Sunyaev (1976) investigate the stability of a thin disk in a general way. The growth rates of density perturbation modes depend on the wavelengths, being smaller for shorter wavelengths. For the thermal instabilities they show fast growth rates, that is, time scales *in seconds* of ~ 0.4 $\bar{\alpha}^{-1}$ $M_X^{-1/2}$ $R_8^{3/2}$, with $R_8 = R_B/10^8$ cm. Shakura and Sunyaev argue that the slow-growing long wavelength perturbation near the boundary separating the stable and unstable zones determines the rate of matter flow into the inner disk. At the antinodes of the standing wave perturbation,

the increase in disk thickness allows an increase in energy radiation through the sides of the enhancement, which suppresses further growth of the instability. The flow across the boundary then proceeds in "batches" regulated by the formation timescale of the perturbation at the boundary

$$\tau_{batch} \sim (\frac{R_B}{H_0})^2 \ \alpha^{-1} \ \omega(R_B)^{-1}, \qquad\qquad 3\text{-}23$$

where $H_0$ is the equilibrium thickness of the disk at $R_B$.
Writing $\omega(R_B) = V_K(R_B)/R_B \simeq (GM)^{1/2} R_B^{-3/2}$ and substituting for $R_B$ from Equation 3-21 gives

$$\tau_{batch} \sim 0.11 \ \alpha^{-6/7} \ \dot{m}_{18}^{-1.2} \ (\frac{R_B}{H_0})^2. \qquad\qquad 3\text{-}24$$

Thus, for $R_B/H_0 \sim 10$, $\tau_{batch}$ is of order 10 seconds. Formation of regular batches in the accreting material at the boundary could give rise to quasi-periodic fluctuations in the flux radiated further in. These batches might break up into smaller clumps due to smaller scale perturbations. Thus, superposed on this slower modulation one might expect to see fluctuations on a spectrum of timescales down to the shortest associated with perturbations near the inner edge of the disk, where

$$\tau_{min} \sim \Omega(R_0)^{-1} \sim [\alpha \ \omega(R_0)]^{-1} \qquad\qquad 3\text{-}25$$

$$\sim 10^{-4} \ \alpha^{-1} \ R_6^{3/2} \ M_X^{-1/2} \ \text{seconds}.$$

The authors point out that the instabilities are likely to have azimuthal as well as radial modes with roughly equal growth rates, so that long wavelength perturbations might produce a spiral structure in the disk,

while those of shorter scale could lead to rotating hot spots with millisecond quasi-periodicities in luminosity due to Doppler effects.

## C. Radiation Mechanisms in Compact Binaries

### 1. X-Ray Emission Continua

The spectrum of radiation from an X-ray emission region depends on the particle densities and temperatures, the particle distribution function in energy, the magnetic field density and the dominant radiation loss mechanism. For a given force, the power radiated from an accelerated charge is proportional to the acceleration squared

$$\frac{dW}{dt} = \frac{2}{3} \frac{e^2}{c^3} a^2, \qquad\qquad 3\text{-}26$$

and hence inversely proportional to the mass squared, so that radiation from the protons in a charge-neutral plasma is typically negligible compared to that of the electrons.

For a relativistic electron in a magnetic field of ambient energy density $U_B$ the radiated power (below the Klein-Nishina limit) is

$$\frac{dW}{dt} = 2 \gamma^2 \sigma_T U_B c \qquad\qquad 3\text{-}27$$

where $\sigma_T$ is the Thomson scattering cross section and $\gamma$ is the electron Lorentz factor. The radiation spectrum can be approximated by a $\delta$-function at energy $\langle E \rangle = 0.44 \gamma^2 \hbar \omega_c$ (Ginzburg and Syrovatskii 1974), where $\hbar \omega_c$ is the cyclotron energy. For an electron power law distribution of number index $\Gamma$ and normalization $A$, the synchrotron radiation spectrum is

$$\frac{dN}{dE}\Big)_s = 1.98 \times 10^{-2} A U_B (4.99 \times 10^{-8} U_B^{1/2})^{\Gamma-3/2} E^{-\frac{\Gamma+1}{2}} \qquad 3\text{-}28$$

For inverse Compton scattering, where the magnetic field energy density $U_B$

is replaced by the electromagnetic energy density U in the expression for radiated power, the average emitted photon energy is

$$\langle E \rangle = 4/3 \; \gamma^2 \; \langle h\nu \rangle \tag{3-29}$$

where $\langle h\nu \rangle$ is the average photon energy of the target photons. For the same power law distribution of electrons, the inverse Compton radiation spectrum is

$$\frac{dN}{dE} )_{IC} = 1.98 \times 10^{-2} \; A \; U \; (1.99 \times 10^{12} \; \langle h\nu \rangle)^{\Gamma - 3/2} \; E^{-\frac{\Gamma+1}{2}} , \tag{3-30}$$

That is, for both synchrotron and inverse Compton processes, a power law electron spectrum of number index $\Gamma$ yields a power law photon spectrum of number index $(\Gamma+1)/2$.

For Coulomb collision losses in a plasma, X-radiation is produced by non-relativistic electrons. If the electron power law distribution is the same as above, the resulting non-thermal bremsstrahlung radiation spectrum is

$$\frac{dN}{dE} )_{NB} = 1.19 \times 10^{-19} \; f(\Gamma) \; A \; n_0 \; E^{-(\Gamma+1/2)} , \tag{3-31}$$

where $f(\Gamma)$ is a factor of order unity and $n_0$ is the proton plasma target density. For a Maxwellian distribution of electrons

$$\frac{dN}{dE} )_{TB} = 1.21 \times 10^{-19} \; g(T,E) \; (kT)^{-1/2} \; E^{-1} \; Z^2 n_e n_0 e^{-E/kT} , \tag{3-32}$$

where $Z$ is the target atomic number, $n_e$ the electron density, $T$ the plasma temperature, and $g(T,E)$ is the free-free Gaunt factor, a logarithmic

C - 2

function of temperature containing the ratio of maximum to minimum impact parameters. ( See, e.g. , Tucker 1975, p 189 ff. )

## 2. Line Emission

In addition to the smooth continua discussed above, X-ray spectra frequently show lines produced during interactions involving atomic electrons having X-ray binding energies. The K-shell binding energies, $E_K \propto Z^2$ (0.0136) keV, are in the X-ray regime for $Z \gtrsim 8$. However, elements with $Z > 30$ are not expected to give significant line emission because of their low abundance. Below 2 keV, several elements yield a multiplicity of lines which require greater spectral resolution than is generally available with proportional counters. Further, interstellar absorption of objects at several kiloparsecs distance makes observations of these lines marginal. [The Solid State Spectrometer (SSS) on HEAO 2 provides sufficient spectral resolution for partial resolution of lines below 2 keV, but the relatively short observations of Circinus X-1 obtained with the SSS reported here coincided with periods of low flux.] For the observations discussed here, emission lines from iron near 6.5 keV are expected to be the most readily observable (see Pravdo 1979) because of the high cosmic abundance of iron ($\sim 4 \times 10^{-5}$ relative to hydrogen) and its high fluorescence yield (discussed below). The principle line production mechanisms for X-ray binaries are probably thermal emission and fluorescence.

## a. Thermal Line Emission

Thermal line emission occurs in high temperature ($T = 10^{6-8}$ K) plasma. If electron collisions control the ionization and emissivity of the gas, the equilibrium ionization state of each atomic species is

determined by the temperature and density. Lines are formed by the decay
to more tightly bound states of collisionally excited electrons or
electrons captured into excited states. For thermal equilibrium, the
volume emissivity due to collisional excitations to level n' of ion Z with
ground state n is given by (Blumenthal and Tucker 1974)

$$\epsilon = 1.9 \times 10^{-16} \ T^{-1/2} \ \overline{\Omega} \ (\frac{\Delta E}{I_H}) \ e^{-\Delta E/kT} \ n_e n_z, \qquad 3\text{-}33$$

where T is the gas temperature, $\Delta E$ the difference in the energy levels, $I_H$
the hydrogen ionization potential, and $\overline{\Omega}$ the effective collision
strength. Calculations of the total emission expected are quite complex
and must be done numerically, usually with the assumption that the optical
thickness of the emitting region is sufficiently small that reabsorption of
the radiation can be neglected. A recent calculation by Raymond and Smith
(1977) (updated in Pravdo and Smith 1979) is used to compare observed line
strengths and line centers with those expected for thermal emission from a
gas having a temperature consistent with the observed continuum under the
assumption of collisional equilibrium. The ratio of line to continuum
photons is usually quoted in terms of the line equivalent width (E.W.),
i.e., the width in energy space of the continuum, centered at the line
energy, which contributes an energy flux equal to the energy flux in the
line. The strongest thermal emission of iron at 6.5-7 keV occurs for a
plasma with kT ~ 3 keV, yielding an E.W. of ~ 1750 eV.

The ionization state of elements in a cloud of cooler gas surrounding
a hot ionizing central X-ray source is likely to be dominated by
photoionization rather than by electron collisions. In this case the
balance of radiative recombination with photoionization will lead to highly

ionized atoms at much lower temperatures, compared to the case of collisional equilibrium (see McCray 1977). For this case, the principle line emission mechanism is likely to be fluorescence.

### b. Fluorescent Line Emission

Fluorescence is a nonthermal line production mechanism which requires target atoms which are not fully ionized and a source of photons or particles with energy greater than the relevant ionization energy. When an X-ray source shines on a distribution of matter, atoms absorb and scatter the incident photons. The characteristic fluorescent radiation emitted by the atoms must then make its way out of the matter to be observed. In the limit that the material is optically thin, the fluorescence is easily calculated. If it is optically thick, one must take into account both dilution of the exciting flux as it progresses through the material and absorption of the fluorescent lines produced.

Strong fluorescence emission from iron is expected for many X-ray binaries (see, e.g., Basko, Sunyaev and Titarchuk 1974; Hatchett and Weaver 1976). Of the cosmically abundant high Z atoms ($\gtrsim 10^{-5}$ times hydrogen abundance), it has the highest fluorescence yield ($\sim 0.347$, Bambynek et al. 1972), i.e., the highest probability of redistributing electrons to fill inner shell vacancies caused by fluorescence by emission of a characteristic photon. For neutral iron, this characteristic $K_\alpha$ line photon has an energy of 6.40 keV. For hydrogen-like iron, the corresponding energy is 6.90 keV.

The fluorescent target may be the surface of the companion, an accretion disk, a shell of material at the Alfven surface of the neutron star, outflowing wind material, or other mass flows in the system. Details

of the line strength, width, energy centroid, and correlations of these parameters with orbit phase may help determine the relative contribution from the various possible sources.

### i)  Optically Thin Fluorescence

For a point source of $S(E)$ photons $s^{-1}$ $sr^{-1}$ $keV^{-1}$ illuminating a volume element $r^2$ $dr$ $d\Omega$ of material with density $n$ and iron abundance $X_{Fe}$ a distance $r$ away, the number of photons absorbed is

$$\int_{E_{th}}^{\infty} X_{Fe}\, n\, r^2\, dr\, d\Omega\, \sigma_{abs}\, \frac{S(E)}{r^2}\, dE, \qquad\qquad 3\text{-}34$$

where $\sigma_{abs}$ is the absorption cross-section and $E_{th}$ is the threshold energy for absorption. For a material with fluorescent yield $\omega$, the fraction per steradian of these yielding fluorescence photons is $\omega/4\pi$. For a source at distance $d$, division by $d^2$ and integration over the volume of target material gives the observed number of line photons $cm^{-2}s^{-1}$:

$$N_{line} = \frac{\omega}{4\pi d^2} \int_{target} X_{Fe}\, n\, dr\, d\Omega \int_{E_{th}}^{\infty} \sigma_{abs}\, S(E)\, dE. \qquad 3\text{-}35$$

If the source is isotropic and not obscured, $S(E)/d^2$ is just $\frac{dN}{dE}$, the observed number spectrum. For this case the equivalent width of the line is then

$$EW = [\frac{dN}{dE}(E_{line})]^{-1} \frac{\omega}{4\pi} \int_{target} X_{Fe}\, n\, dr\, d\Omega \int_{E_{th}}^{\infty} \sigma_{abs}\, \frac{dN}{dE}\, dE. \qquad 3\text{-}36$$

Hatchett and McCray (1977) have discussed the optically thin case for fluorescence from a stellar wind. Close to the X-ray source where the

Ionization parameter $\xi = L_x/n \, r^2$ is $\gtrsim 10^2$, the iron will be predominantly hydrogenic and helium-like. There the emission is technically better characterized as recombination radiation and the resulting line energy will be higher than the neutral fluorescence value of 6.4 keV, ~ 6.7-6.9 keV. The contribution to fluorescence in this region can be estimated by assuming that every excitation leads to a recombination directly to the ground state and setting $\omega = 1$. Further away from the X-ray source where the iron has at least one 2p electron, $\omega \approx 0.34$. Following Hatchett and McCray, we write $n = n_x \, D^2/r_\star^2$, where $n_x$ is the wind density at the X-ray source and $r_\star$ is the distance of the fluoresced material from the star center. Then, from the contributions of the two ionization regions, we have a somewhat broadened line with a net equivalent width

$$EW = [0.34 \, (\frac{\pi^2}{8} D - \frac{D}{4}) + \frac{D}{4}] \, X_{Fe} \, n_x$$

$$\cdot \, [\frac{dN}{dE} (E_{line})]^{-1} \int_{E_{th}}^{\infty} \sigma_{abs} \frac{dN}{dE} \, dE \quad . \tag{3-37}$$

If we take the cross-section used by Basko (1978),

$$X_{Fe} \sigma_{abs} = 1.24 \times 10^{-24} \, (\frac{7.1}{E})^3 \, (\frac{X_{Fe}}{4 \times 10^{-5}}) \, , \tag{3-38}$$

as roughly applying to all the ionization states, and assume the source spectrum to be a power law of number index $\alpha$, the last factor in Eq. 3-37 becomes

$$(\frac{1}{6.4^{-\alpha}}) \int_{E_{th}}^{\infty} E^{-\alpha} \, (\frac{E_{th}}{E})^3 \, dE \; = \; \frac{7.1}{\alpha+2} \, (\frac{6.4}{7.1})^\alpha \; keV \tag{3-39}$$

yielding

$$EW = 0.49 \ n_{x_{11}} \ D_{12} \ (\frac{0.9}{\alpha+2})^{\alpha} \ keV, \qquad \qquad 3\text{-}40$$

where $n_{x_{11}}$ is the number density in units of $10^{11}$ atoms $cm^{-3}$.

Returning to our initial expression for the EW (Equation 3-36) we can rewrite it for the case of uniform shells of material as

$$EW = [\frac{dN}{dE} (E_{line})]^{-1} \ \omega \frac{\Delta\Omega}{4\pi} \int_{target} X_{Fe} \ n \ dr \int \sigma_{abs} \frac{dN}{dE} \ dE$$

$$= [S(E_{line})]^{-1} \ \omega \frac{\Delta\Omega}{4\pi} \ \tau_T \int X_{Fe} \frac{\sigma_{abs}}{\sigma_T} \ (\frac{E_{line}}{E}) \ S(E) \ dE, \qquad 3\text{-}41$$

where we have incorporated the optical depth to Thomson scattering, $\tau_T = \int n \ \sigma_T \ dr$ and used the notation $S(E) = E \frac{dN}{dE}$ for the energy form of the power law spectrum. This last expression has been used by Basko (1978) for fluorescence from a corona. Noting that

$$X_{Fe} \frac{\sigma_{abs}}{\sigma_T} = \frac{1.2 \ 10^{-24}}{6.65 \ 10^{-25}} \ (\frac{E_{th}}{E})^3 \approx 1.8 \ (\frac{7.1}{E})^3 \qquad \qquad 3\text{-}42$$

we can write

$$EW_{corona} = \omega \frac{\Delta\Omega}{4\pi} \ \tau_T \ 1.8 \ \frac{7.1}{\alpha+2} \ 0.9^{\alpha}$$

$$\approx 4.3 \ \frac{\Delta\Omega}{4\pi} \ \tau_T \ (\frac{0.9}{\alpha+2})^{\alpha} \ keV . \qquad \qquad 3\text{-}43$$

For a spectrum as hard as that of Her X-1, with $\alpha = 1$, taking the solid angle of the accretion disk corona to be $\Delta\Omega \sim 4\pi$ gives an EW =

1.2 $\tau_T$ keV. Thus the line EW can become very significant as $\tau_T \to 1$, though as the scattering optical depth increased the line would become smeared and the absorption edge in the spectrum would become increasingly important.

## ii) Optically Thick Fluorescence

For the case of fluorescence of optically thick material, calculations by several techniques have been carried out for cold matter ($\lesssim 10^6$ K) such as a stellar atmosphere. Hatchett and McCray (1977) and Basko (1978) have made analytic calculations based on approximate equations, while Bai (1979) and Felsteiner and Opher (1976) performed Monte Carlo simulations. The various answers are generally in agreement to within $\sim$ 50%. These results can be used to estimate line equivalent widths for X-ray fluorescence of binary system targets such as the surface of the companion, an accretion disk, or a shell of material at the Alfvén surface of an accreting neutron star.

An upper limit to the EW can be obtained by assuming that all X-rays above the threshold are absorbed and re-emitted into the hemisphere viewed. This gives

$$EW < \omega \frac{\Omega}{2\pi} \int_{E_{th}} \left[ \frac{dN/dE}{dN/dE \ (E_{line})} \right] \ dE$$

$$= 0.34 \ \frac{\Omega}{4\pi} \frac{7.1}{\alpha - 1} \ (0.9)^\alpha \ keV, \qquad\qquad 3\text{-}44$$

where we have again taken a power law photon spectrum of index $\alpha$.

When radiative transfer is included, the resulting line EW is considerably smaller.

### 3. Absorption and Scattering Effects

Frequently the spectrum observed from an X-ray binary system does not have one of the simple forms discussed above, but rather shows modifications due to absorption and scattering processes. These modifications take place in the source itself if it is not optically thin, or in intervening material between the source and the observer. Perhaps the simplest example of the latter is photoelectric absorption in the interstellar medium, whose principle effect is a low energy turnover. The photoelectric cross-section is a steep function of energy, roughly $E^{-2.7}$, with absorption edges at the ionization energies of the absorbing elements in the medium. Brown and Gould (1970) and Fireman (1974) have calculated the effective photoelectric absorption cross section for material with interstellar abundances.

In principle, photoabsorption by ionized gas near the X-ray source can be distinguished from cold interstellar absorption if the interstellar absorption does not dominate because the energies of the absorption edges depend on the ionization state of the gas. (Such a distinction, however, requires greater spectral resolution at 1-3 keV than is available with current proportional counters.) Absorption occurring within the system is also likely to show correlation with binary phase or other variation with time.

If there is a cloud of material in the system, acting as a screen through which the primary X-ray spectrum must propagate to be viewed by the observer, the relative strengths of an iron emission line to an iron absorption edge provides some measure of the geometry of the cloud, since the line photons can be scattered into the line of sight from directions out of the line of sight, while the absorption edge is due to material

along the line of sight.

Generally, models of close binary X-ray systems assume as the principle sources of opacity free-free absorption (the inverse process to thermal bremsstrahlung) and electron scattering. At sufficiently low frequency or sufficiently far from the X-ray source (see ionization discussion, below), free-free absorption dominates. If the temperature and density conditions within the energy production regions are such that the source is optically thick to free-free absorption, $\tau$ (= absorption coefficient · depth) > 1, only the surface layer (down to a depth where $\tau$ = 1) is observed, and the emerging spectrum has the Planckian form

$$\frac{dN}{dE} = \frac{8\pi}{c^3 h^2} \; E^2/[e^{E/kT} - 1] \qquad\qquad 3\text{-}45$$

where T is the effective blackbody temperature.

When electron scattering dominates, the effective optical depth is taken to be

$$\tau_{eff}(\nu) = \int \rho \; \sqrt{\kappa_{es}\kappa_{ff}(\nu)} \; dZ \qquad\qquad 3\text{-}46$$

where $\kappa_{es}$ is the electron scattering coefficient, and $\kappa_{ff}(\nu)$ is the frequency dependent absorption coefficient, $\rho$ is the matter density, and Z is the depth inward from the surface. The emitting material is then said to be optically thick or optically thin depending on whether $\tau_{eff}$ is greater or less than unity.

The radiation spectrum is also affected by the "Comptonization parameter", $y \equiv (4 \; kT_e/m_e c^2) \; \tau_{es}^2$, where $T_e$ and $m_e$ are the electron temperature of the gas and the electron rest mass, and $\tau_{es}$ is the electron

scattering optical depth to the point of emission. The factor $(4\ kT_e/m_ec^2)$ is the fractional gain in energy of a photon per scattering and $\tau_{es}^2$ is the average number of scatterings a photon undergoes in reaching the last emitting surface. If $y \ll 1$, Comptonization effects are unimportant. If the emitting material is optically thin $(\tau_{eff} < 1)$, the emerging radiation spectrum has the shape of the primary emission mechanism.

If the source is optically thick $(\tau_{eff} > 1)$ it is viewed to a depth where $\tau_{eff} \sim 1$. The emerging spectrum is that of a "modified blackbody". For an isothermal homogeneous slab of emitting material (an approximation to the emission from a thin disk), the intensity at frequency $\nu$ is given approximately by

$$I_\nu \propto B_\nu\ \kappa_{ff}^{1/2}/(\kappa_{es} + \kappa_{ff})^{1/2}, \qquad 3\text{-}47$$

where $B_\nu$ is the Planck distribution. This reduces to a pure blackbody when $\kappa_{ff} \gg \kappa_{es}$. Otherwise the emissivity is less than that of a blackbody.

For different assumptions of the density distribution, the exact form of the modified blackbody varies. For example, for an exponential atmosphere the power of the opacity coefficients is 1/3 rather than 1/2 and the numerical factors are slightly different.

When $y \gg 1$, Comptonization is said to "saturate": photons continue to gain energy until they come into thermal equilibrium with the electrons. Since the photon number is conserved in the scattering process, the resulting equilibrium spectrum follows a Boltzmann distribution

$$\frac{dN}{dE}\Big)_{Boltz} = \frac{8\pi}{c^3h^2}\ E^2\ e^{-h\nu/kT}, \qquad 3\text{-}48$$

rather than a blackbody spectrum.

The case of "unsaturated Comptonization", with $y \sim 1$ and $\tau_{eff} \ll 1$, requires detailed analysis of the Kompaneets (1957) equation for radiative transfer. For nonrelativistic electrons, Shapiro, Lightman, and Eardley (1976) give an approximate expression for the resulting photon spectrum:

$$I_\nu \propto (\frac{h\nu}{kT_e})^m \, e^{-h\nu/kT_e} \qquad\qquad 3\text{-}49$$

with $m = \frac{3}{2} - (\frac{9}{4} + \frac{4}{y})^{1/2}$, $= -1$ for $y = 1$. They argue that unsaturated Comptonization in the inner part of an accretion disk may explain the hard spectral tail seen from Cygnus X-1.

In addition to its possible profound effect on the observed continuum, Comptonization will tend to spread out any emission line feature and fill in absorption edges (Ross, Weaver, and McCray 1978).

## 4. Ionization Effects

The mass flows in the binary system do not simply provide an inert screen which modifies the initial source spectrum with absorption and emission features. The gas itself may be affected by radiation pressure or heating, a wind outflow may become very asymmetric due to ionization near the X-ray source. In general, gas in the system will have a complex geometry and thermal structure. Still, the highly idealized model of an isothermal, spherically symmetric mass distribution centered on the companion (approximating an extended atmosphere or wind outfow) allows an estimate of the magnitude of one of the potentially most important effects of the X-ray source on the mass flow from the companion from an

observational standpoint. This effect is ionization of the matter in the vicinity of the X-ray source. Apart from possible dynamic changes in the wind which may result, such ionization may largely determine the appearance of the binary system from various orbit orientations, and changes observed with binary phase.

Following Pringle (1973), we can estimate the size of the ionized region around the X-ray source by considering the "Strömgren surface" which bounds it. Along any radius vector from the central X-ray source (assumed to be a point) the distance of the surface is found by equating the number of ionizing photons emitted in a pencil beam to the number of recombinations within it. We can express the number of recombinations per unit time in a pencil beam of elemental solid angle $d\Omega$ and length $R_s$ from the X-ray source as

$$\int_0^{R_s} N_i N_e \, \overline{\alpha}_{rec} \, r_x^2 \, dr_x \, d\Omega \qquad\qquad 3\text{-}50$$

where $r_x$ is the distance from the X-ray source, $\overline{\alpha}_{rec}$ is the effective recombination rate ($cm^{-3}s^{-1}$) of the species being ionized, and $N_i$ and $N_e$ are the electron and ion densities at distance $r_x$ from the X-ray source, taken as equal for a hydrogen-like species.

The distance $r$ from the center of the companion can be expressed in terms of $r_x$ and the stellar separation $D$ as

$$r^2 = r_x^2 + D^2 - 2 \, r_x \, D \cos \theta \qquad\qquad 3\text{-}51$$

where $\theta$ is the angle the radius vector from the X-ray source makes with the line joining the stellar centers (refer to Figure 3-1). Assuming for

Figure 3-1

The size of the ionized region around an X-ray object imbedded in the stellar wind of its companion is estimated using the Strömgren surface analysis of Pringle (1973). The line-of-sight distance from the X-ray source to the Strömgren surface is found by equating the number of ionizing photons in a pencil beam to the number of recombinations within it.



$$r_p^2 = r_x^2 + D^2 - 2\, r_x\, D \cos \Gamma$$
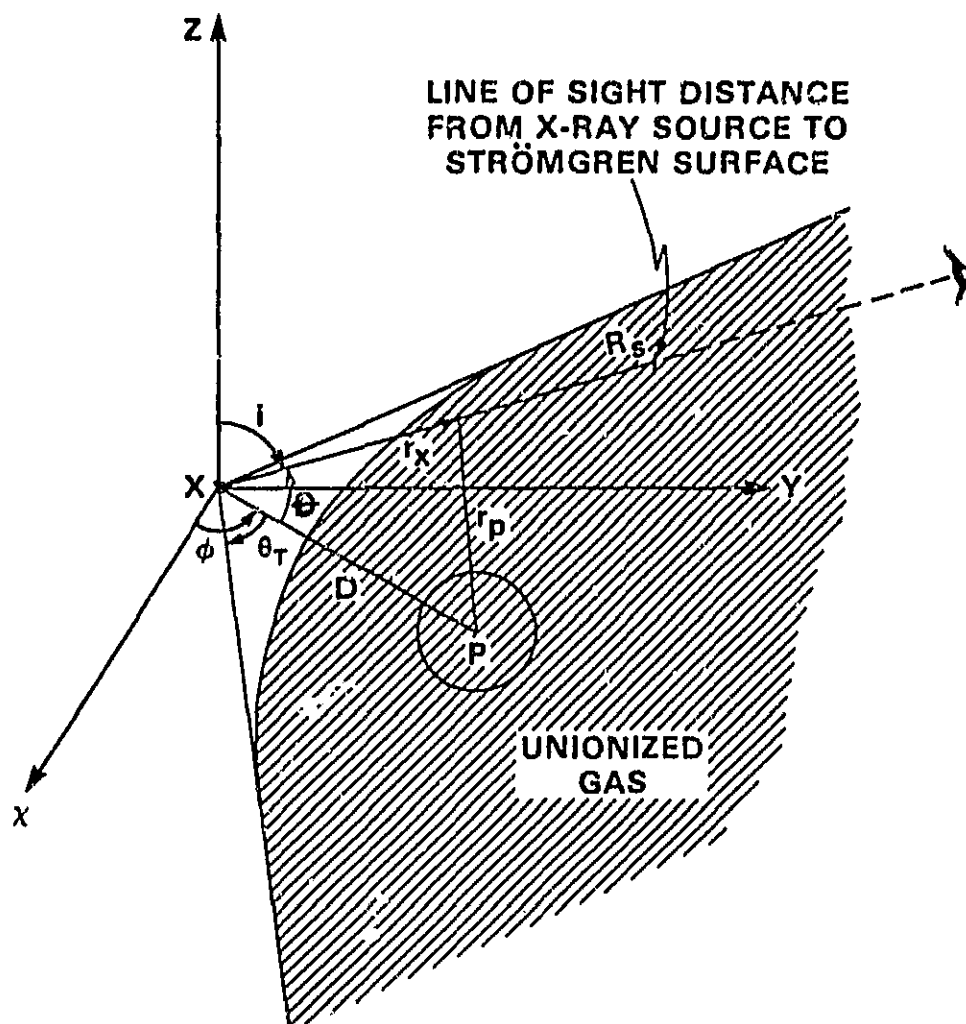
$$\cos \Theta = \sin \Phi \sin i$$

$\theta_T$ = HALF ANGLE OF CONE TANGENT TO STRÖMGREN SURFACE

simplicity a wind density profile that falls off as the inverse square of the distance from the center of the companion, the recombination rate can then be written as

$$N_D^2 \, D^4 \, \overline{\alpha}_{rec} \, d\Omega \int_0^{R_s(\theta)} dr_x \frac{r_x^2}{[r_x^2 + D^2 - 2\, r_x \, D \cos\theta]^2} \, , \qquad 3\text{-}52$$

where $N_D$ is the wind density at the X-ray source, a distance $D$ from the companion. One finds an implicit solution for $R_s(\theta)$, the distance from the X-ray source to the Strömgren surface as a function of $\theta$, by setting the above expression equal to $\frac{d\Omega}{4\pi} F$, where $F$ is the number of ionizing photons from the source emitted isotropically, and performing the integral. This yields

$$\lambda = \frac{F}{4\pi \, D^3 \, \overline{\alpha}_{rec} \, N_D^2} \, , \qquad 3\text{-}53$$

where

$$\lambda = \frac{1}{2 \sin^3 \theta} \quad \frac{\pi}{2} - \theta + \tan^{-1} \left[ \frac{R_s - D\cos\theta}{D\sin\theta} \right] + \sin\theta \cos\theta$$

$$+ \frac{DR_s \sin\theta - 2\, D\, R_s \sin^3\theta - D^2 \sin\theta \cos\theta}{R_s^2 + D^2 - 2\, R_s \, D\cos\theta} \qquad 3\text{-}54$$

Figure 3-2 shows the Strömgren surfaces calculated for various values of $\lambda$. For $\lambda < 1/3$ the ionized regions are bounded by closed surfaces

Figure 3-2


The shape and size of the Strömgren surface depends on the ionization parameter $\lambda = F \ (4\pi \ \varpi_{rec} \ D^3 \ N_D{}^2)^{-1}$, where F is the number of ionizing photons emitted isotropically from the X-ray source, D is the stellar separation, $N_D$ is the wind density at the X-ray source, and $\varpi_{rec}$ is the effective recombination rate. For $\lambda < 1/3$, the ionized regions are bounded by closed surfaces around the X-ray source. For $\lambda > 1/3$, the Strömgren surface is roughly a hyperboloid with symmetry axis along the line passing through the stellar centers.

# STRÖMGREN SURFACES FOR VARIOUS
# VALUES OF $\lambda$
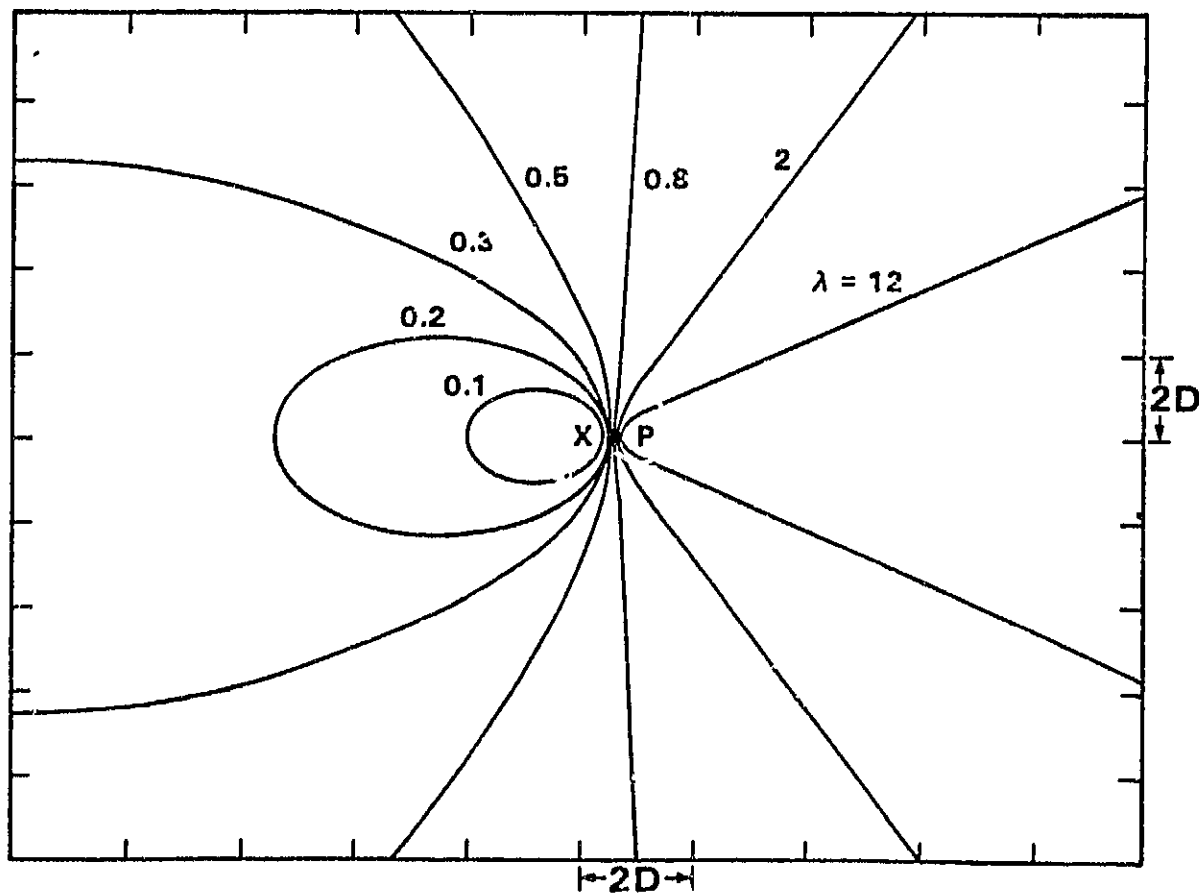
around the X-ray source. For $\lambda > 1/3$, the Strömgren surface is roughly a hyperboloid with an axis of symmetry along the line passing through the stellar centers. The asymptotes to the surface can be calculated by letting $R_s \to \infty$ in the expression for $\lambda$, yielding an implicit expression for the half angle $\theta_T$ of the tangent cone whose vertex lies at the X-ray source, outside of which X-rays can reach the observer without absorption:

$$G(\theta_T) = \frac{\pi - \theta_T + \sin \theta_T \cos \theta_T}{2 \sin^3 \theta_T}. \qquad \text{3-55}$$

A plot of the tangent cone half angle $\theta_T$ versus $\lambda$ is given in Figure 3-3.

The dominant photoabsorbers for X-rays in the range 0.7-7 keV are oxygen ions (e.g., Hatchett and McCray 1977). If we take $10^5$ K as a typical gas temperature near the X-ray source, oxygen is mostly hydrogenic, and we can write the effective recombination coefficient (including the oxygen abundance) as

$$\bar{\alpha}_{rec} \sim X_o \ (3 \ 10^{-10}) \ Z^2 \ T^{-3/4}$$

$$\sim (4.4 \ 10^{-4}) \ (3 \ 10^{-10}) \ (64) \ (1.8 \ 10^{-4})$$

$$\sim 1.5 \ 10^{-15}, \qquad \text{3-56}$$

where the values for the recombination coefficient and the cosmic oxygen abundance have been taken from Allen (1973). The photoionization cross section varies roughly as $\nu^{-3}$ times the threshold energy 0.87 keV, so that source photons with energies $\gtrsim$ 2-3 keV will not contribute much to keeping the gas ionized. If we include only the softer X-ray flux from the source,

Figure 3-3

The cone half-angle $\theta_T$ of the open Strömgren surfaces $(\lambda > 1/3)$ is calculated by noting that the distance to the surface, $R_S$, becomes infinite at the asymptotic limits of the surface. Letting $R_S \to \infty$ in Equation 3-54 gives an implicit expression for $\theta_T$ for a given $\lambda$.
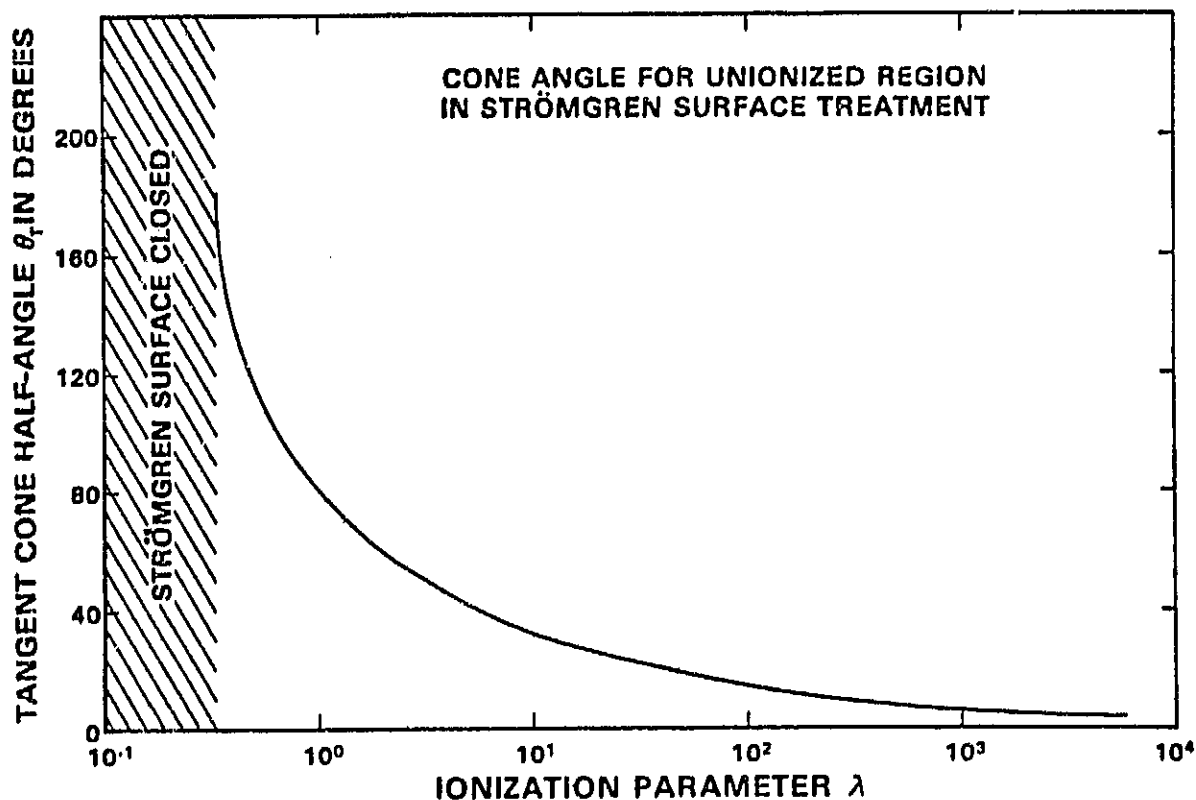
from photons with energy $\sim 1$ keV, we can write

$$\lambda \simeq 50 \, \frac{L_{37}/E_1}{\alpha_{-15} \, N_{11}^2 \, D_{12}^3}, \qquad\qquad 3\text{-}57$$

where we have used dimensionless parameters $L_{37} = L/10^{37}$ erg s$^{-1}$, $E_1 =$ the effective ionizing energy in units of 1 keV, $D_{12} = D/10^{12}$ cm, $N_{11} = N/10^{11}$ cm$^{-3}$, $\alpha_{-15} = \overline{\alpha}_{rec}/10^{-15}$ cm$^3$ s$^{-1}$.

Pringle points out that a proper calculation should take into account both the details of the various absorbing elements and the true source geometry and thermal structure. Hatchett and McCray (1977) argue that the type of analysis used by Pringle should give an upper limit to the size of the fully ionized region which would be calculated under a more careful treatment of the atomic physics.

CHAPTER IV.   INSTRUMENTATION

This chapter describes the instrumentation used to effect the observations reported in this thesis. An outline is given of the physical principles of the detecting devices, followed by a brief discussion of prototypical detectors designed to optimize astrophysical application. Parameters of the actual detectors used in the observations are listed for reference in Table 4-1. Detailed discussions of the various instruments have been given elsewhere, and are cited in the relevant discussions below for the interested reader.

A.   Proportional Counter as X-Ray Detector

A gas proportional counter is used to detect X-rays by means of the photoelectric effect. For simplicity, consider an X-ray photon entering a cylindrical gas volume of diameter "a" surrounding a central collecting wire of diameter "b" which is positive with respect to the outer cylinder. The photon has a probability of interacting with atomic electrons in the gas which depends on the gas thickness (in g cm$^{-2}$) traversed and the quantum efficiency $\mu(E,Z)$ which is a function of the X-ray energy and the atomic number of the gas. The quantum efficiency is a smoothly decreasing function of energy roughly proportional to $Z^4 E^{-2.7}$, except for sharp discontinuities at absorption edges, corresponding to ionization energies of atomic electrons in inner shells. These edges are characteristic of the particular detecting gas. When the photon ionizes an atom, the electron is ejected with a kinetic energy equal to the photon energy less the ionization energy $\varepsilon$, ~ 20-30 eV for typical counter

TABLE 4-1: DETECTOR PARAMETERS[†]

| Satellite | Detector | Area $(cm^2)$ | FOV | Energy Range (keV) | FWHM (keV) | Background $s^{-1}$ | Crab[**] $s^{-1}$ |
|---|---|---|---|---|---|---|---|
| Ariel-5 | ASM | 1 | $4^0 \times 90^0$ | 3-6 | $(\frac{E}{6})^{1/2}$ | $4 \ 10^{-4}$ | 1.25 |
| OSO-8 | A | 263 | $5^0$ circ | 1.6-60 | " | 20 | 800 |
| | B | 37 | $3^0$ circ | 1.6-20 | " | 1 | 70 |
| | C | 237 | $5^0$ circ | 2.5-60 | " | 10 | 370 |
| HEAO-1[***] | A2 MED | 400 | $3^0 \times 3^0$ | 1.6-20 | " | 6.7 | 780 |
| | | 400 | $3^0 \times 1^0.5$ | " | " | 3.9 | 780 |
| | A2 HED3 | 400 | $3^0 \times 3^0$ | 2-60 | " | 9.2 | 700 |
| | | 400 | $3^0 \times 1^0.5$ | " | " | 6.1 | 700 |
| HEAO-2 | SSS | 200 | 3' circ | 0.4-4 | 0.160 | 0.1 | 500 |
| | MPC | 672 | 45'x45' | 1.1-20 | $(\frac{E}{4})^{1/2}$ | 17 | 1600 |

[*]   Approximate values

[**]  Flux from Crab $\approx$ 1000 $\mu$Jy $\approx 2.4 \times 10^{-9}$ erg $s^{-1}cm^{-2}keV^{-1}$ at 5 keV

[***] HEAO-1 "R15 counts" $\equiv$ (HED3 total + MED Layer 2) count $s^{-1}$

$$\approx 3 \ 10^{-9} \ erg \ cm^{-2} \ s^{-1}.$$

gases. This electron distributes the excess energy among neighboring atoms, creating an "avalanche" of ion pairs whose number N is roughly proportional to the incident photon energy divided by the ionization energy: $N \approx E/\varepsilon$.

## 1. Proportional Counter Gain

The applied electric field causes the electrons to drift toward a collecting anode; as they accelerate, they collide with and -- if the field is strong enough -- ionize additional atoms, with the avalanche process repeating until the number of electrons collected at the anode is $M \cdot N$, where M, the "gas multiplication factor" or "gain" of the detector, is a function of $V_o/ \ln(b/a)$, with $V_o$ the applied voltage. As the voltage is increased, the multiplication region moves outward and the number of avalanches increases. The gain also depends on the number of electrons encountered as the electron drifts through the multiplication region, which is proportional to the pressure times the distance a. The typical proportional counter regime for gain gives a factor of $10^3$ - $10^5$ more electrons than the initial avalanche. Since each electron in the initial avalanche produces approximately the same number of cascade electrons, the total charge collected is approximately proportional to the incident photon energy. Departures from proportionality are caused by such effects as losses due to electron scattering and edge effects due to location of this initial avalanche near the boundary of the counter. The influence of end effects due to nonuniform fields at the ends of the cyclinder is minimized with a long narrow cylinder. Losses of electrons through the wall boundary can be parameterized in terms of the range of the electron for a particular gas constituency and pressure relative to the cell size.

For proportional response to incident energy, the charges must also be collected before they recombine and within the relevant integration time. Impurities in the detector gas which can attach to the electron and slow down their drift will also lead to incomplete charge collection. Outgassing of impurities in the detector walls can lead to increased degradation of counter response with time unless special care is taken to minimize their presence.

Another important process which leads to non-proportional response is the escape of fluorescence radiation. This can occur when ejection of an inner shell electron by a photon with energy above a characteristic absorption edge of the gas is followed by cascade of an outer shell electron to fill the vacancy. The counter gas is relatively transparent to its own characteristic radiation, which may then escape. In that case, the net energy recorded for the event will be the initial photon energy less the amount of the resonant radiation. For a noble gas such as argon or xenon, the fluorescence yield is only a few percent; however a hard incident source spectrum can produce a high percentage of low energy counts from high energy photons by this means.

A noble gas is usually chosen as the primary counter gas to reduce such non-ionizing energy loss mechanisms as excitation of low level rotational or vibrational states of a molecule. However a noble gas is transparent to ultraviolet photons emitted by excited noble gas atoms. New multiplication processes may be started by electrons removed from the counter walls, by fluorescing photons or colliding excited atoms. A polyatomic quench gas such as methane is usually added to the counter to absorb UV photons and collisionally de-excite noble gas atoms in metastable states.

## 2. Proportional Counter Resolution

The resolution of the counter is limited by the inherent statistical nature of the number of ion pairs formed in the initial avalanche and by subsequent losses in the multiplication process. The number N of electron-ion pairs created in the initial avalanche is subject to variations depending on which energy levels are excited and losses due to such effects as scattering of the primary electron. For Poisson statistics the variance on N is equal to $<(N - \bar{N})^2> = N$. In this case the rms deviation of the energy distribution deduced for monochromatic incident photons of energy E is $\sigma \sim (\overline{\Delta E^2})^{1/2} \sim \varepsilon N^{1/2}$ where $\varepsilon \sim 30$ eV is the average ionization energy per pair. This would lead to an observed full width half maximum detector response to a $\delta$-function input of $FWHM_{Poisson} = 2\sigma(2\ell n\ 2)^{1/2} = 2.35\ (E\varepsilon)^{1/2}$, which corresponds to a fractional resolution $0.41\ E^{-1/2}$, or a resolution of about 14% FWHM at 3 keV. In fact the variance on the number of electrons is not Poisson; the energy dispersion is lowered by a "Fano" factor less than 1 (Fano 1947) to a value $2.35\ (E\varepsilon F)^{1/2}$. However, the multiplication increases the dispersion back to roughly the Poisson value. In practice, this inherent proportional counter resolution is degraded by incomplete charge collection due to impurities and other losses noted above.

## B. Goddard X-Ray Proportional Chambers

### 1. Detector Design

The Goddard proportional counters on the 8th Orbiting Solar Observatory (OSO-8) and the first High Energy Astrophysical Observatory (HEAO-1) satellites are multiwire gas proportional chambers consisting of

stacked wire grids which partition a common detector gas volume into many long rectangular cells, each with grounded wire boundaries and a central wire anode. Alternate anodes are connected in a logic scheme whereby events which trigger adjacent cells or layers within the integration time are rejected as particle events; unlike X-rays which interact once if at all, incident electrons will leave a trail of ion pairs that usually cross cell boundaries.

Events are also rejected if they occur in the boundary cells adjacent to the detector sides, where Compton electrons produced by low energy $\gamma$-rays entering through the detector walls increase the background substantially. Several of the detectors have an upper veto layer just under the mechanical collimator, filled with neon-propane gas which is transparent to X-rays with energies above 2 keV, but which records the passage of charged particles. The detectors without this veto layer have a lower low energy threshold; cross-comparison with the response of the two-gas detectors can be used to protect against contamination by precipitating electrons, a major source of detector background in the absence of some rejection scheme.

The proportion of X-ray events which are thrown out in this anticoincidence process due to dispersion of the initial electron cloud past a cell boundary, i.e., the anticoincidence loss rate, can be determined in controlled experiments before the detectors are launched into space. As noted in the gain discussion above, the magnitude of this loss will depend largely on the range of the electron in the detector gas relative to the cell size. While this and other such losses are kept to a few percent by considered detector design, effects of this size become important when they exceed the statistical errors. A program of careful

calibration of the detectors by exposure to sources of known energy and strength in a simulated space environment has reduced the systematic uncertainties in knowledge of the detector response on earth to one or two percent. For a detailed discussion of the method used to calculate the detector response function from these calibrations, refer to Pravdo (1976).

The Goddard proportional chambers use ~ 1 atmosphere of argon (Z = 18) or xenon (Z = 54) as the detecting medium, with 10% (by pressure) methane added as a quench gas. With wire diameters of a mil and cell sizes ~ half an inch, operating voltages near 2000 volts give multiplication factors of 2-4 x $10^3$. The collected charges are read out into 32 or 64 pulse height channels, with the 64 channels arranged in a quasi-logarithmic format that doubles the resolution below about 15 keV. The range of energies covered by these channels (roughly 2-20 keV for the argon detectors and 2-60 keV for xenon), depends primarily on the counter window transmission at low energies and the efficiency of the detector gas for absorbing high energy X-rays within the detector volumes. Window thickness (in gm $cm^{-2}$) is constrained by the need to keep diffusion by the detector gas, and the resulting drift in gain, to a tolerable level. The window materials are either thin (~ 2 mil) beryllium foils or thin plastic sheets aluminized to provide grounding on that face of the counter. The detector thickness is constrained by satellite weight constraints and the growing importance of Compton scattering relative to photoelectric absorption, above a few tens of keV.

2. Detector Calibration

Within the energy range of the detectors, the relevant absorption edges are the K-edge of argon at 3.2 keV, and the K edge and three L edges of xenon at 34.6 keV and ~ 4.8 keV, respectively. The effects of resonance

escape due to these edges were determined in a calibration facility at Goddard which provides bremsstrahlung continuum and fluorescent lines from thin metal targets irradiated by electron beams with energies $\geq$ 25 keV.

The well-established energies of the target fluorescent energies could be used to determine the linearity, slope, and intercept of the gain of each detector. These lines in conjunction with characteristic lines from a variety of radioactive sources were used to measure the detector resolution.

Once the detectors were in space, changes in gain and resolution were tracked with weak onboard radioactive sources: an $Fe^{55}$ K-capture source which emitted a 5.9 keV $Mn^{55}$ $K_{\alpha\beta}$ line, and an $Am^{241}$ source that emitted an alpha particle coincidently with prompt gamma-rays at 59.6 keV and 26.3 keV, as well as $Np^{237}$ L X-rays at 13.9 and 17.8 keV. These sources were either commanded into and out of the detector field of view or had associated anticoincidence circuitry to flag the signals. Examples of the calibration pulse height spectra for two OSO detectors are shown in Figures 4-1 and 4-2. The xenon-filled A detector was calibrated with an $Am^{241}$ source. The detector response to the calibration lines used is indicated. The line at the upper threshold is due to the 59.6 keV nuclear line minus the resonant escape energy due to the xenon L-edge at 4.8 keV. The argon-filled B detector was calibrated with the 5.9 keV $K\alpha_1$ line and the line minus the resonance escape peak due to the argon K-edge at 3.2 keV.

In space, the detector gains drifted slowly with time due to diffusion of the counter gas through the window. Figure 4-3 shows the detector gain histories for the three OSO detectors, where the detector gains are quoted in terms of the ratio of photon energy to pulse height channel in

Figure 4-1

The xenon-filled OSO-8 A detector is calibrated in space with a weak $Am^{241}$ alpha-particle emitter, which has associated anticoincidence circuitry to flag the signals during observations of cosmic sources. The crosses in the figure show the complex detector pulse height spectrum from the source. The solid curve indicates the predicted detector response to several narrow lines superimposed on a flat continuum: the 59.6 keV nuclear line (minus the resonant escape energy due to the xenon L-edge at 4.8 keV) shows up at the upper threshold; the lines at 13.9 and 17.8 keV correspond to $Np^{237}$ L X-rays.

OSO-8 A DETECTOR 1975 DAY 450
$Am^{241}$ CALIBRATION SPECTRUM
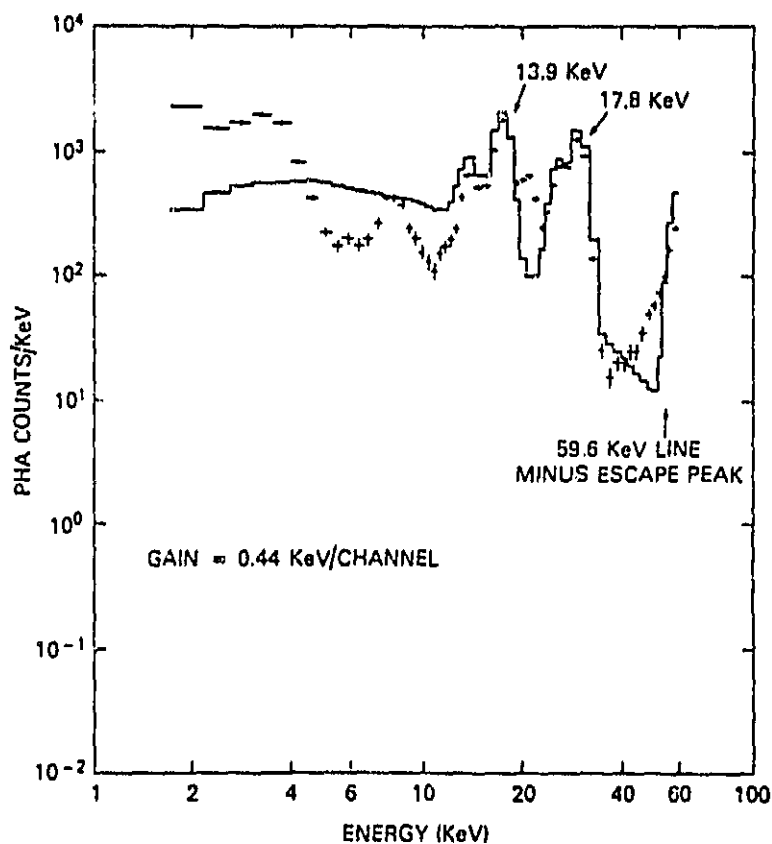
Figure 4-2

The argon-filled OSO-8 B detector is calibrated in space with a weak
$Fe^{55}$ K-capture source which can be commanded into and out of the field of
view. The crosses in the figure show the detector pulse height spectrum
for the 5.9 keV Mn $K_{\alpha\beta}$ line, and the line minus the resonance escape due to
the argon K-edge at 3.2 keV. The solid line gives the predicted detector
response to a narrow line at 5.9 keV.

OSO-8  B DETECTOR  1975 DAY 436
$Fe^{55}$ CALIBRATION SPECTRUM
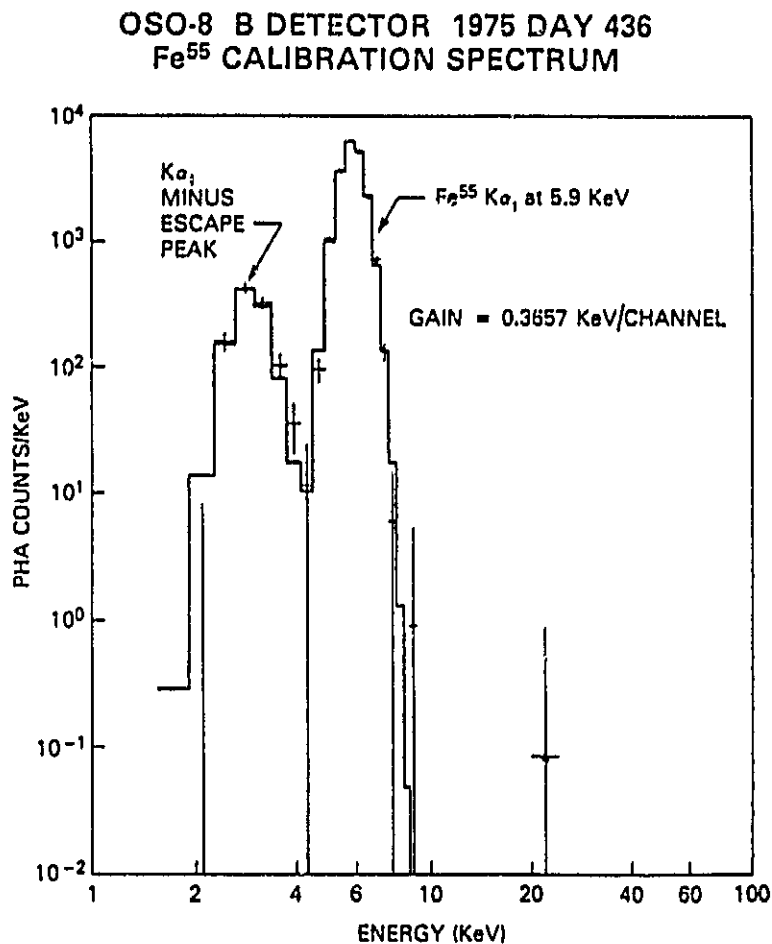
Figure 4-3

The figure shows the slow drift of the OSO-8 detector gains with time
due to diffusion of counter gas through the windows. The detector gains
are quoted in terms of the ratio of the photon energy to the pulse height
channel in keV/channel.

## OSO-8 DETECTOR GAIN HISTORIES
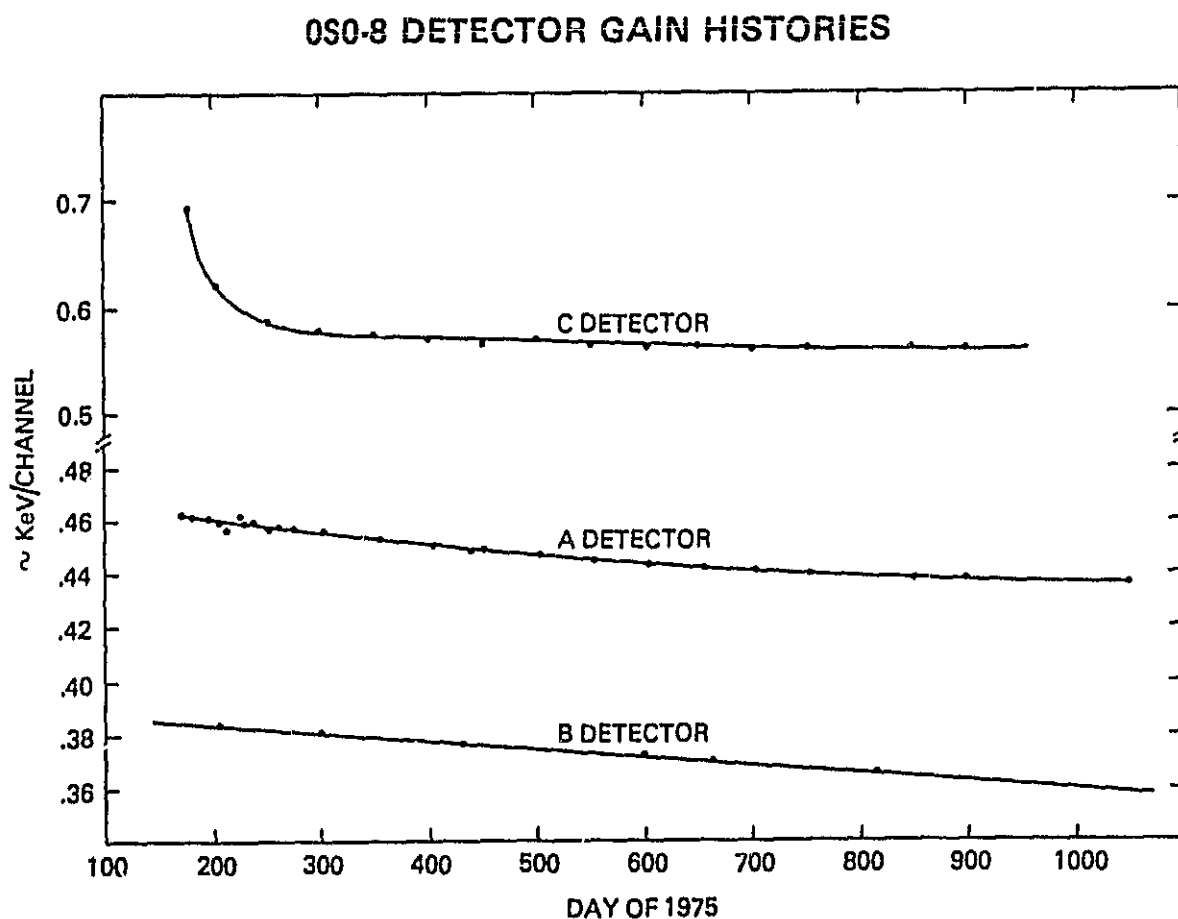
keV/channel, a standard convention which actually states the reciprocal of the gain. As the detector gas pressure dropped slowly, the multiplication factor, proportional to the pressure, was reduced so that a given collected charge required (and a given pulse height channel reflected) a higher photon energy. The relatively rapid gain change of the xenon-filled C detector (note the change in scale of the y-axis) at the beginning of the mission is believed to be due to rapid outgassing of water vapor which had entered the plastic windows of the detector in a humid environment before launch. The observed counter stability and good resolution ($Fe^{55}$ showed a resolution of ~ 17% at 5.9 keV in the B detector) reflect the near absence of impurities in the gas. This condition was achieved by great care in detector assembly, where the inner counter surfaces were carefully cleaned, followed by baking of the assembled detector at $80^{\circ}$ C during evacuation to allow the Al surfaces to outgas. Additionally, a film of calcium metal was evaporated onto the inside of the detector to act as a "getter" for impurities such as water vapor.

## C.  Summary of Instrument Parameters

For the various detectors used to make the observations reported in this thesis, Table 4-1 lists parameters useful for understanding those observations: The fields of view of the mechanical collimators give the potential for isolating sources in crowded regions of the sky. The energy range indicates sensitivity to various spectral components, while the energy resolution measures the ability to identify narrow spectral features. The background rate and count rate observed for the Crab Nebula combine to show the sensitivity to weak flux levels. The observed

rate from the Crab also allows a rough conversion of rates quoted in the text to fundamental flux units (erg $cm^{-2}s^{-1}$) or rates expected from other detectors for a spectrum similar to that of the Crab. Source flux levels in Chapters V and VI are sometimes quoted in units of HEAO-1 "R15 counts", a roughly spectrum-independent measure of 2-20 keV band flux from a combination of detector rates defined in Table 4-1; one R15 count corresponds to $\simeq 3 \times 10^{-9}$ erg $cm^{-2}$ $s^{-1}$, or ~ 1.2 Uhuru flux units for a Crab-like spectrum.

## 1. Proportional Counters

The detectors listed include five proportional counts of the type discussed above: the three OSO-8 detectors (Pravdo 1976) and the Medium Energy Detector (MED) and smallest field of view High Energy Detector (HED3) of the A2 experiment (Rothschild et al. 1979; Shafer 1983) on HEAO-1. Two other proportional counters are listed. The first is the All Sky Monitor (Kaluzienski 1977) on Ariel-5, a small (1 $cm^2$) low data rate (~ 1 bit $s^{-1}$), position-sensitive detector with no spectral information beyond a 3-6 keV band average, which served a crucial role of providing near-continuous coverage of most X-ray sources, monitoring long-term behaviors not accessible to most satellite instruments. Imaging of the X-ray sky in one dimension was accomplished with a resistive anode detecting photons through two pinhole apertures. The geometry of the detector allowed a narrow strip of the sky to be viewed at any instant, with the band moving across the sky as the satellite turned. Along the longest dimension of the strip the source of observed photons could be determined by the ratio of the charge collected at one end of the wire to the sum from both ends. The remaining proportional counter is the Monitor Proportional Counter (MPC) on HEAO-2 (called the Einstein Observatory in

commemoration of Einstein's centennial birthday celebration in the year of launch), which provided low resolution 1-20 keV band coverage of sources simultaneous with viewing by the HEAO-2 Solid State Spectrometer (SSS) (Holt 1976; Joyce et al. 1978).

## 2. Solid State Spectrometer

The principle of a solid state spectrometer is similar to that of a proportional counter. An X-ray "frees" an electron. A voltage applied across the device collects an amount of charge proportional to the X-ray energy. Instead of a gas the medium is a solid, Si, which has been doped with Li to tune the insulating and conducting characteristics of the material. The voltage across it keeps the interior region depleted of electrons and holes, so that no current is flowing except when an X-ray creates a pair. The detector is a reverse-biased np junction. As the operation is similar the energy dispersion is also of the form $2.35 (E\epsilon F)^{1/2}$. Here $\epsilon$ =3.81 eV and F ~ 0.1, predicting FWHM ~ 46 eV (Holt 1976). Other sources of variance increase this to ~ 160 eV. These dominant effects are energy independent.

The SSS on HEAO-2 worked over the energy range ~ 0.4 - 4 keV. The lower limit is determined by the noise, the upper by the telescope cutoff due to focal length. The effective area was ~ 200 $cm^2$ from 0.4 - 2 keV, but only ~ 50 $cm^2$ at 3 keV. The field of view for the SSS was a circle 6' in diameter. The detector, 9 mm in diameter, was placed slightly beyond the focus of the telescope so that the whole detector volume would be utilized.

# V. OBSERVATIONS

This chapter outlines the instruments, data collection modes, and viewing times for the Goddard observations of Circinus X-1. A synopsis is given in Table 5-1.

From the position of the optical counterpart, Circinus X-1 is located to within 1" of 1950.0 celestial coordinates R.A. = $229^\circ.2021$ , Dec = $-56^\circ.989$ (Whelan et al. 1977). This position corresponds to galactic longitude $\ell = 322^\circ.1$ in the plane (b = $0^\circ.04$). Figure 5-1 shows a map of the Circinus region in galactic coordinates, indicating nearby sources and various observational scan paths. Note that longitude increases from left to right, opposite to the convention used in many galactic projections.

## Observation 1: OSO A Detector Point

Cir X-1 was observed by the Goddard Cosmic X-Ray Spectroscopy Experiment "A" Detector (xenon-filled, $5^\circ$ FWHM collimator, $5^\circ$ off-axis) on OSO-8, during a 16.6 day binary period from Day 230 to Day 247 (17 August – 3 September) of 1976. The source coverage was especially good (i.e. high collimator efficiency, low source contamination, good statistics) from a day or so before the transition (i.e., the decrease in soft flux) through the day after. This observation constituted the longest view of Circinus with good statistics with Goddard instruments, and allowed a study of spectral evolution. The slow motion of the aft spin axis through the Circinus region is indicated in Figure 5-1 by a dashed curve. The path was chosen so that the A detector, canted at $5^\circ$ to the spin axis, scanned over the source for 2-3 seconds out of every ~ 10 second satellite rotation. In

ORIGINAL PAGE IS
OF POOR QUALITY

TABLE 5-1a:  SUMMARY OF CIRCINUS X-1 OBSERVATIONS

| OBSERVATION | INSTRUMENTS | MODE | DATES | PHASES |
|---|---|---|---|---|
| 1<br><br>OSO A Point | OSO-8 A Detector<br>6° circular collimator<br>1.7 - 60 keV response | "coning"<br>point | 1976 Days 230-247<br>(17 August - 3 September) | -0.15 - 0.85 |
| 2<br><br>HEAO Scan 0 | HEAO-1 A2, MED & HED3<br>SFOV: $1°5 \times 3°$ FWHM<br>LFOV: $3° \times 3°$ FWHM<br>MED response: 1.5 - 20 keV<br>HED response: 2-60 keV | scan | 1977 Days 236-243<br>(24-31 August) | 0.33 - 0.66 |
| 3<br><br>HEAO Point 1 | HEAO-1 A2, MED & HED3<br>(as above) | point | 1978 Day 48.79-48.93<br>(17 February) | 0.98 - 0.99 |
| 4<br><br>HEAO Scan 1 | HEAO-1 A2, MED & HED3<br>(as above) | scan | 1978 Days 51-57<br>(20-26 February) | 0.12 - 0.48 |
| 5<br><br>OSO C point | OSO-8 C Detector<br>6° circular collimator<br>2-60 keV response | point | 1978 Days 48-56<br>(17-25 February) | -0.07 - 0.41 |
| 6<br><br>HEAO Point 2 | HEAO-1 A2, MED & HED3<br>(as for Obs. 2) | "ping pong"<br>point | 1978 Day 231.54-231.84<br>(19 August) | -0.01 - 0.01 |
| 7<br><br>HEAO Scan 2 | HEAO-1 A2, MED & HED3<br>(as for Obs. 4) | scan | 1978 Days 236-243<br>(24-31 August) | 0.30 - 0.72 |
| 8<br><br>Einstein<br>Point 1 | HEAO-2 SSS & MPC<br>SSS: 6' collimator, 0.4-4<br>keV response<br>MPC: $0°75 \times 0°75$ FWHM,<br>2-20 keV response | point | 1979 Day 49.11-49.99<br>Day 50.29-50.46<br>(18-19 February) | -0.01 - 0.07 |
| 9<br><br>Einstein<br>Point 2 | HEAO-2 SSS & MPC<br>(as above) | point | 1979 Days 230.97-231.05<br>231.49-232.04<br>232.48-232.58<br>234.92-235.02<br>(18-23 August) | -0.05 - 0.05<br><br><br>0.19 - 0.20 |
| 10<br>Einstein<br>Point 3 | HEAO-2 SSS & MPC<br>(as above) | point | 1979 Day 248.14-248.30<br>(5 September) | 0.99 - 1.00 |

TABLE 5-1b:  SUMMARY OF CIRCINUS X-1 OBSERVATIONS

| OBSERVATIONS | COMMENTS ON OBSERVATION AND ANALYSIS |
|---|---|
| 1 | Very slow scan of aft spin axis around source for good efficency of A detector.  Data collected in "TM sync" mode to minimize source confusion.  160 msec rates data available.  64 channel PHA mode. |
| 2 | MED window 28 turned off.  10-sec PHA and 1-sec rates overflowed for peak fluxes. 5-sec scalar rates used to estimate spectra.  LFOV used to obtain 80 msec rates during quasi-oscillations.  32 channel PHA mode.  Source in field of view for $\leq$ 30 seconds out of each ~ 33 min great circle scan of the sky. |
| 3 | LFOV used to estimate spectrum from adjacent source 4U1510-59 (+MSH 15-52) as check on OSO A detector residual spectrum after outburst.  64 channel PHA mode. |
| 4 | 8-color scalar rates used to estimate low-flux spectrum.  Adjacent sources of comparable strength would contribute to PHA accumulation but can be excluded from rates by scan angle limits with SFOV. |
| 5 | Most of (slowly moving) pointed observation had low effective area for Circinus, with up to a factor of 2 greater exposure to 4U1510-59. |
| 6 | Nine maneuvers on and off source over seven hours bracketing transition.  Background taken in off source position near 4U1446-55.  64 channel PHA mode. |
| 7 | 8-color scalar rates for SFOV used to estimate low flux spectrum during scanning maneuver. |
| 8 | Ice factor for SSS large in early part of mission and not well modeled.  Hence spectra fit only down to 1 keV. |
| 9 | |
| 10 | |

Figure 5-1

This galactic-coordinate map of the sky near Circinus X-1 indicates
nearby sources and various observing paths (discussed in the text). Care
must be taken to exclude other sources from the OSO-8 and HEAO-1 A2 fields
of view. The OSO-8 A and C detector $5^0$ circular fields of view, centered
on Circinus are denoted by the large circle; the smaller circle shows the
full width half-maximum efficiency. At peak efficiency for Circinus, the
OSO collimators view the nearby supernova remnant MSH15-52 at about half
efficiency. The A2 SFOV collimators are represented by the $3^0 \times 6^0$
rectangle giving the FWFM response. The FWHM response is indicated by the
smaller rectangle ($1^0.5 \times 3^0.0$). When Circinus X-1 is observed at peak
efficiency in the SFOV, MSH15-52 appears only in the LFOV.

Note that in the figure, longitude increases from left to right,
opposite to the convention used in many galactic projections.

Figure 5-1

MAP OF SKY NEAR CIRCINUS X-I IN GALACTIC COORDINATES
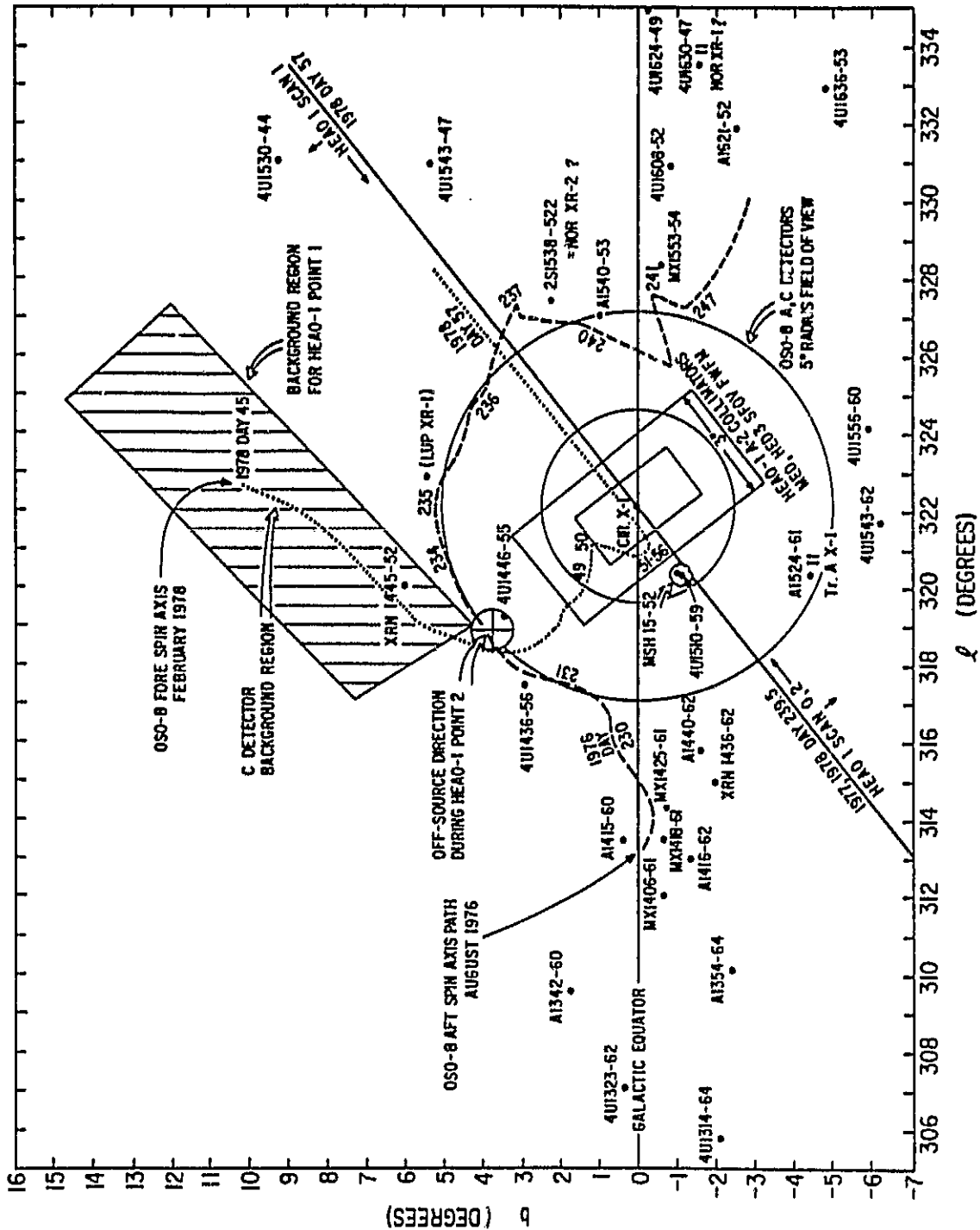
Figure 5-1, a circle of $5^0$ radius centered on Circinus corresponds to the area of the sky viewed with Circinus in the center of the field of view. The smaller circle of $2.5^0$ radius gives the half maximum response of the collimator.

Detector rates superposed in phase with the satellite rotation for a string of rotations are shown in Figure 5-2 for two intervals during the observed outburst. With a satellite rotation rate of 6.06 RPM, there were 61 phase bins. The solid line in Figure 5-2a shows the contribution to the flux from neighboring sources on Day 232, with the peak bins expected for a triangular response of the collimator to point sources tagged for each source. Figure 5-2b shows the dominance of Circinus X-1 during the peak of the outburst on Day 231, with a nearly perfect triangular response to the source. (Minor discrepancies are predominantly from variability of Circinus.)

Because the data were collected in telemetry synchronization mode rather than the more usual spin-synchronized mode, the sectors available for PHA data accumulation precessed and could be chosen to minimize source contamination. Background data were taken from the region of the circuit free from apparent sources.

The combined 2-60 keV aspect-corrected rates from Circinus for a portion of the observation including the outburst are shown in Figure 5-3b. During the peak, the source showed chaotic fluctuations on the $\sim 10$ second rotation timescale, with spectral hardening with increasing intensity. (These fluctuations will be discussed in Chapter VI.) The maximum intensity (for 1000 second averages) was $\sim 0.6$ counts $cm^{-2}$ $s^{-1}$, corresponding to $\sim 160$ Uhuru counts or $\sim$ one-sixth the intensity of the Crab Nebula. This was a moderate outburst for Circinus, which has been

Figure 5-2

Detector rates superposed in phase with the satellite rotation for a string of rotations are shown for two intervals during the observation. With a satellite rotation rate of 6.06 RPM, there were 61 phase bins. The solid line in part A shows the contribution to the flux from neighboring sources on Day 232, where the peak bins expected for a triangular response of the collimator to point sources are tagged for each known source. Part B shows the dominance of Circinus X-1 during the peak of the outburst on Day 231, with a nearly perfect triangular response to the source. (Minor discrepancies are predominantly from variability of Circinus.)

### OSO A DETECTOR RATES WITH SPIN ANGLE
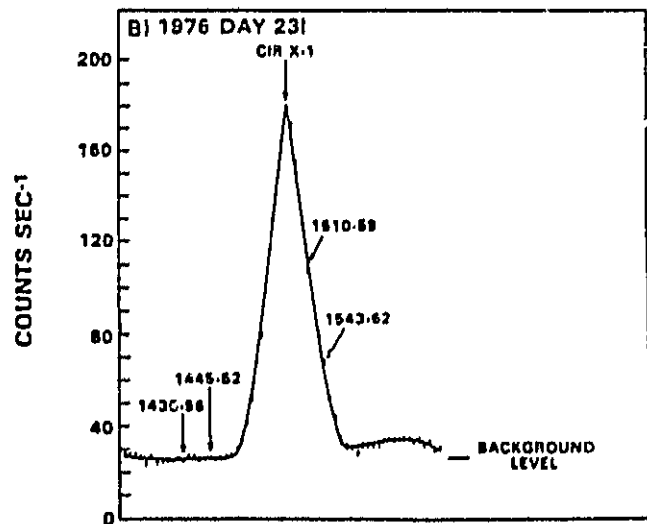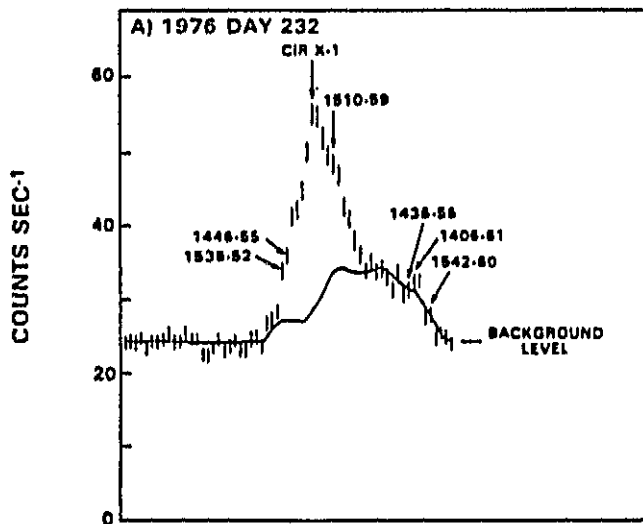
Figure 5-3


This figure demonstrates the behavior of Circinus during Observation 1
averaged over 1000 seconds. It shows:

A) A nine-month 3-6 keV band lightcurve for Cir X-1 in half-day
averages, from the Ariel 5 All Sky Monitor. This puts in context the
outburst covered by the OSO-8 A detector (indicated by dashed circle). The
outburst was of moderate strength (~ 160 Uhuru flux units) and declined
half a day early compared to the ephemeris based on the larger outbursts.
Predicted transitions are indicated by the arrows at the top of the plot.
Quasi-simultaneous radio coverage during the OSO event is discussed in the
text.

B) The portion of the 2-60 keV band OSO-8 light curve including the
outburst, the predicted transition (marked by a dashed line), a hard flare,
and a slow decline.

C) & D) Evolution of a two-component spectral model: A soft
component well fit by a blackbody of kT ~ 0.8 keV is associated with the
outburst, increasing in strength and becoming less absorbed as the flux
increases, then diminishing and becoming more absorbed until it disappears
at transition. A steadier component, described by a power law of photon
index ~ 2 or thin thermal bremsstrahlung of kT ~ 8 keV, persists after the
transition and may never show much more than interstellar absorption. A
brief hard flare, possibly involving an additional component, occurs a few
hours after the predicted transition.

The letters at the bottom (C,D,E,...,O,Q) identify intervals of
spectral accumulation.

Figure 5-3

CIR X-I MODERATE OUTBURST AUGUST 1976
LIGHTCURVE AND SPECTRAL EVOLUTION

A

ARIEL ALL SKY MONITOR

3-6 keV FLUX (photons cm$^{-2}$ s$^{-1}$)

2.00
1.60
1.20
0.80
0.40
0.00

90    130    170    210    250    290    330    370

1 APR 76        1 JUL 76        1 OCT 76        1 JAN 77

B

OSO-8 A DETECTOR

2-60 keV RATE (counts cm$^{-2}$ s$^{-1}$)

0.70
0.50
0.30
0.10
0.00

229    230    231    232    233    234    235    236

PREDICTED PHASE →          PREDICTED TRANSITION (PHASE = 0.0)
0.91    0.94    0.97    0.03    0.06    0.09    0.27; 0.45

C

1-20 keV INTENSITY (10$^{-2}$ ergs cm$^{-2}$ s$^{-1}$)

8
6
4
2
0

HARD FLARE

+ BLACKBODY COMPONENT
+ POWER LAW COMPONENT

90% CONF. UPPER LIMIT
TO B B COMP. = .08

D

N$_H$ (10$^{22}$ atoms cm$^{-2}$)

12
8
4
0

C  D  E G  I    J    K L M    N    O    O
      F H

+ COMBINED ABSORPTION
• BLACKBODY ABSORPTION
• POWER LAW ABSORPTION
▨ RANGE OF VALUES FOR DIFFERENT MODELS

231        232        233        234        237-240
DAY OF 1976

observed at intensities as high a. 2-3 times that of the Crab (Dower 1978; Kaluzienski 1979). It declined half a day early compared to the ephemeris based on the larger outbursts, a fairly common behavior for the smaller outbursts. The vertical dashed line shows the transition predicted by the Ariel 5 All Sky Monitor (ASM) ephemeris (Kaluzienski and Holt 1977). Figure 5-3a shows the ASM 3-6 keV band light curve (Kaluzienski 1977) in half-day averages for a nine-month period surrounding the OSO point. The OSO outburst in this plot is marked by a dashed circle. Results from quasi-simultaneous radio coverage during the OSO event (indicated by the hatched region nearby) are discussed in Chapters VI and VII. Predicted transitions to low flux are indicated by arrows at the top of the plot. After the outburst, a residual flux was detected, with a minimum rate a factor of 10 lower than the peak. Except for a brief flare which peaked a few hours after the predicted transition and declined in about an hour, the residual flux was fairly steady, dropping by no more than about a factor of 2 during the observation.

For spectral analysis, the pulse height data were divided into intervals (indicated at the bottom of Figure 5-3) when the counting rates were approximately constant on the time scale of minutes. Results are presented in Chapter VI for spectra between Days 231 and 234 of 1976 (intervals C through O) and one average spectrum for Days 237 to 240 (interval Q, not shown), when source confusion was minimal.

The spectral data indicated the presence of two continuum components, whose evolution, indicated in parts c and d of Figure 5-3, is discussed in Chapter VI. Note the flare occurring a few hours after the predicted transition.

The source 4U1510-59, tentatively identified in the 4U catalogue with

the supernova remnant MSH15-52, is located ~ $2^0$ away from Circinus and was in the A detector $5^0$ field of view concurrent with Circinus (see Figures 5-1 and 5-2a). While the sources could not be completely separated with the OSO detector, the contribution of 4U1510-59 can be estimated from a HEAO 1 pointed observation in February 1978 (see Observation 3, below), later scanning observations, an overlapping OSO C Detector point in February 1978 and a HEAO 2 point in August 1979. Data from the A2 detectors with $1^0.5$ collimation show 4U1510-59 had a continuum shape not unlike that of Circinus after the outburst but a considerably weaker strength. Assuming the source is steady, as suggested by the HEAO 1 and HEAO 2 data, it can account for no more than about 25% of the persistent, harder component of Circinus during the OSO-8 A detector observation. However, Circinus had a strength comparable to or weaker than that of 4U1510-59 during the majority of the observations reported here. That is, the component which is relatively steady during the cycle observed by OSO-8 is not an invariant feature of Circinus.

OBSERVATION 2: HEAO-1 Scan 0

The HEAO-1 A2 detectors scanned Circinus from Day 236 to Day 243 (24 August - 31 August) of 1977. In this mode the small fields of view (SFOV) of the MED and HED3 passed over Circinus for ~ 15 sec out of every ~ 33 min great circle scan of the sky. For analysis, the $1^0.5$ x $3^0.0$ (FWHM) SFOV for the MED and HED3 were used almost exclusively, to minimize contamination from nearby sources. As the spin axis was stepped across the sky, at a nominal rate of $0^0.5$ per 12 hours to keep the solar panels pointed toward the sun, the leading edge of the $3^0$ annulus swept out by the collimators advanced across the sky. Thus the source at the time of transit moved from

the edge of the $3^0$ (FWHM) collimator through the center to the opposite edge, with maximum efficiency (corresponding to on-axis viewing) occurring in the middle of the observation, on Days 239 to 240. In Figure 5-1 the directions of the great circle scans and their advance with time are indicated for this and succeeding HEAO 1 scanning observations. Also shown is the zero response $3^0x6^0$ rectangle outside of which the SFOV collimator response is essentially zero with Circinus centered in the field of view. The smaller rectangle ($1^0.5x3^0$) gives the half maximum response.

Figure 5-4a shows the combined MED+HED3 SFOV 1.28-second counts as a function of scan angle in the region near Circinus for approximately a one-day accumulation at the beginning of the observation. The contribution from Circinus (at scan angle $322^0.2$) is less than that of 4U1510-59 (at scan angle $320^0.5$). Since both are approximately on the same great circle scan (see Figure 5-1), this indicates that Circinus is in fact weaker at this time. A similar plot for 1977 Days 240.65-241.12 when Circinus was quite strong (Figure 5-4b) shows departures from a triangular response due both to intensity variations and overflows in the 1-sec rates counters. The aspect-corrected ~ 2-20 keV light curve derived from the MED rates for an assumed point source at the position of 4U1510-59 (not shown) is consistent with a constant source of ~ 9 R15 counts. The lower part of Figure 5-5 shows the corresponding light curve for Circinus during this observation. Throughout this observation, one of the pulse height windows for the second layer of the MED (Window 2B, nominally > 3.9 keV) was off, so that the counts from MED Layer 2 covered only the range 1.8 -3.9 keV.

Prior to Day 239 the observed flux from Circinus was low ($\lesssim$ 9 $R_{15}$ counts). On Day 239, the source flux averaged 20-25 $R_{15}$ counts, about the

Figure 5-4

Part A of the figure shows the combined MED+HED3 SFOV 1.28-second counts, as a function of scan angle, in the region near Circinus for approximately a one-day accumulation at the beginning of the observation. The contribution from Circinus (at scan angle 322°2) is less than that of 4U1510-59 (at scan angle 320°5). Since both are approximately on the same great circle scan (see Figure 5-1), this indicates that Circinus is in fact weaker at this time. A similar plot for 1977 Days 240.65-241.12 when Circinus was quite strong (part B) shows departures from a triangular response due both to intensity variations and overflows in the 1-sec rates counters.

CIR X-1 HEAO 1 A-2 SCAN 0 AUGUST 1977
SFOV COUNTS VS. SCAN ANGLE
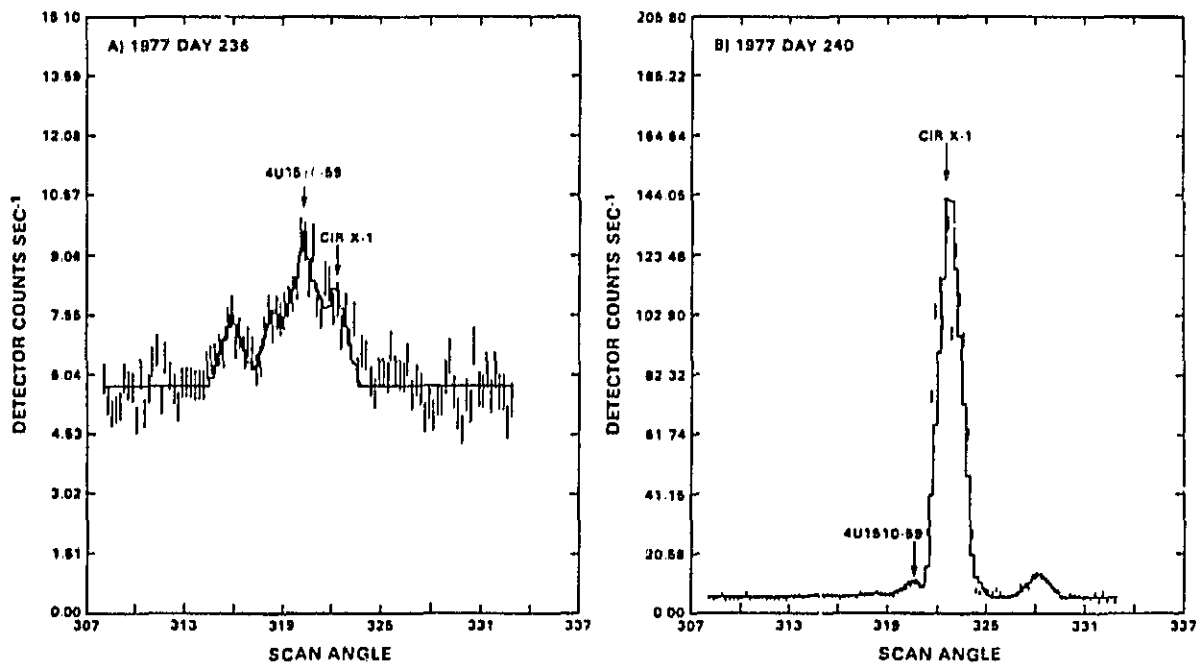
Figure 5-5

The upper plot shows an Ariel-5 lightcurve covering five 16.6-day cycles of Circinus, including one with partial concurrent HEAO-1 A2 coverage and the following cycle which was covered by SAS-3.

The lower plot shows HEAO-1 coverage of approximately half a cycle in August 1977 (called HEAO A-2 Scan 0), including onset near phase 0.5.

The scan-by-scan binning shows erratic changes in flux by large factors from one scan to the next. (The spectral character of the changes are indicated in a succeeding figure.) The Ariel-5 lightcurve shows that the source intensity increased to above that of the Crab nebula (~ 1000 Uhuru flux units) after it left the HEAO-1 A2 field of view. This cycle showed a long duty-cycle (~ 0.5) compared to that covered a year earlier by OSO-8 (< 0.1).

Figure 5-5



**CIR X-I LIGHTCURVE**
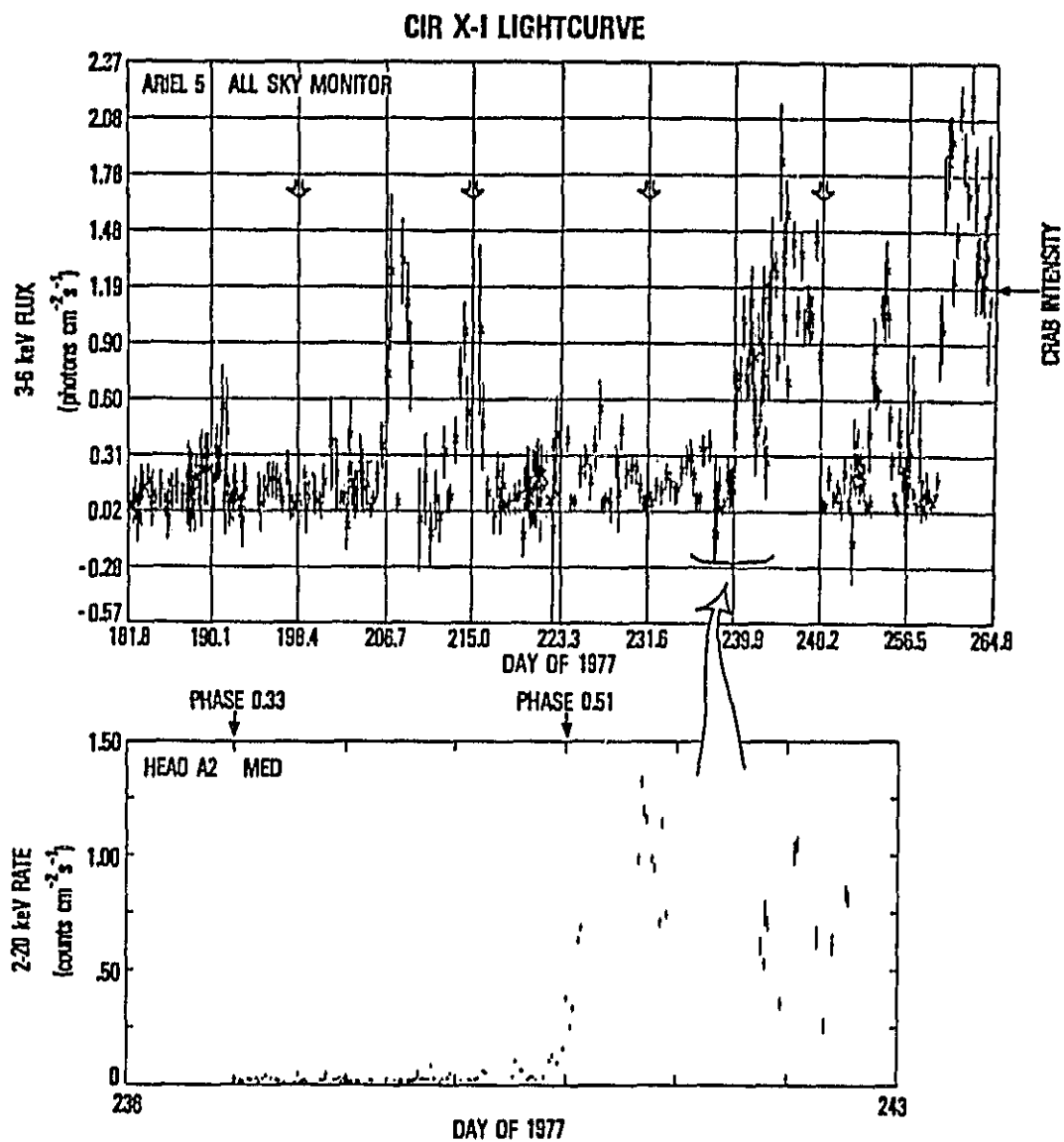
same intensity as the residual component in the first observation. As we will discuss in Chapter VI, the spectrum was different.

Beginning on Day 240 near phase 0.5 of the ASM ephemeris, the source showed erratic behavior, with large intensity variations from scan to scan. The maximum 5-sec average intensity observed was ~ 1.8 x $10^{-8}$ ergs $cm^{-2}$ $s^{-1}$, corresponding to an instantaneous 2-10 keV luminosity of ~ 2.1 x $10^{38}$ erg $s^{-1}$ for a distance of 10 kpc. Overlapping coverage of Circinus by the Ariel-5 ASM (see upper part of Figure 5-5) showed that the flux continued to increase after the HEAO-1 observation ended (~ 5 days before the transition, due to satellite constraints), reaching ~ 25% higher in the 3-6 keV band before falling off. This cycle showed a long duty-cycle (~ 0.5) compared to that covered a year earlier by OSO-8 (< 0.1). The ASM lightcurve for several cycles including the one partially covered by HEAO-1 is shown in the upper part of Figure 5-5. [The preceding cycle was comparable to or a little higher than that seen by the OSO-8 A detector in Observation 1. The succeeding cycle is the quite spectacular one for which Dower (1978) reported SAS-3 observations showing a peak luminosity of ~ 6.6 x $10^{38}$ erg $s^{-1}$ (for a 10 kpc distance) and a wide variety of behavior, as noted in Chapter II.] The 80-msec data obtained with the MED and HED3 large fields of view (LFOV, $3^{\circ} \times 3^{\circ}$ FWHM) showed quasi-oscillations in intensity with amplitudes of a factor of 2 or more on timescales of a few seconds, with rise times as short as 160 msecs. The first column of Figure 5-6 shows the four clearest samples of this behavior. (The autocorrelation functions shown in the figure will be discussed in Chapter VI.)

At the highest intensities, the 10-sec PHA accumulation scalars (8 bits only being assigned) overflowed for HED 3 channels 4 through 6 and MED

Figure 5-6

The HEAO-1 Scan O observation of Cir X-1 shows interesting structure on timescales of seconds or less, including quasi-oscillations of a few seconds.

The first column of plots shows 80-msec rates data (from the MED and HED3, large and small fields of view) for four individual scans across the source on 1977 Day 240 (Data sets 1-4 of Table 6-9). The second column shows the autocorrelation for each scan for lags up to 8 seconds, while the third column shows the logarithm of the respective autocorrelation functions, with representative fits to the characteristic times for short lags.

The autocorrelation functions show nearly linear declines from zero lag to the zero crossing points; the timescales of the declines may be associated with the duration of the peaks or troughs of the quasi-oscillations.

Figure 5-6

# CIR X-1 HEAO A-2
## SCAN 0 - 80 MSEC DATA



LIGHT CURVE — AUTO CORRELATION — LOG OF ACF

COUNTS CM-2 S-1

SECONDS OF DATA — LAG (SECONDS) — LAG (SECONDS)
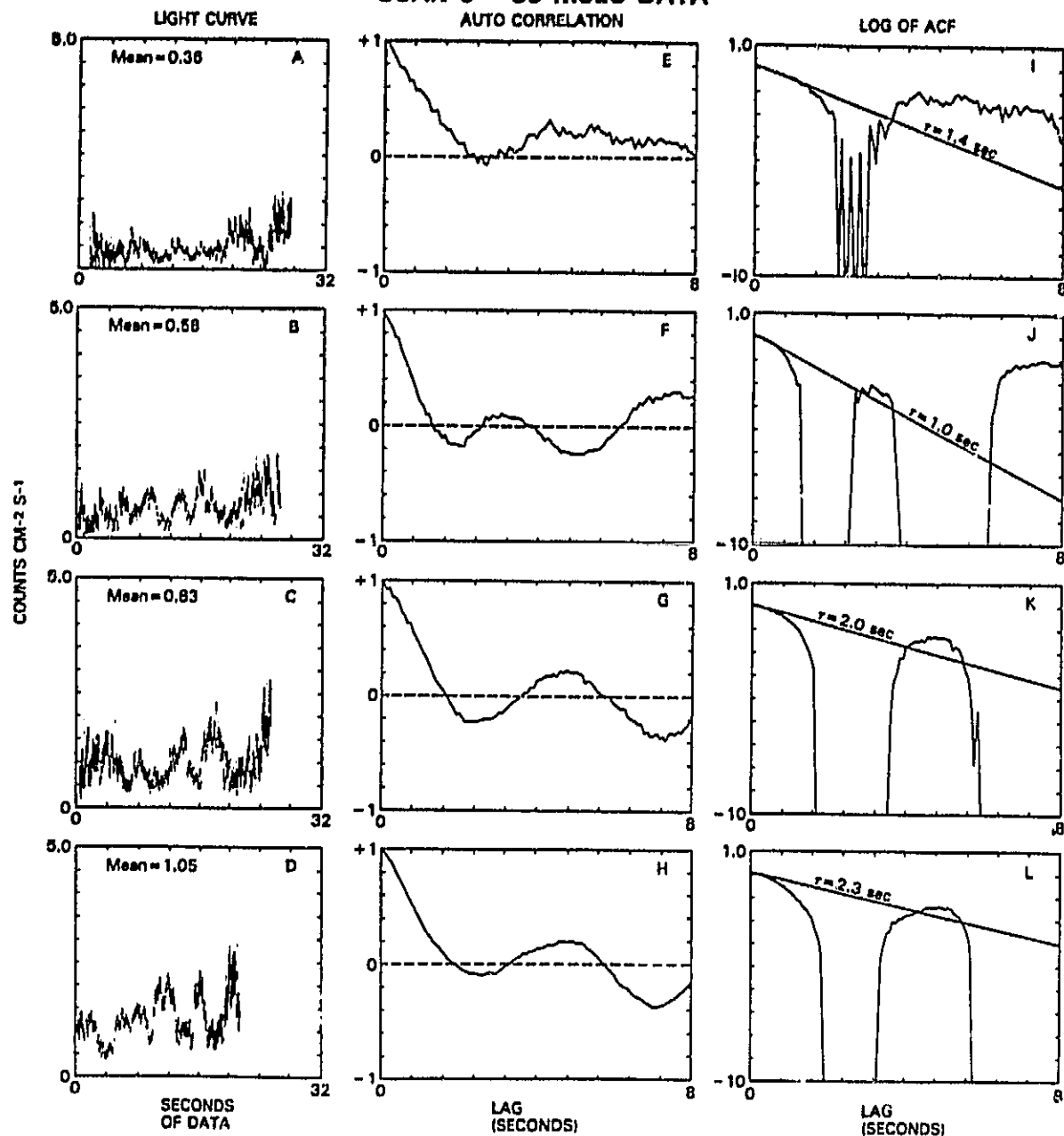
channels 13-17, which contained most of the counts. The 40-sec PHA
accumulations did not overflow, but due to the scanning mode included
sources comparable to Circinus above a few keV. The 1-second scalar rates
for the first layers of the MED and HED also overflowed. Hence the
5-second scalar rates were used to study the changes in the spectrum with
intensity. Tables 5-2 lists the scalar rate energy window (color)
definitions, and the available independent colors during the several HEAO-1
observations.


OBSERVATION 3:  HEAO-1 Point 1

The first HEAO-1 A2 pointed observation took place on 1978 day
48.79-48.93 (17 February), at ~ phase 0.98 according to the ephemeris of
Kaluzienski and Holt (1977). During the point the centers of the detectors
were maintained within a circle of ~ $0.5$ radius of Circinus. Longer term
ASM coverage shows that the outburst for this cycle was moderate, perhaps
comparable to that of Observation 1, and declined early, before this
observation began.

The aspect-corrected HED3 SFOV light curve during the ~ 2.6 hour point
(see Figure 5-7) shows a generally low flux (12-16 R15 counts) with a
substantial double-peaked flare ($\gtrsim$ 80 R15 counts at peak intensity)
lasting ~ 5 minutes from start to finish. The large gaps in the data occur
during periods of earth occultation or high electron flux. Regions of the
data for which spectra were accumulated ("low", "high", and "burst" times)
are indicated in Figure 5-7.

The source 4U1510-59 was present in the LFOV but not in the SFOV.

TABLE 5-2: HEAO-1 A2 SCALAR RATE DEFINITIONS

### a) Color Definitions

| Detector | Color | Nominal Energy Band (keV) | Detector | Color | Nominal Energy Band (keV) |
|---|---|---|---|---|---|
| MED | 1A+1C+1D | 2-6, 8-20 | HED3 | 1A | 2-6 |
| | 1B | 6-8 | | 1B | 6-8 |
| | 2A | 2-3.9 | | 1C+1D | 8-60 |
| | 2B | 3.9-20 | | 2A+2B | 9-60 |

### b) Available Independent Colors

| Observation | Detector | Color | Scalar Rate Combination | Detector | Color | Scalar Rate Combination |
|---|---|---|---|---|---|---|
| Scan 0 | MED | 1A+1C+1D | 2-6 | HED3 | 1A+1C+1D | 2-6 |
| | | 1B | 6 | | 1B | 6 |
| | | 2A | 4 (H2B off) | | 1A+2B | 4 |
| Point 1 | MED | 1A+1C+1D | 2-6 | HED3 | 1A | 2-6-8 |
| Scan 1 | | 1B | 6 | | 1B | 6 |
| Point 2 | | 2A | 4-8 | | 1C+1D | 8 |
| Scan 2 | | 2B | 8 | | 2A+2B | 4 |

Figure 5-7

The Circinus X-1 lightcurve during the first HEAO-1 A2 point shows a generally low flux with a substantial double-peaked flare lasting ~ 5 minutes from start to finish. The large gaps in the data occur during periods of earth occultation or high electron flux. Regions of the data for which spectra were accumulated ("low", "high", and "burst" times) are indicated.

The ~ 2.6 hour point occurred at ~ phase 0.98 according to the ephemeris of Kaluzienski and Holt (1977). Longer term Ariel-5 All Sky Monitor coverage shows that the outburst for this cycle was moderate, perhaps comparable to the OSO outburst, and declined early, before this HEAO point.

## CIR X-1 HEAO A-2 POINT 1 LIGHTCURVE FEB. 1978



DAY OF 1978
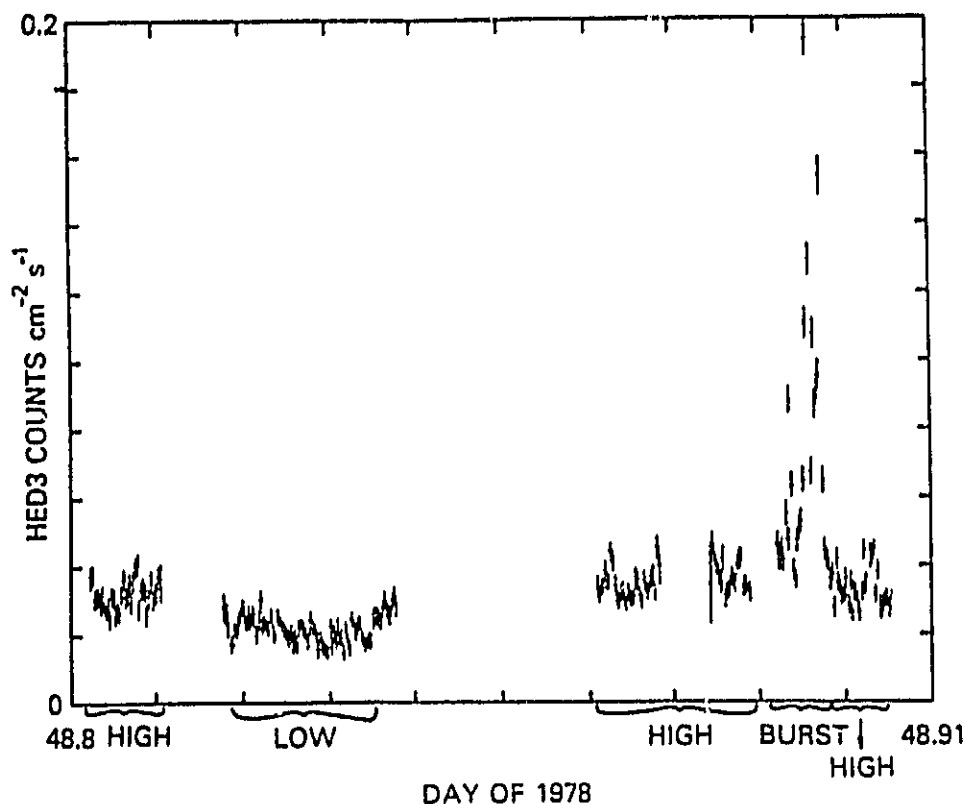
OBSERVATION 4: HEAO-1 Scan 1

This scanning observation with the A2 MED and HED3 detectors began ~ 2 days after the preceding point, covering Circinus during 1978 days 51-57 (20-26 February). In this case, to avoid source confusion during scanning mode data collection, the 1-second scalar rates data were used to estimate the source spectrum rather than the 10-second PHA data, which included sources of comparable strength (particularly 4U1510-59).

Figure 5-8 shows the counts as a function of scan angle for one of these "colors" (the 2-6 keV and 8-20 keV window for MED Layer 1, L1ACD) for superposed scans from 1978 Days 51.58-56.08. The contribution from Circinus (at scan angle $217^{\circ}3$) was again less than that of 4U1510-59 (at scan angle $219^{\circ}4$). The aspect-corrected lightcurve for the total MED rate for the latter (not shown) again indicated a constant source of about the intensity determined for Observation 2. The combined MED and HED3 SFOV lightcurve for Circinus, shown in Figure 5-9, yields an average rate of ~ 5 R15 counts, with no clear evidence for variation. The apparent increase in flux at the beginning and end of the observation are signatures of data collection with low effective area to the source of interest, where aspect-correction can boost small contaminations from other sources or local background.

OBSERVATION 5: OSO-8 C Detector Point

This pointed observation consisted of a slow maneuvering of the fore spin axis of the OSO-8 satellite in the vicinity of Circinus during 1978 Days 48-56 (17-25 February), so that the C Detector viewed both Circinus and 4U1510-59 (see Figure 5-1). A background spectrum was accumulated from 1978 Day 45.36 to Day 46.46, as the fore spin axis moved slowly through a

Figure 5-8

The figure shows the counts as a function of scan angle for the 2-6 keV and 8-20 keV window for MED Layer 1 (L1ACD) for superposed scans from 1978 Days 51.58-56.08. The contribution from Circinus (at scan angle 217°.3) was less than that of 4U1510-59 at scan angle 219°.4).

CIR X-1 HEAO 1 A-2 SCAN 1
MED   L1ACD SFOV COUNTS



1978 DAY 51-56
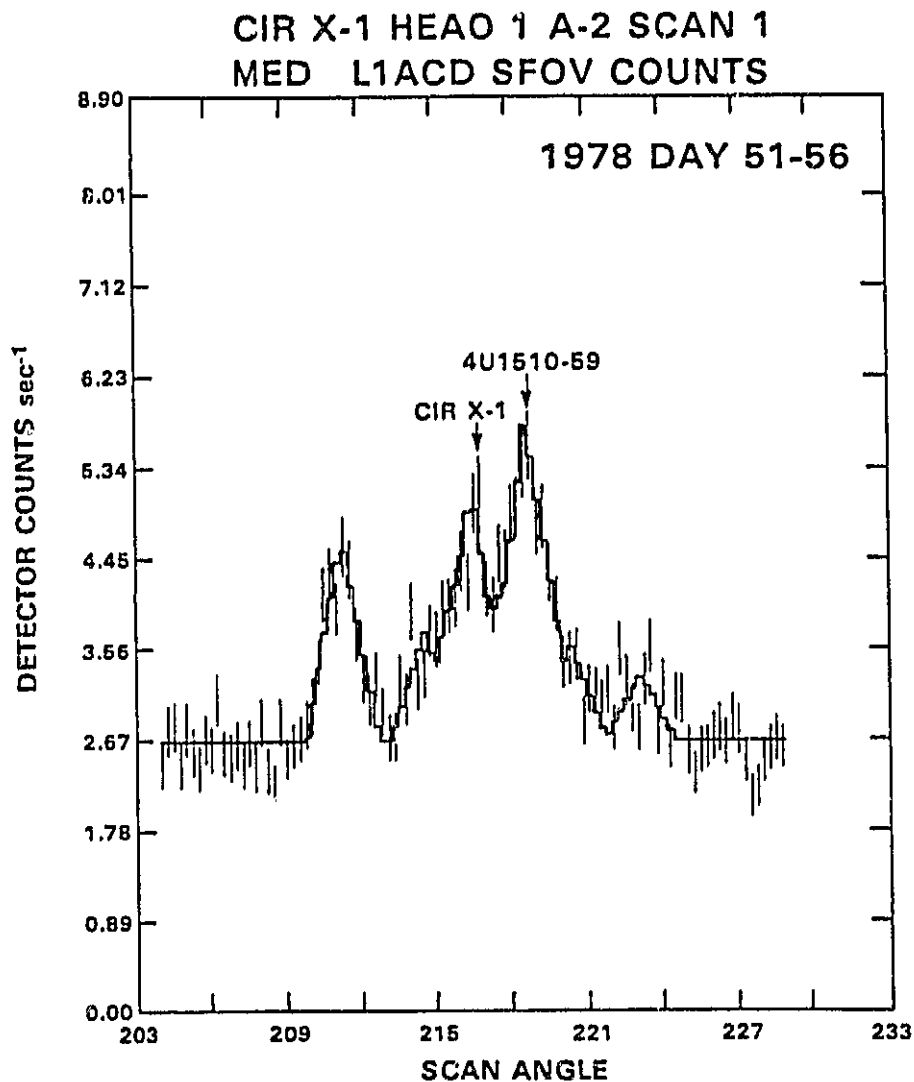
Figure 5-9

The combined MED and HED3 SFOV lightcurve for Circinus yields an average rate of ~ 5 R15 counts, with no clear evidence for variation. The apparent increase in flux at the beginning and end of the observation are signatures of data collection with low effective area to the source of interest, where aspect-correction can boost small contaminations from other sources or local background.

## CIR X-1 HEAO A-2 SCAN 1
## AVERAGED MED + HED SFOV LIGHTCURVE



DAY OF 1977
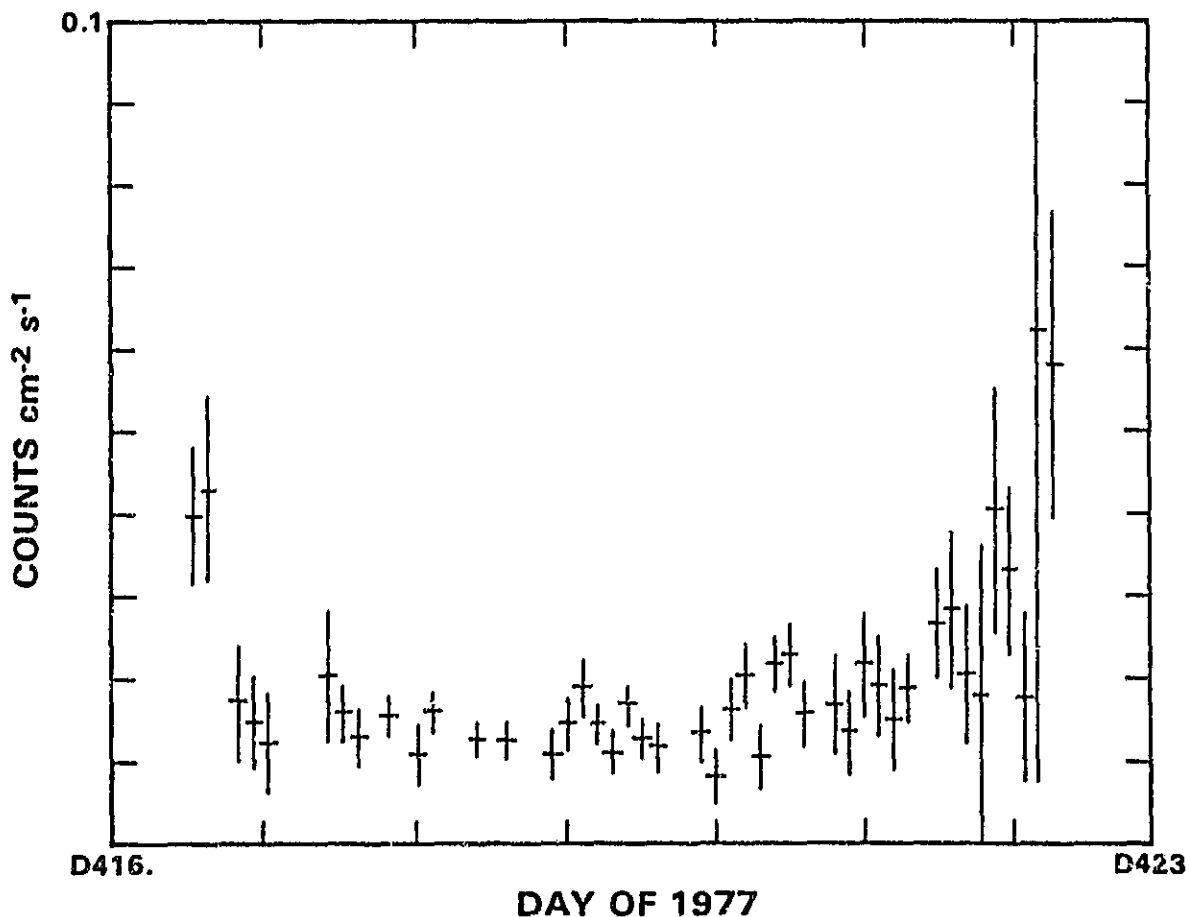
region free of known sources.

The observation was not optimum for delineating Circinus -- it was offset from the source (with consequent reduced efficiency) to avoid inclusion of 4U1538-52 in the $5^o$ field of view; it typically had an effective area for viewing 4U1510-59 about a factor of 2 larger than that for Circinus, at a time when HEAO A2 data (Observations 3 and 4) show Circinus was generally weaker. However, this observational shortcoming can be exploited to constrain the spectrum of 4U1510-59.

## OBSERVATION 6:  HEAO-1 Point 2

This "ping pong" point involved nine maneuvers on and off the source during a seven.hour period bracketting phase 0 (1978 Day 231.655, 19 August). The maneuvers consisted of fast slews between the source and off-source positions (the latter near 4U1446-55, found to be quite weak in HEAO A2 observations), with the pointings confined to circles of $\sim 0^o.5$ radius. The off-source position (indicated in Figure 5-1) was used to obtain background rates and PHA data. There was no major change in flux or spectral character across the nominal transition. The lower part of Figure 5-10 shows the aspect-corrected MED lightcurve during the observation. The apparent changes in source flux are probably real, not being well-correlated with changes in the effective area of the detector (shown in the top part of the figure) in the direction of the source. The source at this time was relatively weak, ($\sim$ 6 R15 counts).

## OBSERVATION 7:  HEAO-1 Scan 2

The last HEAO-1 observation of Circinus, covering 1978 Days 236-243 (24-31 August), corresponded to phases 0.3-0.7. It had a flux level about

Figure 5-10

The second HEAO-1 A2 point at Circinus involved nine "ping pong" maneuvers on and off the source over seven hours. The apparent change' in the source flux shown in the figure are probably real, not being well-correlated with changes in the effective area of the detectors in the direction of the source.

The observation brackets a nominal transition predicted by the ephemeris of Kaluzienski and Holt (1977) on 1978 Day 231.655, but there is no major change in flux or spectral character across the transition.

## CIR X-1  HEAO A-2  POINT 2 ("PING PONG")

EFFECTIVE AREA                    AUGUST 1978

MED LIGHTCURVE

231.54          PREDICTED TRANSITION          231.83
                   DAY OF 1978
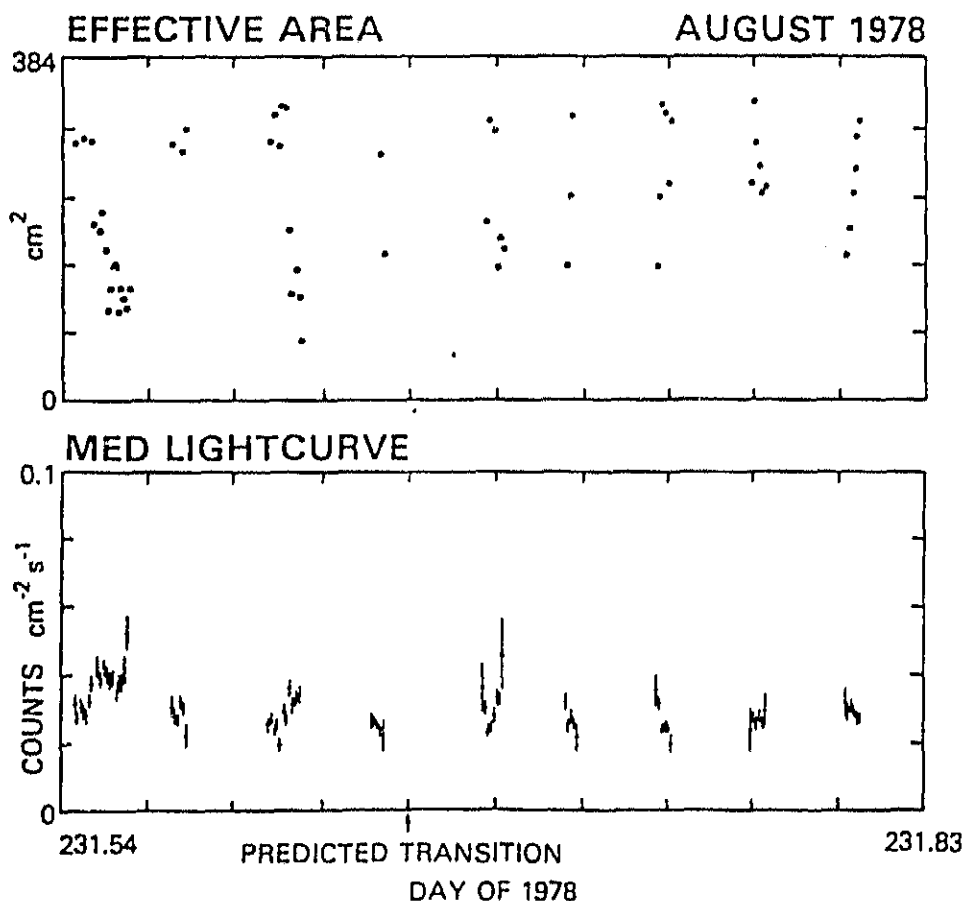
two-thirds of that during Observation 6, a few days before, and the data were sparser (due in part to the scanning mode, but also to loss of data during points at other sources).

OBSERVATION 8: HEAO-2 Point 1

The first HEAO-2 point at Circinus, on 1979 Days 49-50 (18-19 February), involved 15 looks at the source with the Solid State Spectrometer (SSS) and the Monitor Proportional Counter (MPC), lasting 500 to 1500 seconds each, over 1.35 days beginning on 1979 Day 49.11. The SSS, with a 6' diameter collimator, responds to the energy range 0.5 - 4.5 keV with 64 PHA channels, while the MPC, with a $1.^{\circ}5 \times 1.^{\circ}5$ FWFM rectangular collimator has an 8 channel response to the range 1.5 - 20 keV. The low energy response of the SSS was complicated by ice accumulation on the window. While this effect was generally modeled fairly successfully, the correction was difficult to make in the early part of the mission when the ice factor was large. For this observation, the PHA data were not fit below 1 keV, where the effect dominated. Typically the last two channels of the MPC are not reliable because of changing background effects, so they were not used except for high source counting rates during the flaring discussed below.

According to the All Sky Monitor ephemeris (Kaluzienski and Holt 1977), the phases of the 16.6 day cycle covered by this observation were ~ -0.01 to 0.07. There was no abrupt change at phase 0 (~ Day 49.23) though, as shown in Figure 5-11, the flux in both the SSS and the MPC did show a slow decline across the predicted transition (from ~ 6 U.F.U. to ~ 4 U.F.U. in the MPC), and the MPC hardness ratio increased in keeping with typical past observations. It is not clear from concurrent ASM coverage

Figure 5-11

The first HEAO-2 point at Circinus involved 15 looks at the source over 1.35 days, lasting from 500 to 1500 seconds each. According to the All Sky Monitor ephemeris (Kaluzienski and Holt 1977), the phases covered were ~ -0.01 to ~ +0.07. There was no abrupt change at phase 0 (indicated in the figure by arrows at ~ 0.14 of X-axis scale), though the flux in both the SSS (plot A) and MPC (plot B) did show a slow decline across the predicted transition (from ~ 6 U.F.U. to ~ 4 U.F.U. in the MPC), and the MPC hardness ratio (plot C) increased in keeping with typical past observations.

Starting about a day after the predicted transition, flaring was observed from the MPC with the counting rate rising as high as 30 U.F.U. The flaring continued at least until the end of the point.

Figure 5-11

## 102.4 SEC BINS

~ SECONDS OF 1979 DAY 49
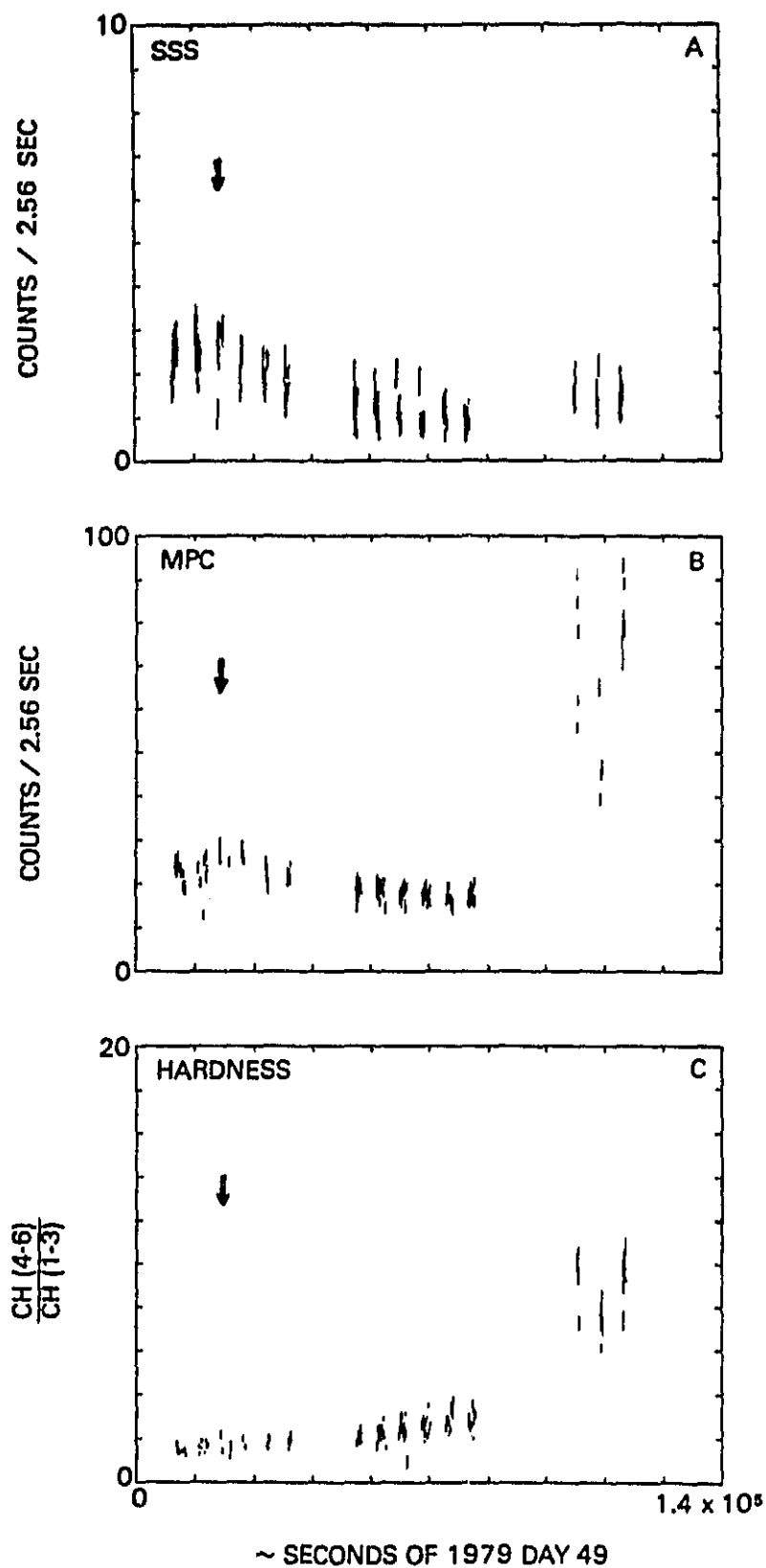
whether there was a small outburst, with an early decline like that of the OSO A detector observation, or whether the flux stayed low throughout.

Starting about a day after the predicted transition, flaring was observed in the MPC, with the counting rate rising to 30 U.F.U. (see Figure 5-11). The flaring continued for at least ~ 4 hours, until the end of the point. (The All Sky Monitor was not sensitive to the flux levels involved.) The modest increase in the SSS rate and the factor of 3-4 increase in the hardness ratio show that the bulk of the flaring occurred above 3 keV. Changes in the SSS spectra from pre-flare to flare times, discussed in the following chapter, rule against the possibility that the flaring came from a source outside the smaller SSS field of view.

Finer time resolution of the flaring is shown in Figure 5-12, where 2.56 second rates are plotted for several detector windows.

OBSERVATIONS 9 and 10:   HEAO-2 Points 2 and 3

The second HEAO-2 point at Circinus took place, on 1979 Days 230-235 (18-23 August), 11 cycles after the first. It sampled phases -0.05 to 0.2 of the 16.6 day period. The third point took place on 1979 Day 248 (5 September) during the last hundredth of the same cycle. In both cases the source flux was fairly weak during a nominal outburst time. The flux during the second point averaged about 4 U.F.U., occasionally ranging as high as 10 U.F.U. The flux during the third point averaged 2.5 - 3 U.F.U., the lowest reported in this work.

Figure 5-12

The flaring during the first HEAO-2 point at Circinus is shown with 2.56-second time resolution in several detector windows. The intensity fluctuations are confined primarily to the MPC channels 4-6. The MPC channels 1-3 and 7-8 and the SSS rates are fairly steady in comparison. The bottom plot shows the hardness ratio of MPC channels 4-6 to MPC channels 1-3.
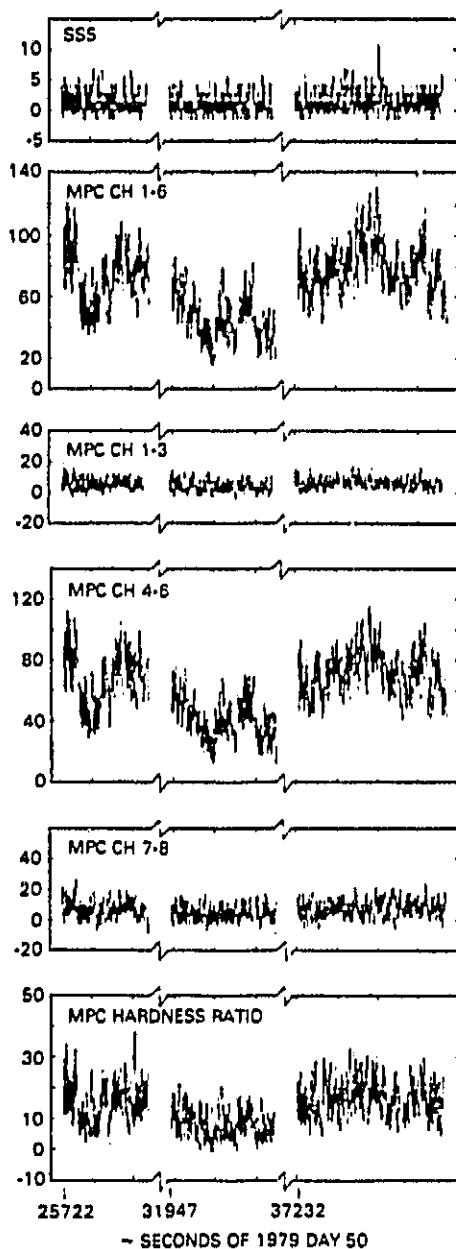
# VI.   RESULTS

This chapter presents the results of spectral and temporal analysis of the observations outlined in Chapter V.

## A.   Circinus X-1 - Spectral Studies

Spectral data were fit using a standard procedure described elsewhere (Pravdo 1976) whereby trial photon spectra were folded through the detector response function and compared with the observed pulse height data using a $\chi^2$ goodness of fit criterion.  A similar procedure allows the counts predicted for various detector bands from a given incident spectrum to be compared with the observed scalar rates data.  The parametric forms used to fit the spectral data are summarized in Table 6-1.  Contact with intrinsic physical parameters is made by comparison with the pertinent equations in Chapter III.

### Observation 1:   OSO A Detector Point

#### a.   Before Transition

During the moderate outburst covered by the OSO A Detector in August 1976, the 2-20 keV data cannot be fit by a single component spectrum modified at low energies by photoelectric absorption.  Instead, it yields a complex spectrum of two components whose relative intensities vary with the source strength:  an optically thick component associated with the outburst of soft flux and a steadier optically thin component.  Figure 6-1a shows the pulse height data at maximum intensity (interval D in Figure 5-3) along

TABLE 6-1: PARAMETRIC FORMS FOR SPECTRAL FITTING

Absorption Cutoff Factor:  $(\frac{dN}{dE}) = e^{-N_H \, \sigma(E)}$

Absorption Edge Factor:  $(\frac{dN}{dE}) = e^{-C \, (E_{edge}/E)^{2.7}}$

Emission Line:  $(\frac{dN}{dE})_{Line} = C_{Line} \, e^{-(E-E_0)^2/(2\sigma^2)}$

Power Law Continuum:  $(\frac{dN}{dE})_{PL} = C_{PL} \, E^{-\alpha}$

Thin Thermal Bremsstrahlung Continuum:[*]  $(\frac{dN}{dE})_{TTB} = C_{TTB} \, g(T,E) \, (kT)^{-1/2} \, E^{-1} \, e^{-E/kT}$

Blackbody Continuum:  $(\frac{dN}{dE})_{BB} = C_{BB} \, E^2 \, [e^{E/kT} - 1]^{-1}$

Boltzmann Continuum:  $(\frac{dN}{dE})_{BOLTZ} = C_{BOLTZ} \, E^2 \, e^{-E/kT}$

Modified Blackbody Continuum:  $(\frac{dN}{dE})_{MBB} = (\frac{dN}{dE})_{BB} \, [\frac{x^{C_1}}{1 + C_2 \, x}], \quad x = g(T,E) \, \frac{(1 - e^{-E/kT})}{(E/kT)^3}$

$C_1 = 0.33$ exponential atmosphere
$\phantom{C_1 = }$ 0.5 homogeneous disk

[*] The Gaunt factor $g(T,E)$ is computed by Karzas and Latter (1961) with interpolation formulae given by Kellogg, Baldwin, and Koch (1975).

Figure 6-1

Part A of the figure shows the pulse height data at maximum intensity (interval D in Figure 5-3) along with the best fit continuum spectrum folded through the detector response: a blackbody component with a kT of 0.82 ± 0.01 keV, plus a power law component with a number index of 1.9 ± 0.3. (All quoted errors are 1σ uncertainties). The corresponding inferred incident spectrum is shown in Part B. The energy fluxes at earth corresponding to the two components were ∼ 6 x $10^{-9}$ and ∼ 1 x $10^{-9}$ erg $cm^{-2}$ $s^{-1}$, respectively. The low-energy cutoff corresponded to an equivalent hydrogen column density of (1.6 ± 0.1) x $10^{22}$ atoms $cm^{-2}$, about what is expected from interstellar material along the line of sight to Circinus. The best fit included a narrow line feature at 6.1 ± 0.3 keV corresponding to 0.005 photons $cm^{-2}$ $s^{-1}$, and had a $\chi^2$ of 45.6 for 51 degrees of freedom.

Figure 6-1



CIR X-1 OSO A DETECTOR AUGUST 1976
SPECTRUM AT PEAK
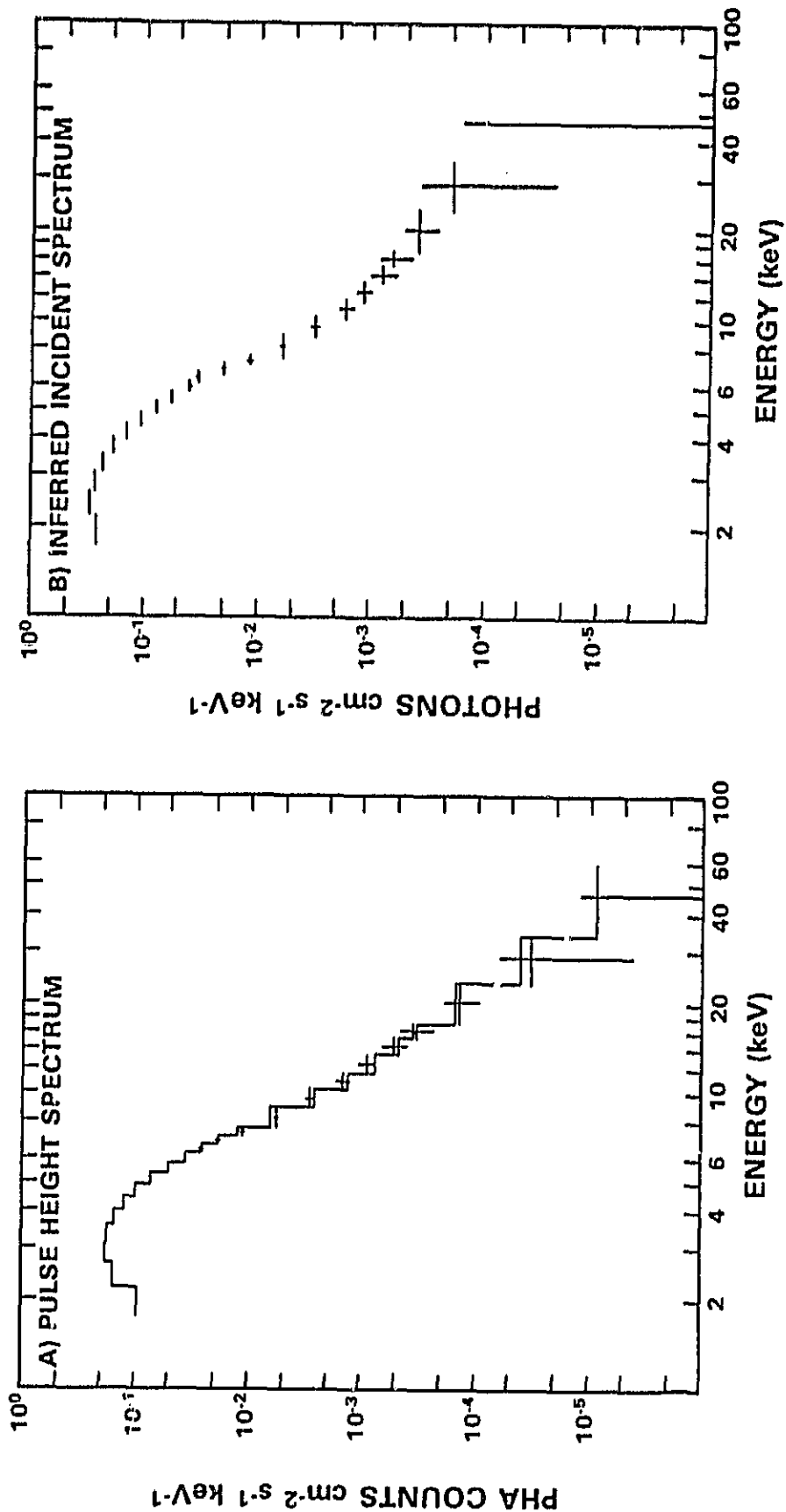
with the best fit continuum spectrum folded through the detector response:  a blackbody component with kT = 0.82 ± 0.01 keV, plus a power law component with a number index of 1.9 ± 0.3.  (All quoted errors are 1σ uncertainties unless otherwise noted.)  The corresponding inferred incident spectrum is shown in Figure 6-1b.  The energy fluxes at earth corresponding to the two components were ~ 6 x $10^{-9}$ and ~ 1 x $10^{-9}$ erg $cm^{-2}$ $s^{-1}$, respectively.  A single absorption parameter was associated with both components when the blackbody was strong because of a lack of uniqueness and statistical significance of separate absorptions.  The resulting equivalent hydrogen column density was (1.5 ± 0.1) x $10^{22}$ atoms $cm^{-2}$, about what is expected from interstellar material along the line of sight to Circinus [21-cm emission measurements give 1.4 x $10^{22}$ $cm^{-2}$ (McGee, Milton, and Wolfe 1966)].  The best fit included a narrow line feature at 6.1 ± 0.3 keV corresponding to 0.005 photons $cm^{-2}$ $s^{-1}$, and had a $x^2$ of 45.6 for 51 degrees of freedom.  Omitting the line from the model gave a best fit $x^2$ larger by 21 for an additional 2 degrees of freedom.  The line is discussed further in part c.  In this composite model, the fit was not very sensitive to the parameters for the harder component when the blackbody was strong.  Nor was it possible to choose between a power law model with photon index near 2 or a thin thermal bremsstrahlung model with kT ~ 8-9 keV for this harder component.  However, since the power law fits to the residual flux after the decline of the outburst were sometimes significantly better than the thermal bremsstrahlung fits (see Tables 6-4 a,b), this component will generally be discussed here in terms of power law fits for continuity and definiteness.

On the other hand, replacing the blackbody component with a power law or thin thermal bremsstrahlung component increased $x^2$ per degree of

freedom ($\chi_\nu^2$ ) from 0.9 to about 10. However a fit to the soft component equally as good as the blackbody was a Boltzmann distribution of the same temperature: $\frac{dN}{d\nu} \propto \nu^2$ exp (- h$\nu$/kT), corresponding to a classical hard sphere distribution. Such a distribution arises in a gas that is optically thin for free-free absorption but thick for electron scattering. The parameters of the Boltzmann fit over the 2-20 keV range were essentially unchanged from those of the blackbody fit, consistent with the fact that Boltzmann and Planck distributions of the same temperature deviate significantly only for h$\nu$ < kT. Thus the optically thick component could be a "grey body" with an emissivity less than 1, rather than a true blackbody.

Modified blackbody models, corresponding to the case where the electron scattering opacity is comparable to that of free-free absorption for at least part of the observed energy range, have been proposed to explain certain X-ray spectra, as discussed in Chapter III. For these models, as the electron scattering increases with increasing energy relative to absorption, the depth of penetration into the source and, thus the emissivity, decreases with energy. The resulting spectral forms (see Table 6-1) for two simple cases -- a homogeneous slab of emitting material (Shakura 1972; Felten and Rees 1972) and an isothermal exponential atmosphere (Zeldovich and Shakura 1969) -- give poor fits to the spectral data during the outburst ($\chi_\nu^2 \sim 2.3$ and 1.9, respectively, compared to $\chi_\nu^2 \lesssim 1$ for the blackbody or Boltzmann forms). However, the approximations used in deriving the spectral forms break down for kT $\lesssim 1$ keV, the regime of the outburst spectra. Thus, an energy-dependent spectral emissivity depressed from 1 may not be ruled out for the optically thick component. For definiteness, however, this component will generally

be discussed in terms of fits to a blackbody form.

As the source intensity varied, the relative contributions of the soft and hard components changed. Figure 6-2 shows an overlay of the incident spectra inferred from fits to the pulse height data for intervals C, D, E, and N (as defined in Figure 5-3). The blackbody component associated with the soft outburst of flux diminished as the intensity decreased, disappearing at the predicted transition. (For this observation, the term "transition" will subsequently refer to the final disappearance of the blackbody, coincident with the ephemeris transition at phase 0, rather than a precipitous decline of soft flux). The hard power-law component was fairly steady, constant to within about 50% before the transition and persisting at a comparable level after the cutoff of the soft flux. When the blackbody strength decreased by 20% (interval I), an acceptable fit to the pulse-height data required different amounts of absorption for the two components rather than the single joint value used when the blackbody was stronger. The column density for the hard component remained comparable to the interstellar value, while that for the blackbody component increased to ~ $10^{23}$ cm$^{-2}$ as the blackbody disappeared (see Figure 5-3d).

Prior to the transition, successive spectra could be fit by varying the strength of the blackbody component, the strength of the power-law component, and the amount(s) of absorption, keeping the blackbody temperature and power law number index fixed. The blackbody temperature was held at kT = 0.82 keV, the best fit value at the intensity peak (interval D), and the power law number index at 2.2, the best fit value for the intensity low prior to transition (interval J) where the power law dominates, as well as for the residual spectrum after the brief hard flare. These constraints on the temperature and power law slope minimize

Figure 6-2

This figure shows a superposition of incident spectra for intervals
before (C), during (D), and just after (E) the peak of the Cir X-1 outburst
covered by OSO.  Spectrum N, a "relaxed" spectrum after the hard flare,
indicates the contribution from the steadier component.  (The open circle
in the plot is a high point belonging to spectrum N.)  In the absence of
the blackbody component, strong narrow iron line emission at 6.5-6.7 keV is
evident, of 400-1000 eV equivalent width.  The data are consistent with the
number of line photons, ~ 0.004 photons $cm^{-2}$ $s^{-1}$, remaining constant
throughout the observation.  See Tables 6-2 and 6-4 and text for details of
spectral parameters.



CIR X-I OSO-8
INFERRED INCIDENT SPECTRA
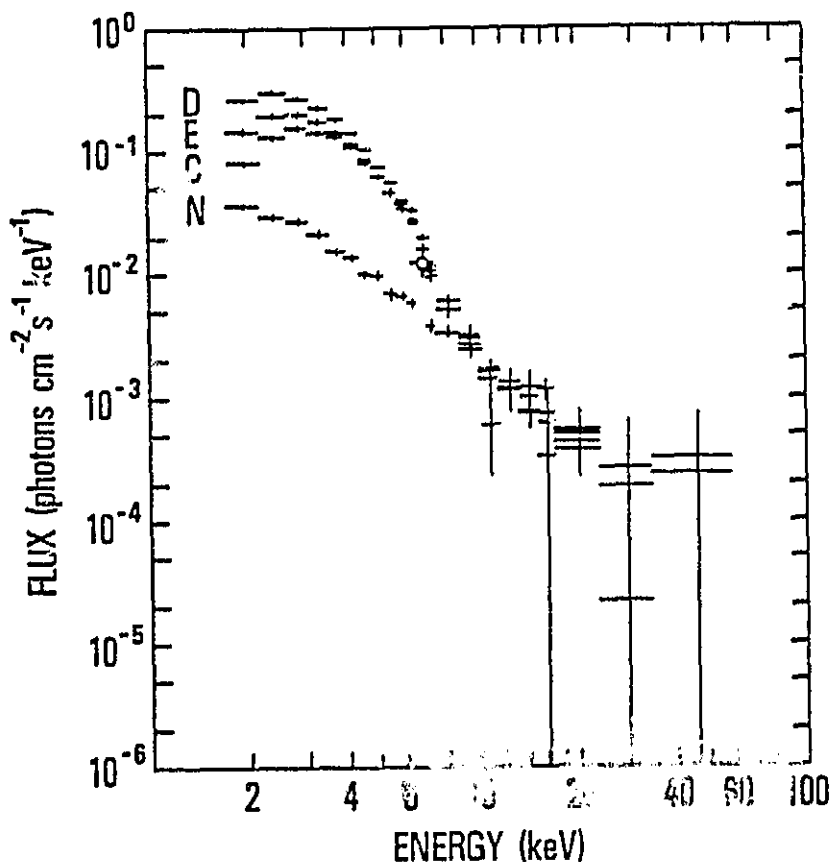
the number of free parameters in the succession of complex spectra without significantly altering the goodness of the fits from their best values when all the parameters are free, as shown in Table 6-2.

The change in intensity of the blackbody component, however, is also compatible with a change in temperature. From the intensity peak (interval D) to the intensity low prior to transition (interval J), the blackbody strength decreased by a factor of ~ 12, if the increased absorption is neglected. A value of kT = 0.4 keV, the 2σ lower limit to the best fit value for kT for interval J (see Table 6-2) could just account for the decrease in intensity.

During the pre-transition peak, the 2-6 keV source intensity showed chaotic fluctuations by a factor of 2 to 3 on a timescale of some tens of seconds. A sample of the observed rate on the ~ 10-sec satellite rotation timescale is shown in the upper left of Figure 6-3. Unlike the spectrally independent 10-20 sec fluctuations reported by Dower (1978), these variations show a strong correlation between intensity and spectrum, in the opposite sense to the longer term softening generally observed with increasing intensity for Circinus. One measure of this short term spectral hardening with intensity is shown in Figure 6-3, where the "softness ratio" of counts < 3 keV over 3-6 keV counts is plotted as a function of the 3-6 keV counting rate. To improve statistics, before the ratios were taken, the 10-sec PHA rates were sorted into 20 intensity bins on the basis of the observed 3-6 keV source strength. Note that this sorting procedure will not reveal spectral change which depends on the time history of the source flux; for example, it will tend to wash out any effect dependent on whether the local trend was increasing or decreasing. However, the strength of the effect apparent in the figure indicates that spectral change associated

## TABLE 6-2: SPECTRAL FITS BEFORE PHASE ZERO

### Parameters[1] for Model with Blackbody + Power Law + Narrow Line

| Interval | Blackbody kT(keV) | Power Law Photon Index $\alpha$ | Line Center E(keV) | Line E.W. (eV) Best Fit | Line E.W. (eV) 90% Conf. Limits | $\chi^{2[2]}$ Best Fit | $\chi^{2[3]}$ Constrained | $\Delta\chi^{2[4]}$ No Line |
|---|---|---|---|---|---|---|---|---|
| C | 0.83±0.03 | 1.4±0.7 | 6.0±0.2 | 260 | 110 - 420 | 61.6 | 63.0 | 8.7 |
| D | 0.82±0.01 | 1.9±0.3 | 6.1±0.1 | 160 | 110 - 210 | 49.8 | 51.4 | 23.1 |
| E | 0.82±0.02 | 1.8±0.5 | 5.9±0.2 | 150 | 50 - 250 | 68.7 | 69.3 | 6.1 |
| F | 0.72±0.04 | 2.9±0.4 | 5.9±0.2 | 410 | 160 - 690 | 65.5 | 69.8 | 7.8 |
| G | 0.75±0.06 | 1.8±0.9 | 5.7±0.2 | 530 | 210 - 910 | 60.9 | 64.6 | 8.4 |
| H | 0.80±0.02 | 2.0±0.5 | 6.1±0.2 | 220 | 90 - 360 | 53.9 | 55.8 | 8.3 |
| I | 0.79±0.03 | 2.9±0.2 | 6.2±0.2 | 190 | 70 - 330 | 51.6 | 53.0 | 17.2 |
| J | 0.7±0.2 | 2.3±0.1 | 6.3±0.1 | 510 | 350 - 690 | 50.9 | 52.4 | 31.6 |

[1]quoted errors are $1\sigma$ values within given model unless otherwise noted.

[2]intervals C through H have 51 degrees of freedom; I, J each have 50 due to an additional absorption parameter.

[3]quoted $\chi^2$ corresponds to best fit under constraints kT = 0.82 keV, $\alpha$ = 2.2; each "constrained fit" has 2 more degrees of freedom than corresponding "best fit".

[4] $\Delta\chi^2$ is increase in $\chi^2$ for best fit with no line present over best fit with line; fit without line introduces 2 more degrees of freedom since 2 line parameters are removed from fit.

Figure 6-3

The upper left figure gives a ~ 3000 second sample of the flickering from Cir X-1 observed during the peak of the outburst covered by OSO-8. The source intensity varies by a factor of ~ 2 from one 10-second bin to the next.

The upper right figure demonstrates the increasing spectral hardness with increasing intensity of the flickering. The data were sorted into 20 bins by the average intensity during one scan across the source as the satellite rotated. Across the x-axis, the intensity intervals are indicated over which corresponding PHA data were accumulated.

At the bottom, the average pulse height spectra (left) and corresponding inferred incident spectra (right) are shown for the upper and lower intensity intervals. Spectra for the two intermediate intervals show the same trend and were omitted for clarity. The increases in flux can be described as resulting predominantly from increases in temperature of a black body of slightly increasing size. The absorption of this component remains nearly constant during the peak (see Figure 6-4).

Figure 6-3



CIR X-I OSO-8  A DETECTOR
FLICKERING AT PEAK OF AUGUST 1976 OUTBURST
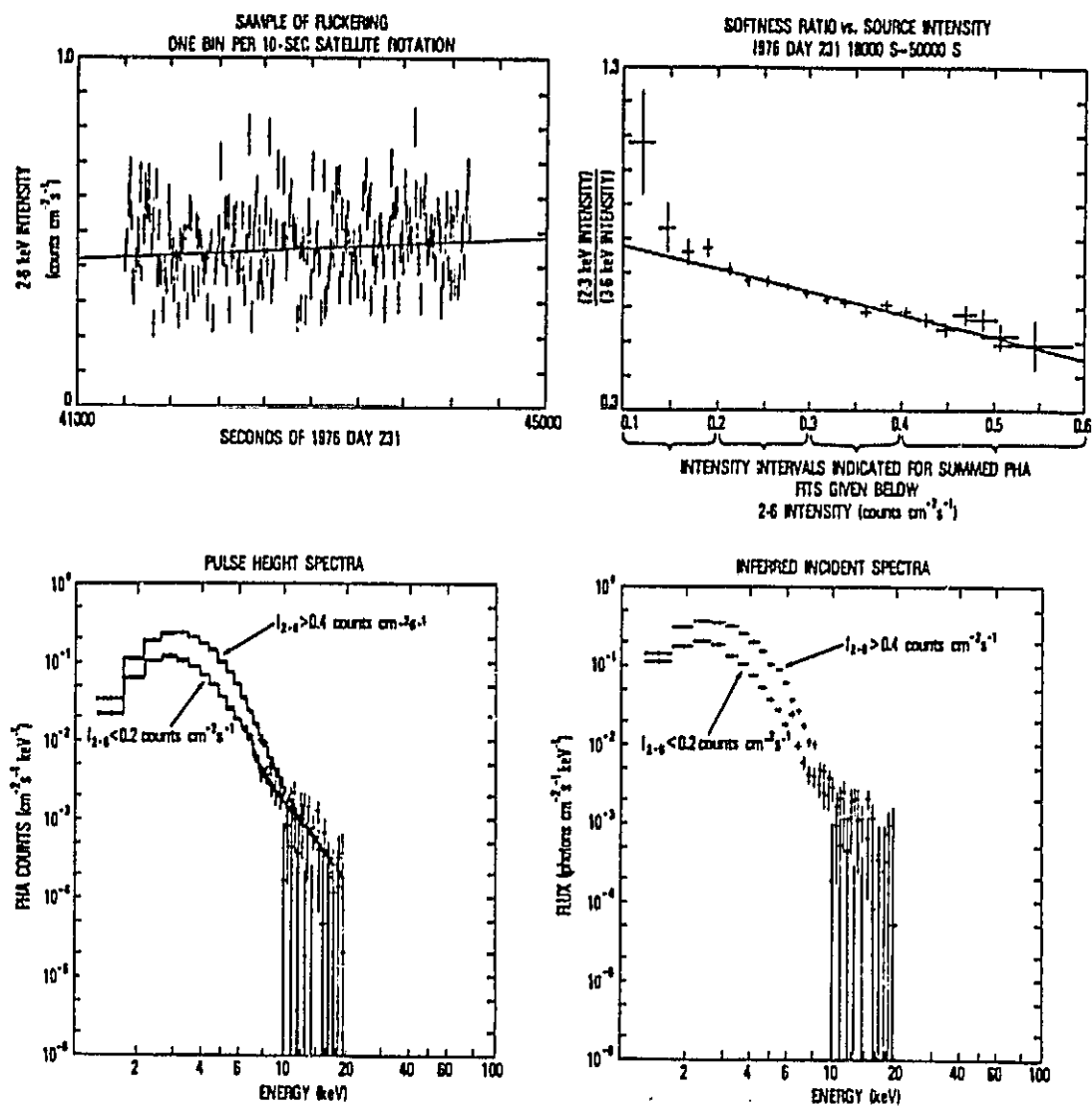
with absolute flux level dominates.

The 10-second 2-20 keV PHA histograms were sorted into four intensity bins by 2-6 keV counting rate (0.1-0.2, 0.2-0.3, 0.3-0.4, 0.4-0.6 counts $cm^{-2}$ $s^{-1}$) before spectral fitting. The histograms for the highest and lowest intensity intervals are shown in the lower left of Figure 6-3. The histograms for the two intermediate levels show the same trend and were omitted for clarity. The best fits for a spectral model with a (variable) blackbody plus a (fixed) power law plus a narrow iron line, all modified by a single absorption parameter (allowed to vary), are shown in Table 6-3. The corresponding inferred incident spectra for the highest and lowest intensity intervals are shown in the lower right of Figure 6-3. The results suggest that the increase in intensity can be explained as an increase in temperature for a blackbody of radius constant to within ~ 12% (35-40 km for a 10 kpc distance). (See the left half of Figure 6-4.)

b. After Transition

After the cutoff of the soft component at the transition, the residual flux briefly flared and hardened, coming to a peak (see interval L, Figure 5-3) about 5 hours after the predicted transition with a rapid decay of the high flux in about an hour and a slower decay of the remaining flux with a characteristic time of about a week. The continuum spectrum could be described by a power law which hardened to a photon index of 1.5 at the hardest, and then steepened again to 2.2 as the flare subsided. Alternately, the hard component could be fit by thin thermal bremsstrahlung spectra with kT of ~ 8.5-9 keV away from the hard flare, where the kT reached as high as 59±25 keV. These thermal fits were somewhat worse than the power law fits but generally acceptable or nearly so. Table 6-4 parts a and b list the parameters for these alternative models, which include an

TABLE 6-3: OSO-8 BLACKBODY FIT PARAMETERS*

For Intensity-Sorted 10-Second PHA Data During Flickering at Peak

| 3-6 keV Intensity Range (cts cm$^{-2}$s$^{-1}$) | Number of Entries[+] | 3-6 keV Aver. Rate ± Disp. (cts cm$^{-2}$s$^{-1}$) | $kT_{BB}$ (keV) | $Radius_{BB}$ (km)[++] | $L_{BB}$ (2-20 keV)[++] (ergs sec$^{-1}$) |
|---|---|---|---|---|---|
| 0.1 - 0.2 | 189 | 0.17 ± 0.08 | 0.72 ± 0.02 | 36 ± 2 | 2.4 10$^{37}$ |
| 0.2 - 0.3 | 607 | 0.25 ± 0.03 | 0.79 ± 0.01 | 35 ± 1 | 3.6 10$^{37}$ |
| 0.3 - 0.4 | 508 | 0.34 ± 0.03 | 0.82 ± 0.01 | 38 ± 1 | 4.8 10$^{37}$ |
| 0.4 - 0.6 | 170 | 0.45 ± 0.05 | 0.83 ± 0.01 | 42 ± 1 | 6.2 10$^{37}$ |

*Model: Blackbody of variable radius and temperature, narrow iron line emission feature of variable strength and centroid, variable joint absorption parameter for blackbody and power law components (corresponding hydrogen column densities of ~ 1.7 - 2.1 x 10$^{22}$ atoms cm$^{-2}$), power law component of fixed number index 2.0 and normalization 0.174 photons cm$^{-2}$ s$^{-1}$ keV$^{-1}$ (with a corresponding luminosity of 7.7 x 10$^{35}$ ergs sec$^{-1}$, for an assumed distance of 10 kpc). Quoted errors are 1σ values, except for the calculated dispersion on the rate.

[+] Number of ~ 2 second views accumulated in this intensity range.

[++] For a spherical emitter at 10 kpc, with an emissivity of 1.

Figure 6-4

Variations in the blackbody parameters during intensity fluctuations
of Circinus outbursts for the OSO-8 peak and the HEAO-1 onset are
compared. The OSO parameters are determined from PHA fits to data averaged
for ~ 2 seconds per 10-second satellite spin. The HEAO parameters are
determined from discovery scalar fits to intensity-sorted 5-second rates.

## CIR X-1 BLACKBODY FIT PARAMETERS
## FOR INTENSITY-SORTED SPECTRAL DATA

| AUGUST 1976 OSO-8 POINT: PULSE HEIGHT DATA FOR FLICKERING AT PEAK | AUGUST 1977 HEAO A-2 SCAN: DISCOVERY SCALAR DATA FOR FLUCTUATIONS IN EARLY OUTBURST |
|---|---|
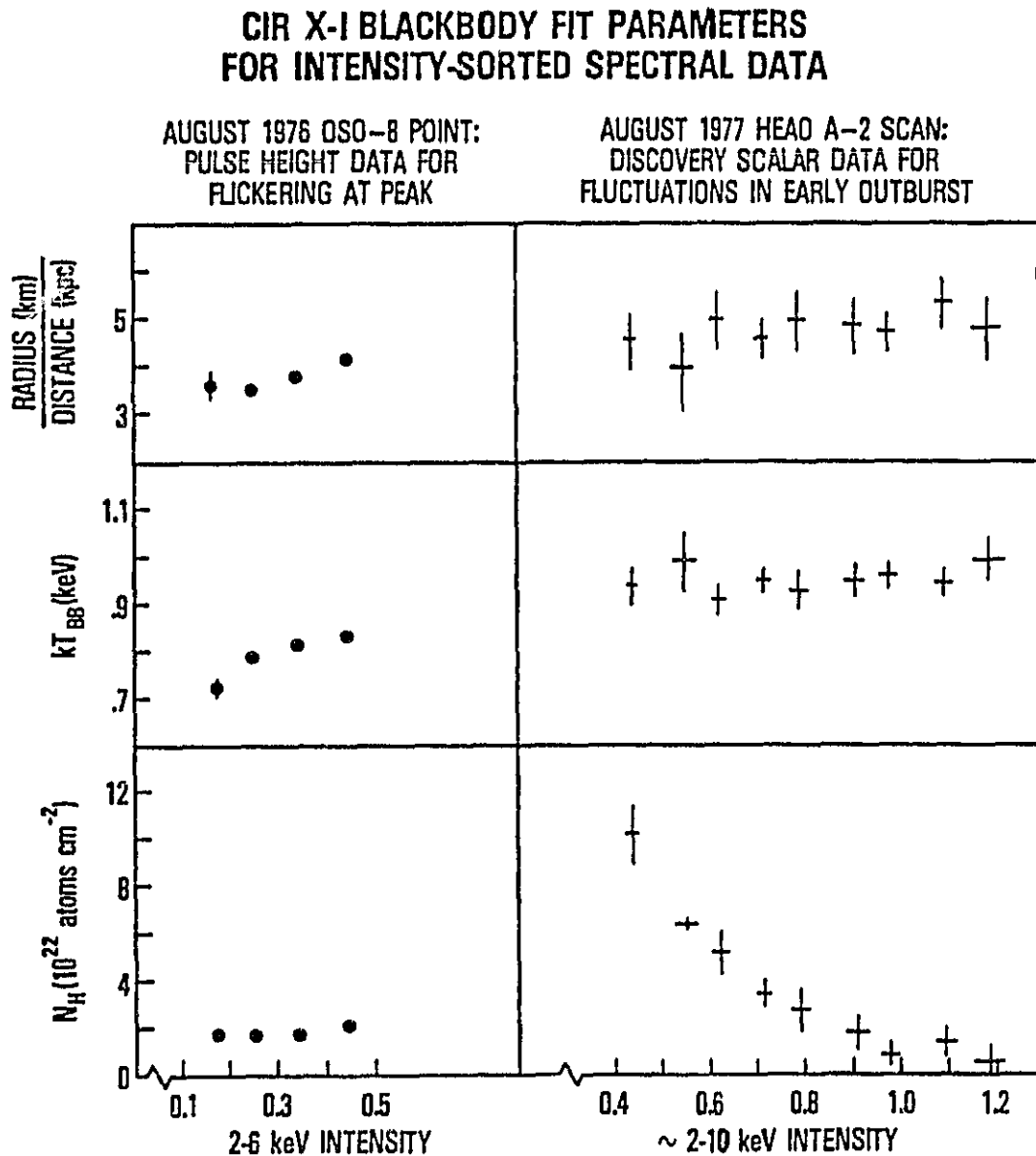
## TABLE 6-4: SPECTRAL FITS[1] AFTER PHASE ZERO

### a) POWER LAW MODEL

| Interval | Photon Index a | Line Center E (keV) | Line E.W. (eV)[2] Best Fit | 90% Conf. Limits | $x^2$ best fit (53 d.o.f) | $\Delta x^{2}$[3] no line best fit (55 d.o.f.) |
|---|---|---|---|---|---|---|
| K | 1.66±.05 | 6.5±0.1 | 530 | 340 - 590 | 66.0 | 30.8 |
| L | 1.54±.10 | 6.9±0.3 | 560 | 200 - 940 | 53.4 | 6.8 |
| M | 1.92±.08 | 6.8±0.4 | 420 | 170 - 590 | 44.6 | 7.7 |
| N | 2.25±.06 | 6.7±0.1 | 590 | 400 - 790 | 57.4 | 27.4 |
| O | 2.23±.08 | 6.7±0.1 | 820 | 590 -1060 | 64.4 | 37.6 |
| Q | 2.28±.04 | 6.5±0.1 | 840 | 710 - 980 | 75.5 | 130.7 |

### b) THERMAL BREMSSTRAHLUNG MODEL

| Interval | kT (keV) | Line Center (keV)[4a] Fit[2] / Predicted | | Line E.W. (eV) Best Fit[2] | Predicted[4b] | $x^2$ best fit (53 d.o.f.) |
|---|---|---|---|---|---|---|
| K | 30 ± 4 | 6.5±0.1 | 6.9 | 440± 90 | 100 - 180 | 83.4 |
| L | 60 ±20 | 6.9±0.3 | 6.9 | 520±250 | < 100 | 57.3 |
| M | 15 ± 2 | 6.8±0.3 | 6.8 | 480±250 | 420 - 600 | 46.9 |
| N | 8.8±0.7 | 6.7±0.1 | 6.8 | 370± 80 | 810 - 900 | 65.6 |
| O | 9.3±0.9 | 6.7±0.1 | 6.8 | 560±140 | 700 - 910 | 66.1 |
| Q | 8.4±0.4 | 6.5±0.1 | 6.8 | 630± 70 | 850 - 960 | 87.9 |

### c) TWO-POWER LAW MODEL, CONTINUUM FIT

| Interval | Steady Component[5] $C_{a_1}$ | $a_1$ | $N_{H_1}(cm^{-2})$ | Flare Component $C_{a_2}$ | $a_2$ | $N_{H_2}(cm^{-2})$ | $x^2$ (53 d.o.f.) |
|---|---|---|---|---|---|---|---|
| K | .36 | 2.2 | 1.44 $10^{22}$ | 0.014±0.008 | 0.9±0.2 | $(7±5)×10^{22}$ | 60.3 |
| L | .36 | 2.2 | 1.44 $10^{22}$ | 0.15 ±0.06 | 1.3±0.2 | $(5±2)×10^{22}$ | 53.4 |
| M | .36 | 2.2 | 1.44 $10^{22}$ | 0.09 ±0.11 | 1.9±0.5 | $(14±9)×10^{22}$ | 44.4 |
| N | 0.35±0.04 | 2.25±.06 | $(1.6±0.2)\ 10^{22}$ | --- | --- | --- | 57.4 |
| O | 0.32±0.04 | 2.23±.08 | $(1.7±0.3)\ 10^{22}$ | --- | --- | --- | 64.4 |
| Q | 0.29±0.02 | 2.28±.04 | $(1.8±0.2)\ 10^{22}$ | --- | --- | --- | 75.5 |

[1] Quoted errors are $1\sigma$ values within given model unless otherwise noted.

[2] Line errors are 90% statistical error limits within given model ($\Delta x^{2}$ = 2.7, with all parameters allowed to vary)

[3] $\Delta x^{2}$ is increase in $x^2$ for best fit with no line over best fit with line.

[4] Predicted thermal line parameters for collisional equilibrium from Raymond and Smith 1977:

a) Predicted line center is a weighting of lines from different ionization states.

b) Range in predicted E.W. corresponds to range in kT for thermal fit.

[5] Steady component was assigned representative fixed parameters during flare.

iron line emission feature near 6.5 keV. Histograms K, L, and M correspond to the flare times, with L covering the peak, while histograms N and O correspond to two successive half-day accumulations afterward. Histogram Q corresponds to a three-day accumulation during optimum conditions after a three-day gap when Circinus could not be as well isolated.

The post-transition flux data were also compatible with a slowly decaying component with low absorption (~ the interstellar value) and constant slope with the addition during the hard flare of a harder, variable component. Such a breakdown into two components is not unique, and the parameters of the additional flare component are poorly determined (though they are not consistent with the brief re-emergence of a blackbody component like that during the peak of the outburst). However, such a spectral model is probably a more natural one than a single component of variable slope for understanding spectral changes in the hard component near the transition. Even if the steady component should turn out to be due to some presently unknown source not related to Circinus (improbable on the basis of correlated SSS/MPC data discussed below), the hard flare just after transition is almost certainly due to Circinus. Table 6-4c gives representative parameters for an additional hard component during the flare, when the "steady" component parameters were fixed at power law number index $\alpha_N = 2.2$, a power law strength typical for this time, and absorption corresponding to the interstellar column density. Parameters for the "steady" component for intervals N, O, and Q are given for comparison. The strength and center of the line feature discussed below were not significantly altered in the two power-law model from the values of the single power-law model. The hard flare occurred during a one and a half day gap in quasi-simultaneous radio coverage at 6 cm. When radio

coverage resumed, the 6-cm flux density was ~ 1.0 Jy, compared to a pre-transition value of ~ 0.25 Jy, and gradually decayed over several days (Whelan et al. 1977). The X-ray flare may be related to the frequently observed post-transition radio flaring. This possibility is examined in Chapter VII.

A summary of the evolution of spectral parameters in the composite model (blackbody and power law) is shown in Figure 5-3c and d. For concreteness, the blackbody temperature and power law index were held fixed at kT = 0.82 keV and $\alpha_N$ = 2.2 before the transition (indicated by the vertical dashed line). Figure 5-3c a shows the inferred blackbody energy flux at earth neglecting photoelectric absorption. There was no evidence for the blackbody fit after transition -- inclusion of such a component did not improve the fit. For the combined spectral data of days 237-240 (interval Q), a 90% confidence upper limit to the blackbody flux was 8.5 x $10^{-11}$ ergs $cm^{-2}$ $s^{-1}$. Figure 5-3c also shows the unabsorbed 1-20 keV power law energy flux at earth. In this model the hard flux increased slowly as the blackbody subsided; then, after the hard flare, it decreased to about half its pretransition strength about 5 days after transition. Figure 5-3d shows the hydrogen column density inferred for the various spectra: a joint value for intervals C-H, separate values for the two components during intervals I and J as discussed above in (a), and a single value for the surviving hard component after the transition.

During the hard flare a single component fit to the continuum yielded a hydrogen column density not much greater than the interstellar value. However, in the two power law model, when the steeper component was fixed with the interstellar column density, the additional flatter component showed a column density as high as ~ $10^{23}$ atoms $cm^{-2}$.

The hatched region in Figure 5-3d applies to the average spectrum during the onset of the outburst. For the standard two-component model, it indicates the range of acceptable column densities for the blackbody component. The absorption of the other component, strongly coupled to the blackbody absorption, is not well determined, but is consistent with the interstellar column.

### c. Line Feature and Absorption Edge

All the data were consistent with the presence of a narrow line feature between 6 and 7 keV corresponding to 0.004 to 0.005 photons $cm^{-2}$ $s^{-1}$. Such a feature reduced the $x^2$ of the spectral fit by more than 17 in 7 out of 14 intervals (see Tables 6-2 and 6-4), with the data for the remaining intervals having considerably poorer statistics. The line was most significant for the spectrum accumulated over the 3 days of interval Q, shown in Figure 6-5, where including the line in the power law fit reduced $x^2$ by 130.7 for 53 degrees of freedom. Tables 6-2 and 6-4 show the variation in the equivalent width of the line, along with 90% confidence limits, for the intervals chosen. A constant value for the number of photons in the line is at least marginally consistent with the data ($x^2 <$ 19 for 13 degrees of freedom, implying a probability of > 0.10).

The best fit line energies for successive spectra with 90% confidence statistical errors are shown in Tables 6-2 and 6-4. There appears to be a systematic difference between the energy of the line before and after the transition. Before (intervals C-J), the weighted mean of the line energies is 6.11 ± 0.05 keV, while after (intervals K-O and Q) the value is 6.56 ± 0.04 keV. A comparison of nearly concurrent A detector and B detector observations of the strong thermal iron line emission from the supernova remnant Cas A during the same satellite epoch indicates that the absolute

Figure 6-5

Part a of the figure shows the pulse height spectrum accumulated for interval Q in Observation 1 when the source flux was low. The fit shown corresponds to a power law of photon index $\alpha_N \sim 2.3$, modified at low energies by an absorbing column density $N_H = 1.8 \times 10^{23}$ atoms $cm^{-2}$, comparable to the interstellar value, with the addition of a highly significant narrow emission line feature at 6.5 keV. The dip at $\sim 9$ keV may indicate greater structure in the spectrum, but its shape is not well fit by an absorption edge.

Figure 6-5



CIR X-1 OSO A DETECTOR AUGUST 1976
HISTOGRAM Q
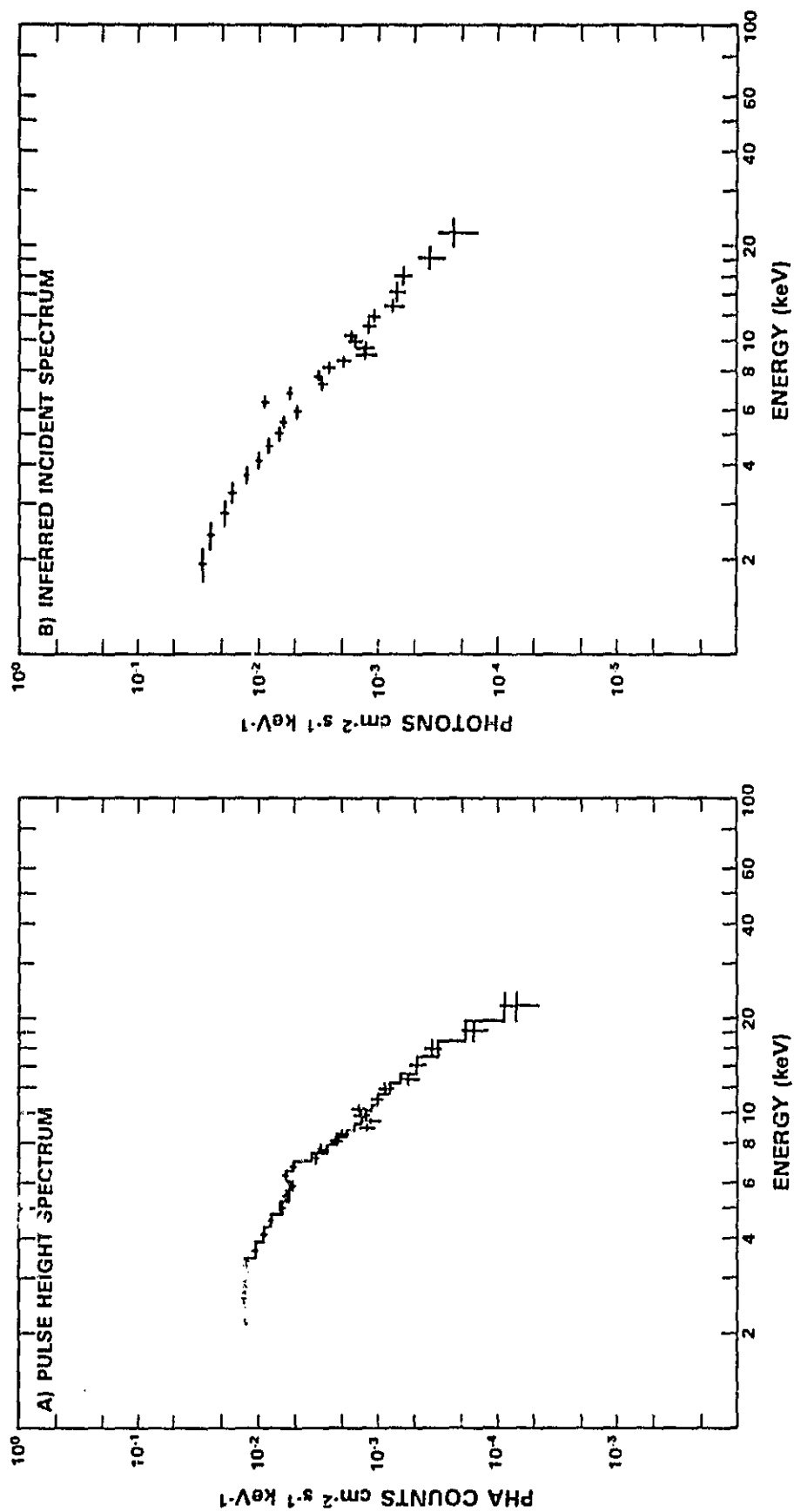
energy calibration of the A detector at that time might be low by ~ 0.05 keV. However, analysis of the Circinus data with a response matrix calibrated 50 days before the Circinus observation will tend to overestimate the line energy in the Circinus spectra by nearly the same amount due to the slow change in gain. Thus the net uncertainty in the line energy arising from the detector calibration is likely to be quite small. In any case, any such calibration offset should affect the line center determinations of all spectra in the same way.

One possible source of systematic differences in the line center before and after the transition is complexity of the pre-transition spectra beyond that implied by the spectral model. While the soft component is clearly not optically thin, it may not be a true (featureless) blackbody. For example, for the spectrum of interval D (which corresponds to the peak intensity and which has the best statistics for the soft component), a blackbody fit leads to a deficiency in observed counts between 7 and 8 keV, which contributes ~ 14 to the total $\chi^2$ of 50 for the fit (for 51 degrees of freedom). Inclusion of an absorption edge of the form $e^{-C}$ $(E_{edge}/E)^{2.7}$, with $C = 0.3\pm0.1$ and $E_{edge} = 7.1$ keV, reduces $\chi^2$ by 10 (significant at a level of > .99) and raises the line center from 6.1 to 6.3 keV. Such an edge implies an absorbing column density of iron amounting to $(8\pm3) \times 10^{18}$ atoms $cm^{-2}$, or, for a standard iron to hydrogen abundance ratio (Fe/H = 3.9 $\times 10^{-5}$), an equivalent hydrogen column density of $(2.0\pm0.6) \times 10^{23}$ atoms $cm^{-2}$. Since the inferred column density from the low energy spectral turnover was an order of magnitude less, this indicates that the ambient material near the X-ray source may be highly ionized during the outburst. While the presence of an absorption edge in the residual flux after the transition is not statistically significant ($\Delta\chi^2 = 2.6$ with the addition of

a two-parameter edge in the fit to Spectrum Q: C = 0.22 to 0.14, E ~ 8.5 keV), a comparable absorbing column of iron can be accommodated without substantial change to the line feature.

Some fraction of the line center discrepancy can also be attributed to the difficulty of fitting a line feature of low equivalent width located in a region of changing spectral slope. Such a situation occurs in these complex outburst spectra, where the soft and hard spectral components have a "cross over" region of comparable flux in the vicinity of the line. To estimate the magnitude of the line shift that might occur from this effect, a data simulation was performed. A model incident spectrum was chosen to match the best fit continuum spectrum during the outburst, with a narrow line feature of 0.005 photons $cm^{-2}$ $s^{-1}$ centered at 6.5 keV. This spectrum was binned in energy, with random Poisson errors assigned to each bin, then folded through the detector response matrix. The standard fitting procedure showed that the assigned line energy could be lowered by as much as 0.2 keV (90% confidence limit).

Thus, the total downward shift in the measured line center during the outburst could be ~ 0.4 keV; the preferentially lower energy of the line center when the blackbody is present, while suggestive (e.g., being the right order of magnitude for redshift near the surface of a neutron star), is probably an artifact of fitting a complex spectrum.

While the nonthermal continuum fit is not significantly preferred over the thermal fit except for histograms K and Q, the line feature appears inconsistent with equilibrium thermal emission from plasma at the measured temperatures (except for histogram M). Table 6-4b compares the measured 90% confidence range of the line centers and equivalent widths (E.W.) for thermal bremsstrahlung continua with values calculated by Raymond and Smith

(1977) for a condition of collisional equilibrium (for the solar number ratio Fe to H of $4 \times 10^{-5}$). The range in predicted E.W. comes from the uncertainty in measured temperature. The predicted line center is the effective energy of a blend of different ionization states expected in a plasma with the measured temperature. The high temperatures inferred for the flare histograms K and L predict much lower E.W. than measured, making (instantaneous) single temperature thermal equilibrium models during the flare less creditable. On the other hand, thermal fits to the relaxed histograms after the flare predict higher E.W. than measured. Also, histogram Q (with quite good counting statistics and little probability of contamination by other sources) indicates a somewhat lower energy for the line center than predicted. (The statistical 90% confidence upper limit to the line center is 6.6 keV, compared to the 6.8 keV value predicted. As noted above, the systematic error in the measured line energy from calibration uncertainties is probably small compared to 0.2 keV, and -- if anything -- would overestimate the inferred line energy.) The discrepancy between the measured and predicted line parameters suggests that a single isothermal plasma in collisional equilibrium is not the source of both the line and the entire continuum.

A standard alternative model to consider for line production is fluorescence from material in a lower ionization state than that expected for plasma with kT ~ 8-9 keV. We discuss in Chapter VII possible fluorescent contributions and conclude that such an interpretation is not sufficient either.

d. <u>The Nearby Supernova Remnant 4U1510-59</u>

Since the harder, more persistent component of the Circinus spectrum seen with the OSO-8 A detector is similar to one which might be

expected from some supernova remnants (thermal bremsstrahlung with kT ~ 8 keV plus a strong iron line), the possible contribution from the nearby source 4U1510-59, tentatively identified with the SNR MSH15-52 was a matter of some concern. With the finer collimation ($1°.5$ FWHM) available with the small field of view of the HEAO A-2 detectors, Circinus and 4U1510-59 could be separated. In observations during the first Circinus point (Observation 3), 4U1510-59 did in fact show a continuum similar to the harder Circinus component seen by the A detector in Observation 2, but, assuming the source strength is constant, it could account for at most 25% of the steady continuum flux.

The contribution to the Fe line feature should be less. The large field of view of the A-2 detectors ($3° \times 3°$ FWHM), which viewed both 4U1510-59 and Circinus during the point, had a smaller line E.W. (400 eV) than did the small field of view (600-800 eV) which excluded 4U1510-59. The large minus small fields of view, to which the contribution of Circinus was minimal, had a line E.W. of $150\pm130$ eV (1 sigma). The 90% confidence upper limit to this line E.W. is not tight: 580 eV for a thermal spectrum, 690 eV for a power law spectrum, but the corresponding limit on the line photons is $1.5 \times 10^{-3}$ photons $cm^{-2}$ $s^{-1}$. When 4U1510-59 is $\gtrsim 2°$ away from the collimator center of the OSO A detector during interval Q of Observation 1, this limit can supply less than 0.25 of the line photons assigned to Circinus.

The OSO C Detector point (Observation 5) shortly after the first HEAO point supports and refines this finding. The composite spectrum showed an iron line E.W. of $210\pm40$ eV. With the normalization factor taken from HEAO scanning rates, this implies a corresponding number of line photons equal to $(6\pm1) \times 10^{-4}$ photons $cm^{-2}$ $s^{-1}$ from both sources.

A HEAO-2 MPC observation of 1510-59 (with $1°5 \times 1°5$ FWFM collimation) shows a spectrum consistent with a featureless power law of number index 1.8±0.2, and a total 2-10 keV flux corresponding to ~ 6 U.F.U.  A simultaneous SSS observation with 6' collimation shows a 0.4-4.5 keV spectrum consistent with a power law of number index 1.7±0.2, with an extrapolated 2-10 keV flux of ~ 3 U.F.U, indicating the presence of additional flux from outside this region.

The inferred rates and spectral parameters for 4U1510-59/MSH15-52 from the OSO, HEAO-1, and HEAO-2 observations are summarized in Table 6-5.  The picture emerging from the combined results is that of a steady, extended featureless power law spectrum more similar to that of the Crab than to that of Cas A, possibly a synchrotron spectrum though a weak iron line cannot be ruled out.  The report by Seward et al. (1982) of a 150 msec X-ray pulsar at the position of the harder compact source increases the analogy with the Crab.

Observation 2:  HEAO Scan 0

On 1977 Day 239 (27 August), just prior to the onset at ~ phase 0.5 of the large, long duty-cycle outburst observed by HEAO 1, Circinus showed a flux of 20-25 R15 counts, comparable to the residual component in the first observation, but with a spectrum that was both much softer and much more absorbed.  Spectral fits (see Table 6-6) to 32-channel PHA for MED Layer 1 yielded a power law index of ~ 3.7 or a thin thermal bremsstrahlung kT of ~ 3.2 keV, with an equivalent hydrogen column density of 2-3 x $10^{23}$ atoms $cm^{-2}$.  Inclusion of a narrow line feature near 7 keV did not improve the fits, but showed that the line E.W. could be as high as 0.5 keV (with large errors), corresponding to a number of line photons about the same

TABLE 6-5: SUMMARY OF RESULTS FOR 4U1510-59/MSH 15-52

a) POWER LAW MODEL

| Observation | 2-10 keV Intensity | $C_{PL}$ photons cm$^{-2}$s$^{-1}$keV$^{-1}$ | $\alpha_N$ | $N_H/10^{22}$ atoms cm$^{-2}$ | $\chi^2$/def |
|---|---|---|---|---|---|
| 1. HEAO 1 Scaler Rates: | | | | | |
| a) Scan 1 | 10.0 ± 0.5 | 0.15 ± 0.04 | 2.2 ± 0.2 | 1.6 ± 0.7 | 4.5/5 |
| b) Scan 2 | 9.9 ± 0.7 | 0.09 ± 0.01 | 2.0 ± 0.1 | < 0.1 | 8.0/5 |
| 2. EINSTEIN SSS Points: | | | | | |
| a) 4U1510-59 | 3.0 ± 0.4 U.F.U. | 0.021 ± 0.004 | 1.7 ± 0.21 | 9 ± 1 | 46.4/57 |
| b) MSH 15-52 radio lobe centroid | 0.28 ± 0.05 U.F.U. | 0.006 ± 0.002 | 2.5 ± 0.3 | 1 ± 1 | 57.9/57 |
| 3. HEAO 1 Point 1 | | | | | |
| MEO L-R (norm from Scan 1) | | 0.09 ± 0.02 | 2.0 ± 0.2 | 0.9 ± 0.6 | 56.4/35 |

90% confidence upper limits:
E.W. = 685 eV
Line photons = 1.4 x 10$^{-3}$ cm$^{-2}$ s$^{-1}$
$\chi^2$ no line = 2.6

Line Parameters for best fit line:
Line center at 6.4 ± 0.4 keV
E.W. = 300 eV
Line Photons = 6.9 x 10$^{-4}$ cm$^{-2}$ s$^{-1}$

| 4. OSO 8 Detector Point | | | | | |
|---|---|---|---|---|---|
| at Cir X-1 + 4U1510-59 (norm from Scan 1) | | 0.10 ± 0.01 | 1.91 ± 0.04 | 0.6 ± 0.3 | 65.0/53 |

Line Parameters for best fit line:
Line center at 6.6 ± 0.1 keV
E.W. = 210 ± 40 eV
Line photons = (5.9 ± 1.2) x 10$^{-4}$ cm$^{-2}$ s$^{-1}$

b) THERMAL BREMSSTRAHLUNG MODEL

| $C_{TB}$ photons cm$^{-2}$s$^{-1}$keV$^{-1}$ | kT keV | $N_H/10^{22}$ atoms cm$^{-2}$ | $\chi^2$/def |
|---|---|---|---|
| 0.022 ± 0.002 | 10 ± 1 | < 0.1 | 6.4/5 |
| 0.021 ± 0.003 | 9 ± 2 | < 0.1 | 12.2/5 |
| 0.00925 ± 0.00249 | 6 ± 3 | 8 ± 1 (−0.7) | 45.1/57 |
| 0.0048 ± 0.0018 | 1.9 ± 0.6 | 0.3 (−0.3) | 58.6/57 |
| 0.018 ± 0.003 | 11 ± 2 | < 0.4 | 36.4/32 |

Line Parameters for best fit line:
Line center at 6.5 keV
E.W. = 230 eV
Line photons = 5.3 x 10$^{-4}$ cm$^{-2}$ s$^{-1}$

90% confidence upper limits:
E.W. = 590 eV
Line photons = 1.3 x 10$^{-3}$ cm$^{-2}$ s$^{-1}$
Predicted collisional equilibrium line
E.W. = 560 – 970 eV
$\chi^2$ no line = 2.7

| 0.120 ± 0.002 | 15.1 ± 0.4 | < 1 | 129/53 |

Line Parameters for best fit line:
Line center at 6.6 ± 3.1 keV
E.W. = 110 ± 20 eV
Line photons = (13.0 ± 0.6) 10$^{-4}$

Predicted collisional equilibrium line
E.W. = 450 – 550 eV
$\chi^2$ no line = 20

TABLE 6-5: CIRCINUS X-1 SPECTRAL FIT PARAMETERS FOR NON-OUTBURST TIMES

A) POWER LAW MODEL WITH IRON LINE FEATURE

| OBSERVATION | | PHASE* | SOURCE INTENSITY | $C_\alpha$ (photons cm$^{-2}$s$^{-1}$keV$^{-1}$) | $\alpha_N$ | $N_H$ ($10^{22}$ atoms cm$^{-2}$) | Line+ E.W. (eV) | Line Center (keV) | Best Fit Line Photons (photons cm$^{-2}$s$^{-1}$) | $\chi^2$/dof | $\Delta\chi^2$ no line |
|---|---|---|---|---|---|---|---|---|---|---|---|
| 1 | a) hard flare peak | 0.01 | 160 UFU | 0.31 ± 0.07 | 1.5 ± 0.1 | 2.0 ± 0.7 | 560 ± 200 | 6.9 ± 0.3 | 0.0087 | 53.4/53 | 6.8 |
|   | b) residual | 0.27-0.45 | 20 UFU | 0.28 ± 0.02 | 2.27 ± 0.04 | 1.8 ± 0.2 | 840 ± 120 | 6.5 ± 0.06 | 0.0033 | 74.7/53 | 130.7 |
| 2 | pre-outburst | 0.45 | 20-25 R15 | 16 ± 8 | 3.71 ± 0.09 | 26 ± 4 | 580 ± 390 | 7.0 ± 0.5 | 0.0048 | 37.1/18 | 1.8 |
| 3 | a) Low | 0.98-0.99 | 12 R15 | 1.0 ± 0.2 | 3.1 ± 0.1 | 4.2 ± 0.4 | 640 ± 120 | 6.7 ± 0.1 | 0.0017 | 56.9/44 | 28.4 |
|   | b) High | | 16 R15 | 0.35 ± 0.07 | 2.3 ± 0.1 | 2.85 ± 0.40 | 410 ± 120 | 6.6 ± 0.2 | 0.0018 | 31.3/44 | 12.7 |
|   | c) Burst | | 40 R15 | 1.70 ± 0.01 | 2.70 ± 0.07 | 4.9 ± 0.4 | 290 ± 70 | 6.1 ± 0.2 | 0.0058 | 46.7/44 | 15.4 |
| 4 | Scan average | 0.12-0.48 | 7 R15 | 0.3 ± 0.2 | 2.9 ± 0.4 | 1.8 ± 1.8 | (1800±1500) | (6.5) | 0.0019 | 1.6/4 | 3.5 |
| 5 | Cir X-1 +1510-59 | 0.07-0.38 | ~ 14 UFU | 0.10 ± 0.01 | 1.91 ± 0.04 | 0.6 ± 0.3 | 210 ± 40 | 6.6 ± 0.1 | 0.0006 | 65.0/53 | 23.8 |
| 6 | a) Average | -0.01-0.01 | 6 R15 | 1.9 ± 0.1 | 3.93 ± 0.04 | 6.5 ± 0.4 | < 600 eV | (7.0) | < 0.0004 | 43.8/33 | 0 |
|   | b) Before 0 | -0.01-0.0 | 6.5 R15 | 3.2 ± 0.9 | 4.4 ± 0.3 | 8 ± 1 | ~ 700 eV | (7.0) | | 35.5/31 | (-2.7) |
|   | c) After 0 | 0.0 -0.01 | 5.5 R15 | 1.1 ± 0.5 | 3.7 ± 0.3 | 6 ± 1 | 800 ± 40 | 7.0 | 0.0007 | 41.3/31 | 4.0 |
| 7 | Scan average | 0.30-0.70 | 4 R15 | 0.08 ± 0.02 | 2.3 ± 0.2 | < 1 | < 1500 | (6.5) | | 12.3/5 | 0 |
| 8 | a) | -0.01-0 | 6 UFU | 0.06 ± 0.01 | 2.0 ± 0.2 | 1.8 ± 0.4 | (< 500) | | | 58/41 | |
|   | b) Pre-flaring | 0.03-0.05 | 4-6 UFU | 0.0067±0.0003 | ~1 | < 1 | (≳ 400) | | | 72.7/41 | |
|   | c) Flaring | 0.06-0.07 | 10-20 UFU | 1.8 ± 0.6 | (2.5) | 27 ± 0.4 | (≲ 200) | | | 42/41 | |
| 9 | a) | -0.05 | 4 UFU | 0.064 ± 0.003 | ~ 2.7 | 3.1 ± 0.2 | (< 200) | | | 74.7/41 | |
|   | b) | -0.03-0.02 | 2-3 UFU | 0.080 ± 0.004 | 3.0 ± 0.5 | 3.4 ± 1.1 | (< 500) | | | 82.6/41 | |
|   | c) | 0.04 | 1-2 UFU | 0.011 ± 0.002 | (2.5) | 2.4 ± 0.3 | (≲ 1250) | | | 49.9/41 | |
| 10 | Average | 0.99-1.00 | 2.5 UFU | 0.052 ± 0.005 | (2.5) | 2.7 ± 0.9 | (< 1000) | | | 58/41 | |

*Phase of 16.6 day cycle according to X-ray ephemeris of Kaluzienski and Holt 1977.

+Quoted line equivalent widths are 90% confidence limits unless enclosed in parentheses.

B) THERMAL BREMSSTRAHLUNG MODEL WITH IRON LINE FEATURE

| OBSERVATION | | $C_{TTB}$ (photons cm$^{-2}$s$^{-1}$keV$^{-1}$) | kT (keV) | $N_H$ ($10^{22}$ atoms cm$^{-2}$) | Line E.W. (eV) | Line Center (keV) | Best Fit Line Photons (photons cm$^{-2}$s$^{-1}$) | $x^2$/dof | $\Delta x^2$ no line | Predicted Line[**] E.W. (eV) |
|---|---|---|---|---|---|---|---|---|---|---|
| 1 | a) | 0.06 ± 0.01 | 60 ± 25 | 1.24 ± 0.50 | 520 ± 210 | 6.9 ± 0.3 | 0.0084 | 83.4/53 | | < 110 |
| | b) | 0.046 ± 0.003 | 8.4 ± 0.4 | 0.46 ± 0.13 | 620 ± 70 | 6.5 ± 0.1 | 0.0027 | 87.9/53 | 85.7 | 850 - 960 |
| 2 | | 0.7 ± 0.5 | 3 ± 1 | 18.2 ± 4.3 | 510 ± 450 | 7.0 ± 0.6 | 0.0042 | 36.4/18 | 1.3 | 1400 - 1700 |
| 3 | a) | 3.9 ± 0.5 | 3.5 ± 0.3 | 2.16 ± 0.25 | 620 ± 130 | 6.8 ± 0.1 | 0.0016 | 66.7/44 | 24.1 | 1700 |
| | b) | | 8 | | 320 ± 120 | 6.6 ± 0.2 | | | 8.2 | 960 |
| | c) | 1.26 ± 0.02 | 7.0 ± 0.5 | 3.29 ± 0.27 | 190 ± 70 | 6.1 ± 0.2 | 0.0041 | 53.0/44 | 7.7 | 1000 - 1200 |
| 4 | | 0.09 ± 0.03 | 2.7 ± 0.2 | 2.14 ± 0.92 | (1060 ± 810) | (6.5) | 0.0012 | 6.6/4 | 0.8 | 1550 - 1700 |
| 5 | | 0.120 ± 0.002 | 15 ± 1 | < 1 | 110 ± 20 | 6.6 ± 0.1 | | 129/53 | 20 | 450 - 550 |
| 6 | a) | 0.16 ± 0.04 | 2.2 ± 0.3 | 3.7 ± 0.6 | < 600 | (7.0) | | 39.7/33 | 0 | 1000 - 1500 |
| | b) | 0.26 ± 0.13 | 1.7 ± 0.3 | 6 ± 1 | ≈ 1170 | (7.0) | < 0.0005 | 35.0/31 | - 2.7 | 100 - 1000 |
| | c) | 0.11 ± 0.04 | 2.4 ± 0.3 | 3.2 ± 0.7 | 1010 ± 420 | (7.0) | 0.0007 | 41.4/31 | 5.0 | 1150 - 1650 |
| 7 | | 0.023 ± 0.006 | 5.4 ± 0.1 | < 1 | < 1400 | (6.5) | | 13.0/5 | 0 | 1100 - 1650 |
| 8 | a) | 0.020 ± 0.001 | (6) | 1.7 ± 0.1 | (< 500) | | | 50/41 | | 1300 |
| | b) | 0.020 | > 30 | ~1 | (≈ 500) | | | 83/41 | | < 130 |
| | c) | | 5-6 | | (≈ 200) | | | 52/41 | | 1300 - 1550 |
| 9 | a) | 0.014 ± 0.001 | 4 | 2.2 ± 0.1 | (< 100) | | | 61/41 | | 1700 |
| | b) | 0.015 ± 0.001 | 3.3 ± 0.1 | 2.3 ± 0.1 | (≈ 500) | | | 60.8/41 | | 1400 - 1650 |
| | c) | 0.0035 ± 0.0005 | 3.5 ± 0.5 | 1.9 ± 0.3 | (≈ 2000) | | | 48.4/41 | | 1700 |
| 10 | | 0.003 ± 0.001 | ~ 6 | (1-4) | (≈ 500) | | | 40/41 | | 1300 |

[**]Predicted thermal line E.W. for collisional equilibrium from Raymond and Smith 1977.

as for Observation 1. The spectrum could also be fit with a blackbody with kT ~ 1.5 keV and a somewhat lower column density (~ 7 $10^{22}$ atoms $cm^{-2}$). Inclusion of an iron line of 0.006 photons $cm^{-2}$ $s^{-1}$ (660 eV E.W.) at 6.5 keV increased the kT to 1.8 keV and reduced the column density to $\lesssim$ the interstellar value.) The power law and thermal bremsstrahlung fits imply the intrinsic (unabsorbed) intensity could be as high ~ 180 UFU, with a corresponding luminosity of 5 x $10^{37}$ erg $s^{-1}$ (for an assumed distance of 10 kpc).

During the periods of high flux which followed, Circinus reached a peak luminosity of $\gtrsim$ 2 x $10^{38}$ ergs $sec^{-1}$. The thermal and power law fits to the average spectrum gave values of temperature and photon index $\alpha_N$, consistent with the values for the day before the outburst, though the (average) absorption was much less for both models. The normalizations were also several times larger, so that the size of the source accessible to view was larger if the underlying spectra are the same. While the number of line photons the fits could accommodate was substantially higher, the equivalent width dropped, so that it was no longer consistent with that expected for thermal emission from a plasma with a kT of ~ 3 keV. A blackbody fit to the average spectrum gave a kT ~ 1.0 ± 0.1 keV and a column density < 4 x $10^{22}$ atoms $cm^{-2}$.

During the periods of high flux which followed, the efficiency-corrected count rate was very variable, even within a scan (Figure 5-6), as well as from scan to scan (Figure 5-5). To exclude the nearby sources and to see how the spectrum changed with the large variations in intensity, the six available 5-second discovery scalar rates (see Table 5-2) were studied. The sets of scalar rates were sorted into 10 bins on the basis of MED Layer 1 (L1) count rate (≈ total intensity for a

soft spectrum). The hardness ratio MED L1/MED L2A showed a clear trend of softening with increasing intensity.

The intensity-binned scalar rates were fit with three simple spectral models: blackbody, power law, and thin thermal bremsstrahlung, each modified by cold matter absorption. Some of the fits listed in Table 6-7 were not acceptable at the 90% confidence level. The poorness of the fits is likely a measure of greater spectral complexity, but the small number of degrees of freedom did not allow for a larger number of model parameters. The spectrum may have been inherently more complex, as in the first observation; it may have varied in some important way on timescales shorter than the 5-second binning time as the intensity underwent quasi-oscillations with a factor of 2 amplitude; or the spectrum may have depended on whether the flux was increasing or decreasing, as noted above for the OSO intensity-sorted PHA data.

A rough check on the influence of faster variability was provided by an intensity-sort of the 80-msec HED/MED hardness ratio. These data provide a monitor of faster temporal change at the expense of sensitivity to spectral change, and the large field of view used includes the possibility of bias by neighboring sources. Nonetheless, the ratio showed a clear trend of decreasing softness with increasing intensity consistent with that expected from the 5-second scalar accumulations. The possible spectral dependence on time history is restricted by a similar result for 80 msec data sorted separately for times (selected by eye during pronounced oscillations) where the trend in intensity change was primarily decreasing or primarily increasing. The softness trends with intensity for the two subsets and for the total data set were consistent.

Figure 6-6 compares the best-fit blackbody models for the maximum and

TABLE 6-7  HEAO SCAN 0: FITS TO SORTED 5-SECOND SCALAR RATES

(a) BLACKBODY MODEL

| BIN | $I_{2-10}$ ($10^{-9}$ erg cm$^{-2}$ s$^{-1}$) | $C_{BB}$ | $kT_{BB}$ (keV) | $N_H$ ($10^{22}$ atoms cm$^{-2}$) | $\chi^2_\nu$ |
|---|---|---|---|---|---|
| 1 | 3.7±0.4 | 4.8±2.8 | 0.80±.06 | 16±3 | 4.6/3 |
| 2 | 5.8±0.3 | 2.1±0.5 | 0.94±0.03 | 10±1 | 3.4/3 |
| 3 | 7.4±0.6 | 1.6±0.6 | 0.99±.06 | 6±2 | 5.9/3 |
| 4 | 8.3±0.3 | 2.6±0.6 | 0.91±.03 | 5±1 | 11.3/3 |
| 5 | 10.1±0.3 | 2.1±0.4 | 0.95±.03 | 3.4±0.6 | 9.1/3 |
| 6 | 11.5±0.5 | 2.6±0.6 | 0.93±0.04 | 2.7±0.8 | 3.6/3 |
| 7 | 13.2±0.5 | 2.4±0.5 | 0.95±0.03 | 1.7±0.7 | 7.5/3 |
| 8 | 14.6±0.4 | 2.3±0.4 | 0.96±.02 | 0.9±0.4 | 15.9/3 |
| 9 | 16.2±0.5 | 2.9±0.6 | 0.94±0.03 | 1.40±0.6 | 10.3/3 |
| 10 | 17.9±0.8 | 2.4±0.6 | 0.99±0.04 | 0.5±0.7 | 1.2/3 |

(b) POWER LAW MODEL

| BIN | $C_{PL}$ | $\alpha_N$ | $N_H$ ($10^{22}$ cm$^{-2}$) | $\chi^2_\nu$ |
|---|---|---|---|---|
| 1 | 6900±2000 | 6.1±0.1 | 30±2 | 7.3/3 |
| 2 | 2400±800 | 5.4±0.2 | 24±1 | 15.9/3 |
| 3 | 1100±200 | 4.9±0.1 | 18±1 | 11.7/3 |
| 4 | 1500±200 | 5.2±0.1 | 16±1 | 18.1/3 |
| 5 | 900±300 | 4.9±0.2 | 13±1 | 6.6/3 |
| 6 | 1100±100 | 4.9±0.1 | 12±1 | 7.0/3 |
| 7 | 1000±400 | 4.9±0.2 | 11±1 | 7.7/3 |
| 8 | 800±200 | 4.7±0.2 | 10±1 | 3.9/3 |
| 9 | 1300±300 | 4.9±0.1 | 11±1 | 3.4/3 |
| 10 | 1000±300 | 4.8±0.2 | 10±1 | 5.7/3 |

(c) THERMAL BREMSSTRAHLUNG MODEL

| BIN | $C_{TB}$ | $kT$ (keV) | $N_H$ ($10^{22}$ cm$^{-2}$) | $\chi^2_\nu$ |
|---|---|---|---|---|
| 1 | 70±30 | 1.4±0.1 | 23±3 | 5.5/3 |
| 2 | 29±8 | 1.8±0.1 | 16±1 | 7.2/3 |
| 3 | 30±9 | 2.0±0.2 | 12±2 | 8.2/3 |
| 4 | 30±7 | 1.7±0.1 | 10±1 | 13.1/3 |
| 5 | 24±4 | 1.9±0.1 | 8.0±0.6 | 5.9/3 |
| 6 | 29±7 | 1.8±0.1 | 7.2±0.9 | 4.5/3 |
| 7 | 26±6 | 1.9±0.1 | 6.1±0.7 | 5.2/3 |
| 8 | 24±4 | 2.0±0.1 | 4.9±0.5 | 6.5/3 |
| 9 | 32±6 | 1.9±0.1 | 5.7±0.6 | 4.5/3 |
| 10 | 27±7 | 2.0±0.2 | 4.9±0.8 | 1.8/3 |

Figure 6-6

To allow a study of spectral changes during the intensity fluctuations
of Observation 2 beginning on Scan 0 Day 240, the 5-second scalar rates
were sorted into 10 intensity bins and fit with simple spectral models.
The best fit blackbody models for the maximum and minimum intensity bins
are compared with the model for the OSO-8 peak spectrum (D).
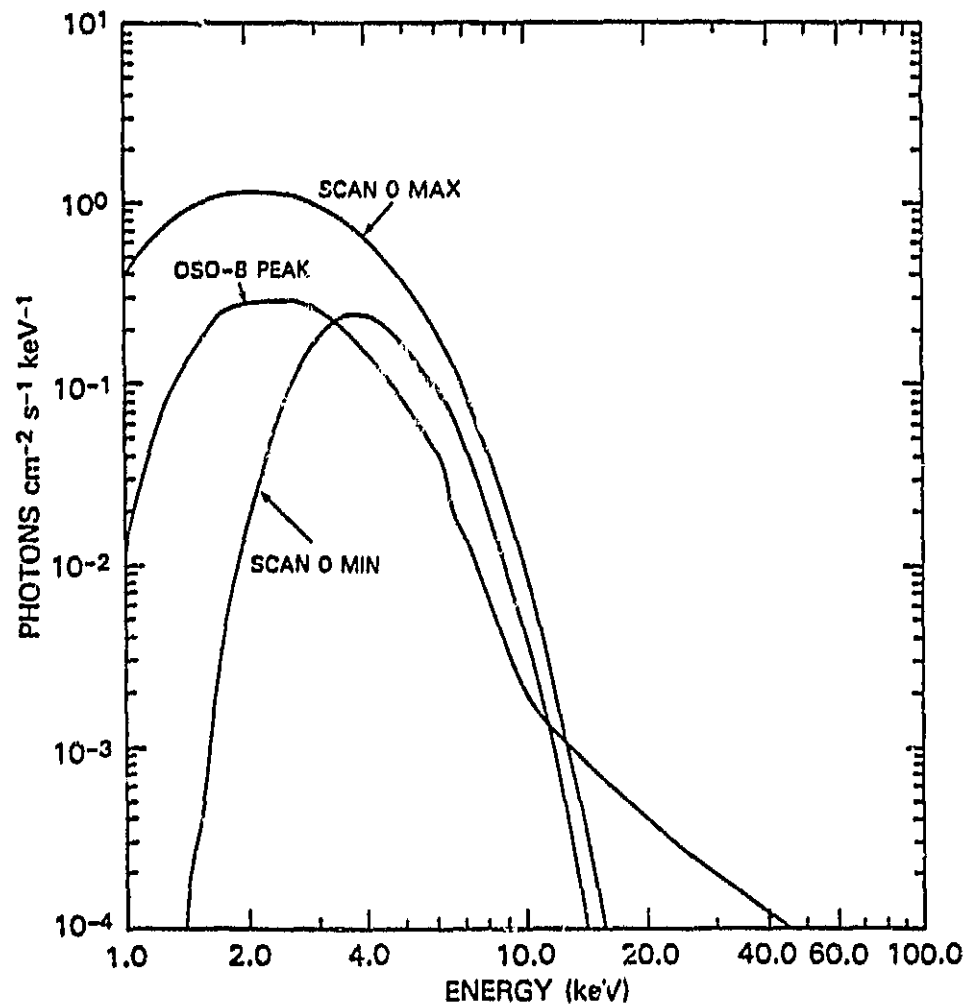
minimum intensity bins with the model for the OSO-8 peak spectrum (D). The temperature during the HEAO peak was higher (kT ~ 0.95 keV compared to 0.82 keV). The simple scalar fit models tend to ignore a low-level harder component such as that found for the OSO observation, in the presence of the large soft component.

Except for the lowest intensity bin (which was most apt to suffer from contamination by nearby sources, and for which any low-level harder component such as that seen in Observation 1 would be fractionally greater) the blackbody and thermal models gave fits where the temperature and normalization remained ~ constant, while the absorption parameter decreased with increasing intensity. For the power law model the bulk of the change was also in the absorption, but the normalization and power law number index showed a slight tendency to decrease with increasing intensity.

The high energy resolution spectral data was available only averaged over the variations within a scan. During several scans when the flux was high, the available 1.28-second rates indicated relatively small changes in flux within the scans. The 10-second accumulations of 32-channel PHA data overflowed the 8 bits/channel assigned for storage, but the correct accumulations were reconstructed from overflow flags to give an average high flux spectrum. The resulting MED and HED3 spectra were significantly better fit by a blackbody model than by bremsstrahlung or power law models. For the MED spectrum, with 23 degrees of freedom, from channel binning, the respective reduced $\chi^2$ values were 1.3, 2.0, and 4.5; for the HED3 spectrum, with 11 degrees of freedom, the values were 1.4, 2.5, and 5.

For the blackbody model, the kT for the two detectors agreed: 0.97±0.01 keV for the MED and 0.99±0.02 keV for HED3. The absorbing column densities, $(1.0\pm0.1) \times 10^{22}$ cm$^{-2}$ and $(2.0\pm0.1) \times 10^{22}$ cm$^{-2}$, respectively,

were not in agreement, but systematic errors for the HED3 measurement probably dominate the statistical errors. The inferred incident blackbody spectra for the two detectors are shown in Figure 6-7. There was no significant improvement in fit if a power law high energy tail was included. The flux in the 10-20 keV band is comparable to that during Observation 1. However a power law component of intensity comparable to that of the Observation 1 residual component would require an absorbing column density in excess of $10^{23}$ atoms $cm^{-2}$. These data show that the blackbody model is a better description when the flux is high. It is likely then that it is the preferred model for the varying soft component. The best fits to a constant value for the 9 highest bins of intensity-sorted scalar rates data gave a blackbody kT = 0.95 keV, a thermal bremsstrahlung kT = 1.9 keV, or a power law photon index = 5.0. For the blackbody fits the hydrogen column density ranged from ~ 2 x $10^{23}$ atoms $cm^{-2}$ to $\lesssim$ the interstellar value (~ 1.4 x $10^{22}$). The thermal bremsstrahlung fits showed nearly the same range, though the highest intensity bin showed a column density greater than 3 times the interstellar value. For the power law fit the highest intensity bin had such a high absorption ($N_H$ ~ $10^{23}$ atoms $cm^{-2}$) that the intrinsic (unabsorbed) peak luminosity implied was a factor of 5 higher (~ $10^{39}$ erg $s^{-1}$ at 10 kpc) than that observed directly.

In all three models, when the temperature or index was held fixed at this best fit value the normalization increased systematically with intensity, but the column density decreased faster. This effect was most pronounced for the blackbody (with factor of 8 change in column density versus a factor of 1.6 change in norm for a factor of 3 change in

Figure 6-7

Shown are the incident spectra inferred from peak intensity 10-second
accumulations of 32-channel PHA during Observation 2. The spectra are
better fit by a blackbody of kT ~ 1 keV then thin thermal bremsstrahlung or
power law models.



CIR X-1 HEAO A-2 SCAN 0
PEAK INCIDENT SPECTRUM
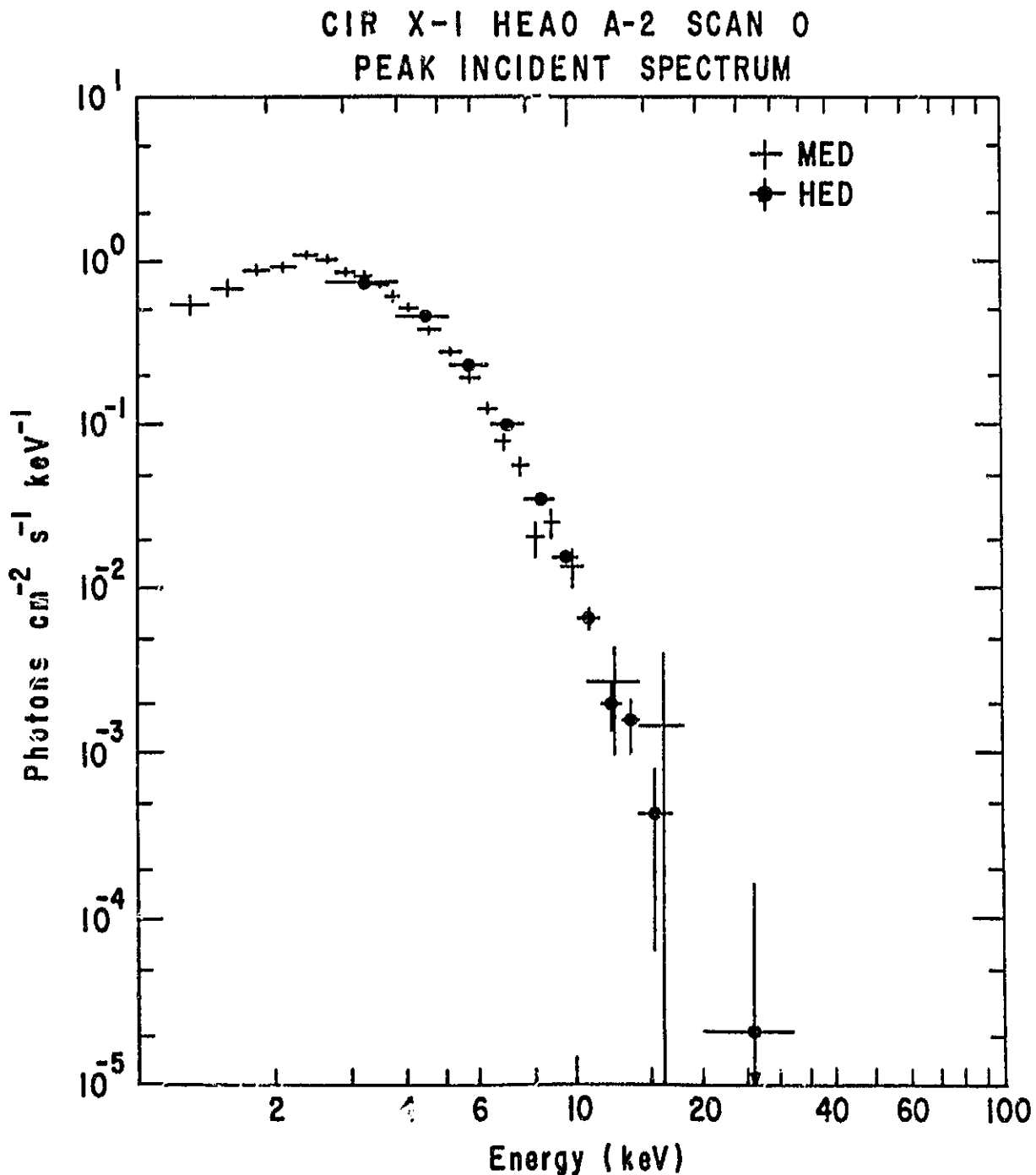
intensity) and smallest for the power law ($\sim 1.5 : 1$). The column density enters into the calculated intensity as an exponent: $\exp(-N_H \, \sigma(E))$, so the effect at low energies ($< 3$ keV) can be characterized as being due primarily to changes in the column density of intervening cold material, at least in these simple models.

The 32-channel data for which the blackbody model was preferred included the 5 highest intensity bins in Table 6-7. Since these encompass only a modest variation in column density, fitting the average spectrum with a simple model was a reasonable procedure and the results argue strongly for interpretation of the spectra as optically thick. The overall tendency during Observation 1 was also a softening of the spectrum as intensity increased, due to an increased contribution from the blackbody relative to the harder component, as well as to a decrease in cold-matter absorption. However for the 10-second intensity fluctuations during the "plateau" of that outburst, the spectrum hardened with intensity, consistent with a description in terms of an increase in blackbody temperature for the same effective source size and column density. In marked contrast with both results is Dower's (1978) report of a lack of major spectral change for the large, rapid intensity variations from SAS-3 coverage of the following cycle.

Figure 6-4 compares the change in blackbody fit parameters as the intensity fluctuates for Observations 1 and 2. There are differences in the two data sets which may be correlated with the different behaviors: the phase of the cycle (phase 0.95 vs. phase 0.5), the peak strength of the source ($\sim 4 \times 10^{-9}$ vs. $\sim 2 \times 10^{-8}$ erg cm$^{-2}$ s$^{-1}$), and longer-term average behavior. In particular, the OSO sample is taken from an approximate plateau, while the HEAO sample is taken during a time of large erratic

hourly changes. However, for these two very different cases, the maximum blackbody size inferred is about the same -- ~ 40 km for a spherical emitter at 10 kpc.

## Observations 3-10:

The timing of the two HEAO-1 and three HEAO-2 points at Circinus was intended to maximize coverage of interesting periods of behavior, to allow further study of spectral and temporal character and variability during times of outburst, to examine details of changes during the transitions and possible flares after. When it appeared that the source was changing its behavior in early 1979 (e.g. Kaluzienski and Holt 1979), with maximum flux occurring after phase 0 of the previous ephemeris, the times of the HEAO-2 observations were slipped accordingly. Unfortunately, the source was generally in a low state during the pointed observations and in the last two HEAO 1 scans, with insufficient flux for detailed studies of possible changes with the available collecting areas and detector sensitivities. Thus, except for the flares during the first HEAO 1 point and the first HEAO-2 point, only the average spectral character during the observations is presented. (For a synopsis, see Table 6-6.)

## Observations 3, 4, and 5: HEAO Point 1, Scan 1 and OSO C Detector Point

The first HEAO-1 pointed observation of Circinus showed behavior with some similarities to that observed during part of the OSO A Detector point: brief hard flaring after an early decline, the presence of strong iron line emission. However, the duration of the flaring was shorter (minutes instead of hours), the overall flux level was lower, and the spectra were softer during this observation.

The lightcurve in Figure 5-7 shows, in addition to a brief flare or burst, regions of two levels of flux differing by ~ 30%. The 64-channel SFOV PHA data for these "low", "high", and "burst" times (marked in the figure) were accumulated separately. Parameters for power law and thermal bremsstrahlung fits to the MED spectral data are given in Table 6-6. The HED fits are similar. Simple blackbody fits to the data are quite unacceptable, with $\chi_\nu^2 > 2.5$ compared to $\chi_\nu^2 < 1.5$ for the power law and thermal models. The fits are not sensitive to the presence of an edge -- an edge did not improve the fit but equivalent hydrogen column densities $\gtrsim 10^{23}$ atoms cm$^{-2}$ could easily be accommodated.

Model incident spectra for the three flux levels are compared in Figure 6-8. The low flux spectrum is consistent with a power law of number index ~ 3 or thermal bremsstrahlung with kT ~ 3.5 keV, plus a narrow iron emission line at 6.6-6.9 keV with an E.W. of 600 eV, corresponding to ~ 0.002 photons cm$^{-2}$ s$^{-1}$ in the line. The expected iron line E.W. for a plasma with kT = 3.5 keV in collisional equilibrium is ~ 1700 eV, about a factor of 2 higher than the upper limit measured. The higher flux spectrum is flatter, with a power law photon index of 2.3 or a bremsstrahlung kT of 8 keV. The number of line photons is about the same, so that the E.W. is lower. The expected thermal emission E.W. also drops (to 960 eV), but remains well above the measured value (~ 300-400 eV). The burst spectrum has a continuum similar to that of the high flux spectrum. The number of line photons is 2-3 times higher, but the resulting E.W. is lower (200-300 eV), again much lower than the thermal equilibrium value ($\gtrsim$ 1000 eV).

The six-day HEAO 1 scanning observation which began two days after the point found the source about a factor of two weaker than during the low part of the point. Spectral fits (listed in Table 6-6) to the 8 available

Figure 6-8

Model incident spectra for the best power law fits to PHA data from Circinus during the two HEAO-1 A2 points. Spectra for Point 1 are shown for the intensity accumulations indicated in Figure 5-7. The average spectrum for Point 2 shows no evidence of the strong iron line emission found in Point 1.

CIR X-1 HEAO A-2 POINTS 1 AND 2
MODEL INCIDENT SPECTRA FOR PHA FITS
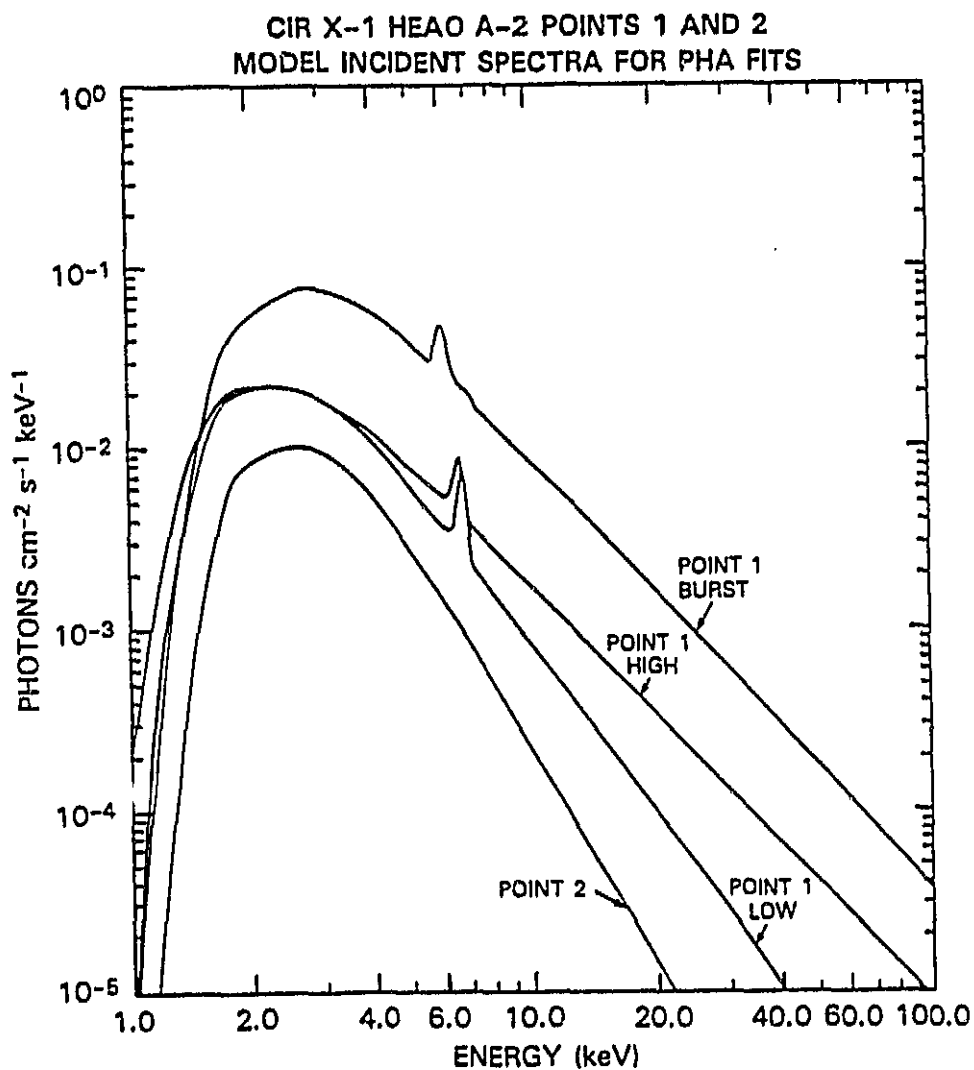
scalar rates (see Table 5-2) show a source continuum similar to that of the low flux spectrum.

## Observations 6 and 7:  HEAO Point 2 and Scan 2

The SFOV 64-channel PHA data accumulated for the entire point show an average spectrum somewhat steeper and more absorbed than the low flux spectrum from the first HEAO point.  Power law and thermal fit parameters are listed in Table 6-6.  Figure 6-8 compares the inferred incident spectrum with spectra from Point 1.  The fit was not sensitive to the presence of an iron line, but the upper limit to the E.W. was ~ a factor of 2 less than that expected (1000-1500) for a thermal equilibrium plasma at kT = 2-2.5 keV.

When the PHA data were accumulated separately before and after phase 0, 90% confidence contours in $\alpha_N$ or kT and $N_H$ overlapped.  However, the best fits (listed in Table 6-6) indicated that the spectrum after phase 0 may have been slighty harder, with the possible presence of a strong iron line.

Spectral fits to the 8 available scalar rates (see Table 5-2) during the six-day scan which began four days later when the source was weaker, showed a considerably flatter continuum with a best fit power law number index of 2.3, similar to the hard component in the OSO A detector observation, and to the high flux spectrum during the first HEAO point (see Table 6-6).  The column density for absorption was $\lesssim$ the interstellar value.  There was no evidence for strong iron line emission near 6.5 keV, though a good limit cannot be set with the poor fits.  The poorness of the fits may be due to the presence of strong nearby contaminating sources.

Observation 8:  HEAO-2 Point 1

During the first part of the first HEAO-2 point at Circinus, which
corresponded to the nominal outburst of soft flux, the flux level was
relatively low (~ 6 U.F.U.) and the spectrum was harder than the standard
outburst spectra.  Figure 6-9a shows the average SSS pulse height spectrum
for the first ~ 8000 seconds of the point.  Quasi-simultaneous SSS and MPC
spectra were consistent with a thin thermal bremsstrahlung fit with $kT \sim 6$
keV, or a power law fit with number index near 2, and a hydrogen column
density of $\sim 2 \times 10^{22}$ atoms $cm^{-2}$.  The best fit blackbody spectrum for the
MPC (with $kT \sim 1.3 - 1.4$ keV) implied a column density much less than the
interstellar value, and was not acceptable for the SSS data.  The inferred
incident spectrum for the combined SSS and MPC data is shown in Figure
6-9c.  As noted in the previous chapter, SSS spectral data for this
observation are only fit down to 1 keV due to difficulties in modeling the
ice accumulation parameter at this time.

After a slow decrease in flux across phase 0, but before the
commencement of flaring, the spectrum became quite hard.  The MPC showed a
number index of ~ 1 for a power law fit or a kT of $\gtrsim 30$ keV for thin
thermal bremsstrahlung, with little absorption.  These fits were
unacceptable for the SSS (which also showed a flat unabsorbed spectrum),
but none better could be found for reasonable ice and background
constraints, so the spectrum was likely more complicated.

Figure 6-9b shows the average SSS pulse height spectrum for the
intervals of MPC flaring which began about a day after phase 0.  The fit
shown, for a power law of number index 0 and a column density of $2.3 \times 10^{22}$
atoms $cm^{-2}$, is unacceptable ($\chi_{\nu}^2 > 2$), but demonstrates that the tail of the
spectrum is harder still if a single component model is used.  The inverted

Figure 6-9

Plot A shows the average SSS pulse height spectrum for data accumulated for the first ~ 8000 seconds of the first HEAO-2 point at Circinus, just prior to the nominal transition, though the flux level was relatively low. The inferred incident spectrum for the SSS is shown in plot C, along with a quasi-simultaneous MPC spectrum.

Plot B shows the average SSS pulse height spectrum for the intervals of MPC flaring which began about a day after the nominal transition. The fit shown, for a power law of number index 0 and a column density of 2.3 x $10^{22}$ atoms $cm^{-2}$, is unacceptable ($\chi_\nu^2 > 2$), but demonstrates that the tail of the spectrum is harder still (if a single component model is used).

The inverted spectrum is shown in Plot D, with two MPC spectra accumulated over times overlapping with the SSS data. All spectral models that give qualitatively good fits to the SSS data result in an upturn of the last three channels, an effect consistent with the MPC spectra shown. It appears that two components are present. A representative breakdown which gives a good fit is: a strongly absorbed power law component of photon index 2.5 which dominates the strongly fluctuating MPC data; and a flatter power law of photon index 1.0, modified by interstellar absorption, which dominates the steadier SSS data, except for the last three channels.

Figure 6-9

## SSS PULSE HEIGHT DATA
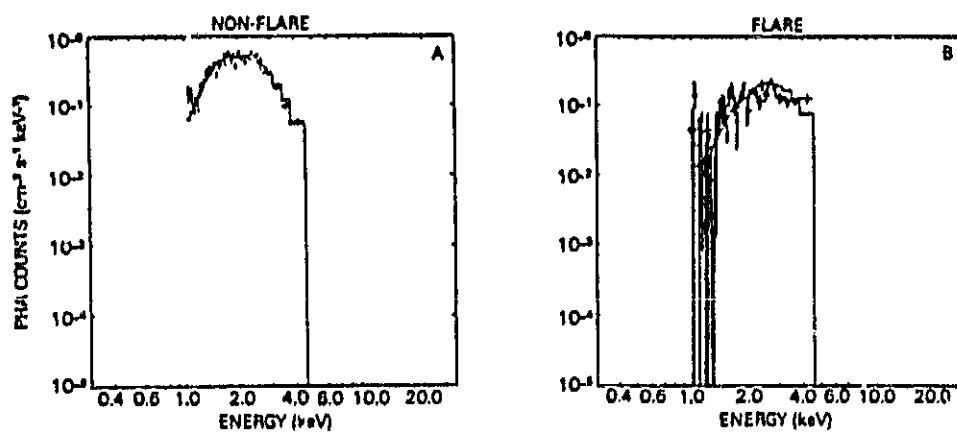


## SSS + MPC INCIDENT SPECTRA
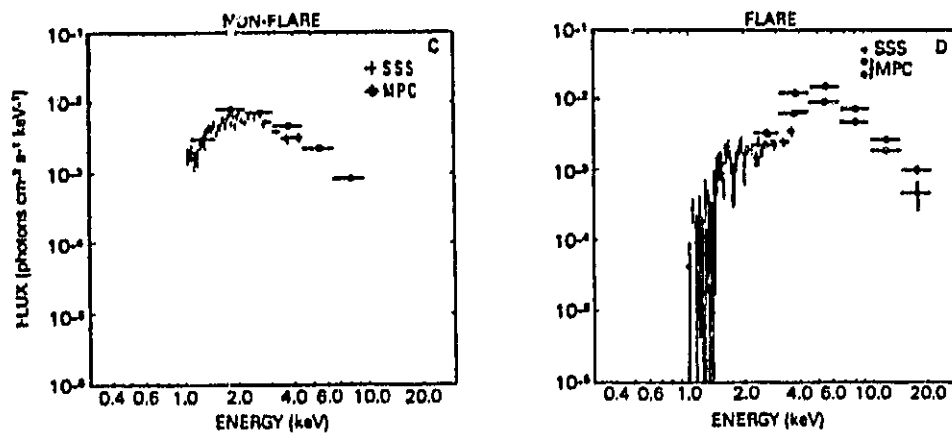
spectrum is shown in Figure 6-9d, along with two inverted MPC spectra deduced from pulse height data accumulated over times overlapping the SSS coverage. By themselves, the MPC data would indicate a large low energy cutoff. (For this plot only, MPC channels 1 and 2 are omitted, while channels 7 and 8 are included. The two lowest channels cannot be reliably inverted for heavily absorbed spectra, while the two highest channels, because of their high flux, do not suffer from their usual background problem.) All spectral models that give qualitatively good fits to the SSS data result in an upturn of the last three channels in the inverted spectrum, an effect consistent with the overlapping MPC data.

The joint SSS and MPC spectra indicate the presence of two components during the flaring -- a flat component modified by ~ interstellar absorption which describes the SSS data except for the upturn in the last three channels, and a heavily absorbed steeper component which dominates the strongly fluctuating MPC data. The agreement of the overlapping portion of the inverted SSS and MPC spectra and the relative steadiness of the SSS data during large changes in MPC flux (cf. Figure 5-12) lend weight to such an interpretation. A representative breakdown which gives a good fit is: a fairly steady power law component of photon index 1.0, modified by interstellar absorption ($\sim 1.4 \times 10^{22}$ atom $cm^{-2}$), and a highly variable power law component of photon index 2.5, with column density $\sim 3 \times 10^{23}$ atoms $cm^{-2}$. This very high column density implies that the intrinsic flaring source intensity could be about four times higher than that observed.

The spectral shape of the flaring component itself may be approximately constant, as shown by the similarity of the two inverted MPC spectra in Figure 6-9d, for two flux levels. The intensity-sorted MPC

hardness ratio (Ch 4-6)/(Ch 1-3) correlates very well with total MPC rate, as shown in Figure 6-10. However, the three lowest MPC channels lie in the domain of the steadier component, and without more precise simultaneity of MPC/SSS PHA accumulations, variations of the two components in the overlapping region are nearly impossible to decouple unless they are large.

This complex post-transition flare spectrum does not look much like the OSO-8 post-transition hard flare spectrum, as shown in Figure 6-11, where model incident spectra for the two are compared. However there are similarities: each may be described in terms of a heavily absorbed highly variable component plus an unabsorbed steadier component. The slopes of the respective components and their relative intensities do not match in the two cases. It is not possible to compare iron line emission near 7 keV for the two cases, since the MPC data are not sensitive to its presence, and any limits are complicated by the large absorption feaature expected nearby with such a large column density for the dominant flaring component.

## Observations 9 and 10:   HEAO-2 Points 2 and 3

For the second and third HEAO-2 Points, spanning the beginning and end of a 16.6 day cycle, Circinus was even weaker than at its minimum during the first point. Simple fits to the pulse height spectra for the SSS and MPC spectra were hard to match, with the SSS consistently showing higher temperatures and flatter power laws. A possible source of discrepancy is variability of the source during coverage by the two detectors that was not quite simultaneous. There was some evidence for occasional harder flaring shortly after phase 0 and near the end of the second point (corresponding to a flattening of $\gtrsim 0.5$ in index for a power law fit) and a softening with time in the third point (by as much as a one-unit steepening in power law

Figure 6-10

During the flaring observed with the MPC during the first HEAO-2 point at Cir X-7, the intensity increases occurred primarily in MPC channels 4-6 (corresponding to an energy band of ~ 3-10 keV), leading to an increasing hardness ratio, MPC (ch 4-6)/(ch 1-3), with increasing MPC count rate, as the figure demonstrates.

## HARDNESS RATIO SORTED BY 2.56 SEC INTENSITY
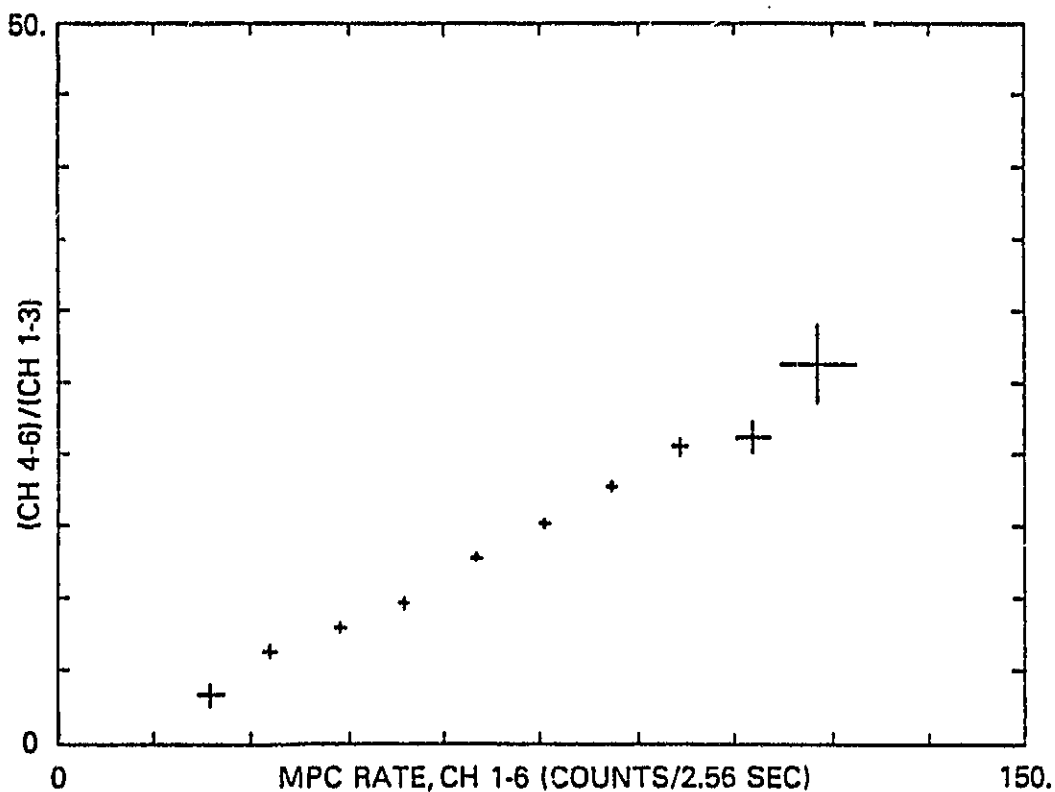
Figure 6-11

Model incident spectra are used to compare the HEAO-2 spectra of Circinus with each other and the hard flare from OSO-8.

The Point 1 and Point 2 "pre-transition" spectra were comparable to each other, so only one is shown for clarity. They were somewhat weaker than the ~ phase 0.1-0.5 average spectrum from the first HEAO-1 scanning observation. The Point 3 pre-transition spectrum was lower in intensity, the lowest reported in this work.
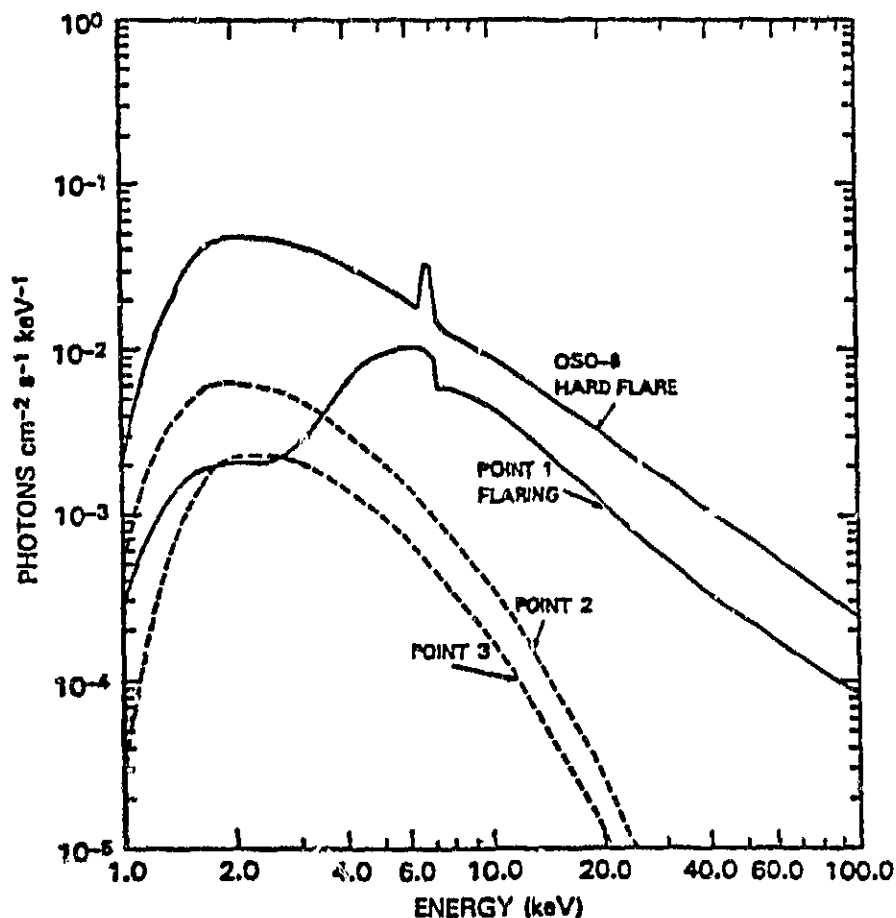
index or a decrease in temperature of 2 keV).

Because of the weak flux levels, the spectra from either detector separately were not considered reliable. Instead, since the MPC has a broader spectral dynamic range while the SSS has better low-energy coverage, the best fit slope or temperature from the MPC was folded through the SSS detector response to determine a value for absorption. If the two inverted spectra roughly agreed, the spectrum so generated was assumed at least qualitatively reliable.

Figure 6-12 shows the resulting spectra for average pre-phase 0 accumulations during the two points. Parts a and b show the SSS PHA data compared with the best "composite" fits, while parts c and d show the inverted spectra for both the SSS and the quasi-simultaneous MPC accumulation. The combined SSS and MPC data yield thin thermal bremsstrahlung fits with kT ~ 4 keV (Point 2) and 6 keV (Point 3), with hydrogen column densities of 1-2 x $10^{22}$ atoms $cm^{-2}$. Table 6-6 lists parameters for similar composite fits for SSS and MPC data at other times during the points. Upper limits to an iron line feature near 7 keV are taken from the automatic MPC fits supplied by Smithsonian Astrophysical Observatory. The model incident spectra corresponding to the Point 2 and Point 3 fits before phase 0 are plotted with dashed lines in Figure 6-11, for comparison to the Point 1 flare spectrum. The Point 2 intensity and the Point 3 shape are comparable to the corresponding parameters for the Point 1 spectrum before phase 0.

## B.   Cincinus X-1 - Temporal Studies

The previous section concentrated on average spectral properties of Circinus over several natural accumulation ti   'related to data mode

Figure 6-12

Plots A and B show the average "pre-transition" SSS pulse height spectra for the second HEAO-2 point at Circinus, eleven cycles after the first, and the third point during the following cycle. For the second point the flux was somewhat weaker than during the first, and the third point was weaker still.

Plots C and D show the respective inverted spectra along with MPC spectra taken during overlapping times.



SSS PULSE HEIGHT DATA
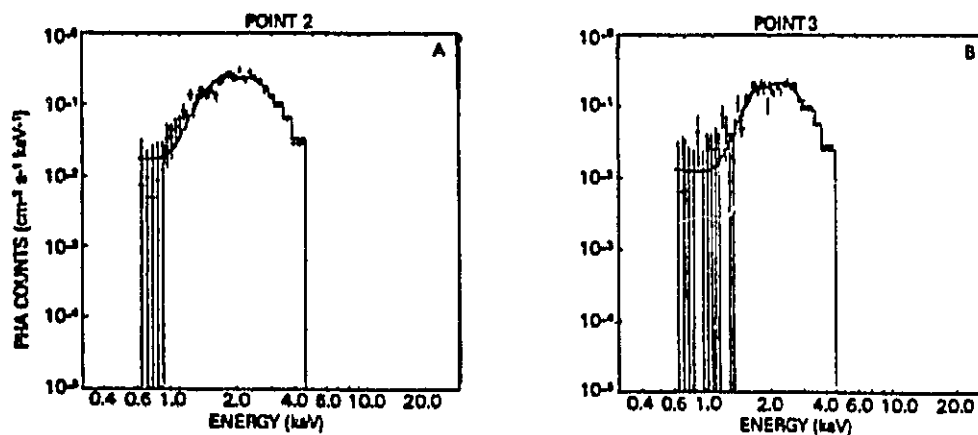
SSS + MPC INCIDENT SPECTRA
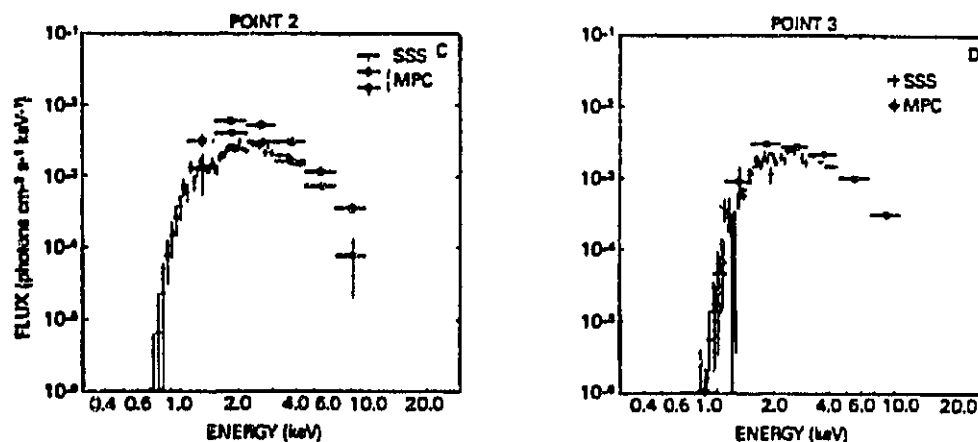
collection or observed changes in the source) and spectral changes associated with local changes in intensity. This section will emphasize studies of temporal structure and timing (relative, for example, to the cycle phase or presence of an outburst) of the events observed. Particularly in a highly variable source such as Circinus, the two discussions are necessarily somewhat coupled. Because of the generally weak flux during most of .the observations, making detailed studies of the temporal charcteristics of Circinus difficult with the available detector sensitivities, this section will address almost exclusively observations 1, 2, 3, and 9 (The OSO A Detector point, HEAO-1 "Scan 0", the first HEAO-1 point, and the first HEAO-2 point). Given the rather broad spectrum of behavior from the source, it is not always clear how to generalize from this sample of "snapshots". However, they do provide additional clues to the nature of Circinus and constraints on whatever picture of Circinus one wants to build, as shown in the following chapter.

## Observation 1: OSO A Detector Point

Possibly in keeping with the modest peak intensity, the outburst covered in this observation was also rather short in duration, with the peak lasting less than a day compared to the 3-5 days of larger outbursts. Data from 1976 Day 230 may indicate the presence of a "front porch" before the main outburst (refer to Figure 5-3b), possibly analogous to that reported for radio observations of Circinus (Murdin et al. 1980). If the effect is real and not the result of source confusion, it indicates a gradual buildup in flux of about a factor of 2 in a day. A similar but scaled up effect has been reported for larger X-ray outbursts (Kaluzienski et al. 1976). On Day 231 there was a more rapid increase, amounting to a

factor of 3 in ~ 2 hours, to the peak level. A downward sloping "plateau"
lasting ~ 3 x $10^4$ seconds showed chaotic fluctuations, with factor of 2
changes in intensity from 10-second spin to spin (see Figure 6-3), as noted
in the previous section. The autocorrelation function of this peak
"flickering" is flat (see Figure 6-13), with the only timescale greater
than the 10-second satellite spin period related to the slow decline of the
plateau. Timescales shorter than the ~ 2-second pass across the source can
be monitored with 160 msec rates data, and samples of this data in Figure
6-14 show structure on subsecond timescales. However, the individual
passes do not have sufficient statistics for autocorrelation analysis.
(For 12 bins of 160 msec data, the deviation from a straight line should be
at least as large as that implied by $\chi_\nu^2$ ~ 3 while a straight line fit to
the data gives only $\chi_\nu^2$ ~ 2.) Summing the passes to improve the statistics
washes out the variations, yielding only a characteristic timescale
of ~ 0.67 seconds, i.e. one-third the sampling time and hence suspect
(though visual inspection of some of the passes shows it could be a
timescale of interest). Possible structure at times between 2 and 10
seconds was not accessible to study because of the data sampling mode.

After the plateau, the flux gradually declined over ~ 12 hours, with
several broad dips and partial recoveries of 5-10 x $10^3$ seconds duration,
arriving at a low level of flux (~ 25 U.F.U.) half a day before phase 0
(again refer to Figure 5-3b). Shortly after phase 0, an episode of hard
flaring commenced, peaking ~ 5 hours after phase 0, then fading in about an
hour, leaving the residual component discussed in the previous section.
Though gaps in the data from earth occultation interfered with a careful
study of the flare structure, there was evidence of a broad "precursor"
flare before a narrow spike lasting ~ 5 minutes which reached a peak

Figure 6-13

The autocorrelation of the peak flickering during the OSO-8 outburst
is flat.   The only timescale greater than the 10-second satellite spin
period is related to the slow decline across the peak.



AUTOCORRELATION OF FLICKERING AT PEAK
2-6 keV FLUX, 10 SEC BINS
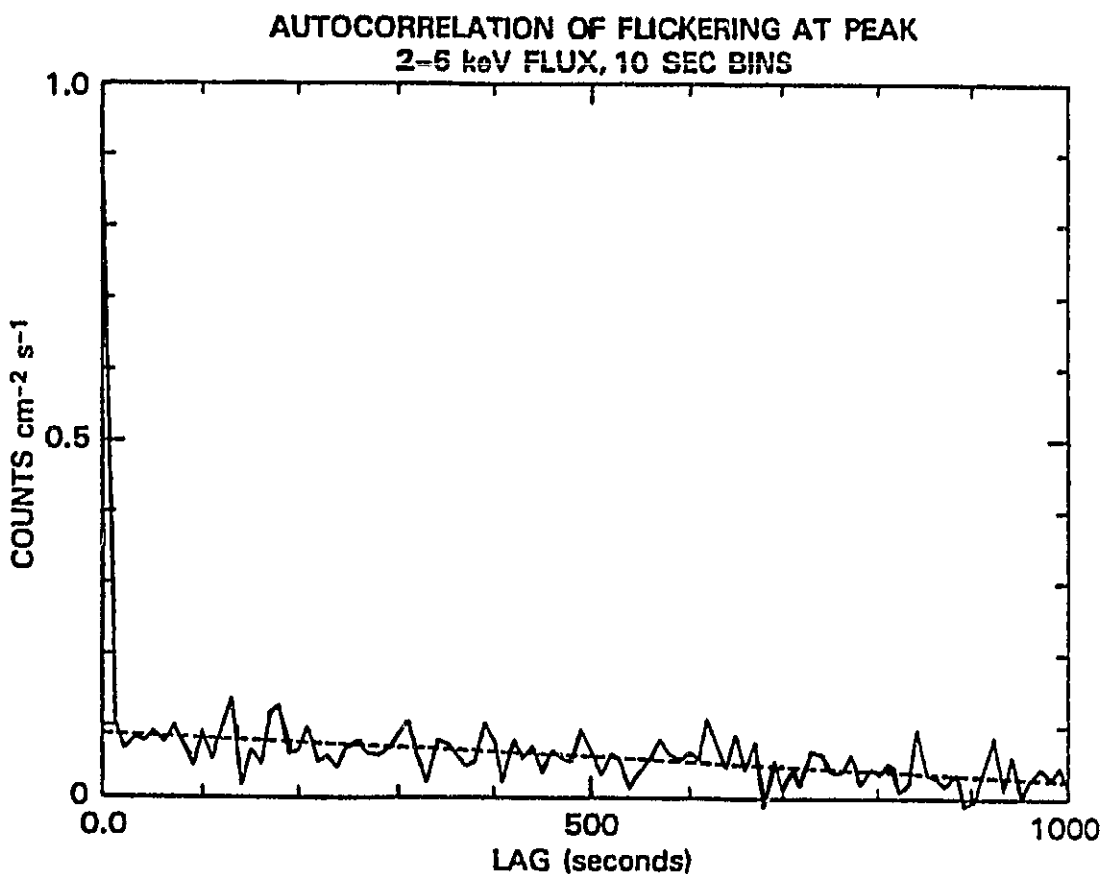
Figure 6-14

For the "flickering" at peak intensity in Observation 1, timescales shorter than the ~ 2-second pass across the source during each satellite rotation could be monitored with 160 msec rates data, and samples of this data in the figure show structure on subsecond timescales. However, the individual passes do not have sufficient statistics for autocorrelation analysis. Summing the passes to improve the statistics washes out the variations.



CIR X-1 OSO A DETECTOR AUGUST 1976
SAMPLE OF 160 MSEC RATES AT PEAK

MEAN = 0.54 COUNTS $cm^{-2} s^{-1}$
$\chi^2 = 121/59$ dof

$\leftarrow$10 SEC$\rightarrow$

COUNTS $cm^{-2} sec^{-1}$

2.4904 x $10^4$

2.4954 x $10^4$

SECONDS OF 1976 DAY 231
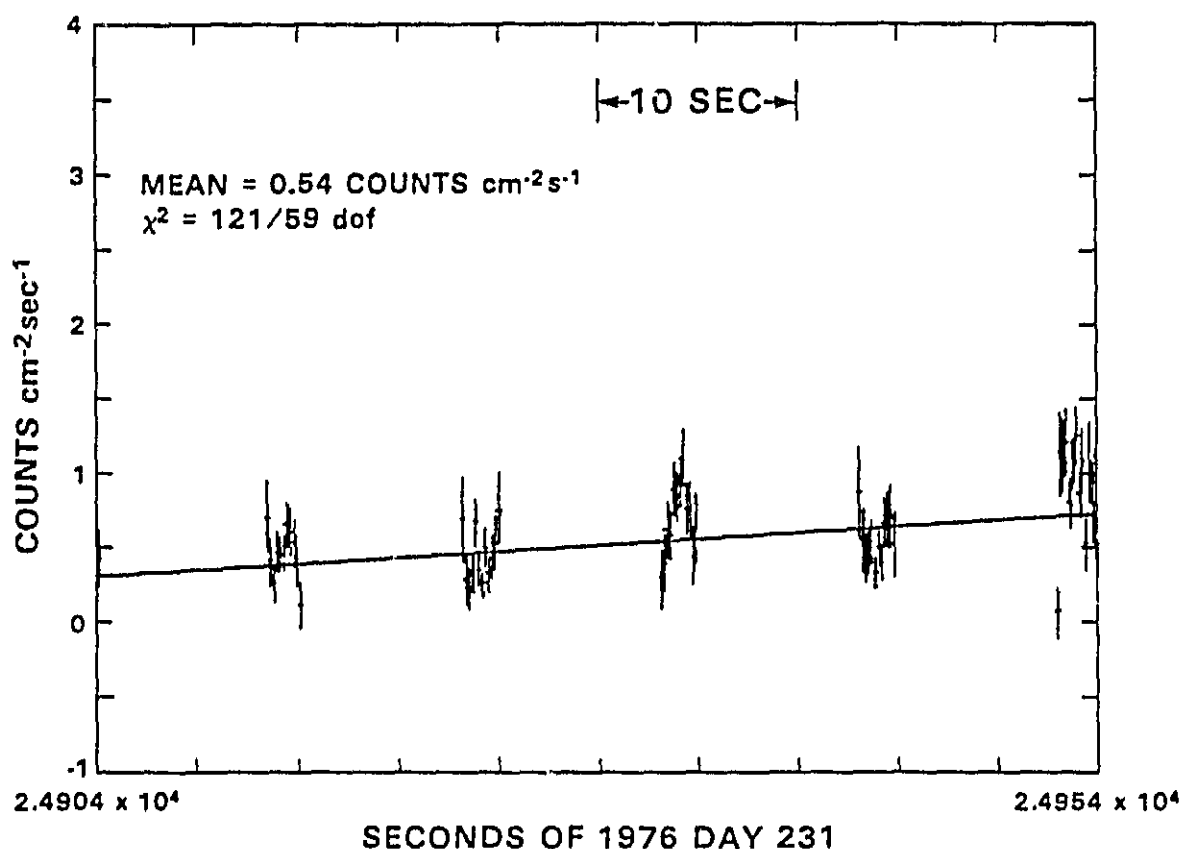
flux $\gtrsim$ 65 U.F.U. (see Figure 6-15). The timing of this flare shortly after phase O and the burst in the first HEAO 1 point just before phase O brings to mind post-transition radio flaring frequently reported, though the duration of the X-ray events is shorter than the radio timescales. As noted in the previous section, quasi-simultaneous radio coverage during the OSO point showed an increase in flux at 6-cm after phase O, though the onset itself was not observed due to antenna-switching at an inopportune time (Whelan et al. 1977).

Observation 2: HEAO 1 Scan O

The second observation of Circinus, covering the onset of a much larger, much longer duty-cycle ($\sim$ 0.5) outburst (refer to Figure 5-5) in scan mode, had much sparser data sampling than during the first observation, but longer contiguous stretches for examining behavior on timescales of a few seconds. The larger effective areas of the MED and HED3 (1600 $cm^2$ versus 263 $cm^2$) yielded better counting statistics for the subsecond structure revealed by 80 msec rates. As noted in the previous section, the intermittent coverage showed large fluctuations in average intensity from scan to scan, with increases in flux attributable to decreases in absorption. The 80-msec sampling showed structure within the scans on timescales of seconds or less, including quasi-oscillations of a few seconds, with rise times as short as 160 msec.

The first column of Figure 5-6 shows the best samples of these quasi-oscillations from four scans across the source on 1977 Day 240, when the effective detector areas were near maximum and the source remained in the field of view for several "cycles". The second column shows the autocorrelation function for each scan for lags up to 8 seconds, corrected

Figure 6-15

The figure shows an episode of hard flaring during Observation 1. It commenced shortly after phase 0, peaking ~ 5 hours after phase 0, then faded in about an hour, leaving a residual component as discussed in the text. Though gaps in the data from earth occultation interfered with a careful study of the flare structure, there was evidence of a broad "precursor" flare before a narrow spike, lasting ~ 5 minutes, which reached a peak flux $\gtrsim$ 65 U.F.U.



CIR X-1 OSO A DETECTOR AUGUST 1976
ASPECT-CORRECTED COUNTS NEAR
HARD FLARE IN 30 SECOND BINS
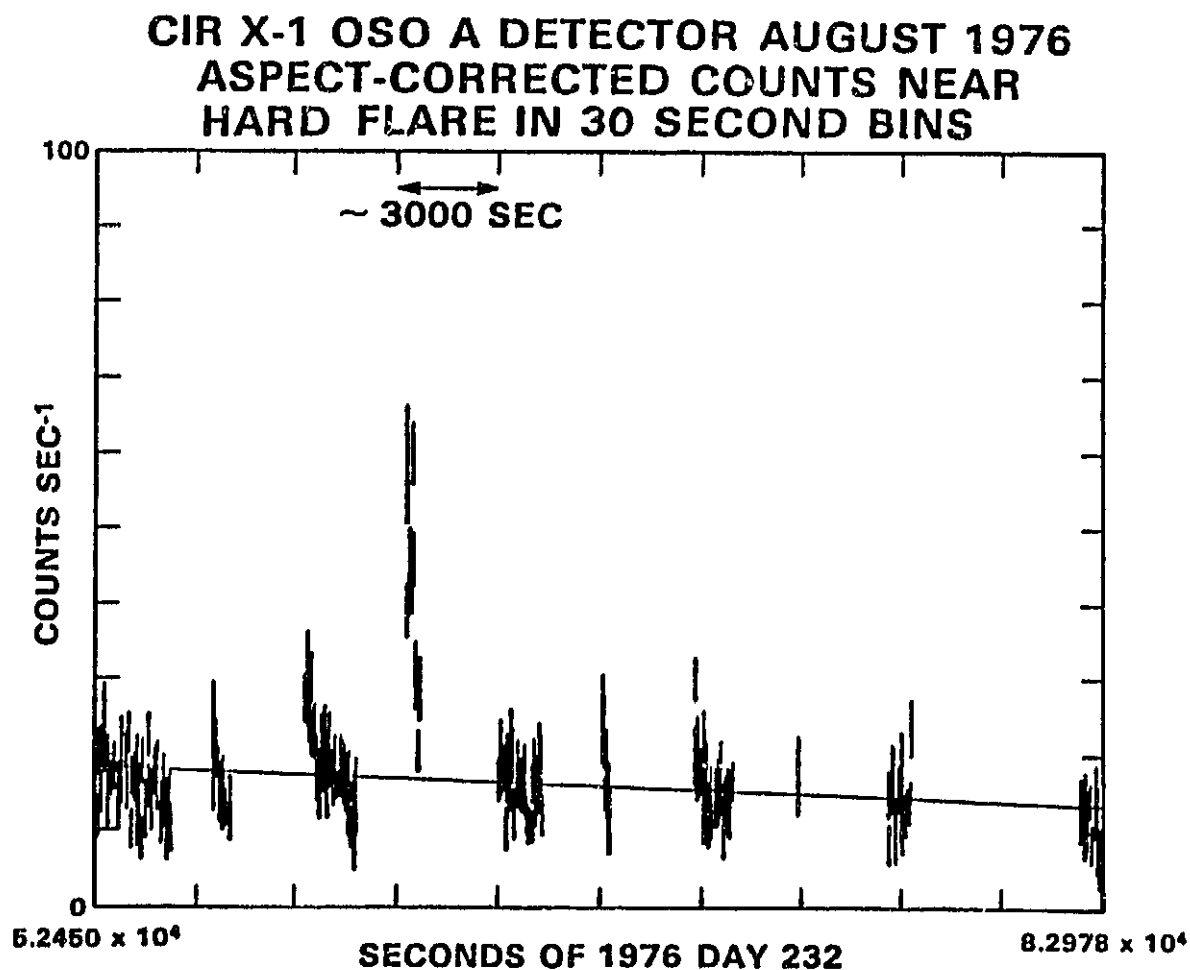
for photon counting statistics; the third column shows the logarithm of the respective autocorrelation functions, with representative fits to characteristic times for assumed exponential declines for short lags. The rapidly changing slope of the log of the autocorrelation function at small lags allowed large changes in the measured timescale for small changes in the fit interval. To provide some consistency in the fit procedure, an iterative process was used to select a fit interval comparable to the fit timescale, as suggested by Tennant et al. (1981).

In a shot noise description of fluctuations, the autocorrelation function at small lags will show an exponential decay if the underlying shots have the usually-assumed exponential form, while linear declines could be produced by rectangular shots. Table 6-8 lists the various relations between the shot parameters for both forms and the first three moments of the count rate distribution, assumed to be corrected for noise (cf. Dower 1978). Table 6-9a lists the moments of the count rate distributions for the four scans shown in Figure 5-6. Table 6-9b gives the decay times and shot parameters derived for assumed exponential shots, while Table 6-9c gives the corresponding values for assumed rectangular shots. The exponential decay times, of order 1-2 seconds, are assigned errors from varying the fit interval in the procedure noted above. The exponential parameters are listed for comparison with values quoted elsewhere for Circinus as well as Cygnus X-1. In fact, the autocorrelation functions are better described by linear declines from zero lag to the zero crossing points [refer to Figure 5-6, column 2; cf. Dower (1978)]. The timescales of these declines, not very different from the exponential fit values, may be associated with the peaks or troughs of the observed quasi-oscillations. Though the variance and third moment track roughly

TABLE 6-8.  AUTOCORRELATION AND SHOT NOISE DEFINITIONS AND RELATIONS

<u>Moments of count rate distribution:</u>

$\bar{S}$      = mean rate      $= \Sigma \; S_i W_i / \Sigma \; W_i$

$V_S$      = variance      $= \frac{1}{N-1} \; \Sigma (S_i - \bar{S})^2 \; W_i / \Sigma \; W_i$

$M_{3s}$      = third moment $= \frac{1}{N-1} \; \Sigma (S_i - \bar{S})^3 \; W_i / \Sigma \; W_i$

         where $W_i$ = weighting factor

             $= 1/\sigma_i^2 = 1/S_i$ for weighted moment

             $= 1$          for unweighted moment

<u>ACF</u>      = autocorrelation function $= \rho(u) = r(u)/r(0)$

$$\text{where } r(u) = \frac{1}{N} \sum_{i=1}^{N-u} \frac{(S_i - \bar{S})(S_{i+u} - \bar{S})}{\sigma_i \; \sigma_{i+u}}$$

<u>Shot Parameters:</u>   $T$ = time bin width
                       $\tau$ = correlation time
                       $h$ = shot amplitude
                       $\lambda$ = shot rate
                       $f$ = shot faction $= \lambda \tau \; hT/\bar{S}$

<u>Shot relations[*]</u> (for $T \ll \tau$):

Rectangular shots:                       Exponential shots:

$h(t) = h \; \theta(t) \; \theta(t-\tau)$             $h(t) = h \; \theta(t) \; e^{-t/\tau}$

$h$    $\simeq M_{3s}/(V_S T)$                $h$    $\simeq 3/2 \; M_{3s}/V_S T$

$\lambda$    $\simeq V_S^3/(M_{3s}^2 \; \tau)$            $\lambda$    $\simeq 8/9 \; V_S^3/(M_{3s}^2 \; \tau)$

$f$    $\simeq V_S^2/(M_{3s} \; \bar{S})$           $f$    $\simeq 4/3 \; V_S^2/(M_{3s} \; \bar{S})$

[*]from Dower (1978); $\theta(t)$ = Heaviside step function

## TABLE 6-9: HEAO 1 SCAN 0 80-MSEC RATES

### AUTOCORRELATION AND SHOT NOISE PARAMETERS

#### a) COUNT RATE DISTRIBUTIONS

| Data Set | Start Time Day | msec | No. of Points N | Mean Rate $\bar{S}$ (WTED/UNWTED) | Variance $V_s$ (WTED/UNWTED) | Third Moment $M_{3s}$ (WTED/UNWTED) |
|---|---|---|---|---|---|---|
| 1 | 240 | 06040835 | 328 | 0.36/0.49 | ?3/0.07 | 0.01/0.02 |
| 2 | 240 | 10122195 | 327 | 0.58/0.69 | 0.07/0.09 | 0.01/0.02 |
| 3 | 240 | 56451796 | 311 | 0.83/0.98 | 0.11/0.16 | 0.04/0.05 |
| 4 | 240 | 60530516 | 263 | 1.05/1.23 | 0.15/0.19 | 0.03/0.04 |

#### b) EXPONENTIAL SHOT PARAMETERS

| Data Set | Decay Time $\tau$ (sec) | Shot Amplitude h (ct $cm^{-2} s^{-1}$) | Shot Fraction f | Shot Rate $\lambda$ ($sec^{-1}$) |
|---|---|---|---|---|
| 1 | 1.4±0.1 | 0.4 | 0.4 - 0.7 | 0.3 - 0.6 |
| 2 | 1.1±0.2 | 0.3 | 0.9 - 1.0 | 1.6 - 2.8 |
| 3 | 1.5±0.5 | 0.5 | 0.5 - 0.6 | 0.4 - 1.1 |
| 4 | 1.8±0.5 | 0.2 | (> 1) | 1.9 - 3.4 |

#### c) SQUARE SHOT PARAMETERS

| Data Set | Zero-Crossing Time $\tau$(sec) | Shot Amplitude h (ct $cm^{-2} s^{-1}$) | Shot Fraction f | Shot Rate $\lambda$ ($sec^{-1}$), |
|---|---|---|---|---|
| 1 | 2.2 | 0.3 | 0.3 - 0.5 | 0.2 - 0.4 |
| 2 | 1.2 | 0.2 | 0.7 | 1.9 - 2.4 |
| 3 | 1.6 | 0.3 | 0.4 | 0.6 - 0.8 |
| 4 | 1.7 | 0.1 | 0.8 | ~ 2.9 |

with the mean count rate, the shot parameters do not seem to be correlated with intensity. With the shortness of the data streams, it is difficult to estimate the errors on the shot parameters; for a larger data sample, one could use the dispersion from scan to scan at a given intensity to assign errors. It is not clear whether the variations in the small sample available represent substantive changes or uncertainties in the determinations. The crudely determined shot parameters nonetheless imply a rather interesting regime, where one or two overlapping shots, lasting one to two seconds each contribute at least half of the observed intensity. The corresponding luminosity per shot is quite high, > $10^{37}$ ergs.

We have performed data simulations which show that quasi-oscillations roughly similar to those shown in Figure 5-6 can be produced by rectangular shots with parameters similar to those listed in Table 6-9c. Thus, the quasi-oscillatory appearance might be a manifestation of underlying shot noise behavior, as Boldt et al. (1975) suggested for Cygnus X-1.

## Other Observations Of Hard Flaring

Observations 1, 3, and 9 showed episodes of hard flaring from Circinus near phase 0 after a period of low flux. Of the three, only Observation 1 viewed the outburst as well, showing a peak flux and duration well below the largest seen from Circinus in other cycles, with a decline of the bulk of the flux about half a day early compared to the abrupt transitions seen in the larger outbursts.

## Observation 3: HEAO-1 Point 1

Ariel 5 All Sky Monitor coverage before Observation 3 showed that a small outburst occurred for that cycle as well, but the relatively low flux

level did not allow its shape to be well monitored by the ASM. In the brief view (~ 3 hours) allowed by the HEAO point after the outburst had subsided, the source underwent a 5-minute double-peaked flare with peak intensity ~ 85 R15 counts, again following a broader, less intense precursor (see Figure 6-16).

Observation 9: HEAO-2 Point 1

The flaring episode in Observation 9 may be a different phenomenon. Prior All Sky Monitor coverage does not clarify the existence of a preceding outburst with an early decline, and due to evolving source behavior over the years, phase assignment at the later epoch is more ambiguous. Nonetheless, the gradual changes in flux and hardness across phase 0 according to the standard ephemeris suggest that it still provides some fiducial point. If so, the flaring observed by the MPC began about a day after phase 0, considerably later than the flaring in Observations 1 and 3. Incomplete data coverage did not allow viewing of the onset or decay, but the character of the flaring also seems different for the later observation -- fairly chaotic fluctuations lasting at least four hours, with no obvious narrow spikes in intensity.

Three intervals of several hundred seconds of contiguous 2.5 second MPC rates data were available for autocorrelation analysis. The light-curves for the three intervals are shown in the left half of Figure 6-17. The right half of the figure shows the corresponding autocorrelation functions, corrected for photon counting statistics for lags up to 512 seconds. Fits to the logarithms of the autocorrelation functions for short lags (as discussed above) indicate possible characteristic exponential correlation timescales of ~ 54 seconds for the first interval and ~ 45

Figure 6-16

In the brief view (~ 3 hours) allowed by the first HEAO-1 point
(Observation 3) after the outburst had subsided, Circinus underwent a
5-minute double-peaked flare with peak intensity ~ 85 R15 counts, again
following a broader, less intense precursor. The figure shows the HED3
light curve during the flare time in 10 second bins.

# HEAO 1 A-2 POINT 1 FLARE

## 10 SECOND BINS



SECONDS OF 1978 DAY 48
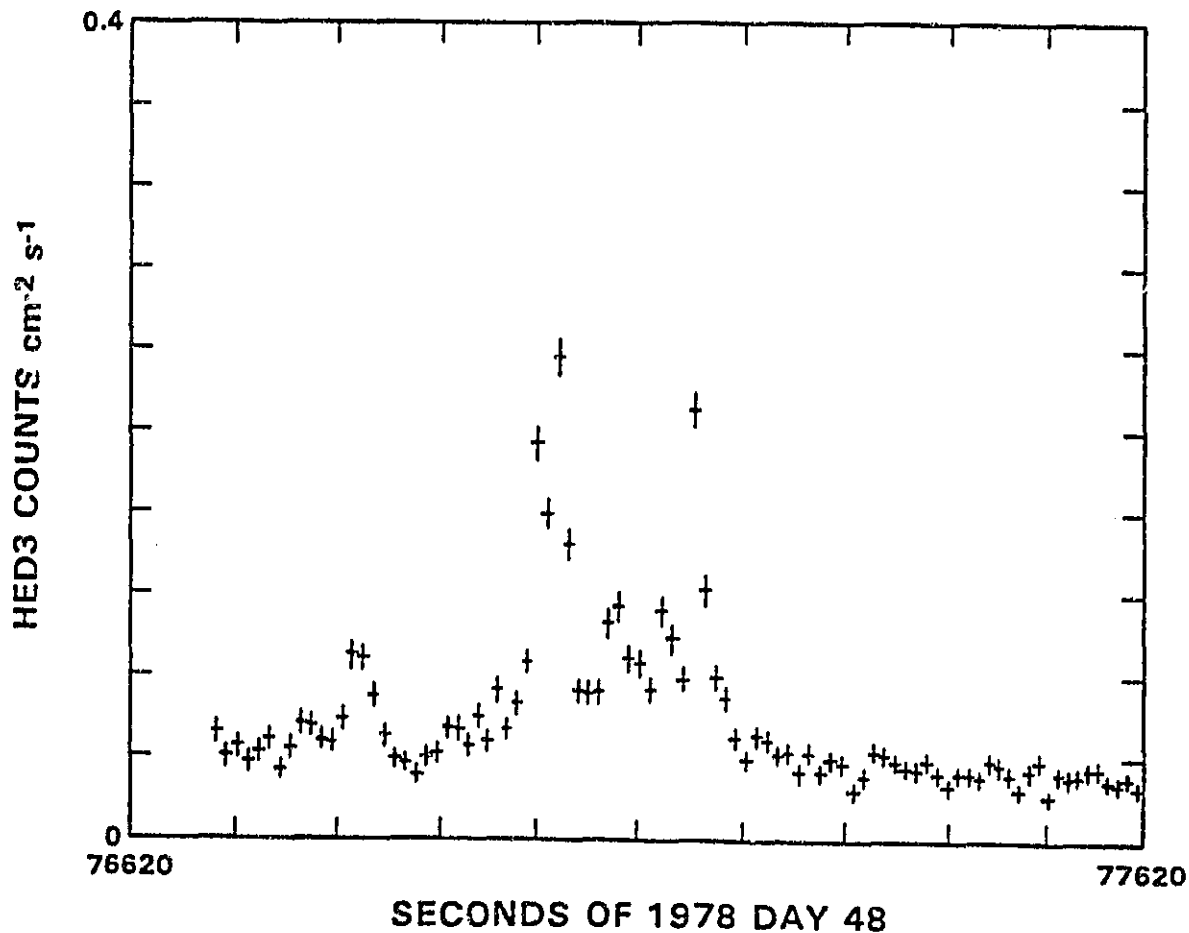
Figure 6-17

Plots A, B, and C are expanded views of three data streams shown in Figure 5-12: 2.56-second rates from MPC channels 4-6 during flaring in the first HEAO-2 point at Circinus. Plots D, E, and F show the respective autocorrelation functions. Possible linear declines are indicated in plot F.
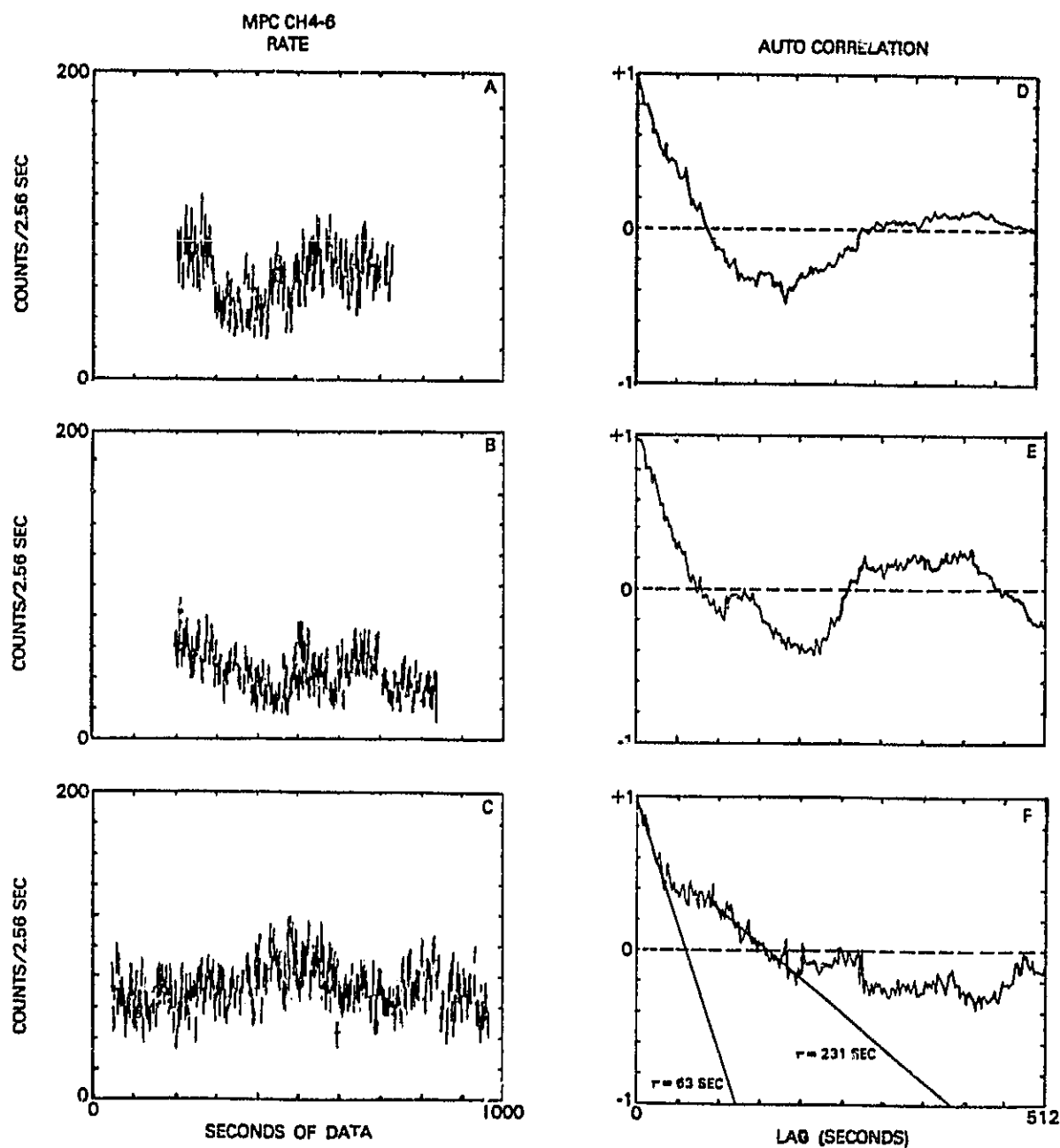
seconds for the second. Timescales for assumed linear declines for these two intervals are somewhat longer, approximately the zero-crossing times. More than one timescale may be operative even within a given data stream, as most clearly indicated by the third and longest interval, whose autocorrelation function shows complex structure. Possible linear decline timescales of ~ 63 and 231 seconds are indicated in part F of the figure. The equivalent timescales for assumed exponential declines are somewhat shorter (as for the first two intervals), 52 and 86 seconds, respectively. These correlation timescales are a factor of $\gtrsim$ 50 times greater than those found for the soft intensity fluctuations at the onset of the large outburst in the second observation.

"... when they come to model Heaven,

And calculate the stars, how they will wield

The mighty frame, how build, unbuild, contrive

To save appearances, how gird the sphere

With centric and eccentric scribbled o'er,

cycle and epicycle, orb in orb."

- John Milton

Paradise Lost

## VII.  DISCUSSION

### A.  The Binary Model

As noted above in Chapters I and II, except for the (1971) era of Uhuru eclipse-like observations (Jones et al. 1974), the soft X-ray lightcurve of Circinus X-1 (Kaluzienski et al. 1976) is not typical of an occulting binary.

### 1.  Absorption By Cold Wind Material

Following up the suggestion that the source shines out periodically for a portion of the orbit, Murdin et al. (1980) proposed a detailed model to explain the shape of the 3-6 keV lightcurves found in the Ariel-5 All Sky Monitor data base from 1974 to 1978, along with the earlier Uhuru lightcurve. Their model invokes the effects of changing optical depth to a constant luminosity X-ray source in a very eccentric orbit through the dense, cold stellar wind of a massive companion. They assume that the observed 3-6 keV luminosity $L_{obs}$ at a given binary phase $\theta$ can be written

$$L_{obs} \sim L_{const}\, e^{-\tau_A(\theta;\ \theta_p,\ i)}, \qquad\qquad 7\text{-}1$$

where $L_{const}$ is the (assumed) constant intrinsic luminosity, and the optical depth to photoelectric absorption, $\tau_A$, is a function of the binary phase $\theta$, the "periastron angle" $\theta_p$, and the inclination angle $i$ of the orbit (refer to Figure 7-1 and Appendix A). They note that the source is not likely to be truly constant, particularly if the luminosity is due to accretion from the wind and not moderated in a disk, but argue that,

Figure 7-1

In conjunction with Appendix A, the sketch indicates the relevant geometry for calculating the instantaneous absorbing column density along the line of sight in terms of the apparent relative position of the two stars. The angle $\phi$ in the figure is related to the "periastron angle" $\theta_p$, which gives the orientation of the major axis to the line of sight, and $\theta$, the "true anomaly" or binary orbit angle measured from periastron, by $\phi = (\frac{3\pi}{2} + \theta_p + \theta)$. For the cold wind case, the column density is integrated from the X-ray source to infinity. When ionization is included, the lower limit is replaced by $R_s$, the distance of the Stromgren surface from the X-ray source along the line of sight.
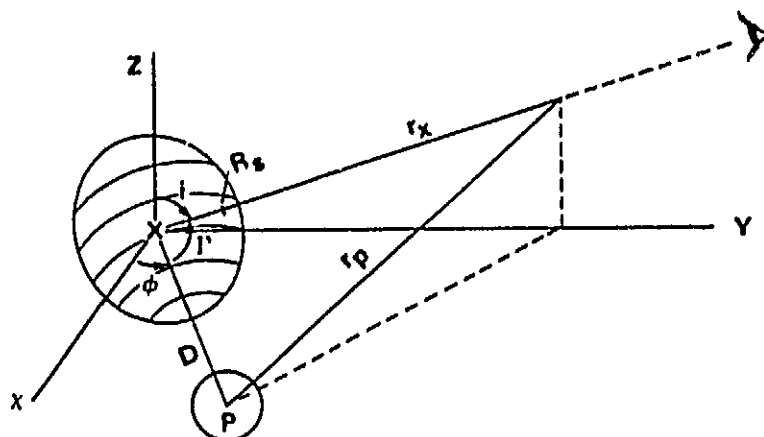


X-Y PLANE = PLANE OF ORBIT
X-Z PLANE = INSTANTANEOUS PLANE WITH LINE OF SIGHT TO X-RAY SOURCE
D = INSTANTANEOUS SEPARATION OF STELLAR CENTERS
$\cos \Gamma = \sin \phi \sin i$
$r_p^2 = r_x^2 + D^2 - 2 r_x D \cos \Gamma$
$R_s$ = DISTANCE FROM X-RAY SOURCE TO STRÖMGREN SURFACE

because the optical depth factor enters as an exponential, it should dominate intrinsic changes in the source.

The observed systematic changes in infrared and optical flux over several years discussed in Chapter II suggest that an early-type supergiant is probably not a viable candidate for the companion. Further, Argue and Sullivan (1975) argue that, after distance and reddening corrections, an OB supergiant would appear about two magnitudes brighter than is consistent with the upper limit based on non-detection with their plate threshold. Figure 7-2, adapted from Murdin et al. (1980) displays in bold lines the radius versus mass curves of several luminosity classes of stars. (I: supergiants, II: giants, V: main sequence stars). At the top of the figure we have added visual magnitudes applicable to main sequence stars. The range of possible candidate masses suggested by Murdin et al., $\log(M_p/M_0) \sim 1.3$-$2.0$, is indicated in the figure. With the revised visual magnitude estimate $M_v \sim \bar{}2.5$ (with rather larger uncertainties due to uncertainties in the reddening correction), we estimate a companion mass < 20 $M_0$, possibly $\sim 10$ $M_0$. This is consistent with a B-type main sequence star or a later-type more evolved star. Either of these types of objects might still produce sufficient wind outflow to fuel the Circinus system. In addition, tidal effects on a less massive companion due to the close passage of the compact object near periastron may be quite large.

Murdin et al. find that an eccentricity $\gtrsim 0.7$ will give lightcurves roughly consistent with those observed and suggest an inclination angle of $\sim 75^0$ so that the soft X-rays are strongly modulated but the harder X-rays are unaffected. They explain the observed evolution of lightcurves from 1971 to 1978 in terms of a changing orbit orientation due to precession, amounting to a shift in $\theta_p$ by about $-10^0$ per year. Figure 7-3

Figure 7-2

The figure, adapted from Murdin et al. (1980), displays in bold lines
the radius versus mass curves of several luminosity classes of stars. (I:
supergiants, II: giants, V: main sequence stars). At the top of the figure
are visual magnitudes corresponding to main sequence stars. The range of
possible candidate masses suggested by Murdin et al., $\log(M_p/M_0) \sim 1.3\text{-}2$,
is indicated in the figure by the double-sided arrow. The revised visual
magnitude estimate leads to a smaller companion mass (indicated by the
arrow decreasing from $\log M_p/M_0 = 1.3$) consistent with a B-type main
sequence star or a later-type more evolved star.

The light solid lines in the figure correspond to the periastron
separation of the stellar centers for a 1 $M_0$ compact object, as a function
of primary star mass for several values of eccentricity.

The dashed lines indicate the approximate size of the Roche lobe of
the primary star at periastron passage of a 1 $M_0$ compact object for the
same eccentricity values as before (the minimum and maximum values only are
labeled to avoid confusion in the figure). For high eccentricity or a
somewhat evolved companion, the Roche lobe at periastron may be *smaller* than
the primary radius, possibly leading to overflow onto the compact object.

Figure 7-2
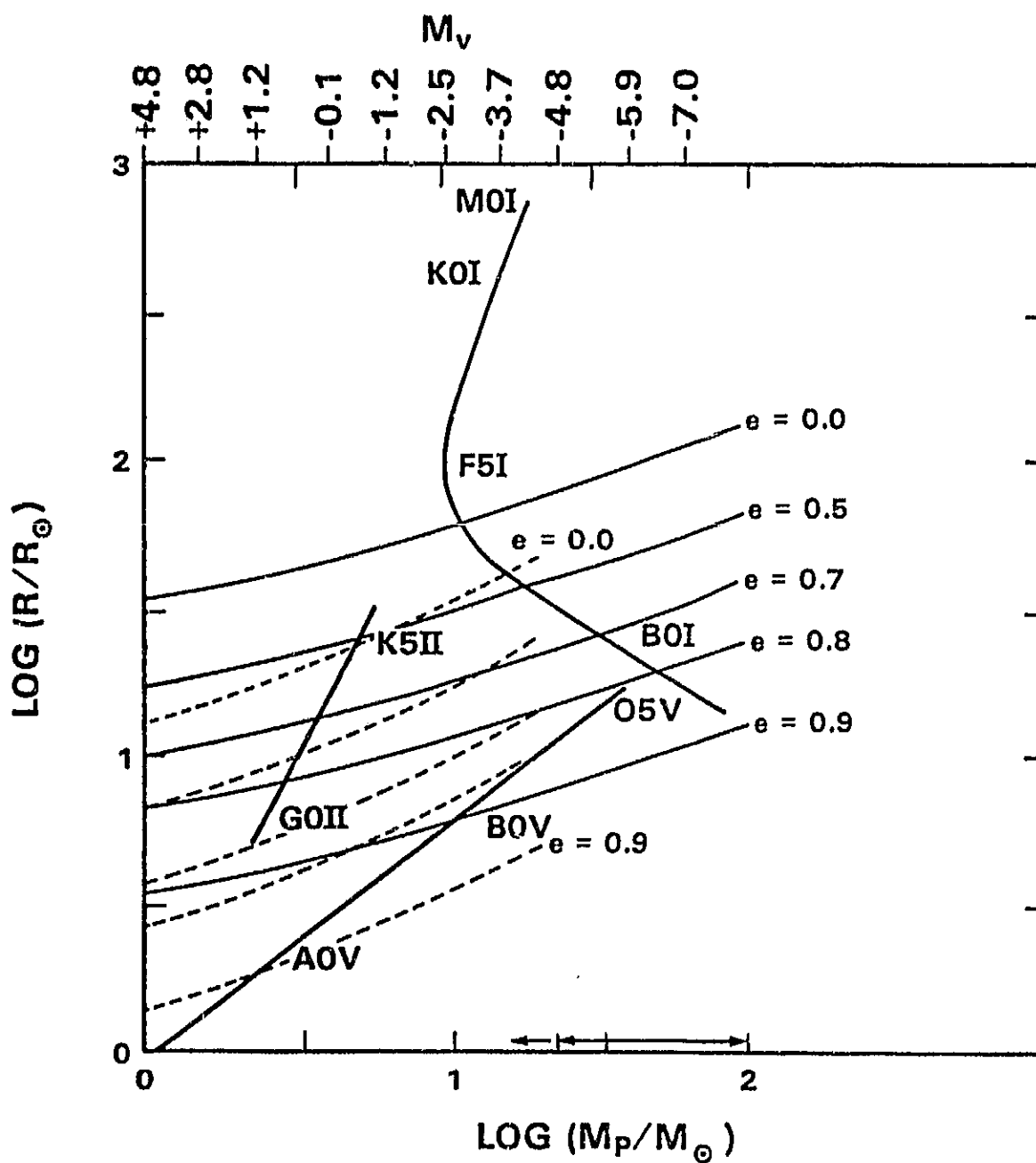
Figure 7-3

A schematic of an eccentric (e ≈ 0.7) binary system similar to that proposed for Circinus X-1 by Murdin et al. (1980).

The primary star, of radius $R_p = 20 R_0$, is located at the focus. Along the elliptical orbit various phases are noted, with phase zero defined to occur at periastron. The hatched region indicates the portion of the orbit where the primary is expected to overflow the instantaneous gravitational equipotential surface of approximate radius $R_{TIDAL}$, as calculated by Avni (1977). (This condition lasts for ∼ 1 day of the 16.6 day orbit for the system parameters of the model.)

The periastron angle, $\theta_p$, is the projection in the orbit plane of the angle from the major axis of the ellipse to the look direction. The approximate look directions during two satellite epochs are indicated, for an assumed orbit precession of $-10°$ per year and the phase assigned by Murdin et al.

Figure 7-3

# SCHEMATIC OF PROPOSED ORBIT FOR CIR X-1



$R_{TIDAL} = R_p$

FOR $R_p = 20 \, R_\odot$

$M_p = 20 \, M_\odot$

$M_x = 1 \, M_\odot$

$\Theta_p \equiv$ PERIASTRON ANGLE
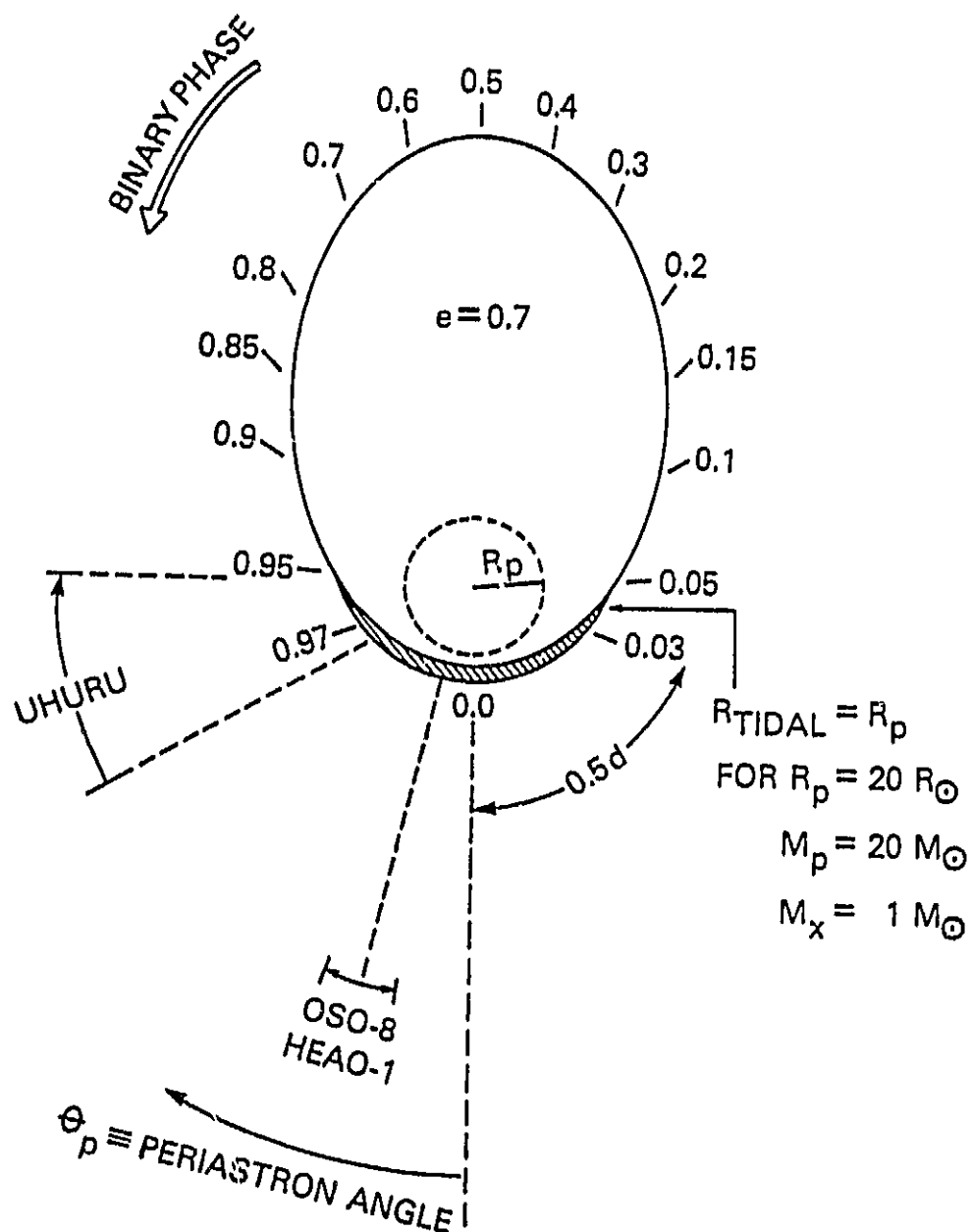
shows a schematic of their proposed eccentric (e ≈ 0.7) binary system with a smaller mass primary ($M_p$ = 20 $M_0$). Along the elliptical orbit, positions of the compact object for various orbit phases are noted. The primary star, of radius $R_p$ = 20 $R_0$ is located at the focus. The hatched region indicates the portion of the orbit where the primary is expected to **exceed** the instantaneous gravitational equipotential surface of approximate radius $R_{TIDAL}$, as calculated by Avni (1977). (See Chapter III§A.2.a.) The periastron angle, $\theta_p$, is the projection in the orbit plane of the angle from the major axis of the ellipse to the look directions. The approximate look direction during two satellite epochs are indicated, for an assumed orbit precession of -10° per year and the precession phase assigned by Murdin et al.

A stellar wind dense enough to provide the observed luminosity should provide observable optical depth effects and there are in fact large column densities sometimes associated with Circinus. However, despite the apparent attractions of the photoelectric absorption model for the soft X-ray lightcurve, it has some serious flaws.

We have reproduced the lightcurves of Murdin et al. as a first step in a more general program of modeling X-ray lightcurves. While we confirm the basic shapes that they find for various orbit orientations, we note that, for optical depths large enough to produce the desired shapes ($\tau_0$ at the surface of the primary is taken to be ~ 5 so that $\tau_0$ $R_*/D$ ~ 1 for $R_*/D$ ~ 0.2), the relative peak intensities change dramatically with look direction. Figure 7-4 shows the lightcurves predicted by the model of Murdin et al. with correct relative normalization. The model peak intensities change by a factor of 4-5 from $\theta_p$ ~ 90° to $\theta_p$ ~ 15°, corresponding to the range of assigned look directions from the 1971 Uhuru

Figure 7-4

With correct relative normalization, the lightcurves predicted by the cold wind absorption model of Murdin et al. (1980) for Cir X-1 ($\sim e^{-\tau}$) have peak intensities which decrease by a factor of 4-5 from the Uhuru epoch ($\theta_p \sim 90^0$) to the HEAO-1 epoch ($\theta_p \sim 15^0$) as the orbit precesses.

LIGHTCURVES FOR ABSORPTION MODEL
WITH CORRECT RELATIVE NORMALIZATIONS
e = 0.7  i = 75°

INTENSITY

UHURU epoch

$\theta_p = 90°$

OSO, HEAO
ep och

60°

45°

30°

15°

0°

BINARY PHASE
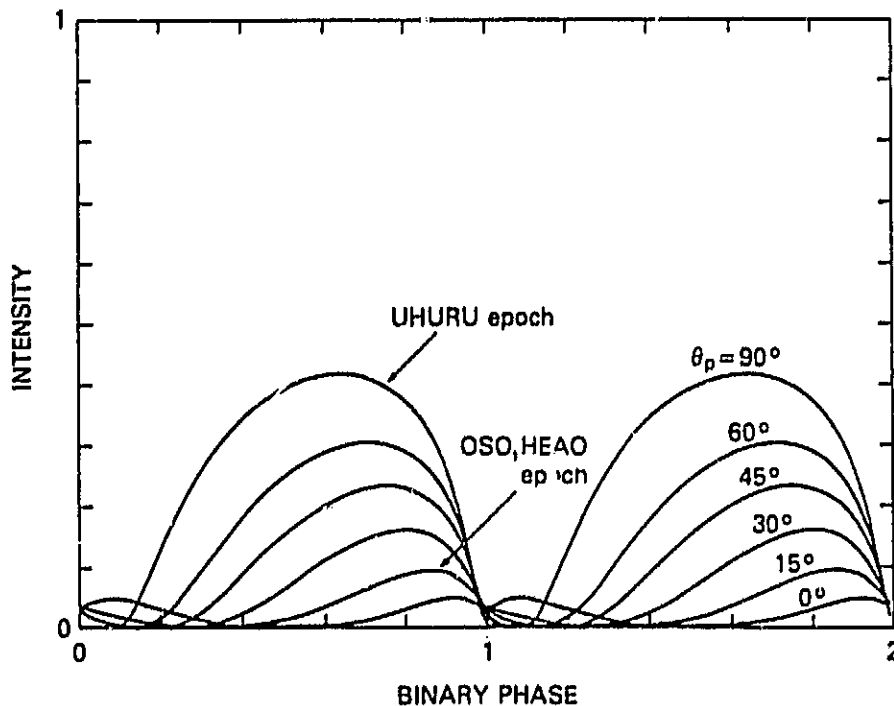
(eclipse-like) epoch to the 1976-7 OSO-8/HEAO-1 observations, while the average peak luminosities did not decline in this monotonic way. Also, the peak ($e^{-\tau}$) efficiency predicted for the HEAO-1 Scan 0 observation and the SAS-3 coverage of the following high cycle is ~ 10%, implying an intrinsic source luminosity during those times of several times $10^{39}$ erg $s^{-1}$.

Figure 7-5 shows the optical depths to photoelectric absorption as a function of binary phase corresponding to the lightcurves shown in the previous figure. The change in photoelectric optical depth corresponding to the column densities measured during the OSO-8 August 1976 observation of Circinus is denoted by a dashed line. The changes in optical depth predicted by the model are too gradual to match the observed change -- a rapid decrease to a low value of $\tau$ for a few hundredths of a cycle followed by a rapid increase--for any values of $\theta_p$ or i. Also, the wind densities required to achieve the desired modulation at ~ 4 keV imply a minimum column density much larger than that observed (roughly the interstellar value) for the proposed orbit orientations.

A further difficulty with the absorption model for the Circinus lightcurve is illustrated in Figure 7-6: not all of the soft flux modulation is due to changes in $e^{-\tau}$. The figure compares the 3-6 keV band lightcurve determined by OSO-8 in August 1976 (denoted by small crosses) with the modulation attributable to the changing optical depth to photoelectric absorption found in the spectral fits discussed in Chapter VI (denoted by larger crosses with closed circles and the hatched box). (The contribution to the rates from the relatively steady "power law" component noted in Chapter VI was first subtracted off.) The binary phase predicted by the X-ray ephemeris of Kaluzienski and Holt (1977) is indicated on the X-axis.

Figure 7-5

The figure shows optical depths to photoelectric absorption predicted by the (cold wind) model of Murdin et al., corresponding to the lightcurves shown in Figure 7-4. The variation in optical depth observed for Cir X-1 in August 1976 by OSO-8 is indicated by the dashed segment.
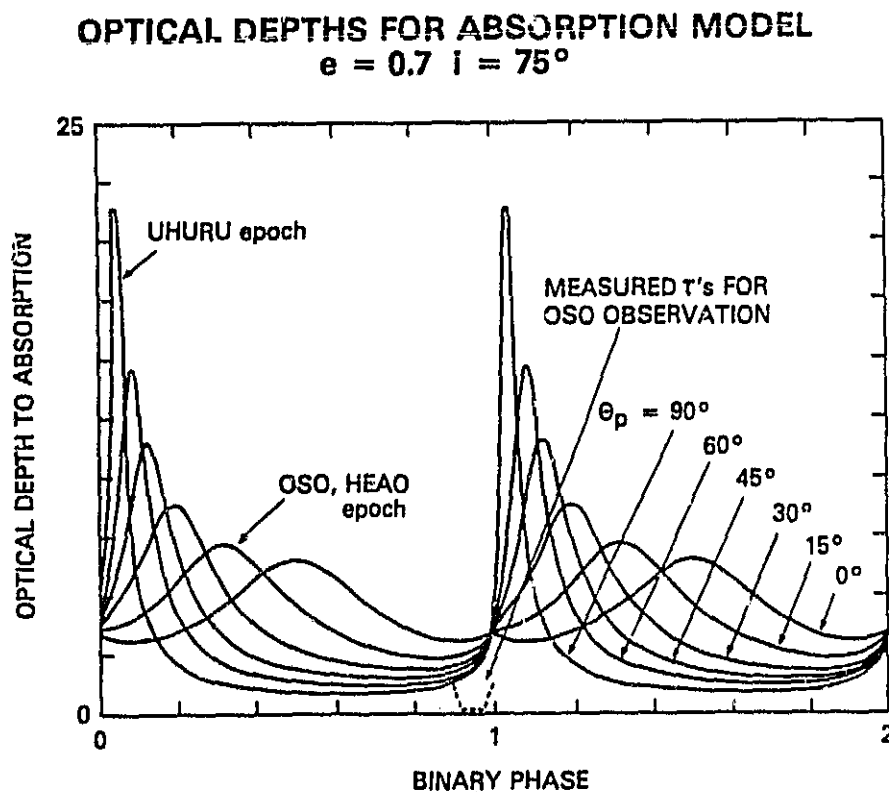
## OPTICAL DEPTHS FOR ABSORPTION MODEL
### e = 0.7  i = 75°

Figure 7-6

The 3-6 keV band lightcurve observed for Cir X-1 in August 1976 (small crosses) is compared with the modulation attributable to the changing optical depths for photoelectric absorption found in the spectral fits (larger crosses with closed circles), after the contribution to the rates from the relatively steady "power law" source was first subtracted off. The binary phase predicted by the X-ray ephemeris of Kaluzienski and Holt (1977) is indicated on the x-axis.

CIR X-1 OSO-8 A DET AUGUST 1976
3-6 keV LIGHTCURVE COMPARED WITH
MODULATION ATTRIBUTABLE TO MEASURED ABSORPTION

POWER LAW
CONTRIBUTION

COUNTS cm$^{-2}$ s$^{-1}$

PREDICTED BINARY PHASE
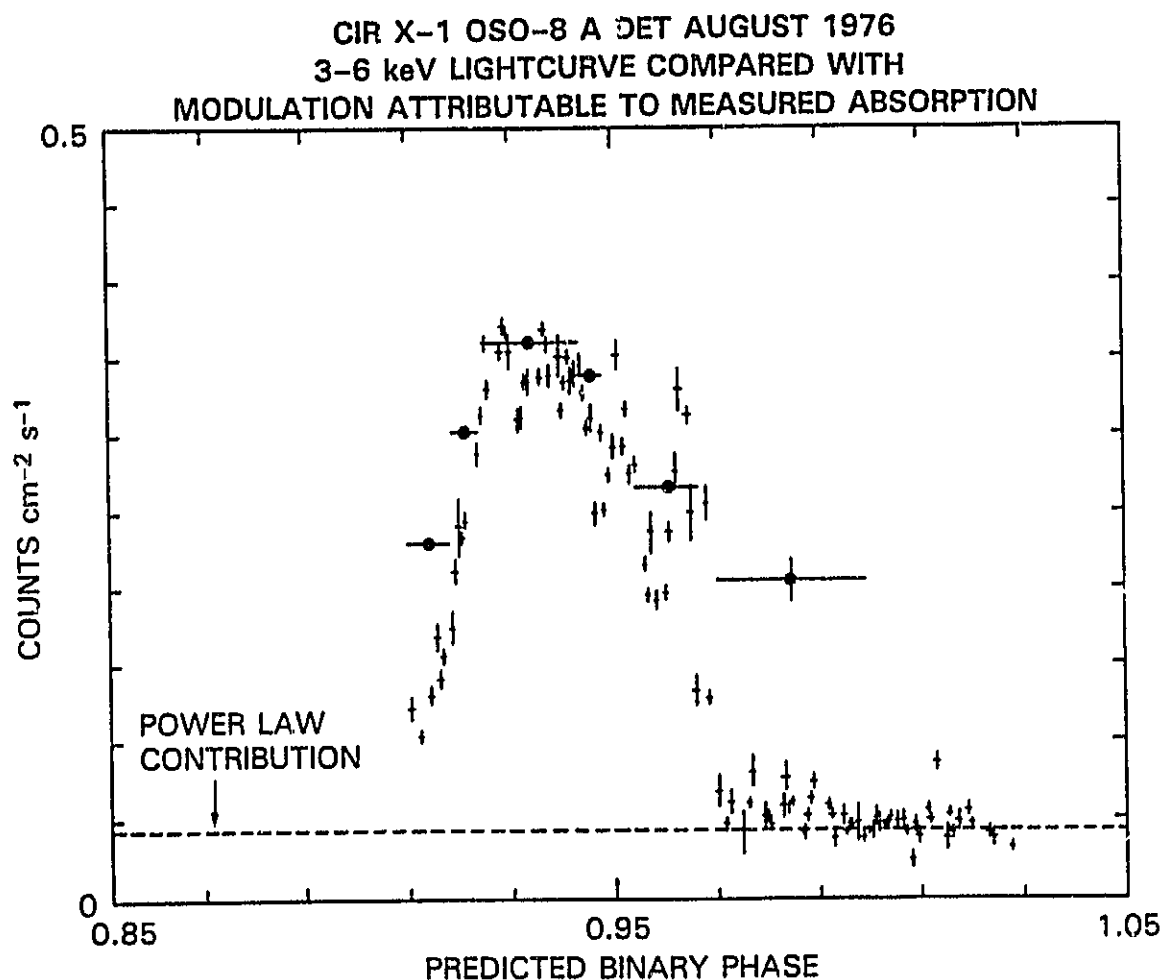
These data show that -- even if some density distribution other than a simple inverse-square law were invoked -- the modulation during this outburst is not principally the result of changing photoelectric absorption.

## 2. Ionization Effects

As a simple modification to the absorption model for the lightcurves, we can include the effect of photoionization of the surrounding stellar wind by the central X-ray source (still taken to be constant in intensity), following the simple Strömgren surface analysis of Pringle (1973) discussed in Chapter III. The (energy independent) optical depth to Thomson scattering, about 10% of the optical depth to absorption at 2.7 keV in the cold wind case, is still calculated for the entire column density. However, in the integral for the absorbing column density along the line of sight (see Appendix A), instead of integrating all the way to the X-ray surface, we then integrate only to the Strömgren surface (see Figure 3-1). For a given orbit orientation, the lower limit of zero on the column density integral is replaced by the line of sight distance $R_s$ from the X-ray source to the Strömgren surface associated with the local ionization parameter $\lambda$. Using the notation of Equation 3-53,

$$\lambda \sim \quad 50 \ (L_{37}/E_1)/(\alpha_{-15} \ N_{11}^2 \ D_{12}^3). \qquad 7\text{-}2$$

The soft outbursts of Circinus covered by OSO-8 in August 1976 and HEAO-1 in August 1977 showed blackbody spectra with $kT \sim 0.8 - 0.95$ keV (peaking at $\sim$ 3kT) with luminosities $\sim 10^{38}$ erg s$^{-1}$. Recalling that the threshold energy for photoionizing hydrogenic oxygen is 0.87 keV, we take

$$(L_{37}/E_1) \sim 10 \ (\frac{0.87}{3 \times 0.9})^{2.7} \ \sim 0.5.$$

For an inverse-square stellar wind density we can write

$$N_{11} = (N_*/10^{11} \ cm^{-3}) \ (R_*/D)^2, \qquad 7\text{-}3$$

where $N_*$ is the wind density at the primary surface, $R_*$ is the primary radius, and D is the instantaneous stellar separation. For the model parameters of Murdin et al., $R_* = 20\ R_0 \sim 1.4 \times 10^{12}$ cm and, to provide $\tau_* \dfrac{R_*}{a} \sim 1$ in the cold wind model, $N_* \sim 3.8 \times 10^{11}$ cm$^{-3}$. Murdin et al. use wind densities such that $\tau_* R_*/a \sim 1$ at 5 keV and then compute lightcurves $e^{-\tau(5\ keV)}$. We use lower wind densities, such that $\tau_* R_*/a \sim 1$ at $\sim 2.7$ keV and compute $e^{-\tau(2.7\ keV)}$. The shapes of the two sets of lightcurves are identical for the cold wind case, but out treatment allows us to include more readily other effects such as ionization and wind accretion for a source such as Circinus, whose optically thick outburst spectra peak near 2.7 keV.

For a 16.6 day period, with $M_* = 20\ M_0$ and $M_x = 1\ M_0$ (values in the model of Murdin et al.), the semi-major axis is, from Kepler's third law,

$$a_{AU} = [P_{yr}^2\ (\frac{M_* + M_x}{M_0})]^{1/3} = 0.35\ AU, \qquad 7\text{-}4$$

or $5.3 \times 10^{12}$ cm. Thus, assuming the intrinsic source luminosity is constant we can write

$$\lambda \sim 25\ \frac{D_{12}}{\alpha_{-15}(N_*/10^{11})^2\ (R_*/10^{12})^4} \sim 2.4\ \frac{(1-e^2)/(1+e\ \cos\theta)}{\alpha_{-15}}. \qquad 7\text{-}5$$

For a recombination parameter $\alpha_{-15} \sim 1$ and e = 0.7, this gives $\lambda$ ranging from $\sim 1.8$ at apastron to $\sim 0.3$ at periastron. While these particular values should only be taken as illustrative because of the somewhat arbitrary choice of rather uncertain parameters (in particular, a rather simplistic estimate of the recombination rate), they show that the ionized

region can be open in one part of the orbit and closed in another for plausible parameters. (We will see below that the change in λ with orbit phase when luminosity is proportional to wind accretion is quite different from the relation found for the constant luminosity case, where $\lambda \propto D$, the stellar separation.)

Whether, for a given orbit phase, the ionized region is closed ($\lambda <$ 1/3) or open ($\lambda > 1/3$; refer to Figure 3-3 for a plot of the half angle of the tangent cone for the unionized region as a function of $\lambda$), the effect on the line of sight column density depends strongly on the relative alignment of the two stars with respect to the line of sight to the X-ray source as well as on the actual stellar separation. For a given $\lambda$, the line of sight distance, $R_s$, to the Strömgren surface scales with the instantaneous stellar separation D for a particular look direction (refer to Equation 3-54 and Figure 3-1), but the column density integral depends on the absolute value of D.

If this type of Strömgren analysis is applied at each position along the orbit, lightcurves analogous to those found by Murdin et al. can be computed, this time with the assumption

$$L(\theta; \theta_p, i, \lambda) \sim L_{const}\, e^{-\tau_{ABS}(\theta,\, \theta_p, i, \lambda)}\, e^{-\tau_{compt}(\theta, \theta_p, i)}, \qquad 7\text{-}6$$

where $\tau_{ABS}$ is now calculated for the line of sight cold material while $\tau_{Compt}$, the optical depth to Compton scattering, is calculated for the total line of sight column density. Figure 7-7 shows the resulting lightcurves when the illustrative values of $\lambda$ discussed above are used to recompute the optical depth to absorption through the unionized matter. The shapes and peak intensities of the lightcurves change substantially

Figure 7-7

The figure shows the effect on the cold wind lightcurves of Figure 7-4 when ionization of the stellar wind material by the X-ray source is taken into account by incorporating the simple "Strömgren surface" ionization model of Pringle (1973); the shapes and peak intensities of the lightcurves change substantially.

## LIGHTCURVE FOR ABSORPTION MODEL
## WITH IONIZATION
### e = 0.7  i = 75°
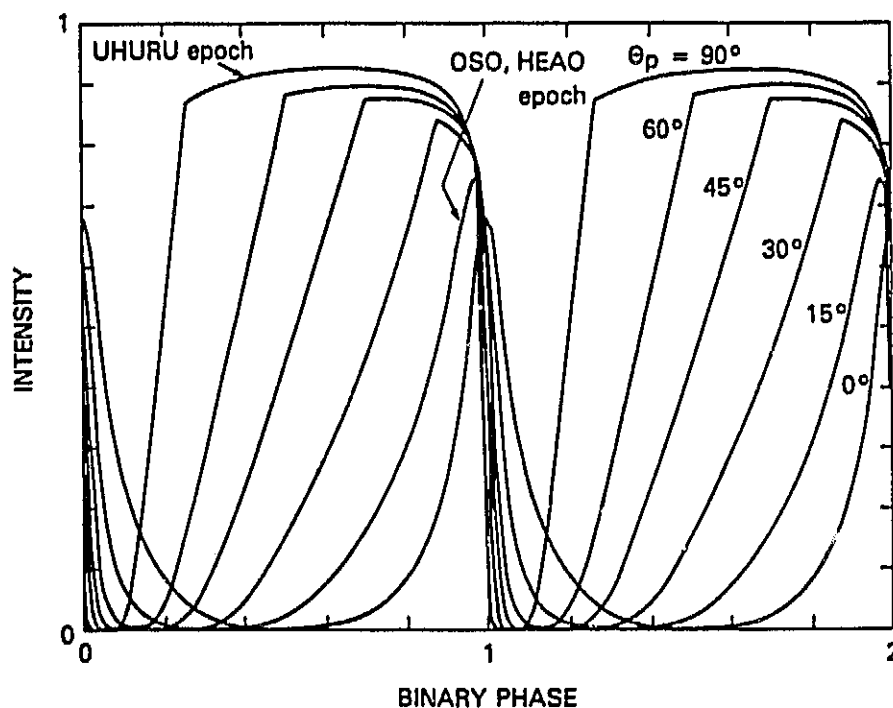
from the cold wind case. The peak efficiencies are more nearly the same,
being different from 1.0 because of Compton scattering effects. The
lightcurve assigned to the Uhuru epoch ($\theta_p = 90^o$) looks somewhat more
eclipse-like, in keeping with the data. However, it should be noted that
the lightcurve assigned to the OSO/HEAO epoch has a much smaller duty-cycle
than that inferred for the HEAO 1 Scan 0 observation (Observation 2) or for
the very intense cycle following that was covered by SAS-3.

While this approximate treatment of changing ionization conditions
throughout the orbit suggests that such effects are likely to be important
in the Circinus system, and they offer a natural way of achieving average
peak efficiencies (for letting through the intrinsic source luminosity)
near 1 for various orbit orientations, a description of the lightcurves in
terms of changing optical depths through a uniform wind to the X-ray source
is not adequate even when ionization is included. It is still true that
not all of the modulation is due to $e^{-\tau}$ effects. The total amount of
material along the line of sight, ionized plus cold, is equal to the amount
of cold material in the previous case. With the absorption cross-section
roughly a factor of 10 larger than the scattering cross-section, the
resulting decrease in flux from cold plus ionized material is at most that
due to all cold material. Thus the excess modulation found in Observation
1 over that predicted by the cold wind case (see Figure 7-5) cannot be
explained by appealing to column densities of ionized material which would
not show up in the $N_H$ determination from the low energy turnover, unless
this material is not part of the smooth wind distribution postulated.
Large changes in the amount of material near the compact object might be
expected for rapid changes in accretion conditions, but then the basic
picture of modulation from optical depth effects would no longer apply.

### 3. Intrinsic Source Variations

Low measured column densities of cold material when the source intensity is low and intensity modulation not attributable to optical depth effects in a uniform wind, even when ionization is included, suggest that, even though matter densities in the system are probably quite large, intrinsic changes in the source intensity may compete with or dominate optical depth effects. For an eccentric binary system, it is natural to investigate the contribution of changes in wind accretion to modulation of the lightcurve.

To do so, we write

$$L_{obs}(\theta) \propto L_{wind}(\theta) \; e^{-\tau(\theta)}, \qquad\qquad 7\text{-}7$$

where the wind accretion luminosity at orbit angle $\theta$ is calculated according to Equation 3-14. This assumes that the accretion is prompt, ignoring, for example, possible formation of an accretion disk.

Chiappetti and Bell-Burnell (1981) argue that including accretion from a fast wind in the lightcurve calculation provides sufficient modulation that the orbit eccentricity and wind density should be reduced from the values of Murdin et al. to keep the envelope from becoming too narrow, and to match the Ariel 5 observations of low hydrogen column densities for Circinus during times of low flux. They suggest that an optical depth at the primary surface $\tau_0 \sim 0.5$ (rather than 5.0), an eccentricity of 0.5 (rather than 0.7) and an orbit inclination near $90^\circ$ gives lightcurves similar to those of Circinus. They do not quote a wind velocity but note that the accretion rate is symmetric with respect to the line of apsides, implying a wind speed fast compared to the orbit velocity, so that $V_{rel}$ in Equation 3-14 does not change substantially over the orbit. Their assumption of an inverse square density law for the wind implies a constant

wind velocity. For a fast, constant velocity wind, the mass accretion rate is roughly proportional to $D^{-2}$. An accelerated wind profile, such as that of Castor, Abbott, and Klein (1975) (see Equation 3-15) which they adopt in a follow-up paper (Chiappetti and Bell-Burnell 1982), would tend to make the peak sharper and reduce the relative fraction of off-peak flux compared to those which they present or which we show in Figure 7-8. For an e=0.5 orbit, the qualitative changes in the lightcurve relative to the constant wind velocity case are not too large even for this rapid acceleration case, though the peak intensity is increased by a factor of ~ 4 since the wind velocity is only ~ 70 percent of maximum at periastron.

Figure 7-8 shows lightcurves for the low density, fast wind accretion model with an assumed orbit semi-major axis of $5.2 \times 10^{12}$ cm, a primary radius of 20 $R_0$ and a constant wind velocity of 1000 km $s^{-1}$. The y-axis is plotted in units of $10^{38}$ erg $s^{-1}$. Three look directions are chosen for illustration of the effects of orbit orientation. The dip in each case marks the passage of the compact object behind the primary, essentially an eclipse phenomenon. The outer envelope of the superposed curves indicates the shape of the wind accretion term for this case before the optical depth effect is included. The look direction determines the relative flux before and after the "eclipse". Orientations near $\theta_p = 180^0$ most closely match the Uhuru eclipse-like curve, while considerably smaller angles ($\theta_p \sim 60^0$ - $120^0$) produce a gradual rise followed by a sharper decline, broadly consistent with the Ariel-5 All Sky Monitor prototypical lightcurve noted by Kaluzienski et al. (1976).

Figure 7-8

The figure shows lightcurves for the low density, fast wind accretion model with an assumed orbit size of $5.2 \times 10^{12}$ cm, a primary radius of 20 $R_0$ and a constant wind velocity of 1000 km $s^{-1}$. The y-axis is plotted in units of $10^{38}$ erg $s^{-1}$. Three look directions are chosen for illustration of the effects of orbit orientation. The dip in each case marks the passage of the compact object behind the primary, essentially an eclipse phenomenon. The combined outer envelope indicates the shape of the wind accretion term for this case before the optical depth effect is included. The look direction determines the relative flux before and after the "eclipse".

## LIGHTCURVES FOR FAST WIND ACCRETION
### $\theta = 0.5$  $i = 90°$



BINARY PHASE
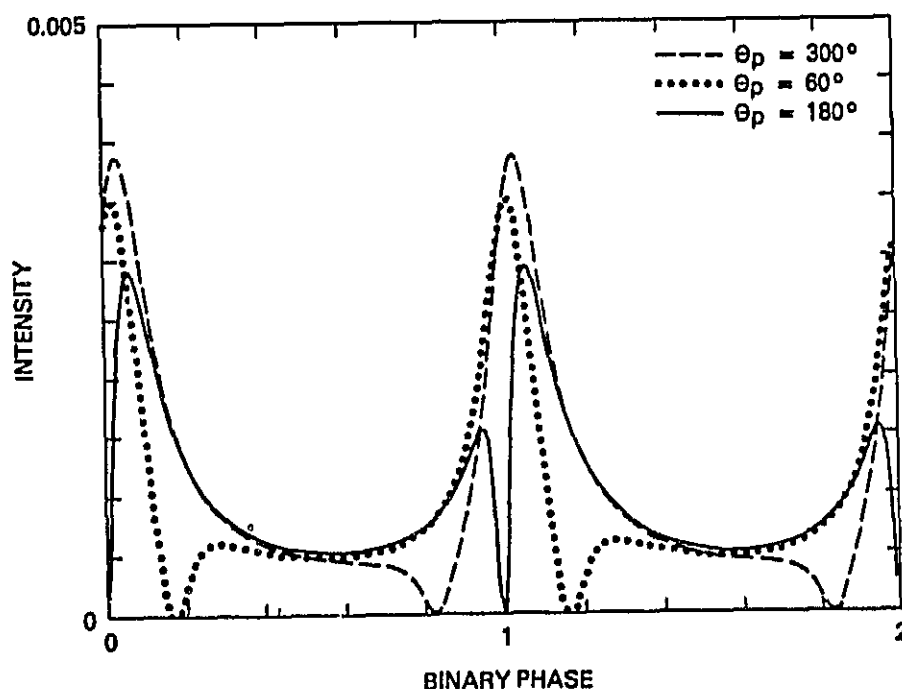
There are several difficulties with the wind accretion model as it stands:

(1) The lightcurves are not particularly compelling reproductions of the data (see Figure 7-8). Turn-ons and cutoffs are not nearly as sharp in the model as are observed. The lightcurve associated with the Uhuru era eclipses is not convincing.

(2) One cannot choose a single consistent set of wind parameters and a reasonable orbital precession value to reproduce both the short duty-cycle OSO outburst (Figure 5-3) and the long duty-cycle HEAO outburst (Figure 5-5) a year later.

(3) The model cannot produce the optical depth evolution observed from Circinus by OSO-8 in August 1976 (cf. Figure 7-5). The optical depth predicted by the model is low most of the time except for a rapid increase followed by a rapid decrease around the eclipse. The OSO data require a rapid decrease followed by a rapid increase.

(4) Last and perhaps most critical, it is difficult to produce the $\gtrsim 10^{38}$ erg s$^{-1}$ luminosities observed for Circinus with a fast low density wind (see Equation 3-14 and Figure 7-8). Chiappetti and Bell-Burnell (1981) plot "relative intensity" for their lightcurves and do not address this problem. In Equation 3-14, the factor $[(\frac{M_x}{M_o})^3 (\frac{R_x}{10^6 \text{ cm}})^{-1}]$ may be considerably greater than unity, but even a value of 10 would yield $< 10^{37}$ erg s$^{-1}$. The mass loss term could be increased, but then absorption would become more important and ionization effects would have to be taken into account. Alternatively, since the accretion luminosity depends so strongly on the local relative velocity of wind and compact object, a more gradual acceleration profile such as that of Barlow and Cohen (1977) (Equation 3-16) or a slower terminal wind

velocity would greatly increase the peak flux for a fixed mass loss rate. However, such a change would also increase the wind density and make the relative velocity factor dependent on the binary phase, and the corresponding lightcurves would be quite different from the fast, low density wind accretion curves of Chiappetti and Bell-Burnell or, equivalently, those shown in Figure 7-8. A slower wind would also increase the likelihood of disk formation, a possibility noted in Chapter III which we discuss further below.

From the longer term modulation of cycle peaks and the variety of spectral and temporal behavior observed from one cycle to the next, we expect that the mass transfer conditions vary strongly with time. If the transfer is primarily via wind accretion, this could imply variable wind density and velocity. If we allow variable wind parameters, we may be able to answer most of the objections noted above. For example, variable wind speed could explain the short duty-cycle OSO outburst in 1976 (Observation 1) in terms of a fast wind, with the longer duty-cycle more luminous HEAO outburst the following year (Observation 2) occurring when the wind was slower.

Figure 7-9 shows the approximate match of the 3-6 keV OSO data points with the smooth curve predicted by wind accretion in an e = 0.7 orbit through a fast (1000 km s$^{-1}$) dense ($\dot{M}_x \sim 2 \times 10^{-5}$ M$_0$ yr$^{-1}$) wind which in turn is ionized by the resulting X-ray source. The model does not account for the residual unabsorbed flux from the persistent component noted in Chapter VI. The match requires a shift of 0.07 of a 16.6 day cycle in the X-ray ephemeris phase 0 with respect to periastron passage.

The ionization effect, required both to achieve sufficient peak luminosity and to describe the observed column density evolution, has a

Figure 7-9

The figure shows the approximate match of the 3-6 keV OSO data points with the smooth curve predicted by wind accretion in an e = 0.7 orbit through a fast (1000 km s$^{-1}$) dense ($\dot{M}_x \sim 2 \times 10^{-5}$ M$_\odot$ yr$^{-1}$) wind which in turn is ionized by the resulting X-ray source. The model does not account for the residual unabsorbed flux from the persistent component discussed in the text. The match requires a shift of 0.07 of a 16.6 day cycle in the X-ray ephemeris phase 0 with respect to periastron passage.



CIR X-1 OSO-8 A DET AUGUST 1976 3-6 keV LIGHTCURVE
COMPARED WITH MODULATION PREDICTED BY WIND ACCRETION MODEL
FOR FAST WIND, HIGH DENSITY, STRONG IONIZATION

PREDICTED BINARY PHASE
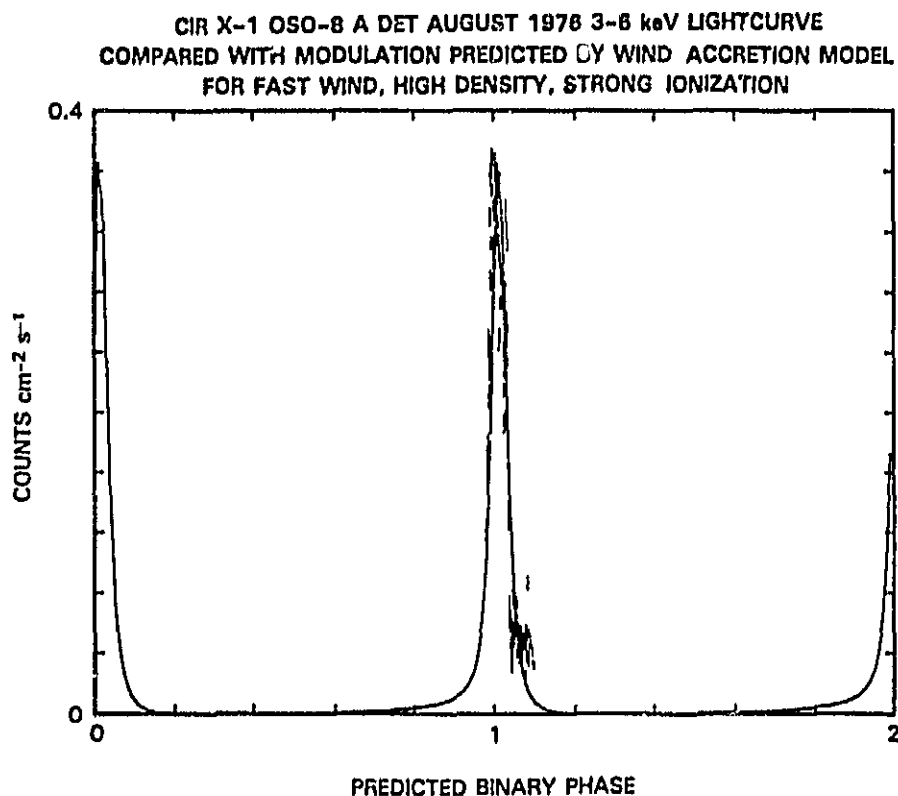
different dependence on the orbit phase than in the constant luminosity case. The ionization parameter for the wind accretion case has the form:

$$\lambda_W \propto$$

$$0.82 \; \frac{\eta}{E_1 \; \alpha_{-15}} \; \frac{1}{D_{12}} \; (\frac{\dot{m}_\star}{10^{-6} \; M_0/yr}) \; \frac{(V_W/10^3 km \; s^{-1})}{(V_{rel}/10^3 \; km \; s^{-1})^3} \; (\frac{M_X}{M_0})^3 \; (\frac{R_X}{10^6 \; cm})^{-1} \; , \qquad 7\text{-}8$$

where $\eta$ is a combined accretion efficiency factor for capture and conversion to soft X-rays. For a fast wind, this gives $\lambda_W \propto D^{-1}$ rather than $\lambda \propto D$. That is, $\lambda_W$ has a maximum value at periastron rather than at apastron.

When the simple Strömgren surface analysis discussed above is applied at each point of the orbit, the resulting modification in $\tau_{ABS}$ from the Murdin case can roughly match the magnitude and evolution of $\tau_{cold}$ found for the blackbody component in the OSO observation for the same phase shift noted above, as shown in Figure 7-10. The plot should be taken only as representing the possibility that the measured optical depths may be approximately reproduced if ionization by a varying X-ray source is taken into account.

### 4. Wind-Fed Accretion Disk

Following the treatment of Shapiro and Lightman (1976) for a circular orbit discussed in §III.B.1, one can calculate the outer edge of a wind-fed accretion disk by balancing the specific angular momentum of accreted gas with respect to the compact object with the specific angular

Figure 7-10

When x-radiation from wind accretion is allowed to ionize the wind material near the X-ray source (under the simple "Strömgren surface" ionization model of Pringle (1973), applied at each point of the eccentric orbit), the resulting modification from the Murdin case in $\tau$ predicted can roughly match the magnitude and evolution of $\tau$ found for the blackbody component in the OSO observation of Circinus. The match requires a dense wind and high efficiencies for producing X-radiation and ionization, and an offset between periastron passage and the X-ray ephemeris (Kaluzienski and Holt 1977) phase 0, defined by the sharp cutoff of the larger outbursts.

## OPTICAL DEPTHS FOR WIND ACCRETION MODEL WITH STRONG IONIZATION CONDITION
### e = 0.7  i = 90°
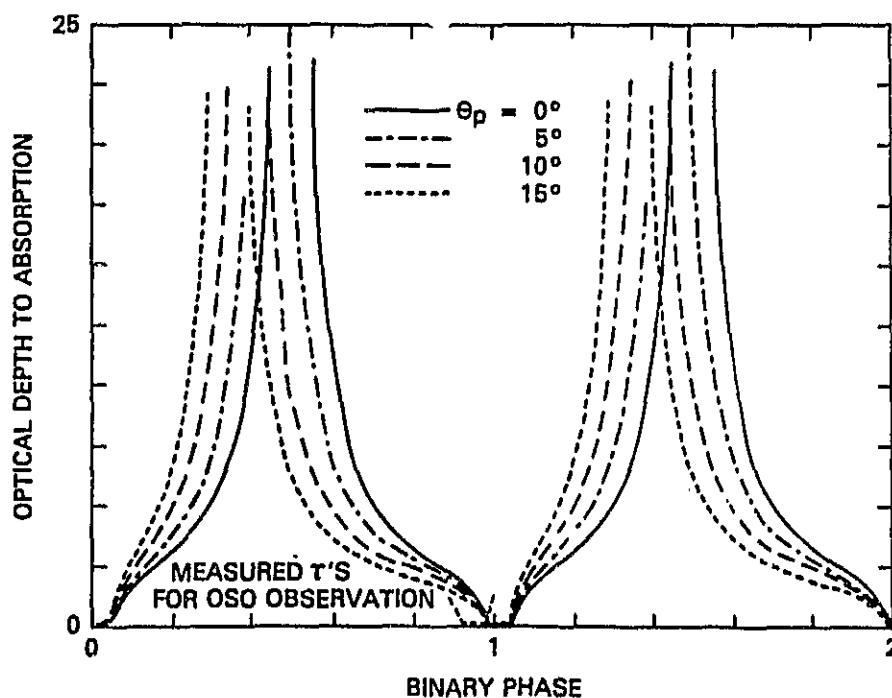
momentum for a Keplerian orbit about the object. In an eccentric orbit through a steady wind, the value so calculated for any point on the orbit depends strongly on the local relative velocity of the wind to the compact object, and less strongly on the orbital separation and velocity:

$$r_{disk} \propto D^{-2} \, V_{orb}^2 / V_{rel}^8 . \qquad\qquad 7\text{-}9$$

The various curves in Figure 7-11 track this value with orbit phase for various wind velocities. The orbit is taken to have $e = 0.7$ and $\langle V_{orb}\rangle$ = 230 km/sec. Without addressing questions of disk dynamics and stability, the plot is useful for estimating the likelihood of disk formation for various cases:

For an asymptotically fast wind (1000 km/sec), with a constant velocity or a strong acceleration profile (e.g., that of Castor, Abbott, and Klein 1975) [lower solid curves], the calculated disk radius is no larger than a neutron star. If a gradual acceleration profile [upper solid curve] is assumed, such as that found by Barlow and Cohen (1977) in infrared observations of OBA supergiants , a disk of $\sim 10^8$ cm radius may form near periastron.

For a wind velocity comparable to the average orbital velocity [dotted curves], a disk of $10^{10}$ cm may form at orbital phase 0.1-0.2. For an even slower wind [dashed curves], the radius may be a factor of 10 larger, with maximum size displaced toward apastron where the orbital velocity is slower.

While the disk may be disturbed at other phases of the orbit by accretion of lower angular momentum gas, or disrupted near periastron passage by overflow or other tidal influences, its existence at some level

Figure 7-11

Following the treatment of Shapiro and Lightman (1976), one can
calculate the outer edge of a wind-fed accretion disk by balancing the
angular momentum with respect to the compact object of accreted gas with
the angular momentum for a Keplerian orbit about the object. The value so
calculated for any point on the orbit depends strongly on the local
relative velocity of the wind to the compact object, and less strongly on
the orbit separation and velocity: $r_{disk} \propto s^{-2} V_{orb}^2 / V_{rel}^8$.

The various curves in the plot track this calculated value with orbit
phase in an eccentric (e=0.7) orbit for various wind velocities (given as
fractions of the mean orbit velocity, where $\langle V_{orb} \rangle = 230$ km/sec).

## RADIUS OF ACCRETION DISK FROM
## WIND ACCRETION
### e = 0.7 ORBIT
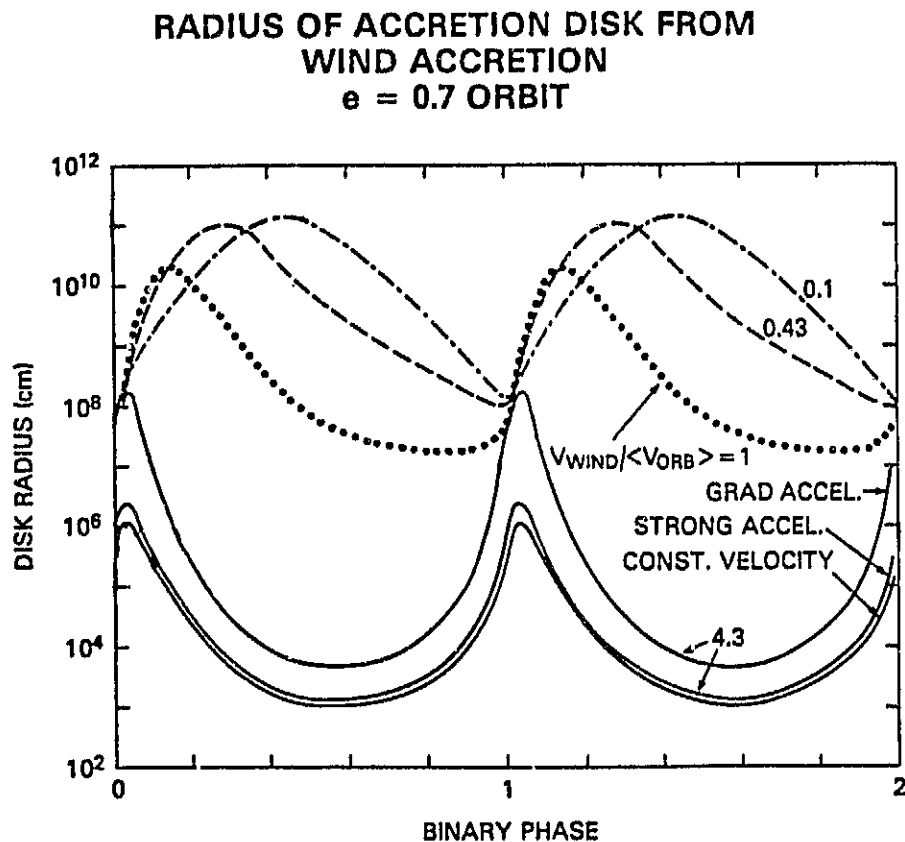
at some times seems highly plausible for conditions expected to be found in the Circinus system.

## B.   Properties of High and Low State Spectra

By combining the spectral results presented in Chapter VI with other spectra from Circinus available in the literature, we can search for systematic spectral behavior with respect to such parameters as source intensity and binary phase.  Figure 7-12 is a composite of information from several different instruments sampling a five year interval from 1975 to 1979, showing the change in spectral character of Circinus X-1 with changing intensity (References:  SAS-3 data, Dower, Bradt, and Morgan 1982; Ariel-5 data, Chiappetti and Bell-Burnell 1982; OSO-8, HEAO-1 and HEAO-2 data, this thesis.)  In some cases only simple power law fits were available, so that spectral form was used for cross comparison, even when the power law fit is poor (particularly for Goddard data at higher fluxes).  The spectra are plotted in terms of power law photon index $\alpha_N$ and inferred neutral hydrogen column density $N_H$, in units of $10^{22}$ atoms $cm^{-2}$, as a function of 2-10 keV intensity, in cgs units.  For an assumed distance of 10 kpc, a flux of $10^{-8}$ erg $cm^{-2}$ $s^{-1}$ corresponds to a luminosity of ~ 1.2 x $10^{38}$ erg $s^{-1}$, close to the Eddington limit for a one solar mass object. For most of the data, the one-sigma uncertainties in intensity and fit parameter are displayed, sometimes equal to the size of the alphabetic or geometric character.  The uncertainties in intensity for the SAS-3 data were not tabulated by Dower et al. (1982).  For the HEAO-2 observations, where the best fit 0.5-4 keV SSS slopes are generally about one unit flatter than the 2-10 keV MPC slopes, the latter values are used because they are determined for a bandwidth similar to that of the remaining

Figure 7-12

This figure is a composite of information from different experiments, showing the change in spectral character of Circinus X-1 at different intensities. In some cases only simple power law fits were available, so that spectral form was used for comparison for Goddard data, even when the fit is poor. The power law index (part B) gives some measure of spectral softness. The value of the equivalent hydrogen column density (part A) is a measure ⟨ the low energy turnover.

[ References: SAS-3 data, Dower, Bradt and Morgan, 1982; Ariel-5 data, Chiappetti and Bell-Burnell, 1982; OSO-8, HEAO-1 and HEAO-2 data, this thesis.]

## CIR X-1  POWER LAW FIT
## PARAMETERS VS. 2-10 keV INTENSITY
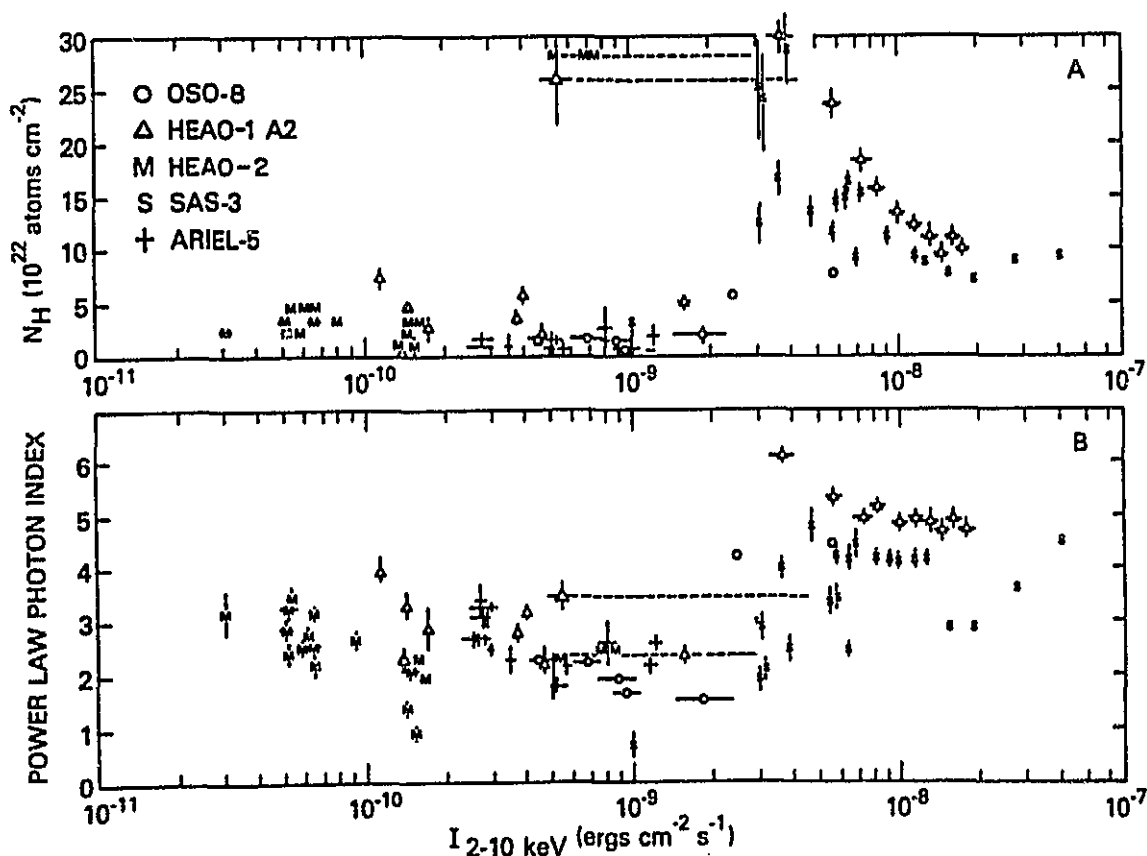
detectors. However, the MPC is fairly insensitive to the low energy cutoff so that the column density displayed is typically that found from fitting SSS data with the MPC slope.

In the plot, the power law index (part B) gives a measure of spectral softness. Particularly at higher fluxes ($> 2\text{-}3 \times 10^{-9}$ erg $cm^{-2}$ $s^{-1}$), the Goddard data, as discussed in Chapter VI, show spectra that are frequently complex, with an optically thick component consistent with a blackbody of $kT \sim 0.8 - 1.0$ keV, plus something harder. At lower fluxes, the spectra are usually well described by a power law or thin thermal bremsstrahlung model (sometimes with a strong iron line emission feature), though a blackbody model cannot always be ruled out.

The value of the equivalent hydrogen column density (part A) is a measure of the low energy cutoff. At higher fluxes it is typically an indication of the intrinsic low energy turnover of the blackbody component which is being fit with a steep power law. It should be recalled, however, that the blackbody fits to the onset of the HEAO-1 Scan 0 outburst showed column densities $\gtrsim 10^{23}$ atoms $cm^{-2}$ for fluxes $\lesssim 6 \times 10^{-9}$ erg $cm^{-2}$ $s^{-1}$ (see Table 6-7).

Because of the power law representation of the data, interpretation of the plot is not transparent, but several important statements can be made.
1)  There are roughly two groups of data reflecting the two spectral types noted above, with a few odd events at intermediate intensities.
2)  The low flux data do not _typically_ show high column densities, so that the observed low fluxes are not the residual optically thick component transmitted through a high column density.
3)  The low flux data do not show a narrow distribution in slope. Nor is there a clean correlation between intensity and power law index. There may

be a preferred range of values of slope near -2 at moderate intensities, possibly indicating the presence of a hard tail similar to that seen in Cygnus X-1 ($\alpha$ = -1.6), but, if that is the case, a steeper component (usually) dominates as the intensity drops. Thus, the parallel to the bimodal spectral states of Cygnus X-1 is not overwhelming.

4)    There are occasional instances of spectra at intermediate intensities which are strongly cut off at low energies. The ones plotted correspond to the low flux spectrum at phase 0.46, on the day prior to a large, early outburst during Observation 2; and the MPC component during the flaring episode at phase 0.06 during the first HEAO-2 point (refer to Chapter VI, Observations 2 and 8). In both cases, if the turnovers are attributed to absorption and the points are plotted in terms of inferred intrinsic intensity rather than observed intensity, they move into the high flux regime (as indicated by the dashed lines in the figure). Such points support the presence of high column densities in the system, though they may be local and transitory rather than pervasive.


### 1.    The Optically Thick Component

The Goddard data from the first and second observations indicate that the regular soft outbursts from Circinus are related to the onset of an optically thick component which is not directly correlated with the more persistent (but still variable) optically thin component. If the outburst spectra are fit by the blackbody model suggested by the first observation, the apparent radius for a spherical emitter at an assumed distance of 10 kpc frequently appears to be roughly 40 km while the blackbody temperature is typically $\lesssim 10^7$ K (kT ~ 0.8-1.0 keV). Figure 7-13 shows the blackbody radius and best fit kT plotted versus 2-10 keV luminosity for several

## Figure 7-13

The figure shows the blackbody radius and best fit kT plotted versus 2-10 keV luminosity for several observations. In each case only the parameters during the maximum observed intensity are used. The OSO-8 and HEAO-1 points correspond to the respective maximum intensity values shown in Figure 6-4. The remaining points are discussed in the text.



CIR X-1 BLACKBODY PARAMETERS AT
PEAK OF VARIOUS OUTBURSTS
(DISTANCE = 10 KPC)
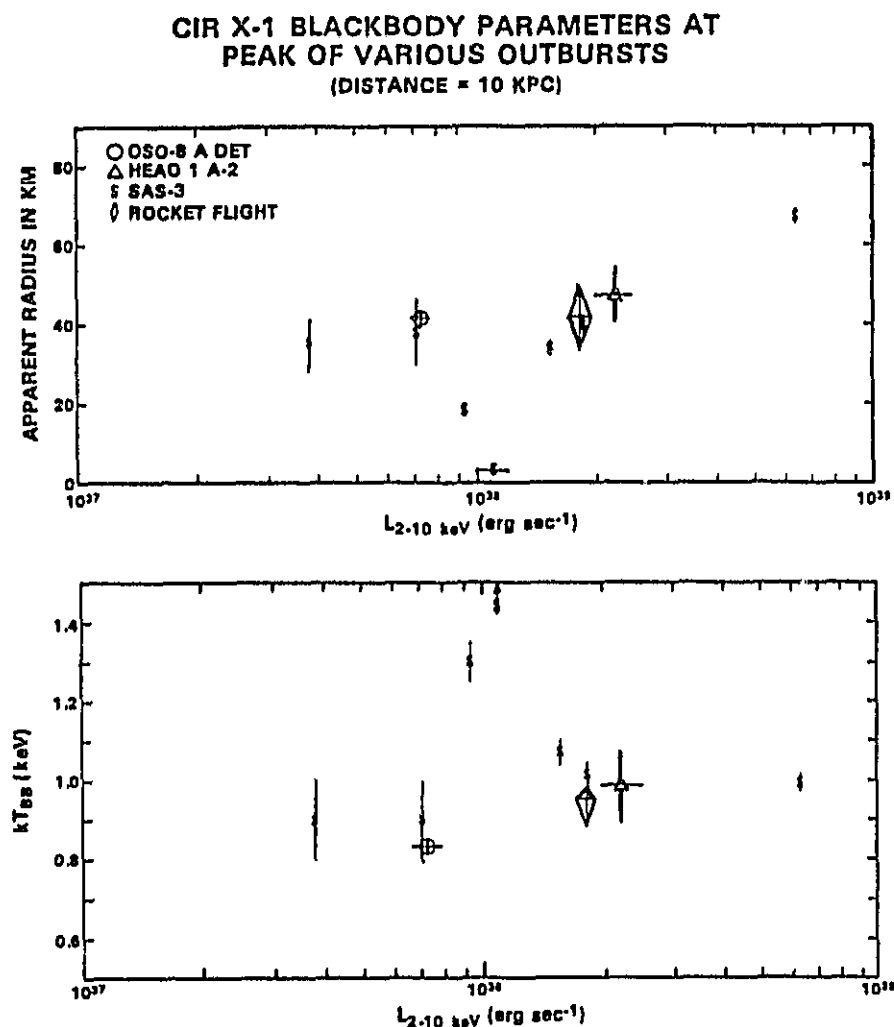
observations. In each case only the parameters from the period of maximum observed intensity are shown. The OSO-8 and HEAO-1 points correspond to the respective maximum intensity values shown in Figure 6-4.

The diamond corresponds to a rocket observation of Circinus reported by Margon et al. (1971), where the error on the blackbody temperature was read from Figure 2 of their paper and the blackbody size is determined from the quoted flux. The remaining points refer to SAS-3 observations of Circinus reported by Dower et al. (1982), with kT taken from their Table 2 and blackbody sizes calculated from the tabulated blackbody normalizations. Two of the SAS observations show spectra which are unusually hard for Circinus outburst peaks. They yield the points near (10 kpc distance) luminosity $\sim 10^{38}$ erg s$^{-1}$ with higher temperatures and smaller sizes than the others shown in the figure. It is not clear whether these points, determined from spectral fits to only 4-5 pulse height channels, correspond to source spectra which are not in fact blackbodies, or whether the blackbody parameters indicate a different regime for the optically thick component. For Goddard observations (5, 9 and 10) of low flux ($\sim 10^{-10}$ erg cm$^{-2}$ s$^{-1}$)   spectra near the nominal phase 0 transition, blackbody fits are statistically as good as power law or thin thermal bremsstrahlung fits, yielding radii of 2-5 km and kT's slightly greater than 1 keV. They are not included in Figure 7-13 because there is no reason to prefer such fits and similarity to other observations in which the emission is clearly optically thin suggests such models are more likely.

Thus, Circinus observations to date distinguish a typical high intensity component which to good approximation is a blackbody with a size approximately 40 km, roughly constant through large variations in

intensity, although not invariable. It is interesting that the source
GX339-4 -- which has been suggested as a black hole candidate on the basis
of fast time variations (Samimi et al. 1979) and demonstration of soft-hard
spectrum transitions analogous to those of Cygnus X-1 (Motch et al. 1983;
Ricketts       1983) -- has a soft component spectrum similar to
Circinus. Overlapping HEAO-1 A2 and OSO-8 observations in 1978 found kT =
0.45 keV, HEAO-2 SSS observations in 1980, kT = 0.55 keV (Robinson-Saba et
al. 1983). Ricketts (1983) did not try a blackbody component, but the
Ariel VI spectra are similar. The distance to GX339-4 is not well known,
but the measured blackbody normalization implies an apparent radius of ~ 36
km for a spherical emitter at the distance of 4 kpc suggested by Doxsey et
al. (1979). This value of $R_a$ is similar to the typical value for
Circinus. The corresponding luminosities were $10^{37}$ erg s$^{-1}$ and $10^{38}$ erg
s$^{-1}$ for the blackbody component for GX339-4 and Circinus, respectively.

The high state spectrum for Cygnus X-1 has been described as a steep
power law, variable in slope (Tananbaum 1972; Boldt 1975). However,
Chiappetti et al. (1983) described Ariel-5 observations of a May 1975
transition in terms of a blackbody with kT = 0.30-0.35 keV and a power law
at energies above 3 keV. OSO-8 data for a transition from low to high
state in November 1975 can be described equally well by a blackbody of
kT ~ 0.37 keV and apparent radius of 74 km plus a relatively flat power
law ($\alpha_N$ = 2.3) as it can by two power laws. Thus the apparent power law
character of the high state for Cygnus X-1 may be an artifact of the
detector bandwidths for high state observations. High state soft X-ray (<
1 keV) observations have not yet been reported.

Recently, velocity curves have indicated two additional black hole
candidates: LMC X-3 (Cowley, Crampton, and Hutchings 1982; Cowley et al.

1983) and LMCX-1 (Hutchings, Crampton, and Cowley 1983). White and Marshall (1983) have pointed out that the spectra of both these sources are as "ultrasoft" in comparison to most compact galactic sources as Cyg X-1 and GX339-4 in its high state. They report thermal bremsstrahlung and power law fits which, by comparison to the fits of Circinus and GX339-4 data to these models, may also give kT < 1 keV for blackbody fits.

Thus a low temperature optically thick component in some states of the system may be characteristic of accretion onto black holes. There are sources which are probably neutron stars which also exhibit approximately blackbody spectra. However, the parameters tend to be significantly different. The peak temperatures of Type I X-ray bursts are ≈ 3 keV. Measurements of the temperature during their decay are made down to ~ 1 keV, but the apparent sizes are ~ 6.5 km (van Paradijs 1978). At least below 15 keV the spectrum of the Cygnus X-3 high state appears optically thick (Serlemitsos et al. 1975), with kT ~ 1.2 keV. Again the apparent radius of 15 km is closer to radii expected for a neutron star than the 35-70 km of the blackhole candidates Circinus, GX339-4 and Cygnus X-1. A good fit to spectra of some galactic bulge sources, including Sco X-1, was obtained for a mixture of optically thick and thin emission (Serlemitsos, Swank and Saba 1980). The values of kT and apparent radius given are for the blackbody components, assuming values of their distances in accordance with available information. Again the apparent radii of the black hole candidates are larger and the temperatures smaller. Some of these galactic bulge sources have been discovered to be bursters in Hakucho observations (e.g. Makishima et al. 1983). By extrapolation we therefore expect most of these sources to be neutron stars.

The recurring values of apparent radius for Circinus (and GX 339-4)

near 40 km thus distinguish these sources from the bursters and from the majority of galactic bulge sources. If we assume the emissivity is indeed ~ 1 and the deduced size a good representation of the size of the emission region, interesting conclusions can be drawn. Given the firm lower limit of 8 kpc to Circinus given by Goss and Mebold (1977), the blackbody emission is not likely to be occurring at the surface of a neutron star. The minimum distance corresponds to an apparent radius of ~ 30 km for a spherical emitter, which lies outside the allowed range of neutron star radii even for the stiffest equations of state usually considered. The hatched area in Figure 7-14 shows the "allowed" region of surface radius R versus neutron star mass M which falls between the soft equation of state which gives the left boundary and a stiff equation of state on the right (cf. Arnett and Bowers 1977). The parallel solid lines give curves of fixed $R/R_M$, where the "gravitational radius"
$R_M = GM/C^2 \simeq 1.48 \; (\frac{M}{M_0})$ km. The line $R = 2 \; R_M$ corresponds to the Schwarzschild radius for mass M. The dashed curves show the variation with mass of true radius from apparent radius, $R_a$, for several values of $R_a$ outside a spherical mass distribution when a general relativistic correction is made for the effect of gravity. In the range $R \geq 3 \; R_M$ for which $R_a \geq 3\sqrt{3} \; R_M$ , the apparent radius as measured by a distant observer is related to the local radius R by the expression

$$\frac{R_a}{R} = [ \; 1 - 2 \; \frac{R_M}{R} \; ]^{-1/2} \; . \qquad \text{7-10}$$

Using the $R(R_a, M)$ curve, we estimate that with the relativistic correction included, an apparent radius of 40 km corresponds to the Schwarzschild radius (= $2 \; R_M$) of a black hole of $\gtrsim 5 \; M_0$. A radius of 40 km

Figure 7-14

The hatched area in the figure shows the "allowed" region of surface radius R versus neutron star mass M which falls between the soft equation of state which gives the left boundary and a stiff equation of state on the right (cf. Arnett and Bowers 1977). The parallel solid lines jive curves of fixed $R/R_M$, where the "gravitational radius" $R_M = GM/C^2 \approx 1.48$ km $(\frac{M}{M_0})$. The dashed curves show the variation with mass of true radius from apparent radius, $R_a$, for several values of $R_a$ outside a spherical mass distribution when the bending of light rays due to gravitational curvature is taken into account.

Figure 7-14
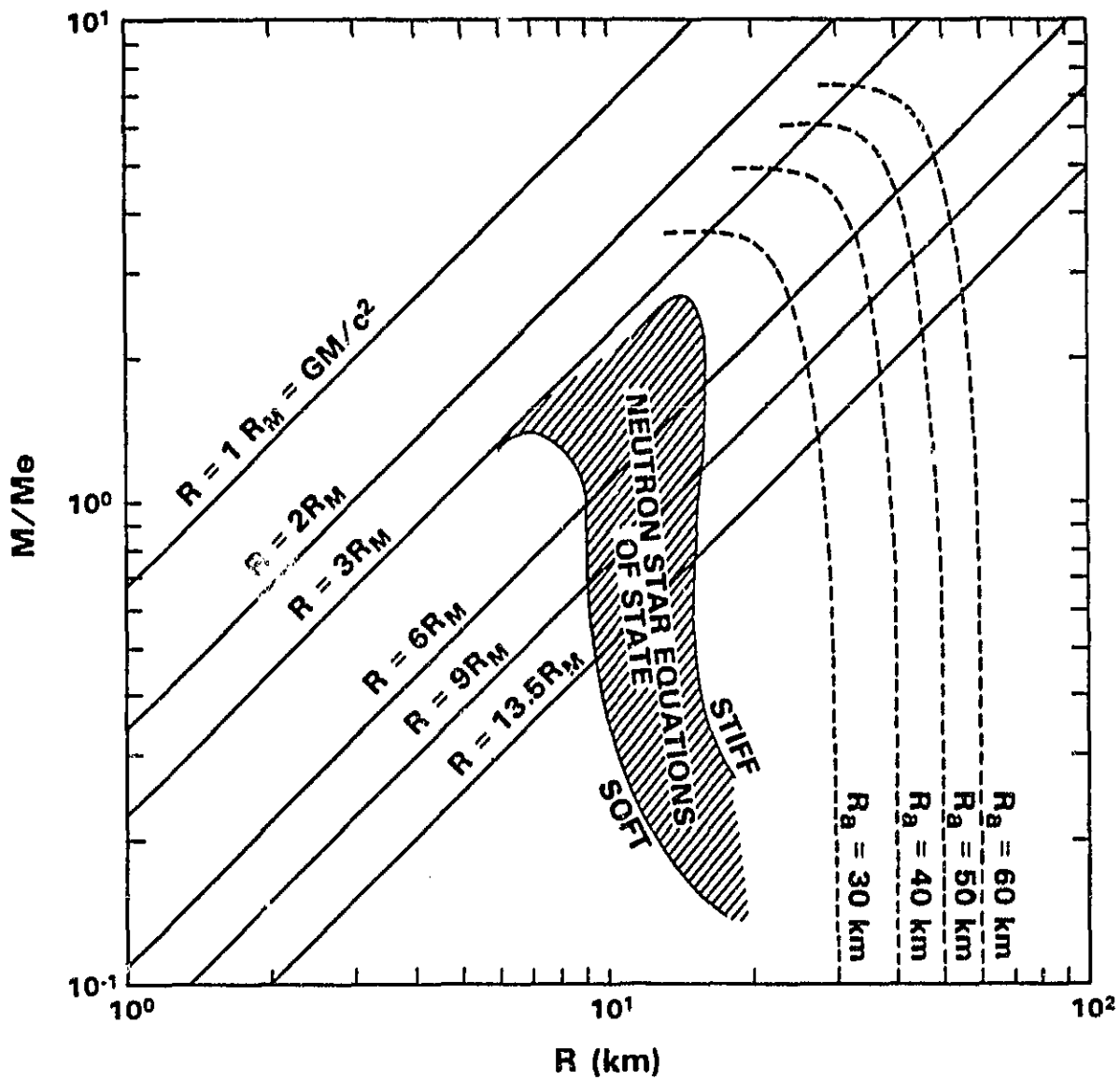
corresponds to the innermost stable orbit ($R_O = 6 R_M$) of ~ a 4 $M_O$ black hole. For a maximally rotating Kerr black hole, the radius of the innermost stable orbit depends on the direction of the orbital rotation relative to the black hole rotation, with $R_O = 1 R_M$ for rotation in the same sense and $R_O = 9 R_M$ for the opposite sense (Bardeen 1970). Thus, an apparent radius of 40 km corresponds to the radius of the innermost stable orbit around a maximal Kerr black hole exceeding 5 $M_O$ for the former case and a mass of ~ 2.6 $M_O$ for the latter. The appropriate relation $R(R_a, M)$ has not been worked out. It would depend on i and optical depths. Applying Thorne's (1974) work on black-hole spin up by mass accretion from a disk, Boldt and Leiter (1981) deduce an expression for the spinup time

$$\Delta\tau = 4 \times 10^8 \ \epsilon(\dot{1}-\epsilon)^{-1}(L/L_{Edd})^{-1} \ yr, \qquad\qquad 7-11$$

with $\epsilon$ a measure of the average radiation efficiency. Taking $\epsilon \sim 1$, we estimate that the time it would take for a black hole in the Circinus system to spin up to the maximal Kerr value from regular episodes of accretion near the Eddington limit is > $10^8$ years, much longer than the estimated age ($10^4$ - $10^5$ years) of the eccentric binary system. Therefore, if the compact object is a black hole, unless it was formed with maximal angular momentum, it is probably not rotating rapidly.

If the emission region corresponds to the brightest annulus of a standard accretion disk near 13.5 $R_M$ (Shakura and Sunyaev 1973) we need to replace the cross-sectional area of a sphere, $\pi R^2$, with the cross-section of the disk annulus perpendicular to the line of sight to determine the appropriate apparent radius:

$$2\pi r_a \Delta r_a \cos i = \pi R_a^{\,2}, \qquad\qquad\qquad 7\text{-}12$$

where $r_a$ is the apparent radius in the disk, $\Delta r_a$ is the width of the emitting annulus and $i$ is the inclination of the disk to the line of sight. Choosing $\Delta r_a \sim r_a$, this yields

$$r_a^{\,2} = R_a^{\,2}/(2 \cos i). \qquad\qquad\qquad 7\text{-}13$$

For $i > 60^0$ the radius of the annulus is larger than the radius of the sphere. Assuming the disk lies in the plane of the binary orbit, we can pick $i = 75^0$ in keeping with the orbital inclination suggested by Murdin et al. (1980) to obtain $r_a \approx 1.4\, R_a \sim 56$ km, consistent with a central object mass of $\sim 3\, M_0$. For an effective emitting radius $R = 13.5\, R_M$, the relativistic correction to the apparent radius is less important than the uncertainty in distance or source geometry, so that a more careful relativistic treatment of the effective size of the emitting region is not warranted.

From Equation 3-21 it appears that an apparent radius of 40-60 km is much too small to be the boundary of the inner region of the disk for a compact object with $M_X \gtrsim 1\, M_0$ and a mass accretion rate $> 10^{17}$ g s$^{-1}$ as required by the observed luminosity. If the inner region was unstable as suggested by Lightman (see discussion in §III. B.3), the expanded inner disk should be optically thin. Lightman's model was developed with Cyg X-1 in mind. The low energy spectrum of Cyg X-1 is a steep power law and the model recommended itself as it could so produce this spectrum with a large low energy flux, possibly from an inner optically thick disk or from cyclotron emission of electrons in coherent magnetic fields in the

accretion disk.  The spectra observed from Circinus and GX 339-4 suggest that either the instability did not occur or that it led to a solution in which the disk is optically thick racner than thin.

## 2.  Low Flux Component(s)

The Goddard observations of Circinus presented in Chapters V and VI provide evidence for one or more components distinct from the optically thick outburst component.  Away from times of outburst, the low level residual flux (Observations 1,3,4), which may be present throughout the outburst (Observation 1), has a spectrum best characterized by a thin thermal bremsstrahlung or power law fit.  At times there is good evidence that this flux includes strong iron line emission (Observations 1,3). Apart from flaring (Observations 1,3,8) sometimes observed around the time of ephemeris phase 0 (marking the end of the larger outbursts), this component shows a fairly steady flux and spectral shape on the timescale of a few days (Observation 1), though these are not invariable from cycle to cycle.  Long term coverage of the source has not been adequate to characterize the appropriate timescales and conditions for variations in this component.  The Ariel-5 All Sky Monitor is not sensitive to the residual flux levels and records no information on the spectral shape. More sensitive instruments with moderate spectral resolution have not monitored the source for several contiguous cycles.  The available snapshots of the source do not show a tight correlation of spectral slope or low energy turnover for this low flux component with either source intensity (refer to Figure 7-11 for $I_{2-10} \lesssim 10^{-9}$ erg cm$^{-2}$s$^{-1}$) or binary phase.  Figure 7-15 shows a plot versus binary phase of the photon index and equivalent column density for power law fits to low state spectra

Figure 7-15


Power law fit parameters for low state spectra are plotted versus
binary phase for observations of Circinus by Goddard instruments and the
Ariel-5 spectrometer. The two points (near phases 0 and 0.45) which show
high column densities are those noted for Figure 7-12, corresponding to a
flaring episode and a pre-outburst period.

# CIR X-1 LOW STATE SPECTRA POWER LAW FIT PARAMETERS VERSUS PHASE

| THIS THESIS

♦ CHIAPPETTI AND BELL-BURNELL 1982
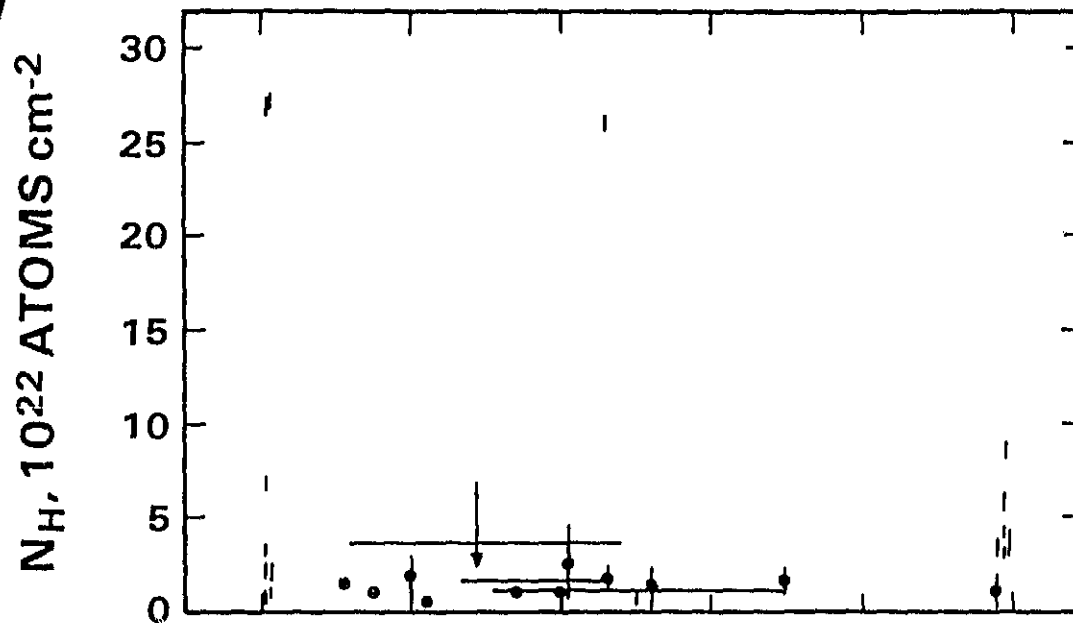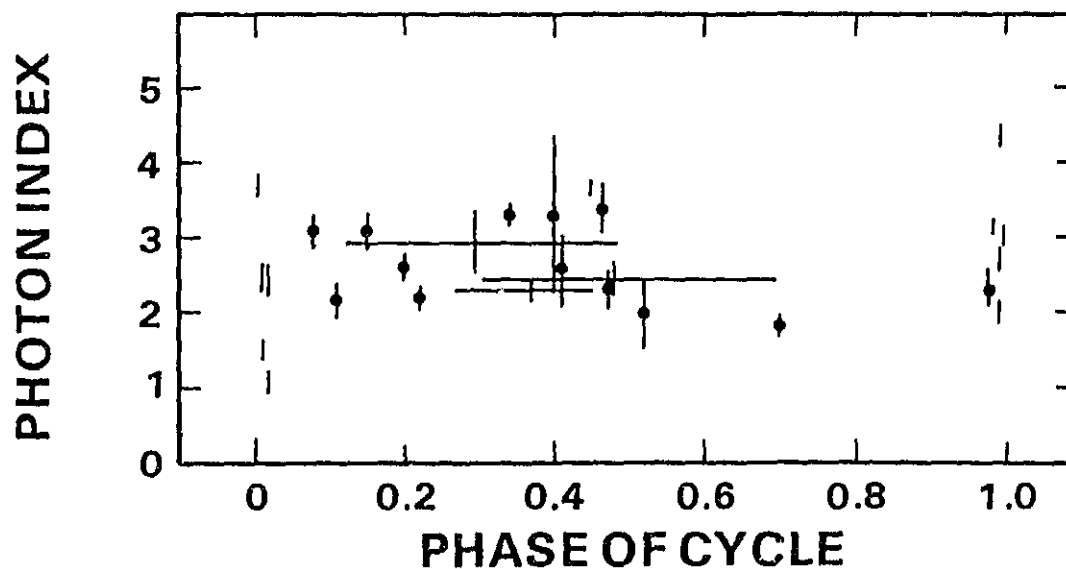
covered by the Goddard instruments (Table 6-6a) and the Ariel-5 spectrometer (Chiappetti and Bell-Burnell 1982). (Only power law fit parameters were published for the latter sample. For the Goddard data, reference to Table 6-6 shows that the power law model frequently gives somewhat better fits than a thin thermal bremsstrahlung model though sometimes neither model is acceptable, even with the inclusion of a narrow iron line feature near 7 keV, which sometimes improves the fits significantly.) The two points in the figure (after phase 0 and near phase 0.45) which show high column densities are those noted above in the discussion of Figure 7-12, corresponding to a flaring episode (Observation 8) and a period just prior to the onset of a large outburst (Observation 2). It may be more natural to associate the latter case with the outburst component: the flux level is a factor of $\sim 3$ higher than that for the two days preceding, the column density is a factor of $\gtrsim 4$ higher, and the inferred intrinsic luminosity is comparable to that seen during the outburst that follows.

It also seems natural to suppose that the post-transition flares (Observations 1,3, and 8) may involve a component different from that of the adjacent low level flux: the flux enhancements are large, involving an abrupt spectral change, on timescales short compared to other observed changes in the post-outburst flux. As discussed in Chapter VI, the flare events in Observations 1 and 8 can be described in terms of the transient presence of an additional component which is flatter and more absorbed than the adjacent lower flux component. The spectral change in the $\sim 5$ minute flare in Observation 3 is not inconsistent with this picture. Apart from these special cases which may represent emission from different regions, the column densities associated with the low flux component are usually

rather low compared to the maximum values associated with the optically thick component. This sample of data shows no clear trend of photon index or column density with phase for the low flux spectra. There is in fact some evidence that the low flux spectrum and intensity, aside from flares, may be roughly steady on a time scale of days. Data from the OSO-8 A detector pointed observation (Observation 1) combined with an Ariel-5 spectrum at the end of the same cycle (Chiappetti and Bell-Burnell 1982) show a ~ 2-20 keV continuum spectrum which can be described by a power law of photon index ~ 2.2, with a source strength which varies by no more than about a factor of e in 15 days. The OSO data are consistent with the presence of this component at comparable strength and column density throughout the outburst of the optically thick component with its strong optical depth evolution.

Comparison of the Goddard spectroscopic observations with the long term All Sky Monitor lightcurve do not show an obvious correlation of the strength or shape of the low flux component with the strength, duty-cycle, or spectrum of the previous outburst, though there may be some tendency for a softer, weaker residual component during times of generally low outbursts. As suggested most clearly by Observation 2, for outbursts which end early compared to the ephemeris for transitions, there may be a period before phase 0 where the flux level is low compared to the peak intensity but higher than the residual after phase 0. If the extra flux represents a component associated with the outburst rather than the steadier source, its presence could complicate a search for systematic changes of the latter.

While further study is required to pin down the properties of this low level, optically thin component, its existence constrains models of the optically thick component in terms of system-wide optical depth effects.

While short-term flares with timescales of some minutes to hours may have high associated column densities, and there has been at least one observation of a highly absorbed pre-outburst spectrum at low flux, there appears to be a quiescent component associated with Circinus for which the absorbing column density is generally low and not obviously correlated with binary phase. Long term variability of the strength and spectral shape of this component, combined with the agreement of the SSS and MPC detections in overlapping energy bands despite their different fields of view argue that its source is truly Circinus. (Any contaminating source would have to be as bright as ~ 20 U.F.U., highly variable and within 3' of Circinus.)

### a. Possible Interpretations of the Optically Thin Component

Interpretations of the optically thin component from Circinus can be roughly divided into two classes, based essentially on size. The emission region could be fairly compact, e.g. $\lesssim 10^{10}$ cm or possibly even < $10^8$ cm, though presumably larger than the ~ 4 x $10^6$ cm of the blackbody component which shows large modulation and large column density effects. In this case the column density of neutral hydrogen across the orbit must be relatively unimportant for modulating low energy X-rays, and the picture of stellar wind optical depth effects presented by Murdin et al. has to be severely modified. A natural emission region to consider in a compact interpretation is an accretion disk. If the emission region is not compact, interpretations can be subclassed on the basis of whether the emission mechanism is thermal or nonthermal.

### i. Synchrotron Radiation

It is natural to ask whether the quiescent X-ray component could

be related to the quiescent radio component. The latter shows a nonthermal spectrum (Haynes et al. 1978) and has been interpreted as synchrotron emission by an electron population with number distribution $\propto E^{-2}$ from weak magnetic fields in the stellar wind (Haynes et al. 1980). Recent observations (Preston et al. 1983) imply that the quiescent radio emitting region is very large ($\gtrsim 3 \times 10^{16}$ cm) compared to the size of the semi-major axis of the orbit ($\sim 7 \; 10^{12}$ cm). The extrapolation of the 1977 May quiescent radio spectrum, $S(\nu) = 0.3 \; (\frac{\nu}{5 \; GHz})^{-0.5\pm0.05}$ Jy, into the X-ray regime is somewhat less than a factor of 2 higher than the quiescent X-ray flux level at $\sim 3$ keV during Observations 1 and 3. The later X-ray measurements show a weaker residual, but there is also evidence that the general level of the quiescent radio component fell during the three years succeeding 1977 (Preston et al. 1983). The X-ray quiescent spectra are steeper than the radio spectra (energy spectral slopes in the range -1 to -2) implying a break in the radiation spectrum, possibly due to a break in the electron spectrum from radiative losses. The radiation spectrum from electrons of energy E peaks at a frequency (Pacholczyk 1970)

$$\nu_{Hz} \approx 0.29 \; \nu_c \simeq 0.29 \; \frac{3e}{4\pi \; mc} \cdot B\perp \; (\frac{E}{mc^2})^2 \qquad 7\text{-}14$$
$$\approx 3.0 \; 10^5 \; B_{gauss} \; \gamma^2$$

The lifetime of an electron of Lorentz factor $\gamma$ to energy loss by synchrotron radiation in a magnetic field B is given by

$$\tau_{sync} \sim \frac{3 \times 10^7}{\gamma \; U_B} \; sec \approx \frac{7.5 \; 10^8}{\gamma \; B^2} \; sec \qquad 7\text{-}15$$

where $U_B = B^2/8\pi$, the magnetic field energy density. Requiring $\nu \sim 10^{18}$

Hz, we can use the above equation to eliminate the magnetic field strength, and write $\tau(\gamma)$ as

$$\tau_{sync} \approx 6.8 \; 10^{-17} \; \gamma^3 \; sec. \qquad\qquad 7\text{-}16$$

For Observation 1, where the quiescent component of the residual flux is steady for $\gtrsim 5$ days, a synchrotron interpretation requires $\gamma \gtrsim 1.8 \; 10^7$ and $B \lesssim 10^{-2}$ gauss, in the absence of continuous replenishment of the high energy electron population.

For the electrons of factor $\gamma$ to be responsible for synchrotron radiation, they must not have decayed by Compton cooling in scattering off of the stellar photons. Compton cooling proceeds with a timescale

$$\tau_{IC} \sim \frac{3 \times 10^7 \, sec}{\gamma \; U_{photon}} \qquad\qquad 7\text{-}17$$

where $U_{photon} = L/4\pi r^2 c = 0.0265 \; L_{38}/R_{14}^2$, with $r_{14} = r/10^{14}$ cm and $L_{38} = L/10^{38}$ erg cm$^{-2}$ s$^{-1}$. That is,

$$\tau_{IC} = \frac{1.1 \times 10^9 \; r_{14}^2 \; sec}{\gamma \; L_{38}} \; . \qquad\qquad 7\text{-}18$$

For $\gamma \sim 2 \times 10^7$, the observed constraint $\tau > 5$ days requires $r_{14}^2/L_{38} \gtrsim 8 \; 10^3$. Taking $L_{38} = 0.1$ as an estimate of the optical luminosity of the companion gives $r_{14} \gtrsim 28$. That is, Compton cooling will be as important as synchrotron radiation unless the emission region has a scale length $r \gg 3 \times 10^{15}$ cm. The quiescent radio emission region size of $r \gtrsim 3 \times 10^{16}$ cm deduced by Preston et al. (1983) meets this criterion.

## 11. Inverse Compton Scattering

Another possible source for the X-ray quiescent flux is inverse Compton scattering of the radio photons off of the electron population producing the quiescent radio synchrotron spectrum. This process is sometimes called synchrotron-self-Compton scattering (SSC). Since the scattered frequency $\nu_c$ is related to the initial frequency by (for $\gamma h\nu_i < mc^2$)

$$\nu_c \approx \gamma^2 \nu_i, \qquad \qquad 7\text{-}19$$

$\nu_c \sim 10^{18}$ Hz implies $\gamma \sim 10^4$ for $\nu_i \sim 10^{10}$, relaxing the lower limit on emission region size required for $\gamma \sim 10^7$ electrons. From Equations 3-28, 3-29, and 3-30, the ratio of the expected inverse Compton scattered flux, $F_{sc}$, to the extrapolation of the radio synchrotron spectrum into the X-ray regimes, $F_{Rx}$, is given by

$$\frac{F_{sc}}{F_{Rx}} = 2.77 \times 10^{-3} \, B^{-(1 + \alpha_E)} \, 10^{10(\alpha_E - 1/2)} \, (0.34)^{-(\alpha_E - 1/2)}$$

$$\cdot \left(\frac{F_R(\nu_1)}{1 \text{ Jy}}\right) \left(\frac{\nu_1}{10 \text{ GHz}}\right)^{\alpha_E} \left(\frac{d_{10}}{r_{12}}\right)^2 \ln\left(\frac{\gamma_2}{\gamma_1}\right), \qquad 7\text{-}20$$

with $\alpha_E$ the spectral index of the synchrotron spectrum, $F_R(\nu_1)$ the radio flux in Janskys at some frequency $\nu_1$, $d_{10}$ the distance to the X-ray source in units of 10 kpc, and $\gamma_1$ and $\gamma_2$ the upper and lower limits on the electron Lorentz factors for scattering into the X-ray regime. The ratio is fairly insensitive to the exact values of the limits.

(For $\gamma_2/\gamma_1$ ranging from 10 to $10^4$, $\ln(\gamma_2/\gamma_1)$ varies only from 2.3 to 9.2.) Taking the observed radio index $\alpha_E \approx 0.5$, $F_R$ (10 GHz) $\sim 0.3$, and $\ln(\gamma_2/\gamma_1) \sim 5$ gives

$$\frac{F_{SC}}{F_{Rx}} \approx 4 \times 10^{-4} \frac{B^{-(1+\alpha_E)}}{r_{12}^2} \qquad \text{7-21}$$

for $d_{10} = 1$. If the quiescent emitting region is as large as $3 \times 10^{16}$ cm as reported by Preston et al. (1983), the SSC process should not contribute much to the observed quiescent X-ray flux unless the B field is quite low ($\sim 10^{-8}$ gauss).

Since the quiescent infrared spectrum (Glass 1979) during the same general time period was more than a decade above the extrapolation of the radio flux into the infrared regime ($\nu_{IR} \sim 10^{14}$ Hz), inverse Compton scattering of IR photons by lower energy electrons ($\gamma \sim 10^2$) could be more important than SSC if the electron distribution producing the radio synchrotron spectrum extends down to this range. The ratio of X-ray flux from SSC scattering by $\gamma_{SC} \sim 10^4$ electrons to inverse Compton scattering of IR photons by $\gamma_{IC} \sim 10^2$ electrons is

$$\frac{F_{SC}}{F_{IC}} \approx \frac{n(\gamma=10^4)\ c\sigma\ \gamma_{SC}^2\ U_R}{n(\gamma=10^2)\ c\sigma\ \gamma_{IC}^2\ \xi\ U_{IR}}, \qquad \text{7-22}$$

where $U_R$ is the radio energy density, $U_{IR}$ is the IR energy density, and $\xi$ is a geometrical factor $\lesssim 1$ to allow for effective dilution of the flux from the compact IR source in the large volume of electrons. For an electron energy spectrum $\propto \gamma^{-\Gamma}$ and $\Gamma = 2$ as suggested by the quiescent

radio spectral index $\alpha_E = 0.5$, we take

$$n(\gamma) \sim \int_{\gamma}^{\gamma+\Delta\gamma} (\gamma')^{-2} \, d\gamma' \sim \frac{1}{\gamma} \, .$$
7-23

This gives

$$\frac{F_{SC}}{F_{IC}} \sim \frac{\gamma_{SC} \, \ell_R \, r_R^{-2}}{\xi \, \gamma_{IC} \, \ell_{IR} \, r_{IR}^{-2}}$$
7-24

If we take $\xi \sim r_{IR}^2/r_R^2$ (i.e. assume the dilution factor approximately offsets the inverse square increase in energy density for a compact photon source), and estimate quiescent radio and infrared luminosities $\ell_R \sim 10^{33}$ and $\ell_{IR} \sim 10^{37}$, we get

$$\frac{F_{SC}}{F_{IC}} \sim 10^{-2} \, .$$
7-25

that is, the contribution to the X-ray flux from inverse Compton scattering (of the IR photons off of $\gamma \sim 10^2$ electrons) may be of order 100 times greater than the contribution from SSC (scattering of the radio synchrotron spectrum off of $\gamma \sim 10^4$ electrons), provided the $\gamma \sim 10^2$ and $\gamma \sim 10^4$ electrons come from the same distribution and $\xi$ is not too small. The steepness of the X-ray quiescent component relative to the radio slope might be accounted for by the apparent rollover in the infrared spectrum. However, as discussed below, the high equivalent widths for iron line emission sometimes associated with the quiescent X-ray component suggests that part of the quiescent flux comes from soft thermal emission which

would also steepen the spectrum compared to the radio slope. If inverse Compton scattering of either the quiescent radio or infrared flux makes an important contribution to the quiescent X-ray flux, long term simultaneous radio and X-ray coverage of Circinus at sufficient sensitivity should show correlated variations of flux.

### iii. Fe Line Emission

The more intense quiescent fluxes show strong evidence of iron line emission. The equivalent widths (E.W.) are high, frequently $\gtrsim$ 500 e., which is greater than typical non-pulsating X-ray binary systems though less than the observed E.W. ($\gtrsim$ 1 keV) for Cyg X-3 during the low state and for 4U1822-37 which has been likened to Cyg X-3 (White and Holt 1982). SS433 and some of the X-ray pulsars show values similar to those of Circinus. While the observed E.W. for Circinus is frequently less than that expected for thermal emission from a plasma in collisional equilibrium (Raymond and Smith 1977) at the best fit temperature (refer to Table 6-6), the values are high compared to those determined for standard fluorescence calculations from available targets in a binary system (discussed in §III.C.2) unless the wind is quite dense or one sums up contributions of fluorescence from the wind, the companion surface, an accretion disk and perhaps a disk corona.

For the typical spectra observed for Circinus, the largest contribution to fluorescence comes from the wind. Following the treatment of Hatchett and McCray (1977) and Basko (1978) in §III.C.L, we can estimate the line equivalenth width from fluorescence of solar abundance iron in the wind of the companion to be

$$E.W. = 0.49 \ N_{11} \ D_{12} \ \frac{(E_{line}/E_{thresh})^{\alpha_N}}{\alpha_N + 2} \ keV \qquad 7\text{-}26$$

where $N_{11}$ is the number density at the X-ray source in units of $10^{11}$ cm$^{-3}$, $D_{12}$ is the separation of stellar centers in units of $10^{12}$ cm, and $\alpha_N$ is the power law photon index of the X-ray continuum. For cool material, the line center, $E_{line}$, is ~ 6.4 keV and the threshold energy, $E_{thresh}$, for fluorescence can be set equal to 7.1 keV. Taking as model parameters for the Circinus system $a = 7 \ 10^{12}$, $e = 0.7$, $R_p = 20 \ R_0$, and using the fast, dense wind parameters used for matching the OSO lightcurve (Figure 7-9) ( $\dot{M} = 2 \ 10^{-5} \ M_0 \ yr^{-1}$, $V_{wind} = 1000$ km s$^{-1}$, $N_{11} \ D_{12}$ ~ 5.6 at periastron passage), yields an E.W. ~ 600 eV, comparable to the values observed. However, fluorescence of the wind material by X-rays from the compact object should show a strong modulation with binary phase. At apastron, the value of $N_{11} \ D_{12}$, and the resulting line E.W. will be nearly a factor of 10 lower. The observed equivalent widths do not appear to show such a dependence on phase. In particular, the two strongest detections of equivalent widths in excess of 500 eV occurred near phases 0 and 0.4.

For optically thick fluorescence off of a surface such as the star or an accretion disk, the line equivalent width is proportional to the solid angle. From Equation 3-44, we estimate

$$E.W. \sim 0.5 \ (\frac{\Omega}{2\pi}) \ (\frac{E_{line}}{E_{thresh}})^{\alpha_N} \ \frac{1}{\alpha_N - 1} \ . \qquad 7\text{-}27$$

Fluorescence of the stellar surface by the compact object should also show a binary phase dependence, the change with phase in solid angle of the surface subtended at the X-ray source. At periastron, with $R_p/a$ ~ 0.2, $e = 0.7$, the line equivalent width is only ~ 60 eV. For a standard

accretion disk model, a similar amount can be achieved (Basko 1978). In the absence of eclipse, a steady disk would not show any particular binary phase dependence for line fluorescence. If the accretion disk has a substantial corona, the line E.W. could be more significant (Basko 1978; Bai 1980). Following Basko (refer to Chapter III. C), we have (cf. Eq. 3-43)

$$E.W._{corona} \simeq 4.3 \frac{\Delta\Omega}{4\pi} \tau_T \frac{(0.9)^{\alpha_N}}{(\alpha_N+2)} \text{ keV.} \qquad \text{7-28}$$

where $\tau_T$ is the optical depth in the disk to Thompson scattering. For $\Delta\Omega \sim 4\pi$ and $\alpha_N \sim 2$, this gives E.W.$_{corona} \sim 0.9 \tau_T$ keV. As $\tau_T \to 1$, this is more than sufficient to explain the observed equivalent width. However, a high optical depth to scattering would also be expected to smear the line. White and Holt (1982) interpret the Fe lines in Cyg X-3 and 4U1822-37 as produced by fluorescence off the disk by continuum X-rays backscattered onto it from a thick corona. The features in those 2 sources appear broadened. Such broadening is not required for the observed line from Circinus although the upper limit cf $\sim 0.75$ keV and the line energy would not be inconsistent with scattering in a corona with optical depth of a few.

It has been suggested (Basko 1980) that the high line equivalent widths observed for pulsating X-ray sources come from fluorescence off the Alfvén shell, which provides a fluorescing target with solid angle $\Delta\Omega \sim 4\pi$. Values of $\tau_T$ required to produce equivalent widths $\gtrsim 500$ eV which are sometimes seen would again be expected to distort the line and continuum if the shell is homogeneous. However, White, Swank and Holt (1983) have suggested that the shell coul be patchy, with thick regions

providing fluorescent material while the spectrum then emerges through the holes. Even if such a scenario can explain the X-ray pulsar lines, it is not clear whether it could also apply to Circinus. The ~ 40 km radius deduced for the optically thick component probably implies that the magnetic field strength is no more than ~ 2 x $10^9$ Gauss). During quiescent times, when the source luminosity is $\lesssim 10^{37}$ erg s$^{-1}$, the Alfvén radius should still be less than ~ 100 km (see Equation 3-17). We have argued above that the quiescent continuum probably comes from a region large compared to that of the optically thick component. Thus, if the fluorescing photons originate interior to the shell, they must not contribute significantly to the observed quiescent continuum. It is not clear whether a reasonable model can be derived which allows the line to be fluoresced by such an unseen continuum, which is heavily absorbed up to some high energy ($\gtrsim 7$ keV).

While high line equivalent widths are hard to achieve with fluorescence, they are readily produced by thermal emission at a few keV. In fact, if all of the observed quiescent flux from Circinus is assumed to be thermal, the observed equivalent widths are typically ~ a factor of 2 less than that predicted for collisional equilibrium from plasma with solar abundances (Raymond and Smith 1977). It seems likely that hot material is present in the system -- even nonthermal processes probably involved in the flares should produce hot gas via shocks. Since it seems reasonable to suppose that there could also be nonthermal flux, a natural explanation for the observed line equivalent widths might be the presence of a thermal component which contributes all or most of the line photons but only part of the continuum. With such a model it is not necessary to invoke an underabundance of iron or a lack of collisional equilibrium to explain the line in terms of thermal emission.

iv. Thermal Interpretation of Quiescent Component

The longest continuous observation of the quiescent component of Circinus with Goddard detectors, during the OSO point (Observation 1), showed no evidence for spectral change over the course of a week (apart from the brief hard flare at phase 0.01). If we assume that the flux was due to thermal emission at the fit temperature of $\sim 10^8$ K (kT = 8.4 keV), from a source which was not continuously heated, we can use the observed limits on its decay to estimate the minimum cooling rate (from thermal bremsstrahlung emission) and thus put a lower limit on the size of the emitting region. The thermal bremsstrahlung cooling time is given by Tucker (1975) as:

$$\tau_{TB} = \frac{3\ N_e\ kT}{L} \simeq \frac{1.8 \times 10^{11}}{N_e}\ T^{1/2}\ \text{sec} \qquad \text{7-29}$$

where L is the luminosity radiated, $N_e$ is the electron number and T is the electron temperature of the plasma.

For optically thin thermal emission from a plasma with cosmic abundances, Tucker writes the luminosity as

$$L \sim \int dV\ (2.4 \times 10^{-27}\ T^{1/2}\ N_e^2)\ \text{erg sec}^{-1}. \qquad \text{7-30}$$

For a uniform emitting region, the integral yields the integrand times the volume. Thus, substituting for $N_e$ in terms of the temperature and the cooling time, we have

$$V \sim 1.3\ 10^{29}\ L_{37}\ T_8^{-3/2}[\tau_{TB}(\text{sec})]^2, \qquad \text{7-31}$$

where $L_{37}$ is the thermal bremsstrahlung luminosity in units of $10^{37}$ erg s$^{-1}$ and $T_8$ is the plasma temperature in units of $10^8$ K. If we require $\tau_{TB} > 1$ week, and take $L_{37} \sim 0.5$ and $T = 8.4$ keV/k, this yields a radius for a spherically emitting volume of $\sim 1.8 \ 10^{13}$ cm, somewhat larger than the estimated major axis of the binary system. That is, if the quiescent component is due to thermal emission from a plasma which is not continuously heated, the emitting region is larger than the binary system.

For a region that large, the Compton cooling of the thermal gas due to scattering of the companion starlight should be less important than radiative cooling by bremsstrahlung. The rate of Compton cooling per cm$^3$ for an electron density $n_e = N_e/V$ is given by

$$P_c = (n_e \ \sigma_T c) \ (\frac{4 \ kT_e}{m_e c^2}) \ (\frac{L_*}{4\pi r^2 c}) \ \text{erg cm}^{-3} \ \text{s}^{-1}, \qquad 7\text{-}32$$

where the first factor is the number of scatterings per second, the second is the average fractional energy loss per scattering (cf. §III.C.3), and the third is the energy density of starlight. The Compton cooling time is just the thermal energy density in the gas divided by this cooling rate:

$$\tau_{CC} = \frac{3 \ n_e kT_e}{P_c} = \frac{3\pi \ r^2 \ m_e c^2}{L_* \sigma_T} \sim \frac{9 \ 10^5 \ r_{12}^2 \ \text{sec}}{L_{*37}}, \qquad 7\text{-}33$$

where $L_{*37}$ is the luminosity of the companion in units of $10^{37}$ erg s$^{-1}$ and $r_{12}$ is the radius of the emission region in units of $10^{12}$ cm. For $r_{12} \sim 18$, this gives $\tau_{CC} \sim 2.9 \ 10^8 \ L_{*37}^{-1}$. If the companion were an early type supergiant with $L_{*37} \sim 10^2$, Compton cooling would be comparable to bremsstrahlung cooling for a thermal emitting region of that size.

However, such a companion is probably ruled out for Circinus (refer to §II.B and Figure 7-2) and $L_{*37}$ is probably < 10. We can compare the bremsstrahlung and Compton cooling rates for the general case:

$$\frac{\tau_{TB}}{\tau_{CC}} \simeq 6.3 \ 10^{-3} \ L_{*37} \ L_{37}^{-1/2} \ T_8^{3/4} \ R_{12}^{-1/2}, \qquad 7\text{-}34$$

with $L_{37}$ the bremsstrahlung luminosity in units of $10^{37}$ erg s$^{-1}$ as before. For any set of values of $L_{*37}$, $L_{37}$ and $T_8$, beyond some minimum size of the emission region, the above ratio is less than unity, i.e. the lifetime against Compton cooling is longer than the thermal bremsstrahlung lifetime, or thermal bremsstrahlung radiation dominates.

### b. X-Ray Flaring Component

There appear to be brief episodes of flaring from Circinus which are not directly associated with outbursts of the optically thick soft component. These events (cf. Observations 1,3,8) seem to occur preferentially after the soft flux transition to low levels, though that could be an observational selection effect based on their greater visibility during periods of low flux. The flaring generally involves spectral hardening, sometimes with an increased column density to absorption apparent. The flares may well involve an absorbed, hard variable component superposed on the lower level, unabsorbed quiescent component. At least for the Observation 1 flare, a power law model is significantly preferred over a thin thermal bremsstrahlung fit (reduced $\chi^2$'s were ~ 1.0 and ~ 1.6, respectively, for 53 degrees of freedom); further, the observed line E.W. of ~ 500 eV was much higher than that expected for thermal line emission for the fit kT = 59 ± 25 keV.

While the observed timescales are different, the X-ray flaring may be related to the radio flares observed after the decline of the soft X-ray outbursts. Most of the quasi-simultaneous coverage during flaring has not had good overlap or spectral information in both wave bands at once. The pictures built up from the accumulated X-ray and radio data suggest that the timescales for the radio events are longer, with rise times of order half a day and decay times of some days (Haynes et al. 1978; Whelan et al. 1977), though multiply peaked structure is observed on the timescale of hours (Thomas et al. 1978). The X-ray flaring episode reported here for Observation 1 (see Figure 5-3), showed a rise time ≲ an hour, a decay of ~ 3 hours and structure, including a large bursting "core" with a characteristic time of ~ 5 minutes (see Figure 6-15), on a timescale of minutes or less. We point out, however, that simultaneous radio and X-ray coverage of a post transition flare reported by Murdin et al. (1980) for 1-5 February 1978 showed similar slow temporal behavior at 5 GHz and in the 3-6 keV band. The X-ray measurement was made with the Ariel-5 All Sky Monitor and thus contained no spectral information, so it is not clear whether the X-ray flux had a spectrum more similar to the soft X-ray outbursts or to the hard X-ray flaring noted above. Overlapping radio and X-ray coverage of a post-transition flare during 23-28 April 1980 again showed a broad 3-10 keV X-ray envelope (Hayakawa 1982), roughly similar to that seen at 2.3 GHz (Preston et al. 1983). The X-ray lightcurve and hardness ratio reported from Hakucho data showed that the post transition flare had a (6-10 keV)/(3-6 keV) hardness ratio about a factor of 3.5 times as large as the soft pre-transition outburst.

Based primarily on good multiple frequency coverage of a radio flare observed in May 1977 (Haynes et al. 1978), the radio flares have been

interpreted in terms of the van der Laan (1966) model of an adiabatically expanding synchrotron plasma, used previously to explain the giant radio outbursts of Cygnus X-3 (Gregory and Seaquist 1974). Such a model accounts for the observed decrease in peak intensity at lower frequencies and explains the delay in occurrence of the peak at lower frequencies in terms of an evolving optical depth during the expansion. This picture is further supported by the slope of the steep rising part of the radio spectrum below ~ 4 GHz: the slope is consistent with the value of 2.5 expected for an optically thick synchrotron source with a power law energy spectrum, but not with the value of 2.0 expected for an optically thick free-free emitting source (Haynes et al. 1978).

Haynes, Lerche and Murdin (1980) suggest that the radio flares result from supercritical accretion onto the compact object near periastron passage. They estimate that the infalling material initially forms an accretion column ~ $10^{12}$ cm high (~ the stellar separation at periastron) with densities at the bottom of the column ~ $10^{18-19}$ cm$^{-3}$, and a density distribution $\propto R^{-3/2}$, measured from the compact object. Then, they argue, rapid buildup of radiation pressure sends a blast wave outward into an essentially stationary medium, with the radius of the shock given by

$$R_{shock} \sim 3 \times 10^9 \, \tau^{4/7} \text{ cm,} \qquad\qquad 7\text{-}35$$

with $\tau$ in seconds. After ~ a minute, $R_{shock} \sim 3 \times 10^{10}$ cm; after a day, $R_{shock} \sim 2 \times 10^{12}$ cm, of order the binary separation, at which point the density at the blast front is ~ $4 \times 10^{11}$ cm$^{-3}$, comparable to the particle density at the stellar surface. The authors argue that the radio spectrum is due to synchrotron radiation from accelerated electrons in the ambient

magnetic fields of the accreted material, with a plausible set of parameters $\gamma \sim 10^3 - 10^5$ and $B \sim 10^{-4} - 10^{-8}$ gauss. The observed evolution of the low energy turnover with time in their picture is then a result of changing synchrotron self-absorption, with the turnover frequency dropping as the shock expands and becomes optically thin to reabsorption at lower and lower frequencies.

Transparency to synchrotron self absorption at frequency $\nu$ requires that the emitting volume be larger than a critical size given by (cf. Tucker 1975)

$$R_{SA} \gtrsim 5.5 \; 10^{15} \; F_{Jy}(\nu)^{1/2} \; B^{1/4} \; \nu_q^{-5/4} d_{10} \; cm \qquad \qquad 7\text{-}36$$

with $F_{Jy}(\nu)$ in Jy, $\nu$ in GHz and $d_{10}$ the distance in units of 10 kpc. For $F_{Jy} = 2$ at $\nu_q = 5$, and $d_{10} = 1$ this requires

$$R > 10^{14} \; B^{1/4} \; cm. \qquad \qquad 7\text{-}37$$

For $B = 10^{-4}$ gauss, the emitting region must be $> 10^{13}$ cm. In the picture of Haynes, Lerche and Murain, the flare would not be seen at 5 GHz until after $\sim 10^5$ seconds when the shock had expanded to a dimension of order the stellar separation.

However, we note that their suggested parameters imply a regime where the Razin effect on propagation of the synchrotron radiation through the plasma should dominate the low energy turnover. This effect is important for frequencies such that (Tucker 1975)

$$\nu < \nu_R = \nu_p^2/\nu_B \approx 20 \; n_e \; B^{-1} \qquad \qquad 7\text{-}38$$

Thus, for $n_e \sim 3 \; 10^{11}$ cm$^{-3}$, $B < 10^{-4}$ gauss, the frequencies below $6 \times 10^{16}$

Hz are affected (i.e., far UV photons). This indicates that either the electron density must be considerably smaller or the B field larger for radio frequencies to be observed. From Equations 3-27 through 3-29, we have

$$n_e \sim k_e \int_{\gamma_1}^{\gamma_2} \gamma^{-2} \, d\gamma \sim k_e \, \gamma^{-1}, \qquad 7\text{-}39$$

with

$$k_e \simeq 1.77 \times 10^9 \cdot 10^{(\alpha_E - 1/2)} (0.95 \times 10^6)^{-(\alpha_E - 1/2)} B^{-(\alpha_E + 1)} \frac{d_{10}^2}{\varepsilon \, R_{12}^3}, \qquad 7\text{-}40$$

for an observed flare flux of 2 Jy at 5 GHz.

Putting $\alpha_E = 1/2$ and $\gamma = 10^4 \, \gamma_4$, this becomes

$$n_e \sim 1.77 \times 10^5 \, B^{-1.5} \frac{d_{10}^2}{\varepsilon \, R_{12}^3} \, \gamma_4^{-1}. \qquad 7\text{-}41$$

This allows us to write the Razin turnover frequency as

$$\nu_R \simeq 3.5 \times 10^6 \, B^{-2.5} \frac{d_{10}^2}{\varepsilon \, R_{12}^3} \, \gamma_4^{-1}. \qquad 7\text{-}42$$

To make $\nu_R < 5 \times 10^9$ Hz for $B \simeq 10^{-4}$ gauss (for which $\gamma_4 \sim 1$ makes GHz radio flux) requires an emitting volume with $R_{12} \gtrsim 200$ for $d = 10$ kpc.

If the radius of the radio emitting region is as small as $10^{12}$ cm (and the B field is $\lesssim 10^{-4}$ gauss), we might expect changes in the radio flux on timescales of order minutes. Changes due to the proposed shock expansion should be rather slow, of order a day, since the shock velocity

$$V_{shock} = \frac{d}{dt} (3 \times 10^9 \, \tau^{4/7}) \simeq 2 \times 10^9 \, \tau^{-3/7} \text{ cm s}^{-1}, \qquad 7\text{-}43$$

is $\sim 100$ km $s^{-1}$ at $10^5$ seconds, implying a characteristic timescale for changes of order

$$\tau_{shock} \sim \frac{R_{shock}}{V_{shock}} \sim 10^5 \text{ seconds.} \qquad 7\text{-}44$$

However, the light travel time across the volume is only 33 seconds, and the cooling time for the synchrotron-producing electrons due to inverse Compton scattering of the IR and optical photons from the companion is quite small for $B \lesssim 10^{-4}$ (requiring $\gamma \gtrsim 10^4$ to produce gigahertz synchrotron radiation):

$$\tau_{IC} \approx 10^2 \ r_{12}^2 \ \gamma_4^{-1} \ L_{37}^{-1} \ \text{sec} \qquad 7\text{-}45$$

(cf. Equation 7-18). Large changes in the radio flux are not seen on timescales this short, suggesting that the emitting region or the B field (or both) should be considerably larger. For a region as small as $10^{12}$ cm, electrons of $\gamma \sim 10^4$ should produce copious X-rays from inverse Compton radiation of the radio synchrotron photons. Again using Equation 7-19 to relate the ratio of synchrotron self-Compton radiation to the extrapolation of the radio flare synchrotron into the X-ray regime, we have for $\alpha_E = 0.5$:

$$\frac{F_{SC}}{F_{Rx}} = 2.77 \times 10^{-3} \ B^{-1.5} \ (\frac{F_R(\nu_1)}{1 \text{ Jy}}) \ (\frac{\nu_1}{10 \text{ GHz}})^{0.5} \ (\frac{d_{10}}{r_{12}})^2 \ \ell n \ \frac{\gamma_2}{\gamma_1} . \qquad 7\text{-}46$$

Taking the observed value $F_R$ (5 GHz) = 2 Jy, assuming $d_{10} = 1$, and estimating $\ell n \ \frac{\gamma_2}{\gamma_1} \sim 5$ gives:

$$\frac{F_{SC}}{F_{Rx}} \approx 6 \ 10^4 \ (B_{-4})^{-1.5} \ r_{12}^{-2}, \qquad 7\text{-}47$$

with $B_{-4}$ the magnetic field in units of $10^{-4}$ gauss. This ratio predicts an X-ray flaring flux $\gtrsim 10^3$ times that observed.

If we apply to the IR flares the argument used above to estimate inverse Compton scattering of the IR quiescent flux by $\gamma \sim 10^2$ electrons, taking the ratio of luminosity in the IR flare to be $\sim 10^4$ times the radio flare luminosity, we again expect that inverse Compton scattering of IR photons will give $\sim 10^2$ times more X-ray flux than the value calculated for SSC, provided the electrons in both cases belong to the same distribution. With this proviso, we again conclude that either the B field is stronger than $10^{-4}$ gauss (so that the observed radio spectrum does not require such a high density of electrons which then contribute to inverse Compton scattering) or the radio emitting region is much larger than $10^{12}$ cm or both. It may be quite reasonable for the magnetic field close to the compact object to be considerably higher than $10^{-4}$ gauss, e.g., due to enhancement in an accretion disk or to the presence of a weak magnetosphere around a neutron star. For $B \sim 10^{-2}$ gauss, the predicted X-ray flux could be brought to a reasonable level by taking a radio emitting region of size $\gtrsim 10^{13}$ cm. This combination of B and R would also be compatible with the criterion that $\nu \sim 5$ GHz be above the Razin turnover before $\tau \sim 10^5$ seconds (measured from periastron passage).

The X-ray flares are observed to show faster changes than the radio. The smaller, shorter-lived flares may occur preferentially before or in the early part of the radio flares. If the X-rays are due to inverse Compton of the IR, they could be coming from a region small compared to the radio emitting region, either because they are generated before the cloud has

expanded to the point where it is transparent to radio frequencies, or because the IR source is compact (e.g., coming from the outer part of an accretion disk).

Whether or not the X-rays are produced by inverse Compton radiation, if there are electrons with $\gamma \sim 10^2$ in the vicinity of the X-ray source of $\sim 10^{37}$ erg s$^{-1}$ luminosity, inverse Compton scattering should produce comparable $\gamma$-ray luminosity at $\sim 100$ MeV. Averaged over the 16.6 day binary period, the average $\gamma$-ray flux expected is about the same as the upper limit estimated from COS B observations of $\sim 2 \times 10^{-6}$ photons cm$^{-2}$ s$^{-1}$ (Bignami 1982). (This value corresponds to the $> 100$ MeV intensity measured for the closest source in the region of the galactic plane near Circinus.)

Similar considerations have been applied by Seaquist et al. (1982) to the source SS433, which shows correlated flare behavior at X-ray and radio frequencies. With more information about the magnetic field in the core of the system, the nature of the optical companion, and details of the radio/X-ray correlations, those authors deduce $B \sim 10^{-2}$, a flare emission region $\gtrsim 10^{14}$ cm from the stellar object and a quiescent source region of radius $\gtrsim 10^{16}$ cm.

### c. Accretion Disk Interpretation of Low Flux Component

As discussed in Chapter II, infrared and optical observations of Circinus -- the approximately constant infrared colors with changing intensity, the double-peaked Hα profiles and the large correlated drop in IR and optical magnitudes -- are most readily interpreted in terms of an accretion disk (Nicolson, Feast and Glass 1980). The expected accretion conditions -- tidal lobe overflow near periastron passage or accretion from

a wind slow enough to produce $\gtrsim 10^{38}$ erg sec$^{-1}$ luminosities -- also argue or the likely presence of at least a small disk ($\sim 10^{10}$ cm) at least some or the time (cf. Figures 7-2 and 7-11). An accretion disk provides a natural mechanism for providing a low level $\sim$ steady flux. From Equation 3-20 we see that the characteristic radial flow timescale for a $10^{10}$ cm disk around a 1-2 $M_0$ compact object with an average accretion rate of $10^{-9}$ $M_0$ yr$^{-1}$ (corresponding to an accretion luminosity of $\lesssim 10^{37}$ erg s$^{-1}$) is 2-3 times the binary period for a value of the viscosity parameter $\alpha = 0.1$. It is not obvious whether the observed quiescent X-ray spectrum (consistent with a power law of photon index $\alpha_N \sim 2$-3 or thin thermal bremsstrahlung of $kT \sim 4$-8 keV) could be produced in a region of the disk outside the $\sim 40$ km radius apparently associated with the highly variable optically thick component, as it probably must be to avoid sharing the heavy absorption of that component. Normally it is assumed that X-rays with energies greater than a few keV are produced in the inner part of the disk.

In any case, if the region emitting the quiescent component is less than or order of the size of the binary system, the lack of observed absorption for it implies that there are no system-wide large optical depths. Thus the observed column densities for the optically thick component and the flares would be transient and local to the regions producing these components.

There is no evidence that this low flux component shows the sub-second chaotic fluctuations of Cygnus X-1 in the low state. While short-term fluctuations do occur for Circinus, they seem to be associated with the softer, optically thick component. Flare events do occur in the absence of the optically thick component, but they appear to be characterized by timescales of minutes or longer.

C-4

The spectral slope of the residual "hard" component for Circinus is steeper ($\alpha_N \gtrsim 2$) than that of the low state hard spectrum of either Cygnus X-1 or GX339-4 ($\alpha_N \sim 1.5$). It is also steeper than the hard tail ($\alpha_N \sim 1.7$) of the high state spectrum of Cygnus X-1, though the high energy tail of GX339-4 may also be quite steep. Goddard OSO-8 A detector observations of GX339-4 and overlapping HEAO A-2 scanning observations in Fall 1978 indicate that the tail at that time had a power law photon index $\alpha_N \gtrsim 3$.

The quiescent component of Circinus has a 2-10 keV luminosity $\lesssim$ a tenth of the total luminosity of the outburst component. If it hides a high energy tail during the outburst, such a tail has a smaller fraction of the total luminosity than does the high energy tail of Cygnus X-1 during the high state. From the spectral fits in Figure 2 of Tananbaum et al. (1972), we find that the 2-10 keV flux in the harder component du ing the high state gives more than 20% of the luminosity; the hard spectrum flux during the low state is slightly higher, giving a comparable fraction of the combined high state flux in the 2-10 keV band. However, the Goddard OSO and HEAO A-2 observations of GX339-4 show that the hard component during the high state gives less than 10% of the 2-10 keV flux, while the hard spectrum during the low state gives nearly half of the combined high state flux in the 2-10 keV band.

Circinus X-1 briefly reaches luminosities ($\gtrsim 2 \times 10^{38}$ erg s$^{-1}$) an order of magnitude larger than those inferred for GX 339-4 and Cygnus X-1 (assuming respective distances 10, 4, and 2.5 kpc). The accretion conditions for Circinus may be sufficiently extreme or sufficiently transitory that the configurations achieved in Cygnus X-1 and GX 339-4 are never reached.

## C. Fluctuations in the Optically Thick Component

As we have shown above, the optically thick outburst component seen from Circinus probably comes from a small region, perhaps the maximum emission region ($\approx 13.5 \ GM_x/c^2$) in the inner part of an accretion disk. However the corresponding fluctuation timescales found for Observations 1 and 2 are of the order of seconds, orders of magnitude larger than the Kepler rotation time, $\sim 4 \ (\frac{M_x}{M_o})^{-1/2}$ msec at a radius of 40 km, or the various other timescales generally associated with the inner part of a disk, such as the light-crossing time or the electron thermal time. Various instabilities in the inner region are thought to scale as $(\alpha \ \omega_k)^{-1} \approx 7 \ 10^{-4} \ \alpha^{-1} \ (\frac{M_x}{M_o})^{-1/2}$ seconds at 40 km or, in some cases, $(\Lambda/H_o)^2$ times as large where $\Lambda$ is the wavelength of the instability and $H_o$ is the disk equilibrium half-thickness (see §III.B). Since $\Lambda << R$ is required to preserve the disk structure, even the last of these will give a timescale $<<$ seconds in the inner disk unless $\alpha$ is quite small. One longer timescale associated with the inner disk is the radial drift time; from Equation 3-20 we find

$$\tau_D \sim \frac{R}{V_R} \sim 13 \ (\frac{M_x}{M_o})^{1/4} \ (\dot{m}_{18})^{-0.3} \ \alpha^{-4/5} \ \text{sec} \qquad 7\text{-}48$$

at a radius of 40 km. It is not clear, however, why this timescale would be associated with the observed fluctuations. Instead, we might expect these fluctuations to be associated with a characteristic timescale from further out in the disk. The Kepler timescale at $R = 10^8$ cm is increased to $\sim 0.5 \ (M_x/M_o)^{-1/2}$ seconds. Shakura and Sunyaev (1976) suggested that matter flow could be regulated into bunches at the outer boundary ($R_B \sim 10^8$

cm) of the radiation pressure dominated region by slowly growing instabilities of long wavelength (see §III.B). This mechanism provides a natural way to obtain fluctuations on timescales of seconds for radiation emitted in the interior of the disk. In their picture, the formation time of the bunches would be reflected in quasiperiodic intensity changes with timescale

$$\tau_{Batch} \sim 0.11 \ \alpha^{-6/7} \ (\dot{m}_{18})^{1.2} \ (R_B/H_o)^2 sec. \qquad 7\text{-}49$$

With $R_B/H_0 \sim 10$, $\alpha \sim 1$, and $\dot{m}_{18} \sim 1$, this yields timescales of order 10 seconds. While the predicted timescale depends on the inverse square of the relative disk thickness at the boundary radius, and roughly linearly on $\alpha^{-1}$ and the accretion rate, the explicit dependence on the mass of the compact object has dropped out. Thus, sources showing quasiperiodic behavior at similar luminosities could have different characteristic timescales, depending roughly on the inverse of their masses. However, for a given object, the timescale should increase almost linearly with the luminosity, assuming constant $\alpha$ and rough proportionality of luminosity with m (i.e., that the effects of radiation pressure are negligible.) Neither of these assumptions may be viable for near-critical accretion rates.

If the various episodes of quasiperiodic behavior seen from Circinus are due to this mechanism, it appears that the breakdown of at least one of these two assumptions has to be invoked. Margon et al. (1971) reported an 8-second pulse train showing a period of $\sim 0.7$ second during a 1969 rocket flight when the source luminosity was $\sim 80\%$ of the peak luminosity seen in Observation 2 reported here (HEAO A2 Scan 0). During the latter

observation we find quasi-oscillations of ~ 3-4.5 seconds during four
20-second scans across the source (see Figure 5-6) near the beginning of
the outburst. For observations during the same days, the HEAO A1 group
reports a period of ~ 2.5 seconds (Sadeh et al. 1979). The exact times of
the A1 scans were not available for comparison, and there was no discussion
of possible changes in period with intensity. From the histogram given in
Figure 3 of Sadeh et al. (1979), we estimate that roughly half of the ~ 250
reported A1 burst intervals fall in the range 2-3 seconds, while ~ 25% fall
in the range 3-4.5 seconds. The longest trains of A1 data were accumulated
with a detector module on the opposite side of the satellite from the A2
detectors which scanned the source 180° out of phase. The source intensity
for two scans in the published figures of the A1 observation appears
comparable to the lowest of the four A2 scans referred to above. It is not
clear whether the shorter periods were observed preferentially at lower
intensities or simply at different times. Within the set of four A2 scans,
the period may track roughly with intensity for the three highest intensity
scans, but the lowest scan of the four clearly does not have the shortest
timescale. The A2 spectral data during this observation (see Chapter VI.A)
suggest that the intrinsic luminosity may be roughly constant during the
outburst, with changes in intensity largely due to changes in the column
density of absorbing material. Further, if Circinus does not have a mass
significantly larger than 1 $M_0$, the observed quasiperiodic behavior may be
taking place during a period of critical or near-critical accretion. Thus,
the observed changes in intensity may not reflect proportional changes in
accretion rate.

Different periods for short data trains is reminiscent of the early
results for Cygnus X-1 and suggests that a shot noise model might apply to

Circinus X-1 as well. Dower, Bradt and Morgan (1982) and Weisskopf and Sutherland (1980) have also analyzed Cir X-1 data in terms of a shot noise model. In view of the complexity of the system it is not surprising that a variety of parameters are obtained in different observations. For both Uhuru and SAS-3 data in post transition observations, correlation was small for lag times $\gtrsim$ 0.3 s. In pre-transition soft spectrum high state data the correlation times were similar to those observed in the HEAO 1 Scan 0 data. The shot rates and shot fractions differed from each other and from those in our observations. Dower et al. concluded that the picture was not appropriate because of instability of results with respect to bin size which they did not see in data from Cygnus X-1 and because the third moment was frequently negative. It is not clear yet whether during times when other changes are not occurring that the shot noise model is not appropriate. Both Cygnus X-1 and GX 339-4 do show fluctuations in the soft state: (1) Sutherland, Weisskopf and Kahn (1978) found little difference between high and low state Cygnus X-1 data from Uhuru and (3) an OSO-8 A Detector observation of Cygnus during a moderately high state showed intensity fluctuations in the 2-12 keV band on the 10-second spin period similar to those found for Circinus at peak intensity during Observation 1. OSO-8 B Detector observations of GX 339-4 showed apparently independent variability of the soft and hard components during a high state on timescales of some tens of seconds (Robinson-Saba et al. 1983).

Circinus does not appear to have a rapidly fluctuating hard spectral state or a hard tail during its soft state similar to those of Cygnus and GX 339-4. If the fluctuating soft component of Circinus is produced in a region and manner analogous to the fluctuating hard components of the latter, the spectral differences may reflect different accretion regimes.

The peak luminosities of Circinus are $\gtrsim 10^{38}$ erg s$^{-1}$, several times the inferred peak values for Cygnus and GX 339-4. While the mass for Circinus is unknown, the apparent radius of 40 km for the luminous optically thick component implies it is not greater than that of Cygnus. Thus, the mass accretion rate is probably considerably higher. Further, the disk in Circinus may never be able to reach a steady state because of the large orbital changes in accretion rate.

## VIII.  SUMMARY AND CONCLUSIONS

The observations of Circinus X-1 discussed in this thesis provide samples of a range of spectral and temporal behavior whose variety is thought to reflect a broad continuum of accretion conditions in an eccentric binary system.  While these samples do not give a complete picture of this system, they provide details which clarify aspects of earlier images of the system and suggest specific areas of inquiry for future observations to address.  In this chapter we recapitulate our basic results and the implications of these results for models of the system. Then we review what is now understood about the Circinus system when these results are considered in the context of previous observations.  We conclude with a discussion of aspects of this picture which need to be verified or explored further.

### A.  Summary of Spectral and Temporal Results

Here we outline the spectral and temporal characteristics found for three X-ray components from Circinus identified by the observations.  We discuss briefly possible interpretations, including likely emission regions.

#### 1.  The Outburst Component:

##### a.  Variations in neutral column density:

The outburst component comes and goes with the outbursts of soft flux, showing heavy absorption at onset and disappearance ($N_H \gtrsim 10^{23}$ atoms $cm^{-2}$); at times it clearly shows modulation which is not attributable to changes in the absorbing neutral column density.

##### b.  Apparent Blackbody Size:

(i) One of the more significant aspects of the outburst

component is the fact that sometimes it cannot be fit with any simple optically thin spectral form such as a power law or thin thermal bremsstrahlung continuum. This is contrary to most earlier deductions based on spectral data with lower resolution.

(ii) During Observation 1, when it is clearly inconsistent with being optically thin, the spectrum is well described by a blackbody with kT ~ 0.8 keV and an apparent radius at peak intensity near 40 km (for an assumed spherical emitter at 10 kpc distance). At other times it is consistent with being a blackbody of about the same size, with the temperature dependent on the observed intensity. Hereinafter this component will be referred to as the optically thick component for definiteness, though such a generalization needs to be confirmed by future observations.

c. Interpretation of blackbody size:

(i) If the emissivity of the optically thick component is ~ 1, so that a blackbody model applies, the apparent radius of 40 km implies an emission region large compared to a neutron star surface. An apparent blackbody size of 40 km is consistent with the maximum emission region of a Shakura-Sunyaev accretion disk about a ~ 3 $M_0$ compact object. This size is small compared to the boundary radius of the inner region of a disk (~ $10^8$ cm for the inferred mass accretion rate) or the Alfvén surface around a magnetic neutron star with a typical surface field of $10^{12}$ gauss (again, R ~ $10^8$ cm for the inferred accretion rate). Requiring the Alfvén surface to be inside this radius implies that the surface magnetic field strength must be $\lesssim 5 \times 10^9$ gauss.

(ii) An apparent blackbody radius of 40 km is larger than that associated with most other galactic sources which sometimes exhibit a

blackbody component (such as the bursters and the galactic bulge sources). The blackbody temperatures shown by Circinus are also cooler than these others. On the other hand, Goddard observations of GX339-4 and Cygnus X-1 show that both of these sources may have blackbody components of roughly similar size to that of Circinus, with slightly cooler temperatures consistent with lower inferred luminosities.

   d. <u>Rapid Variability</u>:

   (i) The optically thick component shows large changes in intensity on timescales of seconds or less, including occasional quasi-periodicities. During Observation 2, these large amplitude quasiperiodic fluctuations could be described in terms of shot noise, with roughly square shots of luminosity $\gtrsim 10^{37}$ ergs, occurring at a frequency of 1-2 per second, with a correlation time of 1-2 seconds. In some sense this component may be analogous to the fluctuating hard components observed during the spectral hard states of Cygnus X-1 and GX339-4. It does not appear to have an associated hard tail comparable to those of Cygnus and GX339-4 during their soft states.

   (ii) The observed fluctuation timescales of seconds are not usually associated with the natural timescales in the inner region of an accretion disk. If the emission region is indeed the inner part of a disk, the fluctuations probably originate further out in the disk, arising from instabilities near the boundary of the inner region or perhaps even further out.

   (iii) If this interpretation of the origin of the fluctuating optically thick component of Circinus is viable, it is a phenomenon not expected from current theories. It remains to be seen whether Cygnus X-1 and GX339-4 have similarly-behaved optically thick components. The rough

agreement in sizes for blackbody fits to soft components during the high states of the two sources noted above suggests this possiblity should be further explored.

## 2. The Low Flux Component:

Goddard observations of Circinus show there is at least one component distinct from the optically thick outburst component. Away from the outburst there is low level residual flux which may be present throughout the outburst. It generally has a spectrum better characterized by a thin thermal bremsstrahlung or power law fit than by an optically thick model such as a blackbody, and sometimes shows strong iron line emission. The low flux spectra typically show low column densities ($\lesssim 10^{23}$ atoms $cm^{-2}$), so that the residual flux is not the residual optically thick component transmitted through a high column density, as has been suggested by most previous workers.

### a. Associated timescale:

Apart from flaring sometimes observed around ephemeris phase 0 (marking the end of the larger outbursts) which may be due to an additional component, this component shows a fairly steady flux and spectral shape on the timescale of a few days, though these are not invariable from cycle to cycle.

### b. Spectral shape:

The low flux spectra do not show a narrow distribution in slope, nor is there a clear correlation between power law index and intensity such as a two-temperature disk model would predict. This component is steeper ($\alpha_N \gtrsim 2$) than the low state hard spectra of Cygnus X-1 and GX339-4 ($\alpha_N \sim 1.5$). It is usually steeper than the hard tail ($\alpha_N \sim 2$)

for the high states of Cygnus X-1 (though the high energy tail of GX339-4 may also be quite steep). While the presence of this component could mask a hard tail similar to that seen in Cygnus X-1, such a tail would have a luminosity at least an order of magnitude less than the outburst component, contrary to the case for Cygnus X-1.

    c.   Low energy turnover:

There is no clear correlation of the low energy turnover with intensity of the component, or of either the turnover or slope with binary phase, consistent with the suggested steadiness on a timescale of days. Observation 1 is consistent with the presence of this component at comparable strength and column density throughout the outburst of the optically thick component with its strong optical depth evolution, suggesting the residual component comes from a larger region.

    d.   Interpretation as compact source:

(i) If the region emitting the quiescent component is less than or on the order of the size of the binary system, the lack of high observed absorption for it implies that there are no system wide large optical depth effects. Then the observed column densities for the optically thick component and flares would be local to the regions producing them.

(ii) An accretion disk interpretation is consistent with the lack of observed change on timescales of days, since the spiral-in time could easily be longer than the binary period. The component would have to be produced outside the ~ 40 km radius apparently associated with the optically thick component to avoid sharing its heavy absorption. It is not clear whether X-rays greater than a few keV could be produced further out, or whether the quiescent component could remain steady during large changes

In the optically thick component. There is no evidence that the quiescent component shows any of the second or subsecond variations shown by the latter.

### e. Interpretation as extended source:

If the quiescent component is not continuously fed, as in an accretion disk, its relative steadiness on the timescale of days constrains the maximum cooling rates from various processes, putting a lower bound on the size of the emission region.

(i) Constraint on size for thermal interpretation:

If the quiescent flux in Observation 1 is due to thermal bremsstrahlung emission, the limit on bremsstrahlung cooling requires a minimum size of radius $\gtrsim 10^{13}$ cm, somewhat larger than the binary system size. Compton cooling of such a thermal gas from scattering by the companion starlight will be less important than radiative cooling provided the companion is less luminous than $\sim 10^{39}$ erg s$^{-1}$. (While an early type supergiant would have a luminosity this high, the large drop in quiescent optical and infrared flux over several years indicates a later type, less luminous star.)

(ii) Constraint on size for synchrotron interpretation:

The quiescent X-ray flux level is $\lesssim$ half the value of the quiescent radio flux level extrapolated into the X-ray regime and shows a steeper spectrum by at least half a unit than the radio component. Assuming that the quiescent X-ray spectrum is an extension of the quiescent radio synchrotron spectrum requires the presence of electrons with Lorentz factor $\gamma \gtrsim 1.8 \times 10^7$ and a magnetic field strength $\lesssim 10^{-2}$ gauss, in the absence of continuous replenishment of the high energy electron population.

Lack of Compton cooling of these electrons from
scattering of stellar photons requires an emission region of radius $\gtrsim 3$
$10^{15}$ $(L_{*37})^{1/2}$ cm, with $L_{*37}$ the luminosity of the stellar photons in units
of $10^{37}$ erg $s^{-1}$. Unless the emission region is considerably larger than
this, Compton scattering will compete with synchrotron radiation as a loss
mechanism. [The quiescent radio emission region size $\gtrsim 3 \times 10^{16}$ cm deduced
by Preston et al. (1983) meets this criterion.]

(iii) Difficulties of synchrotron-self-Compton
interpretation:

Inverse Compton scattering by the electron population
producing the quiescent radio synchrotron spectrum of those radio photons
(SSC) probably does not make an important contribution to the quiescent
X-ray flux. If the radio emission region is as large as $3 \times 10^{16}$ cm, the B
field would have to be quite low ($\sim 10^{-8}$ gauss) to allow the electron
density to be large enough to matter. While the average quiescent B field
might be that low in such a large volume, the corresponding density of $\gamma =$
$10^4$ electrons implies more $\gamma$-ray flux from inverse Compton scattering off
of the high observed flux of IR photons than the current upper limits
allow. Further, if the synchrotron producing electron distribution extends
down to $\gamma \sim 10^2$, the expected X-ray flux from inverse Compton scattering
of the IR photons by these electrons should be a factor of 10-100
larger than the contribution from SSC.

(iv) Inverse Compton scattering interpretation:

Inverse Compton scattering of the IR photons by $\gamma \sim 10^2$
electrons could in fact contribute substantially to the quiescent X-ray
flux. The steepness of the X-ray quiescent component relative to the radio
slope might then be at least partly accounted for by the apparent rollover

in the infrared spectrum. However, the high equivalent widths for iron line emission sometimes associated with the quiescent X-ray emission suggests that part of the quiescent flux comes from soft thermal emission, which would also steepen the X-ray spectrum compared to the radio slope.

### f.   Evidence for thermal gas:

The existence during quiescence of high equivalent width iron line emission which does not show a strong correlation with binary phase argues for the presence of hot gas in the system. The observed line equivalent widths are typically a factor of ~ 2 less than those predicted for equilibrium thermal emission, if the quiescent flux is interpreted as coming from thermal emission from a plasma with solar abundances. Thus nonthermal flux is also likely to be present, in keeping with the likelihood of inverse Compton scattering noted above. Identification of any line component due to fluorescence of the wind, the companion surface, an accretion disk or corona, or an Alfvén shell awaits systematic studies of the line emission with high sensitivity and energy resolution, as a function of binary phase, and quiescent and flare intensity and spectrum. The largest such contributions are expected from wind fluorescence, which would show a binary phase dependence, and an optically thick corona or Alfvén shell, which would probably produce an absorption edge as well. Even a relatively small contribution from fluoresence might be separable with good energy resolution because of the lower line energy expected for cold matter fluorescence relative to hot thermal emission.

### 3.   The Flare Component:

There appear to be brief episodes of flaring from Circinus which are not directly associated with outbursts of the optically thick

component. We suggest that they are also different from the component we have identified as quiescent. The flaring generally involves spectral hardening with a higher low energy cutoff.

a. Possible association of X-ray flares with radio and infrared flares:

These flares have been observed after the transitions of the optically thick component, suggesting a possible association with radio and infrared flares. The flares reported here lasted a few minutes to a few hours (the latter with structure timescales $\lesssim$ minutes), timescales shorter than those seen in the radio and infrared. However there have also been two observations of post-transition X-ray flaring with temporal behavior matching the longer radio flares. One of these longer X-ray flares, observed by Hakucho, was clearly harder than the soft pre-transition outburst, in keeping with the spectral hardening of the shorter flares.

b. Constraints on radio flare interpretation from X-ray data:

Interpretation of the radio flares as synchrotron radiation from an expanding plasma with $\gamma \sim 10^4$, $B \lesssim 10^{-4}$ and an emission region radius $\lesssim 10^{12}$ cm (Haynes et al. 1980) predicts an X-ray flare flux from the synchrotron-self-Compton process $\gtrsim 10^3$ times the observed value. If the electron distribution continues down to $\gamma \sim 10^2$, the resultant X-ray flux from inverse Compton scattering off the IR flare flux is estimated to be more than ten times greater yet. This implies R $\gg 10^{12}$ cm or B $\gg 10^{-4}$ gauss or both. A magnetic field strength $B > 10^{-4}$ is plausible in an accretion disk or near a weakly magnetic neutron star. For $B \sim 10^{-2}$ gauss, the predicted X-ray flux could be brought to a rea⋅ ⋅ble level by taking a radio emitting region size $\gtrsim 10^{13}$ cm. This constrain⋅ is consistent with

the radio flare size estimated by Preston et al. (1983) of 2-20 x $10^{14}$ cm (if their angular size measurement is not affected by scattering in the interstellar medium).

c. Size of X-ray flare region:

The variability of the short X-ray flares implies they come from a region << $10^{13}$ cm. If the X-rays are due to inverse Compton scattering of the IR flare flux by synchrotron-producing electrons, they could come from a region this small because they are generated before the synchrotron emitting plasma has expanded to the point where it is transparent to radio frequencies, or because the IR source is compact (e.g., coming from the outer part of an accretion disk).

d. Possibility of $\gamma$-ray bursts:

Whether or not the flare and quiescent X-rays are produced by inverse Compton radiation, electrons with $\gamma \sim 10^2$ in the vicinity of the X-ray source should produce comparable $\gamma$-ray luminosity from inverse Compton radiation near 100 MeV. Averaged over the binary period, the $\gamma$-ray flux expected approaches the limit estimated from non-detection by the COS B experiment. Gamma-ray observations with better sensitivites should either locate such a source or provide more information about the electron population and magnetic field strength responsible for the radio flares.

e. Similarities to SS433 flares:

The X-ray and radio flare components show some similarities to those of SS433, whose correlated flare behavior at X-ray and radio frequencies is better documented. With more information about the magnetic field in the core of the system, the nature of the optical companion, and details of the radio/X-ray correlation, Seaquist et al. (1982) have deduced

$B \sim 10^{-2}$, a flare emission region $\gtrsim 10^{14}$ cm from the stellar object and a quiescent source region of radius $\gtrsim 10^{16}$ cm. Whether the Circinus flares closely parallel those of SS433 must be decided by future long term broadband observations.

## B.    Implications of Observations for Lightcurve Models

Here we outline the evidence showing that the accretion picture for Circinus is complex, involving a combination of absorption and ionization effects with variable wind accretion or episodic Roche Lobe overflow, moderated by an accretion disk.

### 1.  Difficulties of modeling lightcurve as simple absorption effect:

The periodic modulation of the soft X-ray flux seen from Circinus cannot be explained entirely in terms of system-wide optical depth effects due to an eccentric orbit through a uniform wind. The evidence is varied:

a.    The optical depths of cold material required to produce the observed modulation for the appropriate orbit orientations

(i)   are larger than those observed;

(ii)  imply a strong correlation of peak intensity and duty-cycle with precession epoch which is not observed.

b.    The changes in intensity and column density predicted by the model are more gradual than those observed.  They cannot match

(i)   the frequently sharp cutoffs of soft flux at phase 0, or

(ii)  the rapid decrease followed by an increase in column density of cold matter seen in Observation 1.

c.    The observed spectra are not consistent with such a picture:

(i)   The outburst spectrum is not simply a low energy extension of an absorbed non-outburst spectrum;

(ii) The non-outburst spectrum does not typically show heavy absorption.

d.   The spectral evolution found in Observation 1 demonstrates that the observed modulation cannot always be accounted for by changes in the observed optical depth of cold material; i.e., the modulation cannot be entirely explained in terms of optical depths of cold material in any size region, whether the absorption is local or system-wide.

2.   Partial improvement of absorption model by inclusion of ionization:

A simple modification to the absorption model which takes into account ionization effects removes some but not all of the difficulties noted above for an optical depth model.

a.   On the positive side,

(i)   the peak efficiencies predicted are more nearly the same from epoch to epoch,

(ii)  the predicted cutoffs are sharper, and

(iii) changes in optical depth to cold material such as those found in Observation 1 can be matched.

b.   However, while the lightcurve assigned to the OSO/HEAO epoch matches the OSO data of Observation 1, it has a much smaller duty cycle than that inferred for the HEAO 1 Scan 0 curve found in Observation 2 or

the very intense cycle following covered by SAS-3.

    c. The difficulty still holds that not all of the modulation can be due to optical depth effects of a uniform (though now locally ionized) wind. The total column densities of neutral plus ionized material equal the column density of neutral material in the cold wind case. They change too slowly to explain the modulation found in Observation 1 by changes in the column density of ionized material which would not show up in the $N_H$ determination.

3. <u>Importance of intrinsic changes in source; inclusion of variable wind accretion in model</u>:

    Intrinsic changes in the source intensity over a binary orbit compete with or dominate optical depth effects, even though matter densities in the system may be large.

    a. This result seems a necessary conclusion from combined evidence of modulation not attributable to system-wide optical depth effects and the observation of low column densities when the source intensity is low. Taken together these imply a change in the local source environment on scales small compared to the binary size and orbit time. This change may involve an enhanced accretion rate, clumps of intervening matter or both.

    b. Expected changes in wind accretion over the binary orbit could explain most of the observations if ionization effects are substantial and the wind density and velocity are assumed to vary from cycle to cycle to account for the different peak luminosities and duty-cycles.

(i)   A principal difficulty with the wind accretion picture

is achieving luminosities $\gtrsim 10^{38}$ erg s$^{-1}$. The narrow peak of the smaller

outbursts might be consistent with a fast wind ($\sim 10^3$ km s$^{-1}$) if ionization

can offset the absorption implied by the high wind density needed.  If this

explanation is valid, the unabsorbed residual component must come from a

region larger than the binary system.

(ii) The larger outbursts with their high luminosities and

long duty-cycles require accretion from a slower wind.  Decreasing the wind

velocity by a factor of 2 or more increases the likelihood of formation of

a wind-fed disk as large as $10^{10}$ cm away from periastron.  It is not clear

whether such a disk could survive the tidal effects of a close encounter

with the companion near periastron passage, or accretion of lower angular

momentum material in other parts of the orbit.


4.   Evidence for the presence of an accretion disk:

It seems plausible that an accretion disk occurs in the Circinus

system at least as a transient phenomenon.  It has been previously pointed

out that a variable disk would provide a natural explanation for infrared

flares at roughly constant colors relative to the quiescent values, for

double-peaked Hα line profiles, and for the observed drop in intensity of

quiescent optical and infrared fluxes over several years (see §II.B.1).

Several pieces of X-ray evidence discussed in this thesis support

this suggestion:

a.   The high observed X-ray luminosities imply slow wind

accretion or tidal overflow, either of which is likely to cause disk

formation.

b.   A variable flow rate in a disk might explain abrupt turnons

and turnoffs in the X-ray flux.

      c.   A recurrent apparent radius near 40 km for the optically thick component in Circinus suggests the emission comes from a region which is reproducibly the same size. The size in question is about right for the maximum emission annulus in an accretion disk around a $\sim 3\ M_0$ compact object.

      d.   The quasiperiodic intensity fluctuations sometimes observed in Circinus appear consistent with behavior expected from the onset of instabilities at or outside the boundary of the inner disk region.

## C.   Review of Our Current Understanding of Circinus X-1

      The binary X-ray source Circinus X-1, believed to be powered by accretion of material from a mass-giving companion onto a compact object, shows a rich variety of behavior, including large X-ray outbursts, which exhibit a complex, evolving spectrum, and associated radio and infrared flaring. The source shows large amplitude intensity changes on many timescales, from subsecond chaotic fluctuations reminiscent of the black hole candidate Cygnus X-1 to irregular modulation on a timescale of months, evoking the behavior of long-term X-ray transients. The short duty-cycle, highly asymmetric 16.6-day lightcurve envelope, characterized by a large ratio (10-100) of maximum to minimum luminosity, is interpreted as coming from binary motion in a highly eccentric $(e \gtrsim 0.7)$ orbit. The distance estimate (8-16 kpc) from HI absorption measurements yields peak luminosities during the outbursts greater than the Eddington limit for a 1 $M_0$ object, implying that the accretion takes place in a critical regime or onto a masive object or both.

## 1. Effects of the Binary Environment

The inferred orbital eccentricity implies a continuum of accretion conditions. The variation with orbital phase of stellar separation, gravitational potential, relative velocity, local density, and line-of-sight column density lead to corresponding changes in wind accretion or Roche-lobe overflow (or both), a variable wind- or Roche-fed disk, and varying ionization and optical depth effects. Each of the previous models proposed for Circinus in the literature has invoked the dominance of a single effect in producing the soft X-ray lightcurve: variation in optical depth through a uniform wind to an intrinsically steady source, ionization structure in the wind of an OB supergiant, or cyclic variation in wind accretion in an orbit of eccentricity e ≈ 0.5. The samples of behavior reported in this thesis show that the true picture is more complex and probably involves a combination of absorption and ionization effects with variable wind accretion or episodic Roche-lobe overflow, modulated by long-term changes in outflow from the companion. The infrared and optical observations suggest the presence of an accretion disk which evolves with time.

## 2. Modeling the Irregular clock Mechanism(s)

The cyclic soft X-ray outburst and its typically abrupt cessation are likely to be related to periastron passage, though the mechanisms for producing them are not clear. The 16.6-day outburst cycle has never been an exact clock. Even the rapid turnoff of the larger outbursts, the most periodic feature of the cycle, shows a large amount of phase jitter; smaller outbursts end preferentially earlier (by about half a day compared to the mean phase of the larger outbursts) and more gradually (on a timescale of hours rather than a fraction of an hour).

From the infrared and optical data it is now known that the mass-giving star is not an early-type supergiant, as was assumed in some models of Circinus; however, the data are consistent with a B-type main sequence star or later-type more evolved star, which might have a substantial outflowing wind or episodes of Roche lobe overflow near periastron passage of the compact object. While an accretion disk is generally associated with Roche-lobe overflow, a small wind-fed disk could also result for wind parameters consistent with the observed X-ray outburst luminosities. If a large accretion disk is sometimes present, as suggested by the infrared and optical data, it is probably fed primarily by Roche-lobe overflow.

Cycle-to-cycle changes in the wind or overflow parameters, or in disk conditions, could account for observed changes in the soft X-ray lightcurve shape, duration, and intensity. The small, narrow outbursts could result from accretion of a fast wind, for which the accretion efficiency is low and the modulation with phase is sharp. The large, broad outbursts could come from accretion from a slower wind, accompanied by formation of a disk with radius of up to $10^{10}$ cm, if a larger Roche-fed disk is not already present. Even fast wind accretion could lead to a small disk, of radius $\sim 10^8$ cm -- not big enough to retard accretion for more than about an hour, but sufficient to allow those phenomena (such as the apparent size and the temporal oscillations of the outburst component, which we find for a small outburst as well as a larger one) that we interpret as coming from the inner part of the disk. Significant Roche-lobe overflow might occur in some cycles but not in others if the companion pulsates or otherwise undergoes intrinsic changes on timescales different from that of the cyclic tidal perturbation by the compact object. A given

outburst could reflect outflow conditions during the current orbit, or interception by the compact object of material accumulated in the disk or in the vicinity of the companion from previous passes. Long-term systematic changes in the outflow might explain the apparent long-term evolution of the average envelope of the binary lightcurve, obviating the need for a model invoking rapid precession and the dominance of wind absorption effects, which we find implausible on other grounds (see §VII.A).

3.  The Beginnings and Ends of the X-ray Outbursts

It is possible that several competing factors determine the nature of the turnons and cutoffs of the outburst. The sometimes sudden turnons at a range of binary phases might be explained by the sudden onset of disk dumping due to a change in viscosity or angular momentum of accreting material; alternately, tidal disturbances of the disk near periastron could be important. More gradual turnons could reflect normal disk processing or near-radial infall of wind-accreted material. The prototypical precipitous turnoffs (defining ephemeris phase 0) could be due to occultation of the inner part of the accretion disk by the outer disk or by the companion. The early, abrupt decline of large outbursts could be due to the onset of an instability during critical accretion; the early, gradual decline of the small outbursts could reflect an exhaustion of fuel or motion of the compact object into a region too dense to be ionized effectively by the weaker source.

While the onsets and declines of the outburst component are at least sometimes associated with large changes in absorption, the outburst cannot be modeled simply in terms of variable system-wide obscuration of a constant intensity X-ray source by a uniform cold wind. The predicted

changes in optical depth and intensity are too gradual to match those observed, and the measured column densities cannot account for all of the observed modulation. Inclusion of ionization of the surrounding wind by the X-ray source accounts for the magnitude of the measured column densities, but some form of intrinsic source modulation must still be invoked. Prompt wind accretion describes some lightcurves well, but cannot by itself provide the sharp turnons and cutoffs seen for the larger outbursts. Roche-lobe overflow, instabilities during critical accretion, and perturbation of the accretion disk could all play important roles in determining the properties of the outburst.

### 4. Multiple Emission Regions

The observations analyzed in this thesis support an identification of three or more X-ray spectral components from Circinus, probably associated with distinct emission regions in the system:

a. A luminous ($\sim 10^{38}$ erg s$^{-1}$) optically thick component, associated with the outburst, has a spectrum which is to good approximation a blackbody of kT $\sim 0.8 - 1.0$ keV, with an apparent radius of $\sim 40$ km (for an assumed spherical emitter at a distance of 10 kpc). This component sometimes exhibits large-amplitude quasiperiodic fluctuations on a timescale of seconds. The luminosity, size, and variability suggest this component originates in the inner region of an optically thick accretion disk around a compact object of $\gtrsim 3$ M$_{0}$.

b. A low level component ($\lesssim 10^{37}$ erg s$^{-1}$) which remains after the outburst decline has an optically thin spectrum which shows little absorption and strong iron line emission. The line equivalent width is sometimes quite large for a fluorescence origin, suggesting the presence of thermal gas. The existence of an extended quiescent radio source implies

the presence of nonthermal electrons which, unless their spectrum is peculiar, should lead to significant X-ray flux from inverse Compton scattering of the observed quiescent infrared flux. The quiescent X-ray flux is thus likely to be partly thermal, partly inverse Compton radiation. The observed lack of variability on a timescale of days requires an X-ray emission region of large extent, $> 10^{13}$ cm (the estimated size of the binary system), if the source is not continuously replenished.

c. A post-outburst X-ray flare component, possibly correlated with the radio and infrared flares from Circinus, shows a flat, absorbed spectrum. Variability on a timescale of minutes restricts the size of the X-ray emission region to $<< 10^{13}$ cm, considerably smaller than the X-ray quiescent region we infer and the reported size of the radio flare region. A likely origin of the X-ray flares is inverse Compton scattering of infrared flux by a low $\gamma$ extension of the nonthermal electrons producing the radio flares.

d. There is some evidence for an absorbed pre-outburst component, though its nature is not well understood. The apparent luminosity is low ($\sim 10^{37}$ erg s$^{-1}$), but its high inferred column density implies that the intrinsic luminosity could be comparable to that during outburst. This component could be a manifestation of the outburst during onset.

5. <u>Circumstantial evidence for a black hole in Circinus</u>

While the observations cannot be used to make a definitive statement about the nature of the compact object in the Circinus system, they appear to be more readily interpretable in terms of a black hole rather than a neutron star accretor.

a. The subsecond chaotic fluctuations observed for Circinus, similar to those reported for the black hole candidates Cygnus X-1 and

GX339-4, are not currently thought to be expected X-ray behavior for neutron stars. (Short-term irregular modulation of radio emission from the fastest radio pulsars, however, suggests that possible analogous behavior for X-ray pulsars should be investigated further.)

b. While the observations reported here cannot strongly limit the existence of regular X-ray pulsations because of the data sampling modes used, previous observations have done so (see, e.g. Dower, Bradt, and Morgan 1982). In a magnetic neutron star interpretation, the absence of observed stable pulsations requires that the magnetic axis is parallel to the rotational axis, or that the system has a special orientation so that any beamed radiation never crosses the line of sight. For a black hole accretor, on the other hand, no stable pulsations are expected.

c. The quasiperiodic pulse trains shown by Circinus, similar in some ways to those shown by Cygnus X-1 and GX339-4, suggest variations in the inner part of an accretion disk (with the timescale set by instabilities further out in the disk). For a neutron star with a typical magnetic field strength, the inner disk region would not exist.

d. The soft, complex spectrum shown by Circinus during outburst, is quite different from the spectra (usually quite hard) associated with magnetic neutron stars. It is rather similar to the high state spectra of several black hole candidates, including Cygnus X-1 and GX339-4.

e. The 40-km apparent radius of the blackbody component for Circinus at peak intensity, similar to the (high state) sizes for Cygnus X-1 and GX339-4, is naturally explained in terms of emission from the inner part of an optically thick accretion disk around a compact object with $M \gtrsim M_o$. While the size alone could be consistent with the Alfvén shell for a weakly magnetic neutron star, it is not clear why peak luminosities at or

above the Eddington limit should be associated with emission from that surface rather than a smaller region closer to the neutron star surface. There are no known solutions that allow stable neutron star configurations with a surface radius as large as 40 km. Such a size is not observed in known neutron star sources. If Circinus and sources such as Cygnus X-1 and GX339-4, with blackbody kT $\lesssim$ 1 keV and radii of 40-70 km are neutron stars, they form a separate class whose properties are not predicted by any current model of accretion onto neutron stars.

## D. Prospectus For Future Investigations

We have argued that Circinus X-1 constitutes an astrophysical laboratory for studying the accretion phenomenon: cyclic changes due to an eccentric orbit, modulated by changes in mass outflow from the companion, provide a wide range of accretion conditions. A fundamental understanding of the system requires an unravelling of the contributions from a number of competing factors which operate concurrently. The task is nontrivial but tractable with long-term broadband coverage and occasional intensive studies with high spectral and temporal resolution. This thesis has identified a number of spectral and temporal clues to the nature of Circinus, whose generality and further implications should be checked. Some similarities in behavior are found in other black hole candidates, notably Cygnus X-1 and GX339-4. The extent of correspondence needs to be further explored. Here we sketch several areas of investigation where more work is clearly warranted.

1. <u>What is the nature of the long-term changes seen in Circinus?  Is the soft X-ray lightcurve changing systematically with time?  If so, are the changes due to orbit precession, or do they reflect</u>

systematic changes in outflow from the companion?

These questions can be answered in part by continuing coverage with an X-ray detector similar to the Ariel-5 All Sky Monitor, but with greater sensitivity. Some spectral information is also needed to tell whether the flux seen after ephemeris phase zero is related to the prototypical soft outburst component or whether it is in fact harder as some observations suggest. It is particularly important to have routine monitoring in other wavebands as well, for cross comparisons and to sort out cycle-to-cycle changes in various bands from longer term effects. For example:

a. Systematic studies of Hα flux and Doppler velocity (which probably reflect current outflow as well as disk properties) as functions of binary phase, compared with the behavior of flux in other bands, may allow the disk and wind dependencies to be sorted out, and help pin down the orbit orientation.

b. The quiescent infrared flux level, probably a measure of the mass of the accretion disk, may be correlated with the Hα disk component, or the magnitude and shape of the X-ray outburst (presumably related to the inner disk or its absence).

2. What is the nature of the clock mechanism(s) in Circinus? What role is played by the accretion disk?

A definitive answer to these questions requires broadband coverage of a moderate sample of outbursts, including turnons and cutoffs, with sensitivity sufficient to measure changes on timescales of minutes or less. The X-ray coverage should routinely provide spectral information sufficient to distinguish between changes in column density and temperature, and between optically thin and optically thick spectra. Finer

X-ray temporal resolution with at least moderate spectral information is needed to exploit the use of short-term fluctuations as a probe of the inner disk conditions.

a. With broadband coverage we can learn whether the magnitude of the outburst or the sharpness of its turnon or butoff are correlated with the level of quiescent infrared or optical flux, or with the parameters (size, shape, duration, delay) of subsequent radio, infrared, optical, X-ray, or gamma-ray flaring. (The size of the X-ray outburst, for example, could depend on the total mass in the disk, which the infrared and optical flux might reflect. If a sharp turnon is due to disk perturbation, we might expect to see the infrared flux tracking associated upheavals in the outer disk. If the outburst is quenched during supercritical accretion, flaring afterwards might be more (or, again, less) probable.) While it has been reported that high energy X-ray flux "broadly correlates" with soft X-ray flux, we do not know the details of such a correlation. In particular, we do not know to what energy it extends, over what timescales it occurs, whether there is a phase shift, or how the spectra are related.

b. High resolution spectral and temporal information during the outburst will tell us more about the accretion conditions near the compact object. It would allow us to determine the character of the possible pre-outburst absorbed component, which may be a signature of the onset of accretion. It would show whether the systematic decrease, followed by an increase, in column density (a feature noted during a small outburst) applies generally. The decrease likely denotes the infall and subsequent ionization of material near the compact object. The increase may reflect the failure of the X-ray source to keep the surrounding matter ionized as the local fuel source is exhausted. To date, coverage of the

decline of large outbursts has involved spectral or temporal resolution too coarse to follow the details of the evolution of a complex spectrum.

c. The observations reported here suggest that the outburst component is a blackbody with a radius of roughly 40 km, consistent with an origin in an optically thick inner disk. It appears that several other black hole candidates show a similar blackbody component of comparable size and temperature. These results need to be verified. If the outburst component from Circinus is always a blackbody, a roughly constant size with changing luminosity would support origin in a characteristic emission region such as the inner disk. We need to know whether a hard tail, such as that found for Cygnus X-1, is ever present and, if so, its properties (magnitude, slope, cutoff, variability) and how they correlate with the soft component.

d. The short-term aperiodic variability of Circinus has not been well delineated. A simple shot noise model may frequently not apply, yet results from this thesis suggest that quasi-oscillatory behavior sometimes seen may in fact be a manifestation of high luminosity, roughly square shots whose parameters evolve with luminosity or time. It is not currently known how the presence, magnitude, timescale, and spectrum of the fluctuations correlate with luminosity or other conditions. Such knowledge is crucial to understanding accretion in the inner disk.

3. <u>What is the nature of the residual X-ray component? How is it related to the quiescent radio and infrared components?</u>

This work has identified a quiescent X-ray component which sometimes shows strong iron line emission. We have suggested that the emission is due partly to thermal gas in an extended region and partly to inverse Compton scattering of quiescent infrared photons by the same

electron population which produces the quiescent radio flux. The properties of this X-ray component -- the flux level, spectral slope, low energy cutoff, and line parameters -- should be studied as a function of binary phase. In particular, if the line comes from diffuse thermal emission, it should not show a strong phase dependence; on the other hand, if there is a significant fluorescent wind component, high resolution studies of the line should show its phase dependence and shift in energy, and any related absorption features. Any contribution of nonthermal flux to the continuum might show a correlation with the radio or infrared quiescent components. Some longer-term correlation of the entire continuum with adjacent outbursts and flares seems likely.

4. <u>What is the nature of the post-outburst X-ray flares? How are they related to the radio and infrared flares? Are there gamma-ray flares?</u>

This thesis has given several examples of hard X-ray flaring after the disappearance of the soft flux outbursts. While it seems natural to associate these flares with the radio and infrared flares observed from Circinus, simultaneous extended bandwidth coverage is required to check relative occurrence, phasing, and magnitude. If the X-ray flux comes from inverse Compton scattering of infrared flux as seems plausible, comparable luminosity should appear in gamma-ray flares.

The X-ray observations should be sensitive to fast temporal changes in spectrum and intensity to look for short-term behavior such as quasi-oscillations or subsecond bursting which would suggest an inner disk origin.

## APPENDIX A

Assuming the stellar wind density profile follows an inverse-square law

$$n(r) = n_*(R_*/r)^2,$$

we can write the column density along the line of sight to the X-ray source as

$$\int_0^\infty n(r) \, d\ell = \int_0^\infty n_* R_*^2 \frac{d\ell}{r^2}$$

$$= n_* R_*^2 \int_0^\infty \frac{d\ell}{[\ell^2 + D^2 - 2 \, D\ell \, \sin\phi \, \sin i]}$$

where D is the instantaneous separation of stellar centers and $\ell$ is the distance from the X-ray source along the line of sight (see Figure 7-1). Except when the denominator of the integral vanishes (corresponding to one star being directly behind the other),

$$\int_0^\infty n(r) \, d\ell = \frac{n_* R_*^2}{D} \frac{1}{(1 - \sin^2\phi \, \sin^2 i)^{1/2}} \left\{ \frac{\pi}{2} + \tan^{-1} \left[ \frac{\sin\phi \, \sin i}{(1 - \sin^2\phi \, \sin^2 i)^{1/2}} \right] \right\}.$$

Writing $\phi = \frac{3\pi}{2} + \theta_p + \theta$, where $\theta_p$ is the periastron angle, which gives the

orientation of the major axis, and $\theta$ is the "true anomaly" or binary orbit angle measured from periastron, and defining $s = D/a$ where $a$ is the semi-major axis, and $x \equiv s \cos(\theta+\theta_p) \sin i$, we can write

$$\int_0^\infty n(r)\,d\ell = n_* \frac{R_*^2}{a} \frac{1}{(s^2 - x^2)^{1/2}} \left\{ \frac{\pi}{2} - \tan^{-1} \left[ \frac{x}{(s^2-x^2)^{1/2}} \right] \right\} .$$

The optical depth $\tau$ along the line of sight to the X-ray source can then be written in terms of the optical depth $\tau_*$ to the surface of the primary star, as

$$\tau = \tau_* \frac{R_*}{a} \frac{1}{(s^2-x^2)^{1/2}} \left\{ \frac{\pi}{2} - \tan^{-1} \left[ \frac{x}{(s^2-x^2)^{1/2}} \right] \right\} .$$

For the special case where the X-ray source is directly in front of the primary, the integral of $\frac{1}{r^2}$ gives $1/D$, implying $\tau = \tau_* \frac{R_*}{D}$ for $\theta+\theta_p = 0$. For the case where the X-ray source is directly behind the primary (i.e., the X-ray source is eclipsed by the center of the primary), we take $\tau = \infty$ (or, more precisely, set $e^{-\tau} = 0$ in calculations of the luminosity). Otherwise we do not take eclipses explicitly into account.

# GENERAL REFERENCES

## HISTORY OF ASTRONOMY

Asimov 1972

Harwit 1973

Lang and Gingerich 1979

Milton 1977

Pannekoek 1969

Ruffini 1975

## ACCRETION AND ACCRETION DISKS

Bahcall 1978

Boldt 1977

Bradt, Kelley, and Petro 1982

Lightman, Rees, and Shapiro 1977

Pringle 1981

Verbunt 1982

## RADIATION MECHANISMS

Boldt 1977

Harwit 1973

Lightman, Rees, and Shapiro 1977

Rybicki and Lightman 1979

Tucker 1975

## PROPORTIONAL COUNTERS

Rossi and Staub 1949

# BIBLIOGRAPHY

Abramowicz, M., 1983, Nature 302, 12.

Allen, C.W., 1973, Astrophysical Quantities, 3rd edition, London:Athlone
Press.

Allen, D.A., 1979, IAU Coll., 46, 125.

Allen, D.A., 1980, M.N.R.A.S., 192, 521.

Arnett, D.W., and Bowers, R.L., 1977, Ap. J. Suppl, 33, 415.

Asimov, I., 1972, Biographical Encyclopedia of Science and Technology,
New York: Avon Books.

Avni, Y., 1976, Ap. J., 209, 574.

Avni, Y., 1977, Proc. Enrico Fermi Summer School on Physics and
Astrophysics of Neutron Stars and Black Holes, Varenna, Italy, 1975,
Amsterdam: North Holland.

Avni, Y., and Bahcall, J.N., 1975, Ap. J., 197, 675.

Baade, W., and Zwicky, F., 1934, Phys. Rev., 45, 138.

Bahcall, J.N., 1978, Ann. Rev. Astron. Astrophys., 16, 241.

Bai, T., 1980, Ap. J., 239, 999.

Baity, W.A., Ulmer, M.P., and Peterson, L.A., 1975, Ap. J., 198, 447.

Bambynek, W., et al., 1972, Rev. Mod. Phys., 44, 716.

Bardeen, J.M., 1970, Nature, 226, 64.

Barlow, M.J., and Cohen, M., 1977, Ap. J., 213, 737.

Basko, M.M., 1978, Ap. J., 223, 268.

Basko, M.M., 1980, Astr. Ap., 87, 330.

Basko, M.M., Hatchett, S., McCray, R., and Sunyaev, R.A., 1977, Ap. J.,
215, 276.

Basko, M.M., and Sunyaev, R.A., 1973, Astrophys. and Sp. Sci., 23, 117.

Basko, M.M., and Sunyaev, R.A., 1976, M.N.R.A.S., 175, 395.

Basko, M.M., Sunyaev, R.A., and Titarchuk, L.G., 1974, Astron. Astrophys.,
31, 249.

Batten, A.H., 1973, Binary and Multiple Systems of Stars, Braunschweig:
Pergammon Press, p247.

Begelman, M.C., Sarazin, C.L., Hatchett, S.P., McKee, C.F., and Arons, J.,
1980, Ap. J., 238, 722.

Bell, A.R., 1978, M.N.R.A.S., 182, 147.

Bignami, G.F., et al., 1977, Astron. Astrophys., 57, 309.

Bignami, G.F., 1982, Second Cos-B Catalog, preprint.

Blumenthal, G.R., and Tucker, W.H., 1974, Ann. Rev. Astron. Astrophys., 12,
23.

Boldt, E., 1977, in Recognition of Compact Astrophysical Objects, ed. H.
Ögelman and R. Rothschild, NASA SP-421, p75.

Boldt, E., Holt, S., Rothschild, R., and Serlemitsos, P., 1975, Proc.
Internat. Conf. X-Rays in Space, ed. D. Venkatesan, Univ. of Calgary.

Boldt, E., and Leiter, D., 1981, Nature, 290, 483.

Bradt, H.V., Doxsey, R.E., and Jernigan, J.G., 1979, Advances in Space
Exploration, 3,

Bradt, H.V., Kelley, R. L., and Petro, L.D., 1982, in Galactic X-Ray
Sources, eds. P.W. Sanford, P. Laskarides, and J. Salton,
Chichester:Wiley and Sons, p. 89.

Brown, R.L., and Gould, R.J., 1970, Phys. Rev. D., 1, 2252.

Buff, J., and McCray, R., 1974a, Ap. J. (Letters), 188, L37.

Buff, J., and McCray, R., 1974b, Ap. J., 189, 147.

Buff, J., et al., 1977, Ap. J., 212, 768.

Burbidge, G.R., 1972, Comments on Astrophysics, 105, 105.

Burbidge, E.M., Burbidge, G.R., Fowler, W.A., and Hoyle, F.H., 1957, Rev. Mod. Phys., 29, 547.

Cameron, A.G.W., 1959, Ap. J., 130, 884.

Canizares, C.R., Li, F.K., and Clark, G.W., 1974, Ap. J. (Letters), 191, L75.

Canizares, C.R., and Oda, M., 1977, Ap. J. (Letters), 214, L119.

Castor, J.I., Abbott, D.C., and Klein, R.I., 1975, Ap. J., 195, 157.

Chandrasekhar, S., 1931, M.N.R.A.S., 91, 456.

Chiappetti, L., and Bell-Burnell, S.J., 1981, Space Sci. Reviews, 30, 389.

Chiappetti, L., and Bell-Burnell, S.J., 1982, M.N.R.A.S., 200, 1025.

Chiappetti, L., Blissett, R.J., Branduardi-Raymont, G., Bell-Burnell, S.J., Ives, J.C., and Parmar, A.N., 1981, M.N.R.A.S., 197, 139.

Chiappetti, L., 1981, Space Sci. Rev, 30, 447.

Clark, D.H., and Caswell, J.L., 1976, M.N.R.A.S., 174, 267.

Clark, D.H., Parkinson, J.H., and Caswell, J.L., 1975, Nature, 254, 674.

Coe, M.J., Engel, A.R., and Quenby, J.J., 1976, Nature, 262, 563.

Cooke, B.A., and Pounds, K.A., 1971, Nature Phys. Science, 229, 144.

Cowley, A.P., Crampton, D., and Hutchings, J.B., 1982, IAU. Circ., No. 3751.

Cowley, A.P., et al., 1983, preprint.

Davidsen, A.F., Malina, R., and Bowyer, S., 1977, Ap. J. 211, 866.

Davidson, K., and Ostriker, J.P., 1973, Ap. J., 179, 585.

Davison, P.J.N., and Tuohy, I.R., 1975, M.N.R.A.S., 173, 33p.

Dower, R.G., 1978, Ph.D. thesis, Mass. Inst. Tech.

Dower, R.G., Bradt, H.V., and Canizares, C., 1977, Bull. AAS, 9, 297.

Dower, R.G., Bradt, H.V., and Morgan, E.H., 1982, Ap. J., 261, 228.

Doxsey, R., Grindlay, J., Griffiths, R.E., Johnston, M.D., and Schwartz,
D., 1979, Ap. J. (Letters), 229, L53.

Eardley, D.M., and Lightman, A.P., 1975, Ap. J., 200, 187.

Eardley, D.M., Lightman, A.P., and Shapiro, S.L., 1975, Ap. J. (Letters),
199, L153.

Eddington, A.S., 1917, M.N.R.A.S., 77, 596.

Eddington, A.S., 1918, M.N.R.A.S., 79, 2.

Eddington, A.S., 1926, The Internal Constitution of Stars, Cambridge
University Press.

Fano, U., 1947, Phys. Rev., 72, 26.

Felsteiner, J., and Opher, R., 1976, Astron. Astrophys., 46, 189.

Felten, J.E., and Rees, M.J., 1972, Astron. Astrophys., 17, 226.

Fireman, E.L., 1974, Ap. J., 187, 57.

Forman, W., et al., 1973, Ap. J. (Letters), 182, L103.

Forman, W., Jones, C., and Tananbaum, H., 1976, Ap. J., 208, 849.

Fowler, R.H., 1926, M.N.R.A.S., 87, 114.

Fransson, C., and Fabian, A.C., 1980, Astron. Astrophys., 87, 102.

Friedman, H.V., Byram, E.T., and Chubb, T.A., 1967, Science, 156, 374.

Friend, D.B., and Castor, J.I., 1982, Ap. J., 261, 293.

Gamow, G., 1936, Structure of Atomic Nuclei and Nuclear Transformations,
Oxford: Univ. Press.

Giacconi, R., and Gursky, H., 1974, eds., X-Ray Astronomy, Astrophys. and
Sp. Sci. Libr. 43, Dordrecht: Reidel Publ. Co.

Giacconi, R., et al., 1974, Ap. J. Suppl. 27, 37.

Ginzburg, V. L., and Syrovatskii, S.I., 1964, The Origin of Cosmic Rays,

New York: Pergamon Press.

Glass, I.S., 1976, IAU Circ. No. 2974.

Glass, I.S., 1977, IAU Circ. No. 3095.

Glass, I.S., 1978a, M.N.R.A.S., 183, 335.

Glass, I.S., 1978b, IAU Circ. No. 3217.

Glass, I.S., and Feast, M.W., 1973, Nature Phys. Sci., 245, 39.

Goss, W.M., and Mebold, U., 1977, M.N.R.A.S., 181, 255.

Gregory, P.C., and Seaquist, E.R., 1974, Ap. J., 194, 715.

Gursky, H., and Ruffini, R., 1975, editors, Neutron Stars, Black Holes and
    Binary X-Ray Sources, Astrophys. and Space Sci. Libr. 48, Dordrecht:
    Reidel Publ. Co.

Harries, J.R., et al., 1971, Nature Phys. Sciences, 234, 149.

Harwit, M., 1973, Astrophysical Concepts, New York: John Wiley & Sons, Inc.

Hatchett, S.P., Buff, J.S., and McCray, R., 1976, Ap. J., 195, 157.

Hatchett, S., and McCray, R., 1977, Ap. J., 211, 552.

Hatchett, S., and Weaver, R., 1977, Ap. J., 215, 285.

Hayakawa, S., 1981, Space Sci. Reviews, 29, 221.

Haynes, R.F., Caswell, J.L., and Simons, L.W., 1976, IAU Circ., 2977.


Haynes, R.F., Lerche, I., and Murdin, P.G., 1980, Astron. Astrophys., 87,
    299.

Haynes, R.F., Lerche, I., and Wright, A.E., 1980, Astron. Astrophys., 81,
    83.

Haynes, R.F., et al., 1978, M.N.R.A.S., 185, 661.

Haynes, R.F., Jauncey, D.L., Lerche, I., and Murdin, P.G., 1979, Aust. J.
    Phys., 32, 43.

Hearn, A.G., 1975, Astron. Astrophys. 40, 277.

Hewish, A., et al., 1968, Nature, 217, 709.

Hill, R.W., et al., 1972, Ap. J., 171, 519.

Holt, S.S., 1976, Space Sci. Instr., 2, 205.

Hutchings, J.B., 1976, X-Ray Binaries (NASA S-389), 531.

Hutchings, J.B., Crampton, D., and Cowley, A.P., 1983, IAU Circ. No. 3791.

Illarionov, A.F., and Sunyaev, R.A., 1972, Soviet Astron.-A.J., 16, 45.

Jones, C., et al., 1974, Ap. J. (Letters), 191, L71.

Joyce, R.M., et al., 2978, IEEE Trans. Nucl. Sci., NS-25, 453.

Kaluzienski, L.J., 1977, Ph.C. Thesis, Univ. of Maryland.

Kaluzienski, L.J., 1979, private communication.

Kaluzienski, L.J., Holt, S.S., Boldt, E.A., and Serlemitsos, P.J., 1976,
Ap. J. (Letters), 208, L71.

Kaluzienski, L.J., and Holt, S.S., 1977, IAU Circ., No. 3099.

Kaluzienski, L.J., and Holt, S.S., 1978, IAU Circ., No. 3171.

Kaluzienski, L.J., and Holt, S.S., 1979, IAU Circ., No. 3320.
Karzas, W., and Latter, R. 1961, Ap. J. Suppl., 6, No. 55, 167.
Kompaneets, A.S., 1957, Sov. Phys. JETP, 4, 730.
Kellogg, E., Baldwin, J.R., and Koch, D., 1975, Ap. J., 199, 249.
Kopal, Z., 1959, Close Binary Systems, New York:Wiley.

Kraft, R. P., 1975, in Neutron Stars, Black Holes, and Binary X-Ray Sources
(eds. Gursky and Ruffini), Astrophys. and Space Sci. Libr., 48.

Kruszewski, A., 1963, Acta Astr. 13, 106.

Kukarkin, B.V., et al., 1970, General Catalogue of Variable Stars, 3rd
edition, Moscow: Moscow State University.

Lamb, F.K., Pethick, C.J., and Pines, D., 1973, Ap. J. 184, 271.

Lamb, F.K., 1975, Proc. Int. Conf. on X-Rays in Space, ed. D. Venkatesan,
Univ. of Calgary, Calgary, p613.

Lamers, H.J.G.L.M., and Morton, D.C., 1976, Ap. J. Suppl., 32, 715.

Lamers, H.J.G.L.M., van den Heuvel, E.P.J., and Petterson, J.A., 1976,
    Astron. Astrophys., 49, 327.

Landau, L., 1932, Phys. ∠. Soviet, 1, 285.

Landau, L.D., and Lifshitz, E.M., 1959, Fluid Mechanics, New York:Pergamon
    Press.

Lang, K.R., and Gingerich, O., 1979, A Source Book in Astronomy and
    Astrophysics, 1900-1975, Cambridge, Mass.: Harvard University Press.

Leavitt, H.S., 1912, Harv ʳd College Observatory Circ., No. 173, p. 1.

Lewin, W.H.G., Clarʏ, G.W., and Smith, W.B., 1968, Ap. J. (Letters) 152,
    L49.

Lightman, A.P., 1974a, Ap. J. 194, 419.

Lightman, A.P., 1974b, Ap. J. 194, 429.

Lightman, A.P., Rees, M.J., and Shapiro, S.L., 1977, in Proc. Enrico Fermi
    School on the Physics and Astrophysics of Neutron Stars and Black
    Holes, New York: Academic Press.

Lin, D.N.C., and Pringle, J.E., 1976, in IAU Symp. 73, 237.

Lodenquai, J., et al., 1974, Ap. J., 206, 625.

Lubow, S.H., and Shu, F.H., 1975, Ap. J., 198, 383.

Lynden-Bell, D., and Pringle, J.E., 1974, M.N.R.A.S. 168, 603.

MacGregor, A., Seward, F., and Turiel, I., 1970, Ap. J., 161, 979.

Makishima, K., et al., 1983, Ap. J., 267, 310.

Manchester, R.N., and Taylor, J.H., 1977, Pulsars, San Francisco: W.H.
    Freeman and Co.

Margon, B., Lampton, M., Boyer, S., and Cruddace, R., 1971, Ap. J.
    (Letters), 169, L23.

Matilsky, T., et al., 1972, Ap. J. (Letters) 174, L53.

Matilsky, T., Gursky, H., and Tananbaum, H., 1973, paper presented at
    141st Meeting of Amer. Astr. Soc., Tucson, Ariz.

Mayo, S.K., Whelan, J.A.J., and Wickramasinge, D.T., 1976, IAU Circ. No.
    2957.

McCray, R., 1977, Highlights of Astr., Vol. 4, Part I, 155.

McCray, R., and Hatchett, S., 1975, Ap. J., 199, 196.

McCray, R., and Lamb, F.K., 1976, Ap. J. (Letters), 204, L115.

McGee, R.X., Milton, J.A., and Wolfe, W., 1966, Austr. J. Phys. Suppl,
    No. 1.

Milton, S., 1977, ed., The Cambridge Encyclopaedia of Astronomy, New York:
    Crown Publishers, Inc.

Motch, C., Ilovaisky, S.A., and Chevalier, C., 1983, Astron. Astrophys.,
    109, L1.

Murdin, P.G., 1972, M.N.R.A.S., 157, 461.

Murdin, P., et al., 1980, Astron. Astrophys., 87, 292.

Nicolson, G.D., Feast, M.W., and Glass, I.S., 1980, M.N.R.A.S., 191, 293.

Nolan, P., 1982, Ph.D. thesis, Univ. Calif. San Diego.

Novikov, I.D., and Thorne, K.S., 1973, in Black Holes, Les Houches, C.
    DeWitt and B. DeWitt (eds), New York: Gordon and Breach, p. 343.

Oda, M. et al., 1971, Ap. J. (Letters), 166, L1.

Oppenheimer, J.R., and Snyder, H., 1939, Phys. Rev., 56, 455.

Oppenheimer, J.R., and Volkoff, G.M., 1939, Phys. Rev., 55, 374.

Pacholczyk, A.G., 1970, Radio Astrophysics, W.H. Freeman and Co.,
    San Francisco.

Paczynski, B., 1971, Ann. Rev. Astron. Astrophys., 9, 183.

Pannekoek, A. 1969, A History of Astronomy, New York: Barnes and Noble,
    Inc.

Papaloizou, J., and Pringle, J.E., 1977, M.N.R.A.S. 181, 441.

Petterson, J.A., 1978, Ap. J., 224, 625.

Pilkington, J.D.H., et al., 1968, Nature, 218, 126.

Pravdo, S.H., 1976, Ph.D. thesis, Univ. Maryland.

Pravdo, S.H., 1979, X-Ray Astronomy, (ed. W. Baity and L. Peterson), Oxford:Pergamon, p. 169.

Pravdo, S.H., and Smith, B.W., 1979, Ap. J. (Letters), 234, L195.

Preston, R.A., et al., 1983, Ap. J. (Letters), 268 L23.

Priedhorsky, W.C., 1978, Ph.D. thesis, Cal. Tech.

Pringle, J.E., 1973, Nature Phys. Sci., 243, 90.

Pringle, J.E., 1976, M.N.R.A.S., 177, 65.

Pringle, J.E., 1977, M.N.R.A.S., 178, 195.

Pringle, J.E., 1981, Ann. Rev. Astron. Astrophys., 19, 137.

Pringle, J.E., 1982, Accreting Neutron Stars, (ed. W. Brinkmann and J. Trumper), p. 150.

Pringle, J.E., and Rees, M.J., 1972, Astron. Astrophys., 21, 1.

Pringle, J.E., and Savonije, G.J., 1979, M.N.R.A.S., 187, 777.

Raymond, J.C., and Smith, B.W., 1977, Ap. J. Suppl., 35, 419.

Rees, M.J., 1974, Highlights of Astronomy, 89 (ed. Contopoulos).

Ricketts, M.J., 1983, Astr. Ap., 118, L3.

Robinson-Saba, J.L., Tennant, A.F., and Swank, J.H., 1983, in preparation.

Ross, R.R., Weaver, R., and McCray, R., 1978, Ap. J., 219, 292.

Rossi, B., 1952, High Energy Particles, Prentice-Hall, Inc., Englewood Cliffs, N.J.

Rossi, B.B., and Staub, H.H., 1949, Ionization Chambers and Counters: Experimental Techniques, New York: McGraw-Hill Book Company, Inc.

Rothschild, R., et al., 1979, Space Sci. Instr., 4, 269.

Ruffini, R., 1975, Proc. Internat. Conf. X-Rays in Space, ed. D. Venkatesan, Univ. of Calgary.

Rybicki, G.B., and Lightman, A.P., 1979, Radiative Processes in Astrophysics, New York: John Wiley and Sons.

Ryle, M., et al., 1978, Nature, 276, 571.

Saba, J.R., Boldt, E.A., Holt, S.S., Serlemitsos, P.J., and Swank, J.H., 1977, Bull. Am. Astron. Soc., 9, 297.

Sadeh, D., et al., 1979, Nature, 278, 436.

Samimi, J., et al., 1979, Nature, 278, 434.

Savonije, G.J., 1978, Astron. Astrophys., 62, 317.

Savonije, G.J., 1979, Astron. Astrophys., 71, 352.

Schreier, E.J., et al., 1976, Ap. J. (Letters), 170, 221.

Seaquist, E.R., Gilmore, W.S., Johnston, K.J., and Grindlay, J.E., 1982, Ap. J., 260, 220.

Sedov, L.I., 1959, Similarity and Dimensional Methods in Mechanics, New York:Academic Press.

Serlemitsos, P.J., Boldt, E.A., Holt, S.S., Rothschild, R.E., and Saba, J.L.R., 1975, Ap. J. (Letters), 201, L9.

Serlemitsos, P.J., Swank, J.H., and Saba, J.L.R., 1980, paper presented at Tenth Texas Symposium on Relativistic Astrophysics, Baltimore, Maryland.

Seward, F., 1970, An Illustrated Catalog of Cosmic X-Ray Sources, LLL Report UCID-15622.

Seward, F.D., Harnden, F.R., Jr., Murdin, P., and Clark, D., 1983, Ap. J., 267, 698.

Shakura, N.I., 1972, Astron. Zh., 49, 921.

Shakura, N.I., and Sunyaev, R.A., 1973, Astron. Astrophys., 24, 337.

Shakura, N.I., and Sunyaev, R.A., 1976, M.N.R.A.S., _175_, 613.

Shapiro, S.L., and Lightman, A.P., 1976, Ap. J., _204_, 555.

Shapiro, S.L., Lightman, A.P., and Eardley, D.M., 1976, Ap. J., _204_, 187.

Shklovskii, 1967, Ap. J. (Letters), _148_, L1.

Spada, G. _et al._, 1974, Ap. J. (Letters), _190_, L113.

Stephenson, C.B., and Sanduleak, N., 1977, Ap. J. Suppl., _33_, 459.

Sterne, T.E., 1939, M.N.R.A.S., _99_, 451.

Sutherland, P.G., Weisskopf, M.C., and Kahn, S.M., 1978, Ap. J., _219_, 1029.

Tananbaum, H., _et al_, 1972, Ap. J. (Letters), _177_, L5.

Tarter, C.B., and McKee, C.F.,1973, Ap. J. (Letters) _186_, L63.

Tennant, A.F., _et al._, 1981, Ap. J., _251_, 15.

Thomas, R.M., Duldig, M.L., Haynes, R.F., and Murdin, PG., 1978,
    M.N.R.A.S., _185_, 29p.

Thorne, K., 1974, Ap. J., _191_, 507.

Toor, A., 1977, Ap. J. (Letters), _215_, L57.

Tucker, W.H., 1975, Radiation Processes in Astrophysics, Cambridge:
    MIT Press.

Tuohy, I.R., and Davison, P.J.N., 1973, Nature Phys. Sci., _244_, 121.

van den Heuvel, E.P.J., 1975, Ap. J. (Letters), _198_, L109.

van der Laan, H., 1966, Nature, _211_, 1131.

van Paradijs, J., 1978, Nature, _274_, 650.

Verbunt, F., 1982, Space Sci. Reviews, _32_, 379.

Wall, K.C., 1982, Physics Today _35_, No. 10, 33.

Wang, Y.M., 1981, Astron. Astrophys., _102_, 36.

Webster, B.L., 1974, M.N.R.A.S., _169_, 53p.

Weisskopf, M.C., Kahn, S.M., and Sutherland, P.G., 1975, Ap. J. (Letters),
    _199_, L147.

Weisskopf, M.C., and Sutherland, P.G., 1980, Ap. J., 236, 263.

Whelan, J.A.J., et al., 1977, M.N.R.A.S., 181, 259.

White, N.E., and Holt, S.S., 1982, Ap. J., 257, 318.

White, N.E., Kallman, T.R., and Swank, J.H., 1983, Ap. J., in press.

White, N.E., and Marshall, F.E., 1983, preprint.

White, N.E., Swank, J.H., and Holt, S.S., 1983, Ap. J., in press.

Wilson, A.M., and Carpenter, G.F., 1976, Nature, 261, 295.

Zeldovich, Ya.B., and Shakura, N.I., 1969, Sov. Astr.-A.J., 13, 175.

Ziolkowski, 1978, in Nonstationary Evolution of Close Binaries, ed. A.N.

   Zythow, Polish Scientific Publishers.